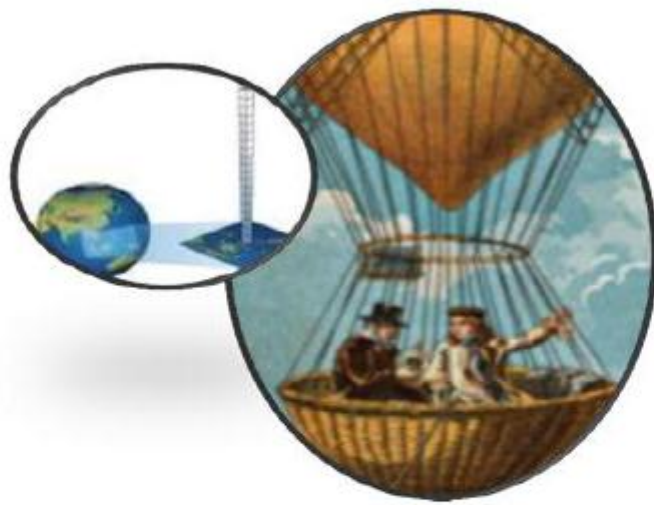


**30<sup>th</sup> Annual Conference of  
SOUTH AFRICAN SOCIETY FOR  
ATMOSPHERIC SCIENCES**



**Modelling and Observing  
the Atmosphere**

**01 - 02 OCTOBER 2014  
POTCHEFSTROOM  
SOUTH AFRICA**

**Peer Reviewed Conference Proceedings**



Peer reviewed and revised papers presented in the 30<sup>th</sup> Annual conference of South African Society for Atmospheric Sciences, 01-02 October 2014, POTCHEFSTROOM, South Africa.

**ISBN 978-0-620-62777-1**

**COPYRIGHT**

All rights reserved. No part of this publication may be reproduced or copied in any form – graphic, electronic, or mechanical, including photocopying, taping, or information storage and retrieval systems – without the prior written permission of the publisher. Contact SASAS for permission pertaining to the overall collection. Authors retain their individual rights and should be contacted directly for permission to use their material separately.

## **COMMITTEES**

### **ORGANISING COMMITTEE**

Prof Stuart Piketh

Mr Roelof Burger

Prof Sivakumar Venkataraman

Ms Michelle Fourie

Mr Jaun van Loggerenberg

### **REVIEW COMMITTEE**

Prof Stuart Piketh

Prof Mathieu Rouault

Prof Sivakumar Venkataraman

Dr Caradee Wright

Dr Micky Josipovic

Dr Scott Hersey

Dr Johan Malherbe

Mr Roelof Burger

## **PREFACE**

The 30th annual conference of South African Society for Atmospheric Sciences has been hosted for the first time at the North-West University in Potchefstroom by the Climatology Research Group (CRG). The theme for the conference was Modeling and Observing the Atmosphere. The theme was chosen to highlight the need for collaboration between researchers in South Africa that model processes to work closer with observational researchers.

The Organising Committee would like to thank all the people who have contributed in any way to the origination of the conference for 2104. These people include the SASAS officers, scientists who reviewed submitted papers and abstracts and members of the CRG who have ensured that the logistics have been organized. Special thanks are due to Michelle Fourie and Jaun van Loggerenberg. Dr Scott Hersey is also thanked for his efforts in the review process.

The two keynote speakers Prof Bruce Hewitson and Dr Rebecca Garland are also thanked for agreeing to make the time to present invited talks that we believe shed light on important topics in South African atmospheric science.

This year we have decided to ask poster presentations to also provide a 10 minute summary of their results in two dedicated conference sessions. This is a practice that I remembered from some of my first Prof. Stuart Piketh and Roelof Burger Conference Chair SASAS conferences that gave mostly student participants the opportunity to also speak to the leading members of the atmospheric community in South Africa. Development of good atmospheric scientists is a critical function of SASAS and I hope this makes a small contribution to that end.



Prof. Stuart Piketh  
Conference Chair

## **MESSAGE FROM THE PRESIDENT**

Dear Delegates

I welcome you to the 30<sup>th</sup> South African Society for Atmospheric Sciences Conference. After the successful 29<sup>th</sup> Conference held in Kwazulu-Natal and organized our vice-president Sivakumar Venkataraman and his team, it is a great pleasure to be in Potchefstroom for this special anniversary SASAS conference hosted by a group newly formed at University of North West under the leadership of Prof Stuart Piketh. This is a fantastic new location for SASAS to develop further and great news for our community. I remind you that SASAS aim is to stimulate interest and support for all branches of atmospheric sciences, to encourage research and education in the atmospheric sciences and to promote collaboration between organisations and institutions interested in atmospheric science in Southern Africa. This includes meteorology, agro-meteorology, climatology, air quality, ocean-atmosphere interaction, troposphere-stratosphere interaction, physical oceanography, hydroclimatology, numerical modelling, and instrumentation. On top of organising an annual conference since 1989, where the general assembly is also held, SASAS annually awards a prize worth R3000 for the best peer-reviewed paper published two years before the conference is held, the Stanley Jackson Award. Best presentation, best student presentation and best poster are also rewarded at the SASAS conference. Proceedings of the conference are peer reviewed and former conference papers and abstract are available on the SASAS web site. A newsletter is also produced by its members. SASAS has a web site <http://www.sasas.org.za>. At the end of the day, we compete for grants, for discoveries, for papers, for awards; and we agree or disagree on how to run things but SASAS unites everybody and the conference is one of the longest running annual conference in Africa. I encourage everybody to fill in the membership form that you will find in your bag and hand it to any of the council member before the assembly and prize giving which I also encourage you to attend. We need to grow the society and therefore welcome any suggestions to improve the society. I also remind you that we do have a constitution that can be amended by a vote by the council. This year we are going to vote for the possibility of awarding a prize every year for achievement in SASAS related field and also if we want to spend our resources on establishing a new journal. We also, will have election for the council and the executive committee.

**Professor Mathieu Rouault**  
President of SASAS

## TABLE OF CONTENTS

Conference Organizing Committee

PREFACE

Message from the President

### Peer-reviewed conference proceedings

**P1. Anthropogenic radiative forcing of southern African and Southern Hemisphere climate variability and change**

Francois A. Engelbrecht, Willem A. Landman and Thando Ndarana

**P2. Analysis of Global Model Output for Statistical Downscaling to Rainfall and Temperature for Southern Africa**

C. Olivier

**P3. Observation of Biomass Burning Aerosols at Cape Point using a GAW Precision Filter Radiometer and CALIPSO satellite**

Nkanyiso Mbatha, Stephan Nyeki, Ernst -G. Brunke and Casper Labuschagne

**P4. Geospatial (Latitudinal and Longitudinal) variability of ozone over South Africa**

Jeremiah Ogunniyi and Venkataraman Sivakumar

**P5. Aerosol properties over an urban site, Johannesburg measured from Sunphotometer**

Joseph A. Adesina, V. Sivakumar, Raghavendra K. Kumar, Stuart J. Piketh, Jyotsna Singh

**P6. A comparison of surface NO<sub>2</sub> mixing ratios and total column observations at a South African site**

Micky Josipovic, Debra W. Kollonige, Roelof P. Burger, Anne M. Thompson, Johan P. Beukes, Pieter G. van Zyl, Andrew D. Venter, Kerneels Jaars, Douglas K. Martins, Ville Vakkari, Lauri Laakso.

**P7. The Rapidly Developing Thunderstorm Product – results of case studies and future plans**

Morné Gijben, Estelle de Coning, Louis van Hemert, Cassandra Pringle and Bathobile Maseko

**P8. A study on Bio-meteorological indices for forecasting heat waves over SA**

Patience T. Shibambu and Willem A. Landman

**P9. Projections of heat waves and health impacts in Africa in a changing climate**

Rebecca M Garland, Mary-Jane Bopape, Mamopeli Matooane, and Francois Engelbrecht

**P10. FROST TRENDS ON A CITRUS FARM IN LIMPOPO, SOUTH AFRICA**

Linda De Wet and A. Stephan Steyn

**P11. The sinuous ways of SOMs**

Liesl L Dyson

**P12. Radar Characteristics of Hailstorms in South Africa**

Craig L. Powell

**P13. Study of Surface Incident Shortwave Flux over Two Major Cities of South Africa**

Jyotsna Singh and V. Sivakumar

**P14. Atmospheric Modelling for Seasonal Prediction at the CSIR**

WA Landman, FA Engelbrecht, JL McGregor and JH van der Merwe

**P15. Can intraseasonal to decadal forecasts benefit from consideration of lunar forcing ?**

Johan Malherbe, Willem A. Landman and Francois A. Engelbrecht

**P16. Impact of ENSO on South African Water Management Areas**

Mathieu Rouault

**P17. Austral summer relationship between ENSO and Southern African rainfall in CMIP5 coupled models**

Bastien Dieppois, Mathieu Rouault, Mark New

**P19. The annual cycle of Central Africa rainfall and its relationship with the surrounding tropical Oceans**

Georges-Noel Tiersmondo Longandjo and Mathieu Rouault.

**P20. Influence of the Subtropical Indian Ocean Dipole on the Agulhas Current**

Mthetho Sovara, Juliet Hermes, and Chris Reason

**P21. Separating local- and synoptic-scale variability in African rainfall**

Piotr Wolski, Chris Jack, Mark Tadross, Lisa Coop, Bruce Hewitson Mthetho Sovara, Juliet Hermes, and Chris Reason

**P22. PREDICTABILITY OF DIFFERENT RAINFALL THRESHOLD VALUES FOR AUSTRAL SUMMER SEASONS OVER SOUTH AFRICA**

Steven Phakula

**P24. Clustering Forecast System for Southern Africa SWFDP**

Stephanie Landman<sup>1</sup> and Susanna Hopsch

**P25. Climate change and potato production in South Africa: impacts on yield and water use efficiency, and possibilities for adaptation**

A.C. Franke , J.M. Steyn , A.J. Haverkort

**P26. Comparison study on high resolution rainfall forecast verification techniques**

Anika Liebenberg and Stephanie Landman

**P27. Study on variability and trend of Total Column Ozone (TCO) obtained from combined satellite (TOMS and OMI) measurements over the southern subtropic**

Abdoulwahab M. Tohir, Venkataraman Sivakumar, Thierry Portafaix and Hassan Bencherif

**P28. Maize yield simulations for small-scale farmers using APSIM for making on-farm decisions in Bethlehem and Bloemfontein, South Africa**

Cassia N Mlangeni, Linda De Wet and Weldemichael A Tesfuhune

**P29. Influence of horizontal resolution and ensemble size on model performance**

Amaris Dalton, Willem A. Landman

**P30. Stability, accuracy and conservation properties of a flux-form advection scheme.**

Michael A. Barnes and Francois A. Engelbrecht

**P31. SPATIAL AND TEMPORAL ASSESSMENT OF ATMOSPHERIC OC AND BC CONCENTRATIONS AT SOUTH AFRICAN DEBITS SITES**

Petra Maritz, Paul J. Beukes, Pieter G. Van Zyl, Engela H. Conradie, Corinne Galy-Lacaux, Cathy Liousse

**P32. AEROSOL OPTICAL DEPTH MEASUREMENTS OVER PRETORIA USING CSIR LIDAR AND SUN-PHOTOMETER: A CASE STUDY**

Lerato Shikwambana and Venkataraman Sivakumar

# Anthropogenic radiative forcing of southern African and Southern Hemisphere climate variability and change

Francois A. Engelbrecht<sup>1,2</sup>, Willem A. Landman<sup>1,3</sup> and Thando Ndarana<sup>1</sup>

<sup>1</sup> CSIR Natural Resources and the Environment – Climate Studies, Modelling and Environmental Health, Pretoria, 0001, South Africa, [fengelbrecht@csir.co.za](mailto:fengelbrecht@csir.co.za)

<sup>2</sup> Department of Geography, Archaeology and Environmental Sciences, University of the Witwatersrand, Johannesburg, South Africa

<sup>3</sup> Department of Geography, Geoinformatics and Meteorology, University of Pretoria, Pretoria, South Africa  
[tndarana@csir.co.za](mailto:tndarana@csir.co.za), [walandman@csir.co.za](mailto:walandman@csir.co.za)

This paper explores the hypothesis that the more realistic depiction of the atmosphere's ability to absorb and release radiation in atmospheric model simulations, through the more realistic representation of the time-varying concentrations of stratospheric ozone, greenhouse gasses, aerosols and sulphur dioxide, can improve the model's skill to simulate inter-annual variability over southern Africa. The paper secondly explores the role of different radiative forcings of future climate change over southern Africa and the Southern Hemisphere. Through a set of AMIP-style experiments, it is demonstrated that including the direct (radiative) effects of aerosols in the simulations decreases the model's bias in simulating near-surface temperatures. Trends in near-surface temperatures are more realistically simulated in the presence of time-varying vs climatological CO<sub>2</sub>. The inclusion of time-varying ozone concentrations, and in particular Antarctic stratospheric ozone, leads to an improvement in model skill in simulating the inter-annual variability in rainfall and circulation over southern Africa. Evidence is presented that radiative forcing from anomalous Antarctic stratospheric ozone played a role in the failure of the teleconnection to southern Africa during the 1997/1998 El Niño. Despite the recovery of stratospheric ozone concentrations to pre-industrial values during the 21<sup>st</sup> century, a pronounced poleward displacement of the westerlies is projected to occur in response to the enhanced greenhouse effect.

*Keywords:* Antarctic stratospheric ozone, enhanced greenhouse effect, AMIP simulations, CCAM.

## 1. Introduction

The objective of this research is to explore the stratospheric and tropospheric radiative forcing of climate variability and change over the Southern Ocean and southern Africa, through a number of climate simulation experiments and dynamic analysis. An atmospheric global circulation model (AGCM), the conformal-cubic atmospheric model (CCAM) is used to perform these experiments. The main hypothesis is that the inclusion of different sources of time-dependent radiative forcing (stratospheric ozone, greenhouse gasses, aerosols and sulphur dioxide concentrations) in model simulations can improve the skill of simulating inter-annual variability, trends and future climate change over the Southern Hemisphere and southern Africa. In many state-of-the-art seasonal forecasting systems applied over the Southern Hemisphere, these forms of time-varying radiative forcing are not included as forms of atmospheric forcing - the long-term climatological averages of these gasses are used instead. One possible reason for the current

situation is the assumption that seasonal forecast skill largely exists due to the lower boundary forcing of the atmosphere by the ocean. Due to the large heat capacity of the ocean, prognostic sea-surface temperature (SST) forcing can be readily included in seasonal forecasting systems, using either persisted or predicted SSTs. Such conventional forecast systems have demonstrated skill in predicting summer rainfall totals over southern Africa. The extent to which updated radiative forcing descriptions can improve the skill of seasonal forecasts over southern Africa remains to be quantified.

Of key importance at climate change time scales is the interplay between stratospheric ozone, which is expected to gradually recover from the currently depleted levels during the 21<sup>st</sup> century, and tropospheric greenhouse gas concentrations, which are expected to continue to rise.

## 2. The conformal-cubic atmospheric model and experimental design

CCAM is a variable-resolution global atmospheric model, developed by the Commonwealth Scientific and Industrial Research Organisation (CSIRO) in Australia (McGregor, 1996, 2005a, 2005b; McGregor and Dix, 2001, 2008). It employs a semi-implicit semi-Lagrangian method to solve the hydrostatic primitive equations. The model includes a fairly comprehensive set of physical parameterizations. The GFDL parameterizations for long-wave and short-wave radiation are employed, with interactive cloud distributions determined by the liquid and ice-water scheme of Rotstajn (1997). A stability-dependent boundary layer scheme based on Monin Obukhov similarity theory is employed (McGregor et al., 1993), together with the non-local treatment of Holtslag and Boville (1993). A canopy scheme is included, as described by Kowalczyk et al. (1994), having six layers for soil temperatures, six layers for soil moisture (solving Richard's equation) and three layers for snow. The cumulus convection scheme uses a mass-flux closure, as described by McGregor (2003), and includes downdrafts, entrainment and detrainment.

CCAM may be applied at quasi-uniform resolution, or alternatively in stretched-grid mode to obtain high resolution over an area of interest. Fig. 1 shows a quasi-uniform conformal-cubic grid, of C48 (about 200 km) resolution.

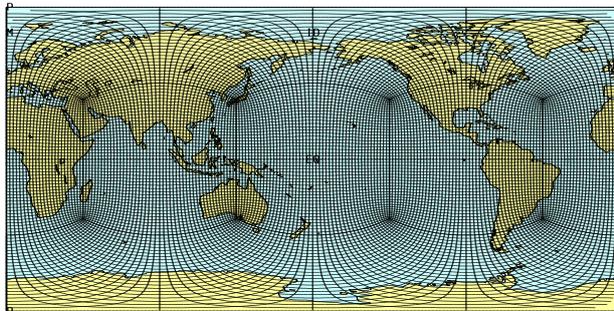


Figure 1. C48 quasi-uniform conformal-cubic grid, which provides a horizontal resolution of about 200 km globally.

In order for the potential improvements stemming from the inclusion of various forms of radiative forcing in model simulations to be objectively determined, a control experiment was conducted first. Here the model was forced with the climatological average concentrations of CO<sub>2</sub> and ozone, and with aerosol and sulphur dioxide values set to zero. This set-up corresponds to that of the current standard set-up when using CCAM for seasonal forecasting at the CSIR. The quasi-

uniform grid displayed in Fig. 1 was used for the control experiment simulations. Lower boundary forcing was provided from observed monthly SSTs and sea-ice). That is, the control experiment is a typical Atmospheric Model Intercomparison Project (AMIP) experiment. The simulations span the period February 1978 to November 2005. An ensemble of simulations was obtained, using a lagged-average forecasting approach, with each ensemble member initialised during a different day of February 1978. For the case of the time-varying radiative forcing experiments, additional AMIP-style simulations were performed. A first ensemble (Experiment 1) was obtained following the experimental design of the control experiment, with the exception that the climatological average CO<sub>2</sub> concentrations were replaced with the actual observed, annually-varying values. The second ensemble (Experiment 2) resembled the control experiment, but with the climatological values of ozone concentrations replaced with time-varying values. The third experiment added time-varying values of aerosols and SO<sub>2</sub> to control experiment, but kept ozone and CO<sub>2</sub> levels at climatological values. The fourth experiment is supposedly the closest to reality, as it was forced by the time varying descriptions for ozone, CO<sub>2</sub>, aerosols and SO<sub>2</sub>.

In addition to the radiative forcing simulations described above, an additional set of simulations was performed for the period 1961-2100, also on the C48 quasi-homogeneous grid, in order to investigate the interplay between recovering stratospheric ozone and increasing greenhouse gas concentrations during the 21st century. In these simulations CCAM was forced at its lower boundary with the simulated SST and sea-ice of six different coupled global climate models (CGCMs), but with all the coupled models responding to radiative forcing from the A2 scenario of the Special Report on Emission Scenarios (SRES).

In all these simulations the model was integrated using 18 levels in the vertical. It may be noted that performing the simulations was reasonably time-intensive, and relied on the use of the computer clusters of Centre for High Performance Computing (CHPC) in South Africa.

## 3. Results and discussion

Figure 3 shows the difference between the 1000 hPa heights of the simulations forced with observed stratospheric ozone (Experiment 3), and those forced with climatological ozone concentrations (control experiment), for the 1997/1998 austral summer (December to February). This season was selected because it was characterised by an exceptionally strong El Niño event, sometimes

referred to as “the El Niño of the century”. However, the usual teleconnection between the Pacific Ocean and southern Africa failed during this event, and as a result the region experienced a normal rainfall season (instead of a typical El Niño induced drought). The seasonal forecasts of the South African Weather Service as well as those of all the leading international seasonal forecasting centres failed for that season. The simulations incorporating the effects of stratospheric ozone forcing of Southern Hemisphere climate variability provide a possible explanation of the failure of the teleconnection during this year (and the failure of typical seasonal forecasting systems to skilfully project rainfall anomalies over southern Africa during the 1997/98 summer). The results indicate that stratospheric ozone anomalies induced a pronounced pole-to-equator pressure gradient across the Southern Ocean during DJF of 1997/1998. This culminated in below-normal atmospheric pressure over the southern African interior, an anomaly that is generally favourable of rainfall over the region (Figure 2).

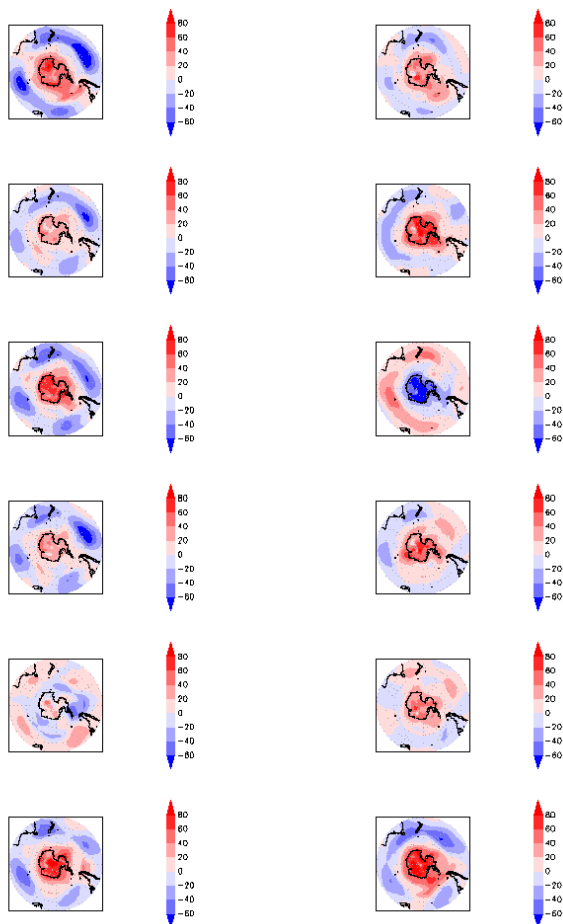


Figure 2. 1000 hPa geopotential difference between the simulations forced with observed stratospheric ozone concentrations and the control experiment, for the DJF of 1997/1998.

Statistical verification of the skill of the different experiments in representing southern African climate and its variability yield the following key results:

- Incorporating the effects of aerosols in the simulations (Experiment 3) reduces the model bias in simulating near-surface air temperatures, through the simulation of aerosol direct effects (that is, radiative cooling effects associated with aerosols).
- Incorporating time-varying CO<sub>2</sub> concentrations (Experiment 1) improves the model simulations of temperature trends over southern Africa (compared to the trends simulated in the control experiment). That is, although the SSTs used for lower boundary forcing in the control experiment implicitly describes the rise in global temperature in response to the enhanced greenhouse effect, direct description of atmospheric radiative forcing by increasing greenhouse gas concentrations leads to the more realistic simulation of temperature trends over southern Africa.
- Model skill in simulating the inter-annual variability in rainfall totals is improved through incorporating time-varying ozone concentrations in the experiments. This is thought to be the result of improved simulation of stratospheric-tropospheric coupling, which occurs in response to anomalous Antarctic stratospheric ozone concentrations and temperatures in spring.
- Experiment 4, incorporating the time-varying effects of aerosols, SO<sub>2</sub>, CO<sub>2</sub> and ozone, is the most skilful in representing climate variability over southern Africa.

One of the most well-documented changes in hemispheric circulation changes that have occurred to date in response to enhanced anthropogenic forcing is the poleward displacement of the westerlies (in the Southern Hemisphere). This is thought to be the result of the combined effects of stratospheric ozone depletion and the enhanced greenhouse effect. However, stratospheric ozone concentrations are recovering as a result of the implementation to the Montreal protocol, with full recovery expected to have taken place by the mid-21<sup>st</sup> century.

Figure 3 illustrates the projected 1000 hPa wind anomalies for July for the far future (2071-2100) relative to present-day conditions (1961-1990). The figure is for one of the six CGCMs downscaled using CCAM. These results are indicative of a pronounced poleward displacement of the westerlies, even for the far-future where stratospheric ozone concentrations have recovered to pre-industrial concentrations. The poleward displacement of the westerlies during winter is the primary reason for the projected

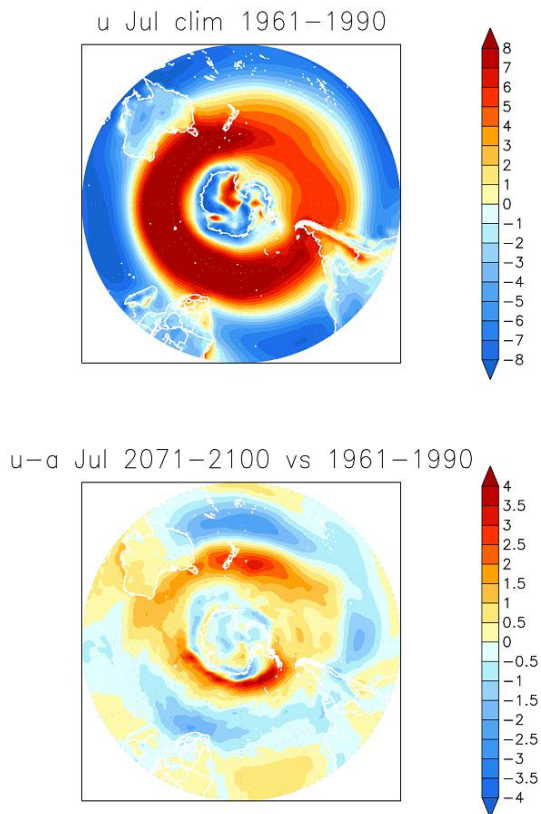


Figure 3. July meridional displacements in the westerlies over the Southern Ocean under climate change.

decrease in winter rainfall over the southwestern Cape region of South Africa (e.g. Engelbrecht et al., 2009). For summer, the poleward displacement of the westerlies implies relatively stronger easterlies, which may well be favourable for rainfall over the eastern interior of southern Africa.

#### 4. Conclusions

A set of AMIP-style experiments aimed at describing the effects of time-varying radiative forcing on southern African climate variability and change have been performed. Inclusion of the direct (radiative forcing) effects of aerosols result in a reduction in the near-surface temperature biases simulated by the model. Regional temperature trends are captured more realistically in the presence of time-varying vs climatological CO<sub>2</sub> concentrations. The inclusion of time-varying ozone concentrations leads to an improvement in simulating the skill of inter-annual variability and circulation over southern Africa. Preliminary results indicate that anomalous stratospheric ozone forcing may have caused the failure of the teleconnection between the Pacific Ocean and southern Africa during the exceptionally strong El Niño event of DJF 1997/1998. Under conditions of enhanced anthropogenic forcing, the poleward displacement of the westerlies is plausible to induce rainfall

decreases over the southwestern Cape in winter, and rainfall increases over the eastern interior in summer.

#### 5. References

- Engelbrecht FA, McGregor JL and Engelbrecht CJ 2009. Dynamics of the conformal-cubic atmospheric model projected climate-change signal over southern Africa. *International Journal of Climatology* 29, 1013-1033. DOI: 10/1002/joc.1742. 29 1013-1033.
- Holtslag AAM and Boville BA. 1993. Local versus non-local boundary layer diffusion in a global climate model. *J. Climate* 6 1825-1842.
- Kowalczyk EA, Wang, Law RM, Davies HL, McGregor JL and Abramowitz G. 2006. The CSIRO Atmosphere Biosphere Land Exchange (CABLE) model for use in climate models and as an offline model. CSIRO Marine and Atmospheric Research Paper 13, 37 pp.
- McGregor JL, Gordon HB, Watterson IG, Dix MR and Rotstayn LD. 1993. The CSIRO 9-level atmospheric general circulation model. CSIRO Div. Atmospheric Research Tech. Paper No. 26, 89 pp.
- McGregor JL (1996) Semi-Lagrangian advection on conformal-cubic grids. *Mon. Wea. Rev.* 124 1311-1322.
- McGregor JL. 2003. A new convection scheme using a simple closure. In "Current issues in the parameterization of convection", BMRC Research Report 93, 33-36.
- McGregor JL. 2005a. Geostrophic adjustment for reversibly staggered grids. *Mon. Wea. Rev.*, 133, 1119-1128.
- McGregor JL. 2005b. C-CAM: Geometric aspects and dynamical formulation. CSIRO Atmospheric research Tech. Paper No. 70, 43 pp.
- McGregor JL and Dix MR. 2001. The CSIRO conformal-cubic atmospheric GCM. In IUTAM Symposium on Advances in Mathematical Modelling of Atmosphere and Ocean Dynamics, P. F. Hodnett (Ed.), Kluwer, Dordrecht, 197-202.
- McGregor JL and Dix MR. 2008. An updated description of the Conformal-Cubic Atmospheric Model. In *High Resolution Simulation of the Atmosphere and Ocean*, eds. K. Hamilton and W. Ohfuchi, Springer, 51-76.
- Rotstayn LD. 1997. A physically based scheme for the treatment of stratiform clouds and precipitation in large-scale models. I: Description and evaluation of the microphysical processes. *Quart. J. Roy. Meteor. Soc.*, 123 1227-1282.

#### Acknowledgements

The WRC is acknowledged for support of the research through project K5/2163.

# Analysis of Global Model Output for Statistical Downscaling to Rainfall and Temperature for Southern Africa

C. Olivier<sup>\*1</sup>

<sup>1</sup>South African Weather Service, 442 Rigel Avenue South, Erasmusrand, Pretoria, Gauteng, South Africa, [cobus.olivier@weathersa.co.za](mailto:cobus.olivier@weathersa.co.za)

Past and current statistical prediction studies of seasonal rainfall and temperature for southern Africa has mostly been focused on the mid-summer season. This is and has been done for good reason, as the predictability outside of the mid-summer season is very limited. However, given the fact that an operational center produces seasonal predictions every month for all seasons in a period of one year, it is important to regularly investigate the all-round performance especially when model configurations and observed datasets update and improve. The purpose then for this study is to reinvestigate the all-round performance of the GCM-MOS seasonal prediction approach, which was done in the past by one comprehensive project, by updating the use of the most recent model configurations, the latest observed datasets and in some part investigate the effect of various predictors. The study finds that there are still major prediction challenges for seasons outside mid-summer, indicating that even though there has been marked advances within the global modeling, this has had little effect on the current seasonal prediction system for southern Africa. This study however has only scratched the surface of GCM-MOS simulations, even though some 160 simulations was done, as comprehensive model and predictor combination schemes has not been explored here. Even though results may not have been ground-braking or even surprising, the operational usefulness from a viewpoint of risk in using a particular prediction is unquestionable.

*Keywords:* Seasonal Prediction, Statistical Downscaling

## 1. Introduction

In the past decade or so, numerous studies have been done on the seasonal prediction of specifically seasonal rainfall totals in southern Africa, for mostly the mid-summer season. Some of the first comprehensive studies to investigate the use of model output statistics (MOS; Wilks 2011) on global circulation model's (GCM's) was Landman and Tennant 2000 and Landman and Goddard 2002 and Landman et al 2009, the latter it should be noted explored the skill for the four main seasons as well. More recent studies also exist such as Landman and Beraki 2012 and Landman et al 2012, the former investigating the benefits of a multi-model approach and the latter investigating the differences between one- and two-tiered global prediction systems. Again most of the focus of these recent studies is on the austral summer period, but for an operational meteorological center such as the South African Weather Service (SAWS) which has the mandate to produce predictions all year round, and maintain and update its prediction systems in the foreseeable future, it is necessary to not only evaluate its operational monthly seasonal prediction system for every season but also to update the prediction system regularly with the latest model configurations and observed data sets.

This paper then attempts to show the predictability for four main seasons of the year, using the same prediction system as the studies mentioned above namely a GCM-MOS approach, but updating the system with the latest GCM configurations and observed datasets.

## 2. Data and Methods

### 2.1 Temperature and Rainfall Datasets

This study will be using the latest Climatic Research Unit (CRU) Time Series (TS) dataset version 3.21 (Jones and Harris 2012). This latest dataset spans from 1901-2012 and include monthly rainfall and monthly average temperature available globally. The spatial resolution of this dataset is a 0.5 degree global grid which is calculated from more than 4000 weather stations. The seasonal average temperature and seasonal total precipitation is calculated for the corresponding GCM hindcast period from 1982-2010.

### 2.2 Global Model Datasets

Three global models will be used for the purposes of this project, two which are operationally maintained at SAWS and one administered by the National Centre for Environmental Prediction

(NCEP). The two local systems at SAWS are the two-tiered (uncoupled) ECHAM4.5 Atmospheric GCM (AGCM) (Roeckner 1996) and a one-tiered (coupled) ECHAM4.5-MOM3-SA Ocean-Atmosphere GCM (OAGCM) (Beraki et al 2013). The NCEP model is the second version of the Climate Forecasting System (CFS) (Saha et al 2014) and is a fully coupled ocean-atmosphere-land model. All three of these models cover the period of interest from 1982-2010. As a further addition for analysis, these three models will also be combined to create a multi-model scenario to be downscaled alongside the three individual models. For this paper a simple combination will be used, by simply averaging the model fields after each model's respective anomaly fields have been added to an observed climatological background, this is an attempt to remove each individual model's mean bias before the combination procedure. The NCEP-DOE Reanalysis version 2 (Kanamitsu et al 2002) was used for an observational dataset of the circulation patterns (specified in the methodology section below) from which the climatology was calculated.

### 2.3 Methodology – Statistical Downscaling

As mentioned above a similar GCM-MOS procedure will be followed as previous studies and indeed the operational procedure employed at the SAWS. The downscaling procedure is entirely done by the Climate Predictability Tool (CPT; developed by the International Research Institute for Climate and Society (IRI)). This statistical downscaling software is used here with a Canonical Correlation Analysis (CCA; Barnett and Preisendorfer 1987) approach to set up the MOS equations for each individual model's (including the multi-model) circulation fields. Five circulation fields was selected based on previous study's results and motivations such as Landman et al 2000 and Landman and Goddard 2002. These fields are 850hPa, 700hPa and 500hPa geopotential heights as well as the 850hPa-700hPa and 850hPa-500hPa thickness fields, all at a 1-month lead time. The predictor fields (model fields) are restricted to an area around the southern Africa subcontinent (20N-50S; 20W-70E) while the predictand (rainfall and temperature) is restricted to an area which includes the southern Africa subcontinent south of the northern Zimbabwean border (15S-36S; 10E-40E). A retro-active analysis is done to mimic a true operational setup and produce a verifiable forecast dataset that is independent of data used in the creation of the MOS equations. To this end a 12-year training period was selected to calculate the equations and apply to the next 16-years hindcast data to be verified. The four main seasons to be evaluated is December-January-February (DJF), March-April-May (MAM), June-July-August (JJA) and

September-October-November (SON). The Relative Operating Characteristic (ROC; Wilks 2011) area scores (averaged over the predictand area) will be the main verification score with selected spatial ROC scores to indicate the general spatial distribution of skill. ROC scores is a discrimination based technique comparing hit and false-alarm rates for the three equally-probable categories (above-normal, near-normal and below-normal) for which predictions are made. However ROC scores can only be considered a potential skill measure as it is insensitive to conditional and unconditional biases. Only if perfect calibration of predictions are achieved, can it be considered actual skill. It is generally advised that reliability diagrams be utilized along with ROC scores for a comprehensive probabilistic skill analysis of the prediction system.

### 3. Results and Discussion

A total of 160 downscaling simulations was performed, four models (CFSv2, ECHAM4.5 AGCM, ECHAM4.5-MOM3-SA, Multi-model), five predictors (850hPa, 700hPa, 500hPa, 850hPa-700hPa thickness, 850hPa-500hPa thickness), two predictand's (Total rainfall, Average temperature) and four target seasons (DJF, MAM, JJA, SON) at a 1-month lead time. Figures 1 and 2 show the ROC area scores for the above-normal and below-normal total precipitation probability categories respectively. Figures 3 and 4 show the same but for average temperature.

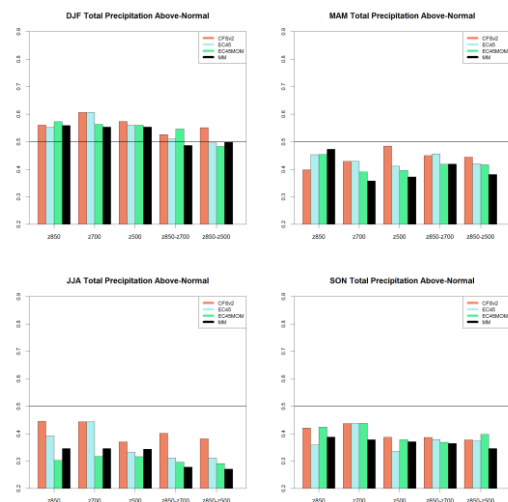


Figure 1: ROC area scores for all models and predictors for DJF (top left), MAM (top right), JJA (bottom left) and SON (bottom right) for the above-normal probability category.

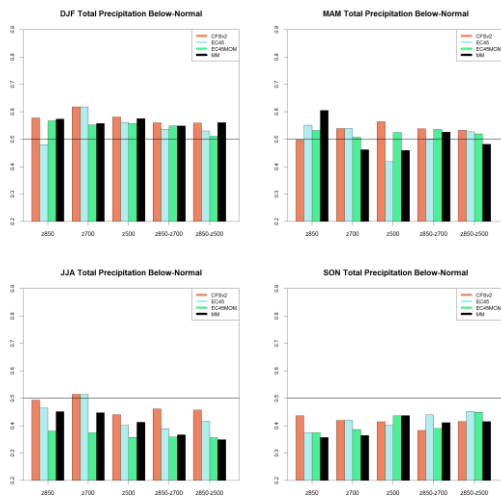


Figure 2: As Figure 1, for the below-normal probability category.

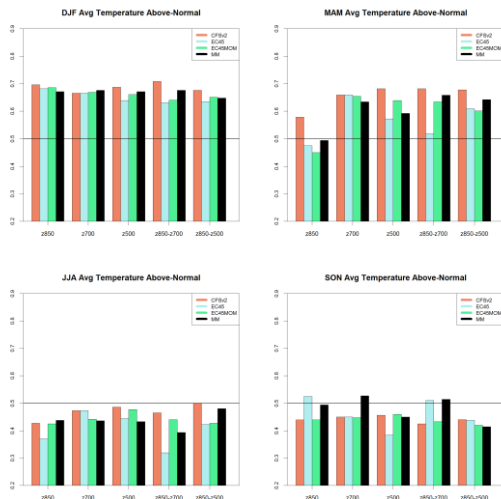


Figure 3: As Figure 1, for average temperature.

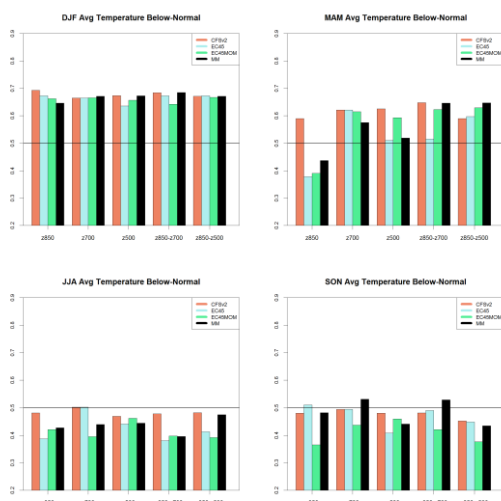


Figure 4: As Figure 2, for average temperature.

From the above figures it is clear that, considering all predictors used in this study, that summer (DJF) season is the most predictable season for rainfall and temperature, with autumn (MAM) showing some usable skill levels for mostly only temperature. The winter (JJA) and spring (SON) seasons struggle across the board with notably only the multi-model exhibiting some useful skill for temperature. It should be noted that most predictors perform relatively equally with the notable exception of MAM temperatures where the 850hPa predictor for all models are subpar, especially the two ECHAM4.5 models. These figures are however overall scores averaged for the area of interest, the spatial ROC scores is often more revealing on where in the area of interest one finds useful skill. Considering that there are 160 simulations it is obviously not feasible to present them all in this paper, and for that reason we will only discuss summer (DJF) and winter (JJA) rainfall and temperature for the multi-model here. Figures 5 and 6 show the above- and below-normal ROC scores in summer (DJF) for rainfall and temperature respectively. Figures 7 and 8 show the same but for winter (JJA).

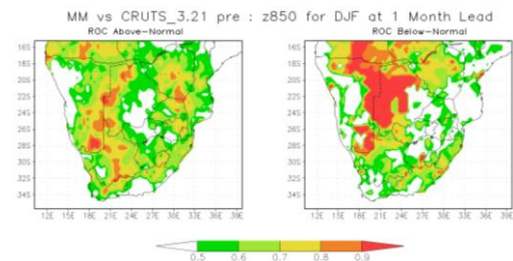


Figure 5: Spatial ROC scores for above- (left) and below-normal (right) summer (DJF) total rainfall for the multi-model (MM) 850hPa geopotential heights.

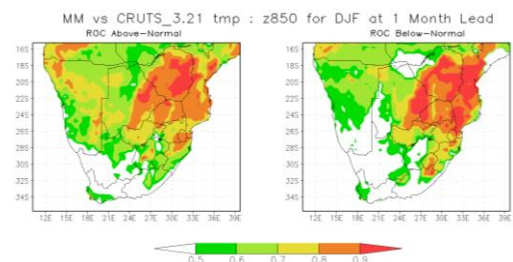


Figure 6: As Figure 5, for average temperature.

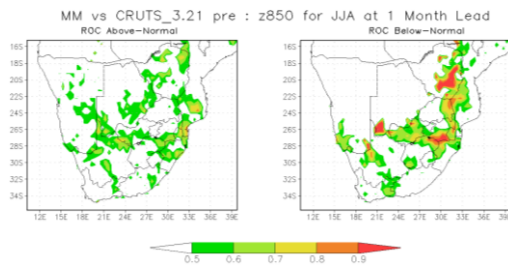


Figure 7: As Figure 5, for winter (JJA).

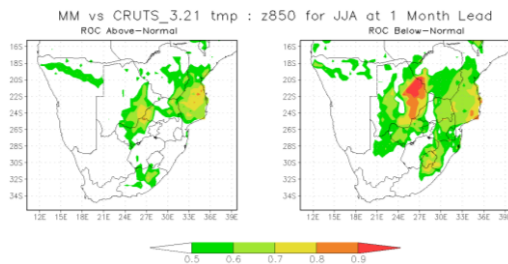


Figure 8: As Figure 6, for winter (JJA).

Most of the model-predictor scenarios indicate similar spatial distribution of above- and below-normal ROC scores for the same respective season. Some notable results are that 500hPa geopotential heights have a better spatial distribution of usable skill in the below-normal category for total rainfall, and for both above- and below-normal categories for average temperature in summer (DJF). Winter (JJA) ROC scores for southern Africa remain very low with the exception of localized areas, which unfortunately do not include winter rainfall areas of the south west.

#### 4. Conclusions

The predictability of total rainfall and average temperature remain a significant challenge outside the mid-summer season, it is however important to note that the overall averaged scores, although easier to interpret given a multitude of simulations, can in some cases be misleading with regards to the spatial extent. The specific method of combining the three models into a multi-model also does not seem to be ideal as single model simulations frequently outscore this multi-model setup. Even though this paper has focused on the relative skill differences with regards to models, predictors and seasons, the bottom line aim is to inform or remind the user community about the stark differences in predictability of summer rainfall and temperature predictions to that of the other main seasons of autumn, winter and spring. Moving forward, there is still massive amounts of work to be done in order to improve predictions for these seasons including the improvement of GCM's, multi-model combination

schemes as well as predictor combination and selection schemes.

#### 5. References

Barnett, T. P., & Preisendorfer, R. (1987). Origins and levels of monthly and seasonal forecast skill for United States surface air temperatures determined by canonical correlation analysis. *Monthly Weather Review*, 115(9), 1825-1850.

Beraki, A. F., DeWitt, D. G., Landman, W. A., & Olivier, C. (2014). Dynamical Seasonal Climate Prediction Using an Ocean-Atmosphere Coupled Climate Model Developed in Partnership between South Africa and the IRI. *Journal of Climate*, 27(4), 1719-1741.

Jones, P., & Harris, I. (2012). University of East Anglia Climatic Research Unit (CRU) Time Series (TS) high resolution gridded data version 3.20. NCAS British Atmospheric Data Centre.

Kanamitsu, M., Ebisuzaki, W., Woollen, J., Yang, S. K., Hnilo, J. J., Fiorino, M., & Potter, G. L. (2002). Ncep-doe amip-ii reanalysis (r-2). *Bulletin of the American Meteorological Society*, 83(11), 1631-1643.

Landman, W. A., & Tennant, W. J. (2000). Statistical downscaling of monthly forecasts. *International Journal of Climatology*, 20(13), 1521-1532.

Landman, W. A., & Goddard, L. (2002). Statistical recalibration of GCM forecasts over southern Africa using model output statistics. *Journal of Climate*, 15(15), 2038-2055.

Landman, W. A., Engelbrecht, F. A., Beraki, A., Engelbrecht, C., Mbedzi, M., Gill, T., & Ntsangwane, L. (2009). Model output statistics applied to multi-model ensemble long-range forecasts over South Africa. *Water Research Commission, Pretoria, Project Report*.

Landman, W. A., & Beraki, A. (2012). Multi-model forecast skill for mid-summer rainfall over southern Africa. *International Journal of Climatology*, 32(2), 303-314.

Landman, W. A., DeWitt, D., Lee, D. E., Beraki, A., & Lötter, D. (2012). Seasonal rainfall prediction skill over South Africa: one-versus two-tiered forecasting systems. *Weather and Forecasting*, 27(2), 489-501.

Roeckner, E., & Arpe, K. Coauthors, 1996: The atmospheric general circulation model ECHAM-4: Model description and simulation of present-day climate. *Max-Planck-Institut für Meteorologie Rep*, 218, 90.

Saha, S., Moorthi, S., Wu, X., Wang, J., Nadiga, S., Tripp, P., ... & Becker, E. (2014). The NCEP climate forecast system version 2. *Journal of Climate*, 27(6), 2185-2208.

Wilks, D. S. (2011). *Statistical methods in the atmospheric sciences* (Vol. 100). Academic press.

# Observation of Biomass Burning Aerosols at Cape Point using a GAW Precision Filter Radiometer and CALIPSO satellite

Nkanyiso Mbatha<sup>\*1</sup>, Stephan Nyeki<sup>2</sup>, Ernst -G. Brunke<sup>1</sup> and Casper Labuschagne<sup>1</sup>

<sup>1</sup> South African Weather Service, c/o CSIR, P.O. Box 320,

Stellenbosch 7599, South Africa, Nkanyiso.Mbatha@weathersa.co.za

<sup>2</sup> PMOD/WRC, Dorfstrasse 33, CH-7260 Davos, Switzerland, stephan.nyeki@pmodwrc.ch

In this study, a Precision Filter Radiometer (PFR) installed in Cape Point (CPT) Global Atmospheric Watch (GAW) station (34.36°S, 18.49°E) together with the overpasses of the Cloud-Aerosol Lidar and Infrared Pathfinder (CALIPSO) satellite are used for the first time to study a biomass burning event over the Western Cape, South Africa. Concentrations of Radon (<sup>222</sup>Rn) measured at CPT-GAW station were used to identify the origin of air masses in terms of continental or marine during the biomass burning episode. Special attention was given to the biomass burning episode that took place between the 4<sup>th</sup> and the 10<sup>th</sup> of April 2014. Both AOD and other trace gases (e.g. CO and O<sub>3</sub>) display strong temporal variation which correlated with the arrival of the continental air over the station. The CALIPSO satellite also reflected high total backscatter coefficients during the biomass burning event.

**Keywords:** Aerosols, AOD, PFR, CALIPSO, Biomass, Burning.

masses over CPT-GAW station during the month of April 2014.

## 1. Introduction

A continuous study of the injection of biomass burning aerosols into the troposphere is important as biomass burning is a major contributor of trace gases and aerosols to the overall atmospheric composition. Trace gases and aerosols have been demonstrated to affect the chemical and optical characteristics of the atmosphere. Atmospheric aerosols play an important role in the global energy balance by contributing to a net reduction of 5 to 10% in solar energy received at the Earth's surface (Fuzzi *et al.* 2006) whereas trace gases predominantly have the opposite effect. Thus, a better understanding of the dynamics of the atmospheric aerosol load is of vital importance for the scientific community and policy makers alike (Fuzzi *et al.* 2006).

Previous studies have presented details about biomass burning trace gases measured at CPT (e.g. Brunke *et al.* 2001) and aerosols in selected areas (e.g. Mielonen *et al.* 2013), as well as the global distribution of different types of aerosols (e.g. Mao *et al.* 2014).

In this paper, the observation of biomass burning plumes from a selected wildfire event over the Western Cape is presented. Satellite mounted lidar (aboard the CALIPSO satellite) as well as the Cape Point (CPT) Global Atmosphere Watch (GAW) station (34.36°S, 18.49°E) based PFR were used to detect the injection of biomass burning in the troposphere. We also investigated the CO variation, and identified the origin air

## 2. Instruments and Data

### 2.1 Aerosol Optical Depth (CPT-PFR)

In this study, a Precision Filter Radiometer (PFR), manufactured by the Physical and Meteorological Observatory Davos/World Radiation Centre (PMOD/WRC), Switzerland, operating at four wavelengths ( $\lambda = 368, 412, 500$  and  $862$  nm) (Wehrli, 2000), was used to investigate the Aerosol Optical Depth. The CPT measurements of AOD commenced in February 2008 and are available via the World Data Centre for Aerosols (WDCA; ebas.nilu.no), in NILU (Norsk Institute for Luftforskning), Norway. The wavelength dependent AOD presented in this paper was calculated using the Lambert-Beer law.

The primary calibration procedure for this instrument is conducted against three reference PFRs located at PMOD/WRC, which themselves are regularly calibrated at high-altitude stations (Mauna Loa, Hawaii, USA, 3397 m; Izaña, Tenerife, Spain, 2371 m) using the Langley technique. The PFR calibration uncertainty is estimated at 0.5% whilst the uncertainty of the CPT PFR is estimated at less than 1%, based on pre- and post-deployment calibrations (unpublished data). A schematic diagram in Figure 1 summarizes the data assimilation, processing and submission procedure followed during the production of the PFR data.

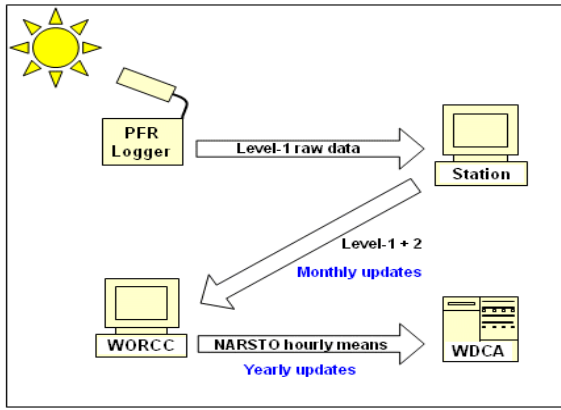


Figure 1. Data hierarchy from data acquisition and processing at the GAW station to data submission at WDCA.

## 2.2 CALIPSO

Data measured by the Cloud-Aerosol Lidar with Orthogonal Polarization (CALIOP), an instrument aboard the Cloud-Aerosol Lidar and Infrared Pathfinder Satellite Observation (CALIPSO) was used in this study. CALIOP measures the vertical structure of the atmosphere in three channels, received as back scattering from a (pulsed) laser light to the receiver. One of the three channels measures the total backscattered signal at 1,064 nm, whilst the other two channels, at 532 nm, are orthogonally polarized. The CALIPSO satellite has a spatial resolution of 333 m along the orbital path. A typical CALIPSO satellite repeat cycle is 16 days.

For the purpose of this work, we used the level 2, CALIOP version 3.1 aerosol profile product (backscattering and extinction coefficients at 532 nm). More details about this instrument are given by Winker *et al.* (2003) and Vaughan *et al.* (2004).

## 3. Results

There was a biomass burning event which took place between the 4<sup>th</sup> and the 10<sup>th</sup> of April 2014 within the Cape Point South African National Park (SANParks). This provided a unique opportunity to study and present the results associated with this biomass event in this work.

Figure 2 shows AOD values at 500 nm, measured by the CPT-PFR for the period from the 1<sup>st</sup> to the 30<sup>th</sup> of April 2014. It is apparent from the figure that during the biomass burning episode, a strong temporal variation in the AOD existed, with the highest values reaching 0.2. This event is demarcated by a black box in the figure. Elevated AOD values are observed on the

6<sup>th</sup> of April and persisted for about a week until they subsided on the 14<sup>th</sup> to “normal” expected background levels. This increase of AOD takes place concurrently with the biomass burning activity within the Cape Point Nature Reserve.

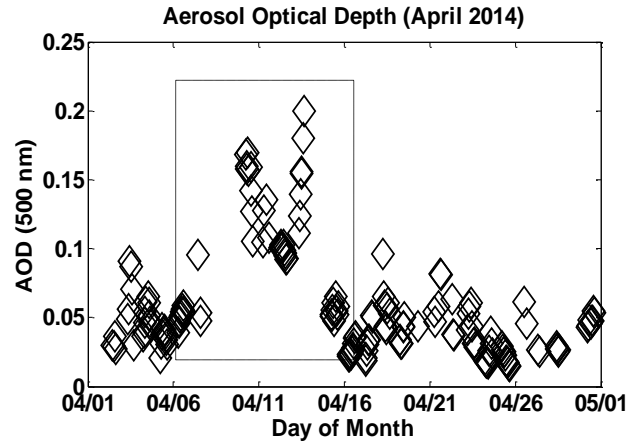


Figure 2. Time series of the CPT aerosol optical depth during the period from the 1-30 April 2014.

Most trace gases (e.g. CO, CO<sub>2</sub>, O<sub>3</sub>, CH<sub>4</sub>, N<sub>2</sub>O) measured during the biomass burning event showed strong variation. Here we only focus on CO. Figure 3 shows the time series of 30 min averaged CO data. There is a sharp increase of CO mixing ratios during the biomass burning episode which started on the 7<sup>th</sup> of April and lasted until the 14 of April. The highest CO values reached approximately 340 ppb which are 2 orders of magnitude higher than clean background values expected for that time of the year.

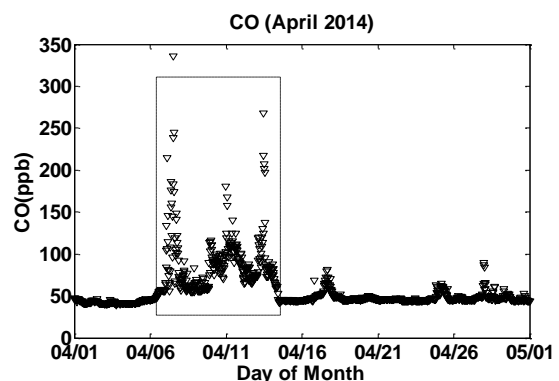


Figure 3. Time series of surface CO measured at CPT-GAW station for the period from 1-30 April 2014.

Radon (<sup>222</sup>Rn) is one of the daughter radionuclides of <sup>238</sup>U which is a primordial radionuclide of terrestrial origin present in the

Earth's crust over the geological period (Evens 1969). It is the only daughter of  $^{238}\text{U}$  found in the gaseous state and can thus easily diffuse through soil, and has a life time of  $\sim 3.82$  days.

$^{222}\text{Rn}$  has been established as the most effective single criterion for determining the origin of air masses in terms of continental, marine or mixed air (Brunke *et al.* 2004). Consequently, this radioactive trace gas was effectively utilised in this study to determine the origin of air masses at CPT.

In this study, we used a 1500 L dual flow loop two filter radon detector, designed and built by the Australian Nuclear Science and Technology (ANSTO) group, and installed at CPT-GAW station, South Africa in 1999. Detailed information about this instrument can be found in a report by Werczynski *et al.* (2011). Figure 4 shows the time series of  $^{222}\text{Rn}$  measured at CPT for the period from 1 to 30 April 2014.

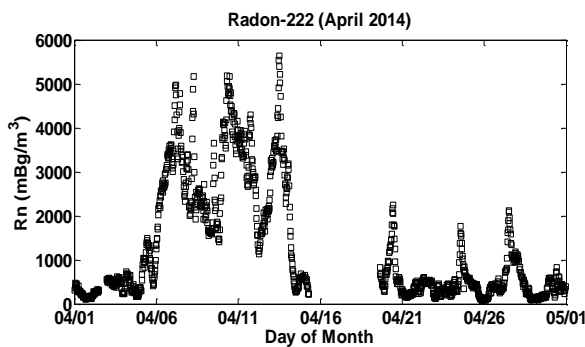


Figure 4. Time series of  $^{222}\text{Rn}$  measured by the 1500 L radon detector installed in CPT-GAW.

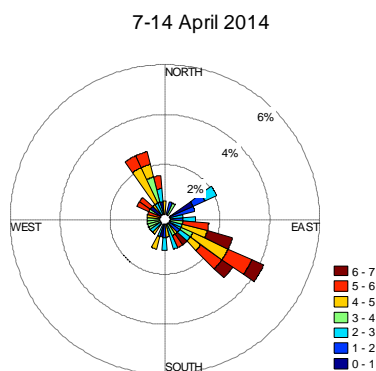


Figure 5. Wind rose for surface wind at Cape Point Station.

It is generally accepted that high  $^{222}\text{Rn}$  values are associated with air masses having a continental origin while lower  $^{222}\text{Rn}$  values are

considered to be of marine air (or clean air) (Whittlestone *et al.* 1998). In Figure 4 it is apparent that on the 6<sup>th</sup> of April  $^{222}\text{Rn}$  values started to increase gradually, reaching a maximum value of approximately  $5800 \text{ mBq/m}^3$ . This air mass which originates from the north of CPT, seems to have transported biomass burning products to the CTP station, hence the response of AOD and CO as depicted in Figure 2 and 3, respectively.

Figure 5 shows the wind rose for the days from 7 to 14 April 2004 at CPT-GAW station. The figure shows that the dominant prevailing wind directions is from east south-east (ESE) and from north north-west (NNW). The prevailing wind for NNW seems to be responsible for depositing biomass burning polluted air into CPT-GAW station because biomass burning too place in the region north of the station.

There is an interesting feature on the 15<sup>th</sup> of April where a significantly cleaner air mass is transported into the region, resulting in both AOD and CO displaying temporarily decreasing trends. During this period,  $^{222}\text{Rn}$  is observed to reach values less than  $250 \text{ mBq/m}^3$ , clearly indicating the arrival of an unpolluted marine air mass.

Figure 6 shows the scatter plot of PFR-AOD and CO measured at CTP-GAW station. The correlation between the two parameters is also indicated. There is a positive correlation ( $R=0.57$ ) between PFR-AOD and CO values. This positive correlation reflects arrival of the plume.

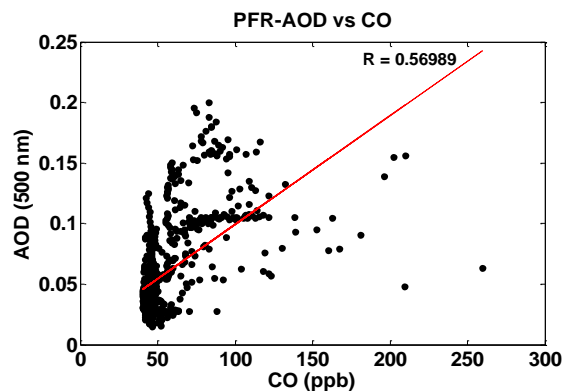


Figure 6. Scatter plot of AOD (500nm) vs CO for CPT-GAW station.

Figure 6 shows the pressure versus latitude total backscatter coefficient taken as the CALIPSO satellite overpasses the closest to the CPT. This closest overpass is within  $\pm 2.2^\circ$  in longitude. The color scale is indicated in the right hand side of the figure.

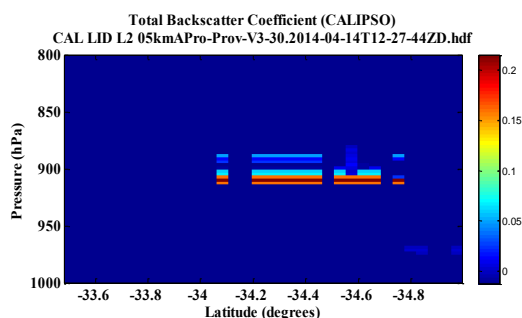


Figure 7. Pressure-latitude colormap of CALIPSO measured total backscatter coefficient for 12 April 2014.

It is apparent from the figure that as the satellite overpasses at a latitudinal position closest to the biomass burning episode site, it recorded a strong signal of total backscatter coefficient at around ~900 hPa pressure level. This is feature was observed from the 34.1°S to about 34.8°S latitude.

Our collective observations suggest that there was indeed an injection of biomass burning plumes into the troposphere during the biomass burning event. However, there were also other, further distant biomass burning activity which took place within the Overstrand region at approximately the same time as the burning at the Cape Point Nature Park. Thus, there is a possibility that the strong signal observed by the CALIPSO satellite was also contributed to by more than one fire event in the region.

#### 4. Conclusion

A biomass burning episode was detected at CPT during April 2014. Both the AOD and CO measurement values showed a strong variability during the biomass burning period. There is an indication that the biomass burning aerosols were trapped for few days in the vicinity of Cape Point after the burning ended. CALIPSO satellite also recorded a possibility of injection of the aerosols in the troposphere.

In future, this study will be extended by utilizing MODIS satellite data, which has a better spatial resolution. Other trace gasses, such as ozone, measured by satellite as well as by ground based instruments will also be investigated. The CALIPSO satellite data will also be used to study the wider aerosol climatology within the Western Cape region.

#### Acknowledgements

The authors wish to acknowledge Cloud-Aerosol Lidar and Infrared Pathfinder Satellite Observation (CALIPSO) for providing data. Also, Special thanks to the whole Cape Point Global Atmosphere Watch team.

#### References

- Brunke E.-G, C. Labuschagne, H. E Scheel. 2001, 'Trace gas variations at Cape Point, South Africa, during May 1997 following a regional burning episode', *Atmospheric Environment*, **35**, 77-786.
- Brunke E.-G, C. Labuschagne, B.A Parker, H.E. Scheel and S. Whittlestone. 2004, 'Baseline air mass selection at Cape Point, South Africa: application of  $^{222}\text{Rn}$  and other filter criteria to  $\text{CO}_2$ ', *Atmospheric Environment*, **38**, 5693-5702.
- Evans R.D. 1996, 'Atomic nucleus. McGraw-Hill, New York, 927 p, 1996.
- Fuzzi M.O. Andreae B.J. Huebert M. Kulmala, T.C. Bond M. Boy S.J. Doherty A. Guenther M. Kanakidou K. et al. Critical assessment of the current state of 2006, 'scientific knowledge terminology, and research needs concerning the role of organic aerosols in the atmosphere, climate, and global change', *Atmos. Chem. Phys*, **6**, pp. 2017–2938.
- Mielonen T. Aaltonen V. Lihavainen H. et al. 2013, 'Biomass Burning Aerosols Observed in Northern Finland during the 2010 Wildfires in Russia', *Atmosphere*, **4**, 17-34; doi:ao.3390/atmos4010017,.
- Vaughan M. Young S. Winker D. Powell K. Omar A. Liu Z. Hu Y. Hostetler C. 2004, 'Fully automated analysis of space-based lidar data: An overview of the CALIPSO retrieval algorithms and data products', *Proc. SPIE* 2004, 5575, 16–30.
- Wehrl C. 2000, 'Calibrations of filter radiometers for determination of atmospheric optical depths', *Metrologia*, **37**, 419-422.
- Werczynski S. Chambers S. Sisoutham V and Zahorowski W. 2011, 'Commission of a 1500 L radon detector at the Cape Point Global Atmosphere Watch station in South Africa', *A report to the South African Weather Service*, February 2011.
- Whittlestone S. Zahorowski W. 1998, 'Baseline radon detectors for shipboard use: development and deployment in ACE-1', *Journal of Geophysical Research*, **103** (D13), 16743-16751.
- Winker D.M. Hunt W.H. McGill M.J. 2007, 'Initial performance assessment of CALIOP', *Geophys. Res. Lett*, **34**, L19803, doi: 10.1029/2007GL030135.
- Winker D.M. Pelon J. McCormick M. P. 2003, 'The CALIPSO mission: Spaceborne lidar for observation of aerosols and clouds', *Proc. SPIE*, 4893, 1–11.

# Geospatial (Latitudinal and Longitudinal) variability of ozone over South Africa

Jeremiah Ogunniyi<sup>\*1</sup> and Venkataraman Sivakumar<sup>1</sup>

<sup>1</sup>School of Chemistry and Physics, University of KwaZulu-Natal, Westville, Durban 4001, South Africa

Room 078, Discipline of Physics, School of Chemistry and Physics, UKZN, Durban, Private Bag X54001

Email: [jerryogunniyi@yahoo.com](mailto:jerryogunniyi@yahoo.com)

## Abstract

This study presents the climatological characteristics and variability of total column ozone observed over South Africa. The data used are from the Ozone Monitoring Instrument overpasses from October 2004 to December 2013. The result reveals that the southern part of South Africa has more total ozone compared with the central part and the northern part. The north western part of South Africa had higher total ozone measurement compared to other northern part linked with biomass burning in surrounding regions. The monthly variation of total ozone shows a nearly annual cycle with maximum concentration during spring/winter and minimum concentration during autumn/summer months.

Keywords: biomass burning, variation, concentration, spring, autumn, winter, summer, maximum, minimum.

## Introduction

Ozone is an important greenhouse gas. It constitutes about 0.00004 % of atmospheric constituents. Despite its low concentration, a change in its column concentration contributes significantly to global climate change (Anton et al., 2010). Most ozone in the atmosphere is present in the stratosphere and it prevents harmful ultraviolet radiation from penetrating the surface of the earth. Research into atmospheric ozone have increased since 1985 when total column ozone decreased by about 30 DU over southern mid-latitudes attributed to a combination of westerly phase QBO (Quasi-Biennial Oscillation) and the switch from easterly to westerly phase early in the year (Bodeker et al., 2007). Satellite measurements are effective in determining total ozone distribution on global coverage. Since the 1980s, satellite measurements have shown a negative trend in total column ozone measurements significantly in middle and high latitudes of both the southern and northern hemisphere (Solomon et al., 1996). Ground based measurements in these latitudes agree with the satellite overpass. Chandra et al. (1996) used ~14 years TOMS measurement to study total ozone in the northern mid latitude and showed that ozone trend are influenced by annual variability associated with dynamical perturbations in the atmosphere. They also

presented an ozone trend reduction of 1 to 3 % per decade. Bodeker et al. (2007) showed that the southern hemisphere mid latitude total column ozone (TCO) anomaly in 1985 was due to westerly phase QBO throughout the year which suppressed mid latitude ozone. They also showed a QBO phase switch from easterly to westerly early in the year which reduced in the mixing of ozone rich air from tropical source region to mid-latitudes. Mahendranth and Bharathi (2012) estimated tropical annual and seasonal trends of TCO and showed an increasing trend of 1.88 DU per year or 0.61 % per year. They also presented the maximum and minimum diurnal variability of TCO as 28 DU (9.19 %) and -36 DU (-11.8 %) respectively. Nair et al. (2013) also presented the total ozone trend at a northern mid latitude station which indicated a decline in column ozone before 1997 attributed mainly to positive ozone depletion substances. Kirchhoff et al (1991) presented a 10 year ozone climatology for a subtropical site and showed maximum concentration during spring in September/October. This maximum was about 5 % higher than the annual average for TCO.

South Africa has four distinct seasons: summer (December, January, February), autumn (March, April, May), winter (June, July, August) and

spring (September, October, November). Meteorological parameters such as temperature, wind speed, precipitation and relative humidity vary throughout the seasons. Laakso et al., (2012), presented the meteorological characteristics of South Africa. Their result showed that wind speed is highest over South Africa in spring. This can be a possible reason for maximum ozone observed in spring as winds transfer ozone from the ozone rich regions in the higher latitudes to the middle latitudes. Their result also showed that temperature is highest during spring and summer months. This would increase the photolysis of oxygen, hence, the production of more ozone. The impact of precipitation and relative humidity on ozone concentration has not been established in this work.

In this paper, we have managed to study the geo-spatial variation of total ozone (ToZ) over complete South Africa using OMI satellite data and the obtained results are presented here. South Africa was divided into three parts as illustrated by the earlier study on aerosol climatology over South Africa by Tesfaye et al., (2011). They have classified with respect to aerosol loading in South Africa and is shown in figure 1.1. We pre-assume that the similar classification would hold good for the ozone variations and is adopted for this study to examine the ozone climatology over South Africa.

	Latitude		Longitude	
	Min	Max	Min	Max
South Africa	22	35	17	32
Southern Part A	31	35	18	31
Central Part B	27	31	17	33
Northern Part C	22	27	20	32

Table 1.1:- Latitudes and longitudes for the division of South Africa to three parts

The data used for this section are obtained from OMI instrument from October 2004 to December 2013. OMI instrument was selected due to its close measurements of total ozone with the Dobson instrument (Balis et al., 2007). OMI has also been noted for accurate total ozone measurements (Liu et al., 2009). The data are filtered to within  $2\sigma$  for better quality.

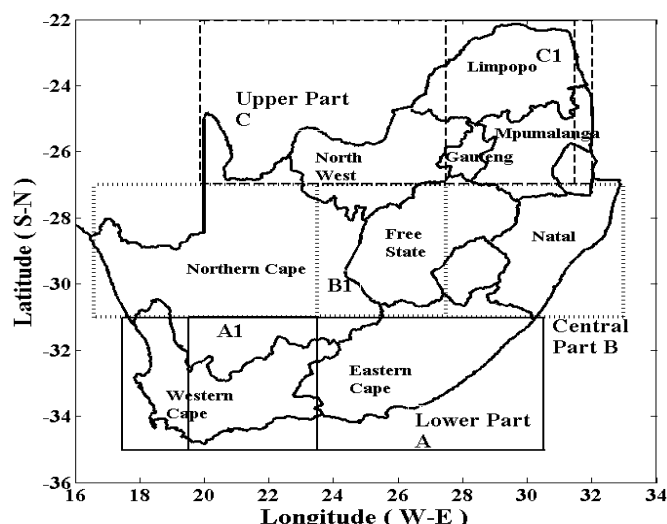


Figure 1.1:- Geographical map of South Africa with the three different layers of classifications (as adopted from Tesfaye et al., 2011)

## Results

### Seasonal variations

Ten years of seasonal average is presented in figure 1.2. The seasonal average was obtained by grouping the data in terms of the four seasons in South Africa irrespective of the years of measurements and then averaged. Monthly ozone variations are from 260 DU to 290 DU for all seasons. For better understanding the monthly variation for winter, the colormap scale is stepped down by 5 DU while those of summer and autumn are further stepped down by 5 DU. The result shows maximum total ozone in spring. Spring time ozone has been discussed in earlier chapter. For all seasons, the southern part of South Africa has the highest total ozone. This is expected since higher ozone concentration is expected in higher latitudes than in mid-latitudes and higher total ozone in mid-latitudes than in the tropics of both the Northern and Southern Hemispheres (Susan Solomon 1988). This may be one of the reasons for higher ozone in southern part of South Africa. As the latitude reduces through north, total ozone also reduces. Diab et al (2004) attributed photochemical reactions, biomass burning, lightning production, and biogenic emissions as some of the reasons for spring maximum over Irene, a South African station. Average spring maximum for southern part corresponds to 290 DU, 285 DU for central part and about 278 DU for northern part. Large photochemical reactions take place in the lower part of South Africa which enhances the ozone level. This ozone is

primarily from maritime sources attributed to dominant winds from SE-W (Zunckel et al., 2004). Figure 1.2 shows ozone minimum in autumn corresponding to ~265 DU for lower part but there was no much variation in total ozone for central part and upper part.

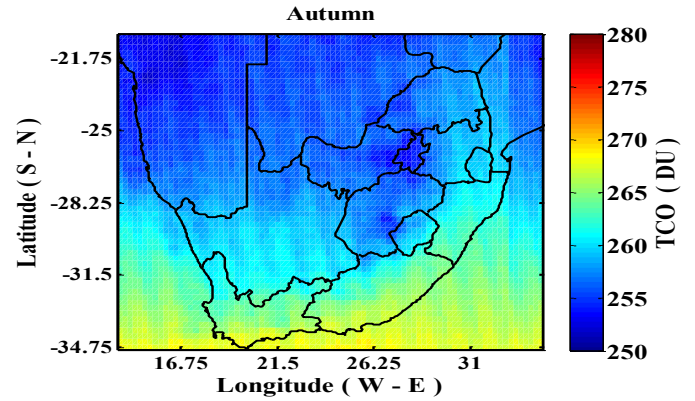
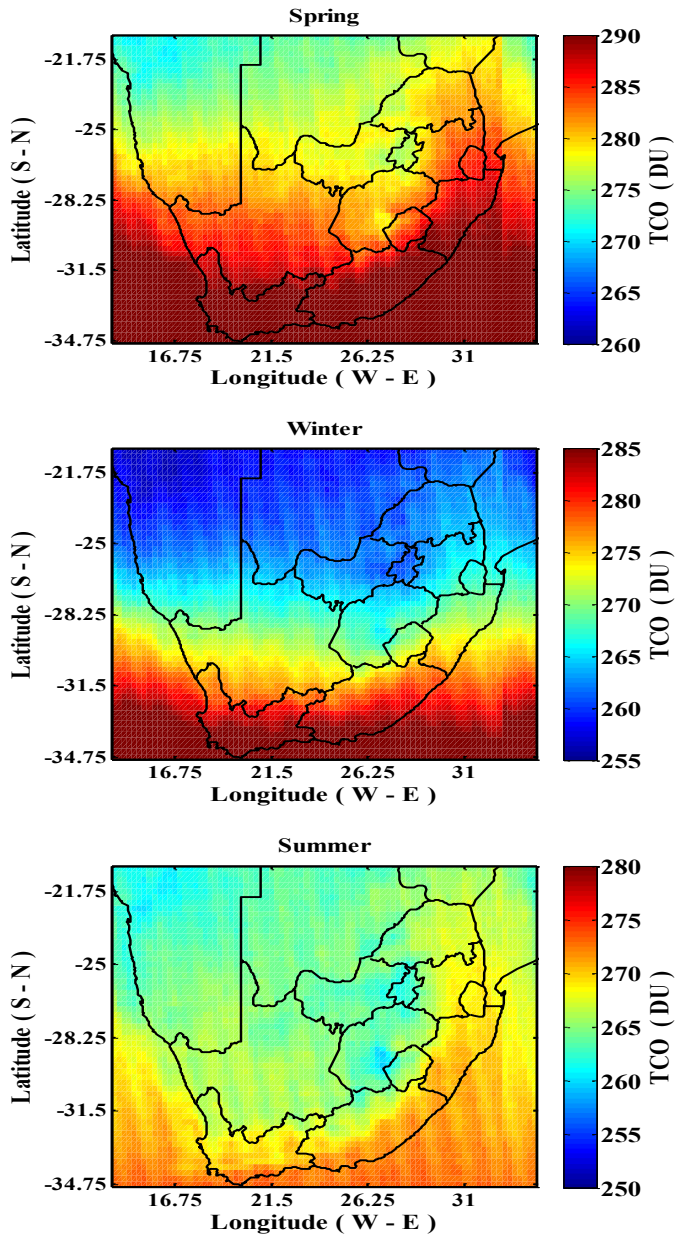


Figure 1.2. Seasonal variation of ozone over South Africa for (i) spring (ii) winter (iii) summer (iv) autumn (change in colour map scale for better understanding).

### Monthly variation of ozone over South Africa

The monthly ozone overpass was obtained by grouping the datasets into month irrespective of the years and then averaged. All datasets in the lower part, central part and upper part of South Africa were combined individually and their mean was to compare with the results obtained in earlier sections. The monthly variations are from 240 DU to 320 DU as presented in figure 1.3. The result obtained shows that ToZ in the lower part of South Africa corresponds to ~300 DU in during spring while those of the central part and upper parts corresponds to 288 DU and 284 DU respectively. This result is consistent with the result obtained in section two where maximum ToZ over Irene was ~284 DU. Irene is located in the upper part of South Africa. May minimum is observed for measurements in central and upper part of South Africa while for the upper part shows a month early minimum. The wave propagation into the stratosphere when the wind is westerly can be related to the seasonal variation over South Africa.

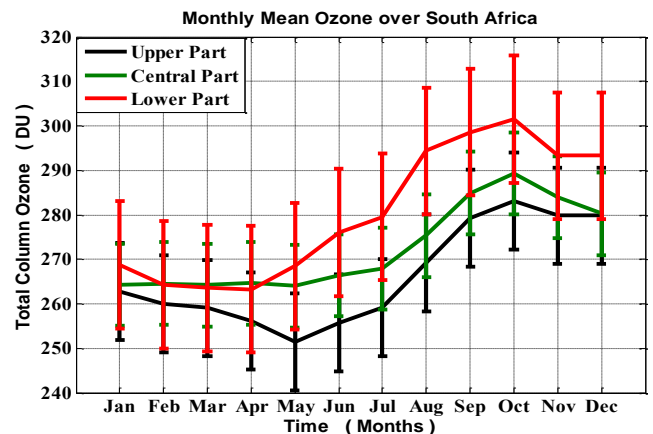


Figure 1.3: Average monthly mean ozone overpass over South Africa

### Summary and Concluding Remarks

The climatological characteristics and variability of total column ozone over South Africa has been presented in this paper using satellite data from Ozone Monitoring Instrument from 2004 to 2013. The result revealed the southern part of South Africa having the highest total ozone while the northern part had the lowest ozone. The result of seasonal variability showed an austral spring time maximum and an autumn minimum while total ozone was maximum in October for all parts of South Africa.

### References

- Anton, M., M.E. Koulouli, M. Kroon, R.D. McPeters, G.J. Labow, D. Balis and A. Serrano (2010), Global validation of empirically corrected EP-Total Ozone Mapping Spectrometer (TOMS) total ozone column using Brewer and Dobson ground-based spectrometer, *J. Geophys. Res.*, 112, JD006823
- Balis, D., M. Kroon, M.E. Koukouli, E.J. Brinksma, G. Labow, J.P. Veefkind and R.D. McPeters (2007), Validation of Ozone Monitoring Instrument total ozone column measurements using Brewer and Dobson ground-based spectrometer, *J. Geophys. Res.*, 112, JD008796
- Bodeker, G.E., H. Garny, D. Smale, M. Dameris and R. Deckert (2007), The 1985 Southern Hemisphere Mid-Latitude Total Column Ozone Anomaly, *Atmos.Chem.Phys.Discuss.*, 7, 7137-7169
- Chandra S., C. Varotsos and L.E. Flynn (1996), The Mid-Latitude Total Ozone Trend in the Northern Hemisphere, *Geophysical Research Letters*, Vol. 23, No. 5, pp. 555-558, 1996
- Diab, R.D., A.M. Thompson, K. Mari, L. Ramsay and G.J.R. Coetzee (2004), Tropospheric ozone climatology over Irene, South Africa from 1990 to 1994 and 1998 to 2000, *J. Geophys. Res.*, 109, JD00479
- Kirchhoff, V.W., R.A. Barnes and A.L. Torres (1991), Ozone Climatology at Natal, Brazil from In Situ Ozonesonde Data, *J. Geophys. Res.*, Vol. 96, No. D6, pp. 10, 899-10,909
- Laakso, L., V. Vakkari, A. Virkkula, H. Laakso, J. Backman, M. Kulmala, J.P. Beukes, P.G. van Zyl, P. Tiitta, M. Josipovic, J.J. Pienaar, K. Chiloane., S. Gilardoni, E. Vignati, A. Wiedensohler, T. Tuch, W. Birmili, S. Piketh, K. Collett, G.D. Fourie, M. Komppula, H. Lihavainen, G.de Leeuw and V.M. Kerminen (2012), South Africa EUCAARI Measurements: Seasonal Variation of Trace Gases and Aerosol Optical Properties. *Atmos.Chem.Phys.*, 12, 1847-1864
- Liu, X, P.K. Bhartia, K. Chance, R.J.D. Spurr and T.P. Kurosu (2009), Ozone Profile Retrievals from Ozone Monitoring Instrument, *Atmos.Chem.Phys.Discuss.*, 9, 22693-22738
- Mahendranth, B. and G. Bharathi (2002), Inter-annual Variability and Temporal Variation of Total Column Ozone in Visakhapatnam from Ground-Based Observations, Asia-Pacific, *J. Atmos. Sci.*, 48(2), 191-195
- Nair, P.J., S. Godin-Beekmann, J. Kuttipurath, G. Ancellent, F. Goutail, A. Pazmino, L. Froidevaux, J.M. Zawodny, R.D. Evans, H.J. Wang, J. Anderson and M. Pastel (2013), Ozone Trends Derived from Total Column and Vertical Profiles at a Northern Mid-Latitude Station, *Atmos.Chem. Phys.*, 13, 10373-10384
- Susan Solomon (1988), The Mystery of the Antarctic Ozone Hole, *Review of Geophysics*, Vol. 26, pp. 131-148
- Tesfaye, M., V. Sivakumar., J. Botai and G. Mengistu Tsidu (2011), Aerosol Climatology over South Africa based on 10 years of Multiangle Imaging Spectroradiometer (MISR) data, *J. Geophys. Res.*, Vol. 116, D20216
- Zunckel, M., K. Venjonoka, J.J. Pienaar, E.G. Brunke, O. Pretorius, A. Koosiale, A. Raghunandan and A.M. van Tienhoven (2004), Surface Ozone over Southern Africa: Synthesis of Monitoring Results during the Cross Border Air Pollution Impact Assessment Project, *Atmos.Enviro.* 38, 6139-6147

# Aerosol properties over an urban site, Johannesburg measured from Sunphotometer

Joseph A. Adesina<sup>1\*</sup>, V. Sivakumar<sup>1</sup>, Raghavendra K. Kumar<sup>2</sup>, Stuart J. Piketh<sup>3</sup>, Jyotsna Singh<sup>1</sup>

<sup>1</sup>Discipline of Physics, School of Chemistry and Physics, College of Agriculture, Engineering and Science, Westville Campus, University of KwaZulu–Natal, Durban 4000, South Africa.

<sup>2</sup>Key Laboratory for Aerosol-Cloud-Precipitation of China Meteorological Administration, School of Atmospheric Physics, Nanjing University of Information Science and Technology, Nanjing 210044, Jiangsu Province, China

<sup>3</sup>School of Geo- and Spatial Science, Unit for Env. Sc. and Management, North-West University, Potchefstroom

\*corresponding author: [jadesina173@gmail.com](mailto:jadesina173@gmail.com)

## ABSTRACT

In this paper, we present results using ground based Sunphotometer (a passive remote sensing instrument designed to study aerosol properties) as a part of NASA's AERONET data. The analysis was based on the winter and spring (June – November, 2009) seasonal variations of aerosol optical and microphysical properties. Aerosol optical depth ( $AOD_{440}$ ) varied from  $0.12 \pm 0.06$  to  $0.18 \pm 0.08$  in winter and between  $0.19 \pm 0.07$  to  $0.26 \pm 0.06$  in spring and the seasonal increment which may be attributed to the effect of biomass burning and long range transport of smoke particles from forest fires. While the Angstrom exponent ( $\alpha_{440-870}$ ) varied from  $1.23 \pm 0.33$  to  $1.46 \pm 0.33$  and  $1.40 \pm 0.19$  to  $1.60 \pm 0.21$  during winter and spring seasons, respectively. The volume size distribution which is of bimodal log-normal structure has its fine mode dominance at about  $0.15 \mu\text{m}$  and the coarse mode at about  $4 \mu\text{m}$ . The single scattering albedo (SSA) generally decreased with wavelength for both seasons depicting the presence of absorbing aerosol. The asymmetry parameter (ASY) and the refractive index (both real and imaginary) were also wavelength dependent.

Keywords: AERONET, AOD, Size distribution, SSA, Refractive Index.

## I. INTRODUCTION

The chief source of energy for the earth is the sun and it influences both meteorology and climatology of the earth's surface with aerosol constituting one important component of the system that retain high degree of uncertainty (Kumar et al., 2013a). The knowledge of spatial-temporal aerosol characteristics at a local and global scale remains an important area of atmospheric research (Sivakumar et al., 2010). Although ground based aerosol remote sensing does not provide global average, its wide angular and spectral measurements of solar and sky radiation are best suited to reliably and continuously derive the detailed optical properties in key locations (Dubovik et al., 2002).

The winter and spring seasons were chosen to understand the impact of long range pollutants transported from South Atlantic Ocean passing over the Indian Ocean and

seasonal biomass burning (Kumar et al., 2013a, Eck et al., 2003).

## II. SITE AND DATA COLLECTION

### a) Study region

Johannesburg is situated on the Highveld which is the eastern plateau of South Africa having a subtropical highland climate at an elevation of 1,753 meters. It serves as the provincial capital of Gauteng with a population of about 10 million within its metropolitan area. It receives normally about 604mm of rain per year with high rainfall during January and low in July. It receives the lowest rainfall in July and highest in January. The average daily maximum temperature ranges from  $16.6^\circ\text{C}$  in June to  $26.2^\circ\text{C}$  in January. July is the coldest month and winter is the sunniest time of the year with cool days and cold nights. As the second largest city in Africa and the economic hub of South Africa, manufacturing industries extend across a

range of areas with a reliance on heavy industries including steel and cement plants.

#### b). Instrumentation

The data was collected from the AERONET website <http://aeronet.gsfc.nasa.gov> for the University of Witwatersrand (28.029E, 26.193S, 1775 asl) which began its operation in 2002. Sunphotometer operation, calibration and errors have been discussed by many earlier researchers (Dubovik & King, 2000; Holben et al., 1998; Smirnov et al., 2002). Out of the eight channels of retrievals (340, 380, 440, 500, 675, 870, 940, 1020nm) used for the direct sun radiances, 940nm is used for retrieval of column water vapor content while others are for retrieval of aerosol optical depth (AOD). The sky radiance measurement both at the principal and almucantar plane is at (440, 675, 870 and 1020nm) which helps in retrieving single scattering albedo (SSA), asymmetry parameter (ASY), volume size distribution (VSD), refractive index (RI) and the radiative forcings of aerosol.

### III. RESULTS AND DISCUSSION

#### a) Monthly mean and seasonal Variations in AOD, CWV and $\alpha_{440-870}$

The AOD (the measure of transparency or the degree to which aerosol prevents transmission of solar radiation through absorption or scattering), the columnar water vapor and the Angstrom exponent (the measure of the relative dominance of fine over the coarse particle) were made up of 193 daily observations obtained from version 2 direct sun algorithm of AERONET datasets. The AOD (Fig 1a) was lowest in July during the winter  $0.15 \pm 0.07$  and begin to rise until September  $0.26 \pm 0.06$  in spring during which the biomass burning peaks and afterward started decreasing to the end of spring (Eck et al., 2003). Winter had an average AOD of  $0.15 \pm 0.08$  while spring was  $0.23 \pm 0.08$ . Generally these values were comparable to some other locations in the South Africa. (Kumar et al., 2013b; Queface et al., 2011). The columnar water vapor (Fig1b) was also lowest in July of  $0.48 \pm 0.17$  and afterwards continues to rise to the end of the spring when it reached to  $1.76 \pm 0.16$ . Relative humidity is generally very low during the winter while spring is the planting season and marks the onset of rain. The Angstrom exponent ( $\alpha_{440-870}$ ) as shown in (Fig 1c) was constantly increasing through the two seasons apart from October where there was a sudden dip of  $1.23 \pm 0.33$  and increased to

$1.60 \pm 0.21$  in November. It was generally high throughout the seasons showing the presence of fine particle aerosol. Sivakumar et al., (2010) found similar trend of  $\alpha_{440-870}$  with a monthly average of above 1.5 over Johannesburg.

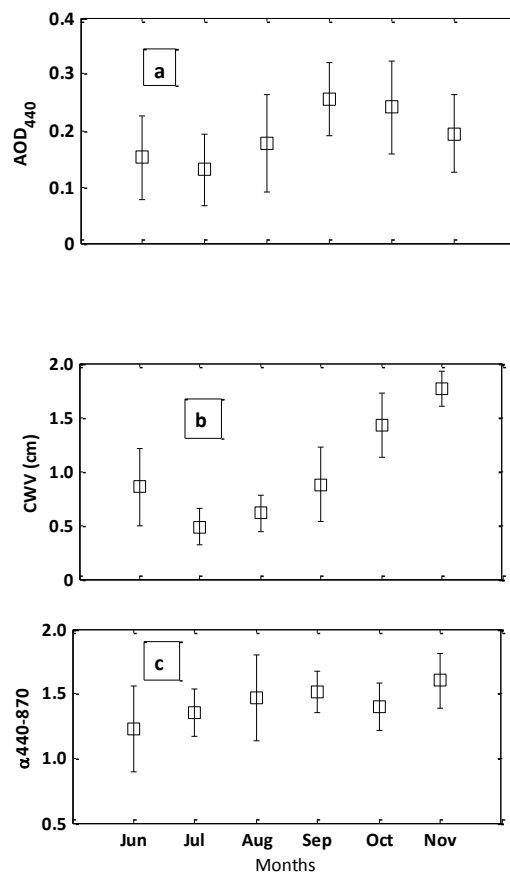


Fig 1. Johannesburg monthly mean variations of a) AOD, b) CWV and c)  $\alpha_{440-870}$  with their standard deviations

#### b) Seasonal Volume Size Distribution

The climatic effect of aerosol is often being deduced from its radiative and microphysical properties like the SSA, ASY, RI and VSD. This is obtained from the AERONET version 2 almucantar retrievals dataset made up of 117 daily measurements. The volume size distribution (VSD) is dependent on the mixture of different aerosol types present. VSD is determined from 22 bins radius ranging from  $0.05 \mu\text{m}$  to  $15 \mu\text{m}$ .

The aerosol VSD shown in Fig 2 is bimodal with the fine mode dominant at about  $0.15 \mu\text{m}$  and the coarse mode at about  $4 \mu\text{m}$  radius. The fine mode peak is during the spring and quite doubled that of the winter while the coarse peaks at winter, the result is similar to

that obtained from Pretoria another urban city about 55km away from Johannesburg (Kumar et al, 2013).

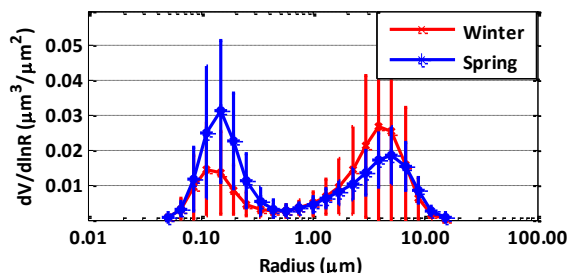


Fig 2 Seasonal aerosol VSD over Johannesburg with standard deviations

### c) Seasonal Single Scattering Albedo

The ratio of scattering to extinction normally referred to as single scattering albedo (SSA) sums up the scattering and absorption when photons hit aerosol particles. It depends on particle size, shape and material refractive index. Fig 3 shows the wavelength dependence of SSA with lower value at longer wavelengths. The winter values at 440nm (1020nm) was  $0.85 \pm 0.04$  ( $0.81 \pm 0.05$ ), and for spring  $0.93 \pm 0.03$  ( $0.89 \pm 0.05$ ). Lower values of SSA at longer wavelengths indicate the presence of absorbing aerosols (fine aerosol from sources such as biomass burning, vehicular emission and industrial pollutants) whereas higher values of SSA at longer wavelengths indicate scattering aerosols (coarse aerosol from activities such as heavy industrialization, sea salts rapid urbanization and construction) (Alam et al., 2012). Dubovik et al. (2002) found SSA for biomass burning of African savannah, Zambia to range between 0.88 to 0.78 from shorter to longer wavelength. While Queface et al. (2011) suggested that SSA in the region ( $20^{\circ}\text{S}$ ) and below of southern Africa will have a more appropriate value of  $0.90 \pm 0.03$  as the northern part of southern Africa is more affected by biomass burning. Eck et al. (2003) further stated that aerosols including fossil fuel burning, industrial and aeolian coarse mode types contribute to the aerosol mixture in South Africa.

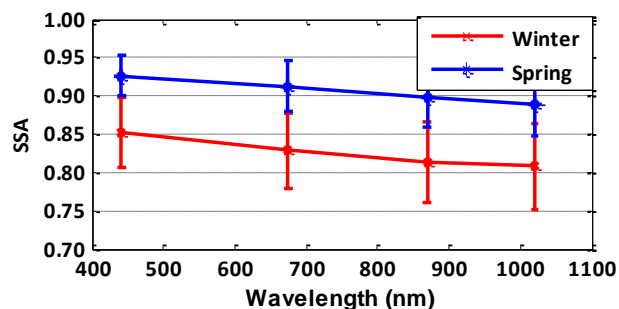
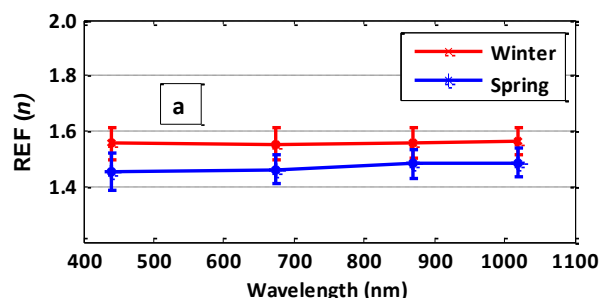


Fig 3 Johannesburg seasonal spectral wavelength dependence of single scattering albedo

### d) Seasonal Refractive Index

The index of refraction of aerosol is made of real part  $REF(n)$  which indicates the degree of scattering of aerosol with higher values corresponding to higher scattering and the imaginary part  $REF(k)$  indicating degree of absorption. It characteristically depends on the particle size distribution and SSA. Fig 4 (a&b) show the real and imaginary parts of the RI over Johannesburg, respectively. In winter, the real part ranges between  $1.55 \pm 0.05$  and  $1.56 \pm 0.05$  at wavelengths from 440nm to 1020nm and during spring  $1.45 \pm 0.07$  and  $1.48 \pm 0.05$ . While the imaginary part of RI ranges between  $0.024 \pm 0.018$  ( $0.010 \pm 0.001$ ) and  $0.022 \pm 0.017$  ( $0.009 \pm 0.003$ ) for winter (spring) from lower to higher wavelengths. During winter and spring seasons, the imaginary part of RI exceeds 0.01 which indicates the dominant aerosol is absorbing type (black carbon) produced from agricultural waste and biomass burning (Dubovik et al., 2002).



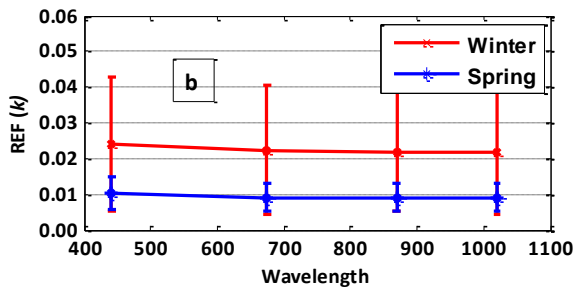


FIG 4 Johannesburg Seasonal spectral dependence of the (a) Real and (b) Imaginary refractive indices

#### e) Seasonal Asymmetry Factor

When light is scattered by aerosol the preferred direction is deduced from the asymmetry parameter (ASY) which is the average cosine direction as influenced by the phase function. For cloud free conditions to polluted atmosphere, it varies from 0.1 to 0.75. In Fig 5, winter value ranges between  $0.67 \pm 0.03$  and  $0.62 \pm 0.03$  and in spring from  $0.69 \pm 0.03$  to  $0.56 \pm 0.03$  from shorter to longer wavelength, respectively. There was a sharp decrease in ASY values between 440nm and 675nm in winter, while the spring characteristics suggest the abundance of anthropogenic pollutants such as biomass burning and urban industrial aerosol (Alam et al., 2012).

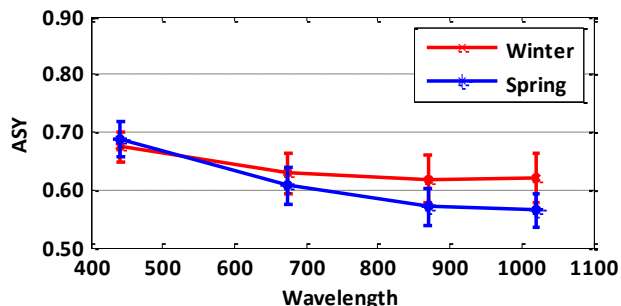


FIG 5 Seasonal spectral dependence of asymmetry parameter over Johannesburg

## IV. CONCLUSION

The winter and spring analysis of aerosol properties over Johannesburg for the year 2009 has been presented. The mean aerosol optical depth ( $AOD_{440}$ ) was found to be higher during spring than in winter. The fine mode aerosol was dominant during spring with the dominance of coarse mode during the winter. The SSA, RI and ASY were all wavelengths dependent and showed similar observations as that reported by earlier researchers.

## V. ACKNOWLEDGEMENTS

The authors wish to thank the University of KwaZulu-Natal for the enabling suitable environment to carry out this work. Our special thanks go to Prof J. Stuart (PI of AERONET, Wits\_ University site and the staff for maintaining the instrument and making the online data available.

## REFERENCES

- Alam, K., Trautmann, T., Blaschke, T., & Majid, H. (2012). Aerosol optical and radiative properties during summer and winter seasons over Lahore and Karachi. *Atmospheric Environment*, 50, 234-245.
- Dubovik, O., Holben, B., Eck, T. F., Smirnov, A., Kaufman, Y. J., King, M. D., . . . Slutsker, I. (2002). Variability of absorption and optical properties of key aerosol types observed in worldwide locations. *Journal of the atmospheric sciences*, 59(3), 590-608.
- Dubovik, O., & King, M. D. (2000). A flexible inversion algorithm for retrieval of aerosol optical properties from Sun and sky radiance measurements. *Journal of Geophysical Research: Atmospheres (1984–2012)*, 105(D16), 20673-20696.
- Eck, T., Holben, B., Ward, D., Mukelabai, M., Dubovik, O., Smirnov, A., . . . Queface, A. (2003). Variability of biomass burning aerosol optical characteristics in southern Africa during the SAFARI 2000 dry season campaign and a comparison of single scattering albedo estimates from radiometric measurements. *Journal of Geophysical Research: Atmospheres (1984–2012)*, 108(D13).
- Holben, B., Eck, T., Slutsker, I., Tanre, D., Buis, J., Setzer, A., . . . Nakajima, T. (1998). AERONET—A federated instrument network and data archive for aerosol characterization. *Remote sensing of environment*, 66(1), 1-16.
- Kumar, K. R., Adesina, A. J., & Sivakumar, V. (2013). *Aerosol radiative forcing from spectral solar attenuation measurements due to aerosol loading using AERONET over Pretoria in South Africa*. Paper presented at the Emerging Research Areas and 2013 International Conference on Microelectronics, Communications and Renewable Energy (AICERA/ICMiCR), 2013 Annual International Conference on.
- Kumar, K. R., Sivakumar, V., Reddy, R., Gopal, K. R., & Adesina, A. J. (2013b). Inferring wavelength dependence of AOD and Ångström exponent over a sub-tropical station in South Africa using AERONET data: Influence of meteorology, long-range transport and curvature effect. *Science of The Total Environment*, 461, 397-408.
- Queface, A. J., Piketh, S. J., Eck, T. F., Tsay, S.-C., & Mavume, A. F. (2011). Climatology of aerosol optical properties in Southern Africa. *Atmospheric Environment*, 45(17), 2910-2921.
- Sivakumar, V., Tesfaye, M., Alemu, W., Sharma, A., Bollig, C., & Mengistu, G. (2010). Aerosol measurements over South Africa using satellite, Sun-photometer and LIDAR. *Advances in Geosciences, Volume 16: Atmospheric Science (AS)*, 16, 253.
- Smirnov, A., Holben, B. N., Dubovik, O., O'Neill, N. T., Eck, T. F., Westphal, D. L., . . . Slutsker, I. (2002). Atmospheric aerosol optical properties in the Persian Gulf. *Journal of the atmospheric sciences*, 59(3), 620-634.

## A comparison of surface NO<sub>2</sub> mixing ratios and total column observations at a South African site\*

Micky Josipovic<sup>1\*</sup>, Debra W. Kollonige<sup>2,3</sup>, Roelof P. Burger<sup>1</sup>, Anne M. Thompson<sup>1,2,4</sup>, Johan P. Beukes<sup>1</sup>, Pieter G. van Zyl<sup>1</sup>, Andrew D. Venter<sup>1</sup>, Kerneels Jaars<sup>1</sup>, Douglas K. Martins<sup>2</sup>, Ville Vakkari<sup>5</sup>, Lauri Laakso<sup>1,5</sup>

1. Unit for Environmental Sciences and Management, North-West University, Potchefstroom Campus, Private Bag X6001, Potchefstroom 2520, South Africa
2. Department of Meteorology, Pennsylvania State University, 503 Walker Building, University Park, PA. 16802-5013, USA
3. University of Maryland – ESSIC, College Park, Md, USA
4. NASA, Goddard Space Flight Center, Greenbelt, Md, USA
5. Finnish Meteorological Institute, Research and Development, P.O. BOX 503, FI-00101, Finland

The total column density nitrogen dioxide (NO<sub>2</sub>) retrievals collated by a ground-based sun-tracking spectrometer (Pandora/GSFC) and the satellite-borne (Aura) Ozone Monitoring Instrument (OMI) were compared to the volume mixing ratios measured by a ground-based gas-analyser at Welgegund, North-West University (NWU) atmospheric monitoring station (Potchefstroom, South Africa). An assessment of the comparability between columnar and surface NO<sub>2</sub> measurements was performed. The concurrent ground measurements results over January-March, 2011, were averaged over one hour to correspond to the closest local OMI overpasses (~12:00 UTC).

A novel method for estimating surface mixing ratios from total-column retrievals, via a planetary boundary layer (PBL) height correction factor as tested by [Knepp \*et al.\* \(2013\)](#) in the USA was applied. This PBL correction factor largely corrects for boundary-layer variability throughout the day, and allows conversion into mixing ratios. The data for the ground instruments were in agreement within the expected uncertainty for each technique and between two remote sensing instruments. However, NO<sub>2</sub> between the ground gas analyser and satellite borne instrument were out of the expected uncertainty limits.

**Keywords:** NO<sub>2</sub>, gas analyser, ground-based spectrometer, boundary layer, total column density, volume mixing ratio, remote sensing.

### 1. Introduction

Understanding of the column density-to-surface fraction relationship should enable comparisons with surface mixing ratio measurements, which are often compared against numerical units associated with an established ambient air quality (AQ) standard. A significant challenge in this relation is accounting for variability in the planetary (atmospheric) boundary layer (PBL).

Because of NO<sub>2</sub> short photolytic life time outside of the boundary layer and the temperature-dependent partitioning between NO<sub>2</sub> and NO, most of the tropospheric NO<sub>2</sub> column density resides in the PBL ([Sluis \*et al.\*, 2010](#); [Sitnikov \*et al.\*, 2005](#); [Pisano \*et al.\*, 1996](#)). However, the height of the PBL is variable throughout the day, responding to local surface heating and other synoptic and meso-scale forcing, emissions being typically well mixed throughout this layer. Therefore, if emissions and removals are constant, it is reasonable to expect pollutant mixing ratios to vary inversely with PBL height while the column density would remain constant ([Knepp \*et al.\*, 2013](#)).

Recently a methodology has been developed for conversion of total-column observations to surface mixing ratio estimations ([Knepp \*et al.\*, 2013](#)). In this study we applied that method and compared column-density measurements derived from two columnar instruments, a ground-based spectrometer and overpassing satellite-borne instrument with the continuous surface-level mixing ratio measurements by a gas analyser.

### 2. Location

The Welgegund measurement site (26°34'10"S, 26°56'21"E, 1480 m a.s.l.) is located approximately 100 km south-west of the Johannesburg-Pretoria conurbation with a population of over 10 million ([Lourens \*et al.\*, 2012](#)). There is no significant local pollution source close to the measurement site. However, it is frequently impacted by air masses from a number of country's major pollution source regions. Importantly, air masses, passing over the regional background from the west of Welgegund where no significant point sources exist, regularly arrive at Welgegund ([Beukes \*et al.\*, 2014](#)).

\*Based on the IUAPPA 2013 conference proceedings, Cape Town, 29 September – 4 October 2013, with extra data analysed.

### 3. Methods and instrumentation

#### 3.1 NO<sub>2</sub> Instrumentation

The surface mixing ratios are measured by a molybdenum-oxide converter with NO detected chemiluminescence after reaction with O<sub>3</sub>, (Teledyne AU 200 gas analyser). The instrument records NO and NO<sub>x</sub> concentrations from which NO<sub>2</sub> is determined by subtraction of NO from NO<sub>x</sub>.

The ground-based spectrometer named “Pandora” used in this study has been validated against similar sun-tracking instruments (Wang *et al.*, 2010), MAX-DOAS and zenith-looking instruments (Peters *et al.*, 2012) and Aura satellite-borne OMI (Herman *et al.*, 2009). Pandora provides NO<sub>2</sub> vertical-column densities from direct sun observation that serve as a proxy for satellite-derived observations, such as OMI, with 2-minute resolution, thereby allowing direct comparison of *in-situ*/column observations throughout the day as boundary layer dynamics, emissions and atmospheric chemistry change. OMI retrievals were sourced from NASA (Boersma *et al.*, 2002; Bucseba *et al.*, 2006).

#### 3.2 ABL determination

Two methods were used: in first, PBL structure and evolution was modelled using Monin-Obukhov similarity theory. The Hong and Pan (1996) boundary layer parameterization scheme was used for the MM5 model runs using NCEP (NOAA) reanalysis data as input. The hourly boundary layer height was then estimated using a scheme similar to Cimorelli *et al.*, (2004) (Figure 1).

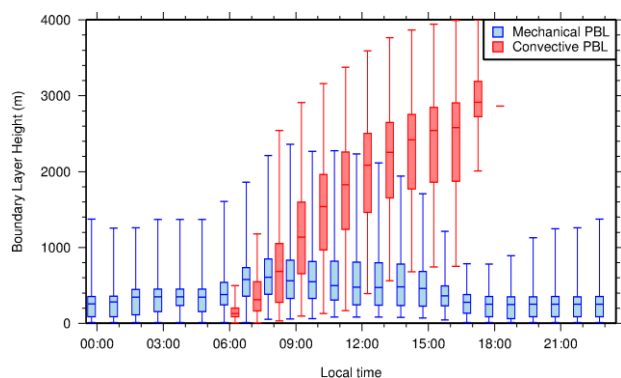


Figure 1: Modelled diurnal planetary boundary layer (PBL) heights above Welgegend over study period. The box-and-whiskers plot show the minimum, 25 percentile, median, 75 percentile and maximum hourly values.

In second, observed PBL heights were derived from Atmospheric Infra-Red Sounder (AIRS, Aqua satellite-borne) Level 2 Version 6 temperature and humidity profiles (100 layers, with a nominal grid

spacing of about 25 hPa in the PBL). Herein the PBL height can be defined as the height where strong/sharp gradients in both temperature and relative humidity are evidently distinguishable. Thus such AIRS dataset has the potential to provide reliable PBL height information as it contains global observations of the PBL structure that are useful for both spatial and seasonal variability studies (Martins *et al.*, 2010).

#### 3.3 Methods

In this study we applied the methodology developed for the analysis of data collected at NASA’s Langley Research Center for the DISCOVER-AQ field campaign in Maryland, USA for conversion of a total-column observation to a surface mixing ratio estimation (Knepp *et al.*, 2013).

Pandora (and similarly OMI) tropospheric NO<sub>2</sub> values were converted to molar ratio values via Equation (1) where Pandora<sub>col</sub> is the total column density measured by Pandora in molec/cm<sup>2</sup>, OMI<sub>strat</sub> is the stratospheric component as measured by OMI, PBL is the boundary-layer height in cm, N is the number density of air in molec/cm<sup>3</sup>, using calculated hourly PBL to properly account for the influence of PBL variability.

$$ppb = \frac{(Pandora_{col} - OMI_{strat}) * 1E9}{PBL * N} \quad (1)$$

The NO<sub>2</sub> surface mixing ratios were obtained from the Teledyne NO & NO<sub>x</sub> gas analyser, logging at 1 minute time resolution. These data were subsequently quality-controlled and scientifically flagged per standard procedures and averaged into 15 minutes averages (Vakkari *et al.*, 2011; Laakso *et al.*, 2008).

Pandora’s algorithms, which retrieve ground-based total column NO<sub>2</sub> amounts, use direct-sun irradiances between 280 nm and 525 nm at a resolution of approximately 0.5 nm (Brinkma *et al.*, 2008; Herman *et al.*, 2009; Tzortziou *et al.*, 2012). Pandora has a 1.6-degree field of view (FOV, a circle of ~120 m in diameter at 4 km altitude) and is mounted on a precision pan-tilt tracking device to follow the position of the centre of the sun. Pandora retrieves total columns approximately every 2 minutes. Clouds, ambient temperature, and absorption cross sections all introduce uncertainties into the Pandora total column NO<sub>2</sub> retrieval, and must be corrected in the instrument retrieval algorithm (Herman *et al.*, 2009; Tzortziou *et al.*, 2012). Absolute error in Pandora retrievals is ±0.1 DU, with a precision of about ±0.1 DU in clear skies. This error grows with noise created by clouds in a given retrieval (Reed *et al.*, 2013). The Pandora data were quality-controlled and flagged (mainly for instrument non-functioning periods and cloud cover threshold exceedances). For the purpose of this study, 15 minute averages were created for comparison to the gas analyser.

\*Based on the IUAPPA 2013 conference proceedings, Cape Town, 29 September – 4 October 2013, with extra data analysed.

OMI Level 2, Version 3 Total and Tropospheric Column NO<sub>2</sub> (OMNO<sub>2</sub>) data from the NASA GES DISC (“Goddard Earth Sciences Data and Information Services Center”) provide (13 x 24 km resolution) total column NO<sub>2</sub> retrievals for direct comparisons. OMI retrievals within 100 km distances to the station were selected and averaged. In addition to the total column amount, OMI data files included quality control flags for conditions that could cause erroneous retrievals. The cloud fraction retrieved by OMI (retrievals with cloud fraction <30 % were selected) and the ‘Row Anomaly’ flag were used to filter data when Level 1B OMI radiances are compromised by a high signal/noise.

Daily OMI-derived stratospheric column NO<sub>2</sub> data (using the OMNO<sub>2</sub> data) were interpolated to the same temporal frequency as the quality-controlled Pandora measurements and subtracted from the Pandora-column observations at the site to yield tropospheric NO<sub>2</sub> column densities applicable to the study period. As a result of poor (cloudy/rainy) weather conditions at the station, 25 days between January 25 and March 15, 2011 could be used for the analysis.

## 4. Results

### 4.1 Surface gas analyser vs. Pandora comparison

Preliminary comparisons of the gas analyser surface NO<sub>2</sub> mixing ratios with the Pandora converted surface NO<sub>2</sub> mixing ratios indicate that Pandora was generally underpredicting the surface NO<sub>2</sub> concentration (Figure 2). The mean surface mixing ratio for this study as measured by the gas analyser is ~ 2 ppb as compared to the Pandora converted surface mean of ~ 1 ppb of NO<sub>2</sub>. The percent difference between the gas analyser and Pandora is about 50 % when outliers are not included; however, in many instances the Pandora converted surface mixing ratio was within the uncertainty limit of the gas analyser.

### 4.2 Surface gas analyser-Pandora-OMI inter-comparison

The comparison of all three measurements of NO<sub>2</sub>: gas analyser surface mixing ratio, Pandora converted surface mixing ratio, and OMI total column concentration as well as its BL converted VMR indicates that results are sensitive and responsive to evident changes in boundary layer concentrations for both remotely sensed (Pandora and OMI) and surface gas sampling. These results demonstrate the potential application for Pandora to provide surface mixing ratio estimates at similar temporal frequencies as gas analysers. Estimated OMI surface NO<sub>2</sub> is sometimes within the

ground/Pandora uncertainty limits when using AIRS-derived PBL heights, but OMI surface NO<sub>2</sub> in clean air remained difficult to capture (Figure 2).

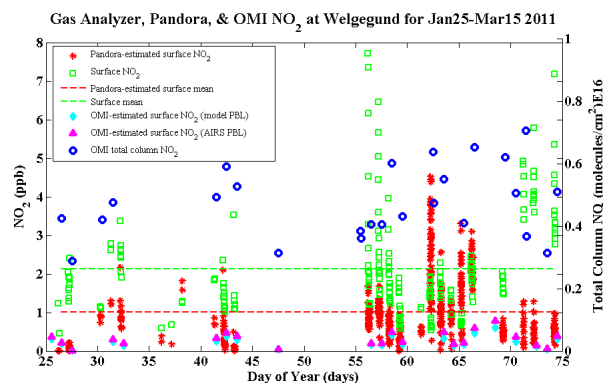


Figure 2: Gas analyser (green circles) vs. Pandora (red stars) vs. Ozone Measuring Instrument (OMI) surface mixing ratios of NO<sub>2</sub> (cyan diamonds) with modelled planetary boundary layer (PBL) and OMI surface mixing ratios of NO<sub>2</sub> (magenta stars) with observed, Atmospheric Infra-red Sounder (AIRS) PBL over Welgegund.

## 5. Conclusions

For the first time in this region, a quantitative comparison of remotely sensed trace gas columns with gas analyser surface-level NO<sub>2</sub> mixing ratios was undertaken. The data for the ground instruments were in agreement within the expected uncertainty for each technique and between two remote sensing instruments. However, NO<sub>2</sub> between the ground gas analyser and satellite borne instrument were out of the expected uncertainty limits. Both observed and modelled PBL heights were used in the PBL correction, which is likely the greatest uncertainty in the conversion of column to surface NO<sub>2</sub>. This study contributes to further exploration of this technique in varied environments as encouraged by the initial study.

## 6. Acknowledgments

We herewith thank: NASA and Pennsylvania State University (PSU), the USA, University of Helsinki (UH), and Finish Meteorological Institute (FMI), Finland, South African Weather Service (SAWS), and North West University (NWU), South Africa. The deployment of a Pandora at Welgegund was made possible by Aura Validation support to PSU during the residence period of a “J. W. Fulbright Scholar” award to A.M. Thompson.

## 7. References

Beukes, P., Vakkari, V., van Zyl, P. G., Venter, A., Josipovic, M., Jaars, K., Tiitta, P., Laakso, H.,

\*Based on the IUAPPA 2013 conference proceedings, Cape Town, 29 September – 4 October 2013, with extra data analysed.

- Kulmala, M., Worsnop, D., Pienaar, J., Järvinen, E., Chellapermal, R., Ignatius, K., Maalisk, Z., Cesnulyte, V., Ripamonti, G., Laban, T., Skrabalova, L., du Toit, M., Virkkula, A., and Laakso, L. 2014, Source region plume characterization of the interior of South Africa, as measured at Welgegund, *manuscript in preparation*
- Boersma, K. F., Bucsela, E., Brinksma, E., Gleason, J. F. 2002, NO<sub>2</sub>, Algorithm Theoretical Baseline Document: OMI Trace Gas Algorithms, K.Chance (ed.), vol. IV, ATBD-OMI-04, version 2.0
- Bucsela, E. J., Celarier, E. A., Wenig, M. O., Gleason, J. F., Veefkind, J. P., Folkert Boersma, K., Brinksma, E. J. 2006, Algorithm for NO<sub>2</sub> Vertical Column Retrieval From the Ozone Monitoring Instrument. IEEE Transactions on Geoscience and Remote Sensing, 44, doi: 10.1109/TGRS.2005.863715
- Cimorelli, A.J., Perry, S.G., Venkatram, A., Weil, J.C., Paine, R.J., Wilson, R.B., Lee, R.F., Peters, W.D., Brode, R.W., Paumier, J.O. 2004, AERMOD: Description of model formulation, Research Triangle Park, North Carolina
- Herman, J., Cede, A., Spinei, E., Mount, G., Tzortziou, M., Abuhassan, N. 2009, NO<sub>2</sub> column amounts from ground-based Pandora and MFDOAS spectrometers using the direct-sun DOAS technique.: Intercomparisons and application to OMI validation, J. Geophys. Res.-Atmos., 114, doi:10.1029/2009JD011848
- Hong, Song-You, Hua-Lu Pan, 1996, Nonlocal Boundary Layer Vertical Diffusion in a Medium-Range Forecast Model. Mon. Wea. Rev., 124, 2322–2339
- Knepp, T., Pippin. M., Crawford, J., Chen, G., Szykman, J., Long, R., Cowen.L., Cede, A., Abuhasan, N., Herman, J., Delgado, R., Compton, J. Berkoff, T., Fishman, J., Martins, D. Stauffer, R., Thompson, A.M., Weinheimer, A., Knapp, D., Montzka, D.Lenschow, D., Neil, D. 2013, Estimating surface NO<sub>2</sub> and SO<sub>2</sub> mixing ratios from fast-response total column observations and potential application to geostationary missions, J. Atmos. Chem.DOI 10.1007/s10874-013-9257-6,
- Laakso, L., Laakso, H., Aalto, P., Keronen, P., Petäjä, T., Nieminen, T., Pohja, T., Siivola, E., Kulmala, M., Kgabi, N., Molefe, M., Mabaso, D., Phalatse, D., Pienaar, K. and Kerminen, V.-M. 2008, Basic characteristics of atmospheric particles, trace gases and meteorology in a relatively clean Southern African Savannah environment. Atm. Chem. Phys., 8, 4823-4839
- Lourens, A. S., Butler, T. M., Beukes, J. P., van Zyl, P. G., Steffen, B., Wagner, T., Heue, K.-P., Pienaar, J. J., Fourier, G., and Lawrence, M. 2012, Re-evaluating the NO<sub>2</sub> hotspot over the South 15 African Highveld, S. Afr. J. Sci., 108, 1146, doi:10.4102/sajs.v108i11/12.1146
- Martins, J. P. A., J. Teixeira, P. M. M. Soares, P. M. A. Miranda, B. H. Kahn, V. T. Dang, F. W. Irion, E. J. Fetzer, and E. Fishbein 2010, Infrared sounding of the trade-wind boundary layer: AIRS and the RICO experiment, Geophys. Res. Lett., 37, L24806, doi:10.1029/2010GL045902
- Pisano, J., Drummond, J., Hastie, D.R. 1996, A lightweight NO<sub>2</sub> instrument for vertical height profiles, J. Atmos. Ocean Tech., 13, 400-406
- Piters, A. J. M., Boersma, K. F., Kroon, M., Hains, et al. 2012, The Cabauw Intercomparison campaign for Nitrogen Dioxide measuring Instruments (CINDI): design, execution, and early results, Atmospheric Measurement Techniques, 5, doi: 10.5194/amt-5-457-2012
- Reed, A. J. Thompson, A. M. Kollonige, D. E., Martins, D. K., Tzortziou, M. A., Herman, J. R., Berkoff, T. A., Abuhassan, N. K., Cede, A. 2011, Effects of Local Meteorology and Aerosols on Ozone and Nitrogen Dioxide Retrievals from OMI and Pandora Spectrometers in Maryland, USA during DISCOVER-AQ, J Atmospheric Chemistry, 2013.doi:10.1007/s10874-013-9254-9
- Sitnikov, N.M., Sokolov, A.O., Ravegnani, F., Yushkov, V.A., Ulanovskiy, A.E. 2005, A chemiluminescent balloon-type nitrogen dioxide meter for tropospheric and stratospheric investigations (NaDA), Phys. Inst. for Ecol. Med. Biol., 48, 136-141
- Sluis, W.W., Allaart, M.A.F., Piters, A.J.M, Gast, L.F.L. 2010, The development of a nitrogen dioxide sonde, Atmos. Meas. Tech., 3, 1753-1762, doi:10.5194/amt-3-1753-2010
- Tzortziou, M., Herman, J. R., Cede, A., Abuhassan, N. 2012, High precision, absolute total column ozone measurements from the Pandora spectrometer system: comparisons with data from a Brewer double monochromator and Aura OMI, J. Geophys. Res., 117, D16303, doi: 10.1029/2012JD017814
- Vakkari, V., Laakso, H., Kulmala, M., Laaksonen, A., Mabaso, D., Molefe, M., Kgabi, N. and Laakso, L. 2011, New particle formation events in semi-clean South African savannah, Atmos. Chem. Phys. 11, 3333-3346. DOI: 10.5194/acp-11-3333-2011
- Wang, S., Pongetti, T.J., Sander, S.P., Spinei, E., Mount, G.H., Cede, A., Herman, J. 2010, Direct Sun measurements of NO<sub>2</sub> column abundances from Table Mountain, California: Intercomparison of low- and high-resolution spectrometers, J. Geophys. Res.-Atmos., 115, D13305, doi: 10.1029/2009JD013503

# The Rapidly Developing Thunderstorm Product – results of case studies and future plans

Morné Gijben\*<sup>1</sup>, Estelle de Coning<sup>1</sup>, Louis van Hemert<sup>1</sup>, Cassandra Pringle and Bathobile Maseko<sup>1</sup>  
<sup>1</sup> 442 Rigel Ave South, Erasmusrand, Pretoria, Gauteng, 0181, South Africa, morne.gijben@weathersa.co.za

In the past year the Nowcasting Satellite Application Facility's software was installed and tested over the South African and southern African domains. The Rapidly Developing Thunderstorms product promised to be a very useful tool for nowcasting purposes, especially in regions where radar systems are not available or operational. If intense and/or severe convective systems can be detected using satellite (and numerical weather prediction model data) input, this could be beneficial for data sparse regions, such as Africa. The usefulness of the RDT product was validated using case studies from the recent summer periods. Both the quantitative as well as qualitative evaluations delivered favourable results. There is a good visual agreement between the RDT product and radar as well as lightning, while statistical scores show that RDT identified close to 70% of the moderate to intense lightning cells detected by the SALDN for 10 cases. Evaluations of RDT against WWLLN data indicates that HK scores ranged between 0.5 and 0.6 for 10 cases.

**Keywords:** satellite, numerical weather prediction models, thunderstorms, data sparse regions.

## 1. Introduction

Remote sensing tools, such as radar systems, lightning detection networks and satellites, play an important role in the nowcasting (0-6 hour forecasts) of thunderstorms (de Coning *et al.*, 2011). Radar systems are the most important tool for nowcasting, since it provides continuous information on the size, shape, intensity, speed and direction of movement of individual storms (VAISALA 2010). Unfortunately many developing and especially least developed countries do not have access to radar or lightning systems. Alternative solutions, which do not require expensive ground-based systems, need to be utilized for the nowcasting of thunderstorms.

The Meteosat Second Generation (MSG) satellite has proved to be particularly useful in data sparse regions where the Infrared (IR), Visible (VIS) and Water Vapour (WV) single channels as well as combinations of the channels can be applied for the nowcasting of thunderstorms (de Coning *et al.*, 2011; Siewert *et al.* 2010).

Satellite Application Facilities (SAF) are centres of excellence with experts in various fields, which aim to process satellite data to develop products for specific purposes. One of the products developed by the Nowcasting SAF is the Rapidly Developing Thunderstorm (RDT) product. The aim of the RDT product is to identify, monitor and track intense cloud systems and also to detect rapidly developing storm systems (NWC SAF <http://www.nwcsaf.org>).

The RDT product was recently implemented at the South African Weather Service (SAWS). MSG satellite data is used as initial input and numerical weather prediction model data from the local version of the Unified Model (UM) is utilised to enhance the RDT product. An advantage of the RDT product is that output is available every 15 minutes when the new satellite data is received.

Evaluations over the South African domain as well as the Southern African Development Community (SADC) region proved that the RDT product can be useful for the nowcasting of intense thunderstorms when used in addition to other ground based observations such as radar and lightning systems in South Africa (SA). In regions without radar and lightning detection systems, such as SADC, this product will certainly benefit nowcasting procedures.

## 2. Data and Methods

Qualitative, as well as quantitative, evaluations were performed on the RDT product over both the SA and SADC domains. Ten case study dates were used over the SA domain and 10 cases over the SADC domain. Visual evaluations between the RDT product and radar as well as satellite imagery were done for the SA region, while for the SADC region only satellite imagery could be used due to the absence of radar systems over the subcontinent. Quantitative evaluations were performed against lightning data from the South African Lightning

Detection Network (SALDN) and the World Wide Lightning Location Network (WWLLN) over the SA and SADC regions, respectively.

The SALDN detects cloud-to-ground (CG) lightning with a detection efficiency of 90% over most of the country (Gijben, 2012). The WWLLN network, operated by the University of Washington, is a global ground-based lightning detection network, which detects very low frequency (VLF) radio waves and identifies lightning sferics (Collier et. al., 2010). WWLLN is able to detect lightning occurrence globally by using only a few sensors since the attenuation of the signal for VLF waves is much lower (Collier et. al., 2010). By using only a limited amount of sensors the detection efficiency is reduced quite significantly. Studies have shown that when the WWLLN network is compared to ground-based LDN (such as the SALDN), the detection efficiency of WWLLN is approximately 10%, which means that only about 10% of all the lightning that occurred was detected by WWLLN (Virts et. al., 2013).

Each of the lightning detection networks has its own limitations when evaluating the RDT product. The SALDN detects primarily CG lightning. This means that the intra-cloud (IC) lightning, which contributes more to the total amount of lightning, could not be used in the evaluation of the RDT product. Since the RDT product deals with developing and mature thunderstorms, the lack of IC lightning could have negatively affected the statistical scores since IC lightning dominates in these two phases of the storm. The WWLLN network only detects about 10% of the total lightning, which means that statistical scores will be negatively affected by the 90% of lightning strokes not detected by the network.

Every RDT time step was evaluated against lightning that occurred in the 30-minutes following the period of interest. For SA, the first evaluation method looked at the percentage of grid boxes containing more than 20 lightning strokes which fell inside the RDT polygons. The second method used a contingency table approach for grid boxes with more than 20 lightning strokes. The 20 lightning stroke threshold is used to consider only moderate to intense lightning cells in order to filter out all the weak lightning cells not associated with intense and/or rapidly developing thunderstorms. This approach was also followed by the validation reports of the RDT product (NWC SAF <http://www.nwcsaf.org>). Over the SADC region all grid boxes with one or more lightning strokes were compared to the RDT polygons.

### 3. Results

Figure 1 (a) illustrates the RDT and lightning and Figure 1 (b) the coinciding radar reflectivities on 9 October 2012 at 15:30 UTC. The storms indicated

by the arrows show that the RDT polygons correlate well with the areas where large amounts of lightning as well as high radar reflectivities occurred. In the circled area, intense lightning and relatively high reflectivity patterns could be seen where the RDT did not identify a storm polygon. The RDT thus missed this storm.

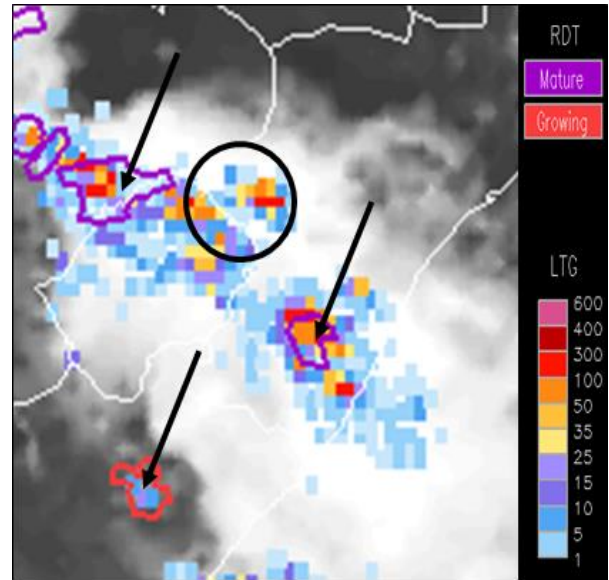


Figure 1. a) Visual comparison between the RDT product and the occurrence of lightning on 9 October 2012 at 15:30 UTC.

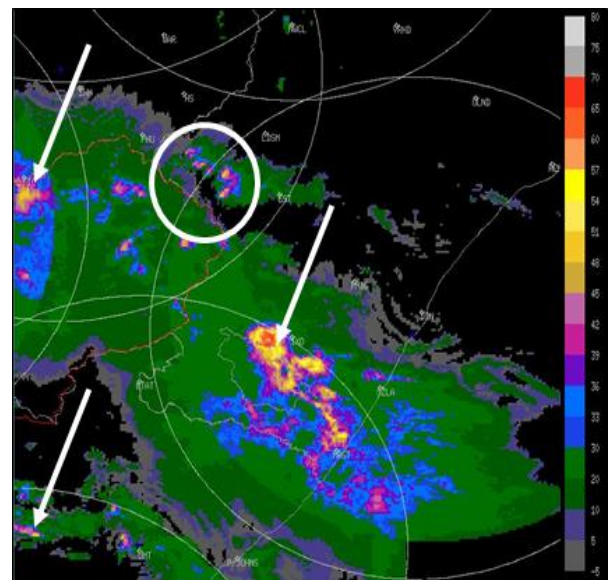


Figure 1. b) The radar reflectivity pattern which coincides with the RDT and lightning on 9 October 2012 at 15:30 UTC

Figure 2 shows another example on 9 November 2012 at 11:30 UTC where the (a) RDT could identify a storm in the KZN area (arrow), where no radar data was available (b). This illustrates the usefulness of

this product in areas without radar systems or when radar systems are down. Intense lightning cells were also detected well with RDT and corresponds with the storms on the radar.

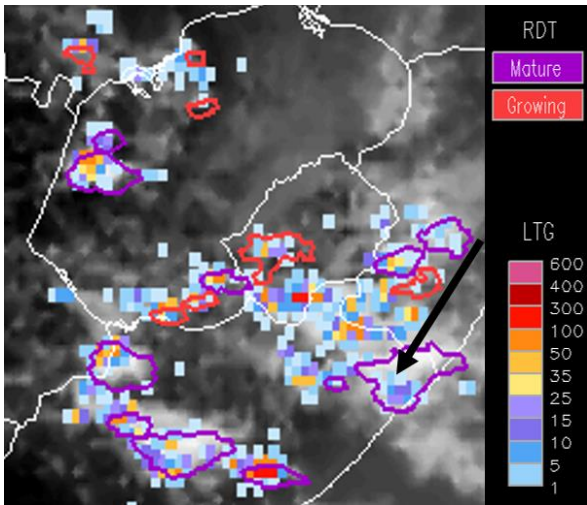


Figure 2. a) Visual comparison between the RDT product and the occurrence of lightning on 9 November 2012 at 11:30 UTC

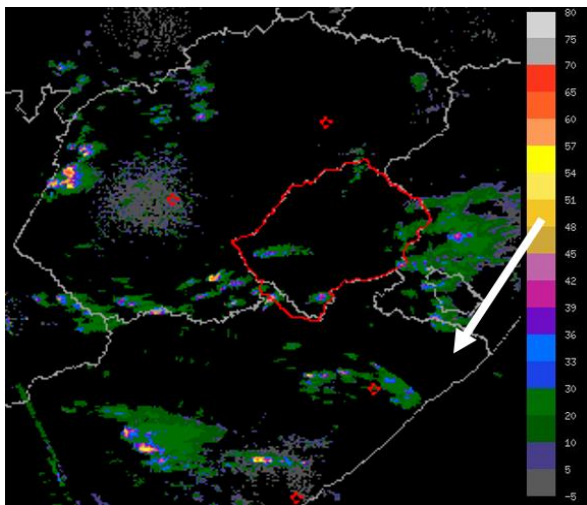


Figure 2.b) The radar reflectivity pattern which coincides with the RDT and lightning on 9 November 2012 at 11:30 UTC

Figure 3 shows (a) the RDT over the southern parts of Zimbabwe on 28 December 2013 at 12:00 UTC and (b) the TRMM rainfall for the 3hour period surrounding the RDT time (10:30 UTC – 13:30 UTC). It is clear that intense rainfall occurred in the same area where the RDT identified a mature storm indicated by the purple polygon.

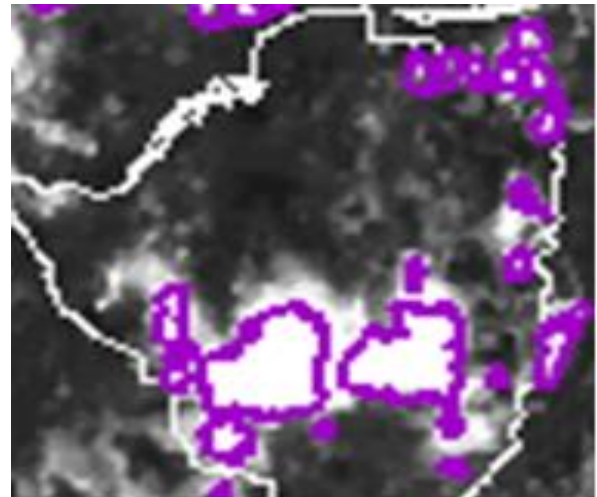


Figure 3. a) The RDT product on 28 December 2013 at 12:00 UTC

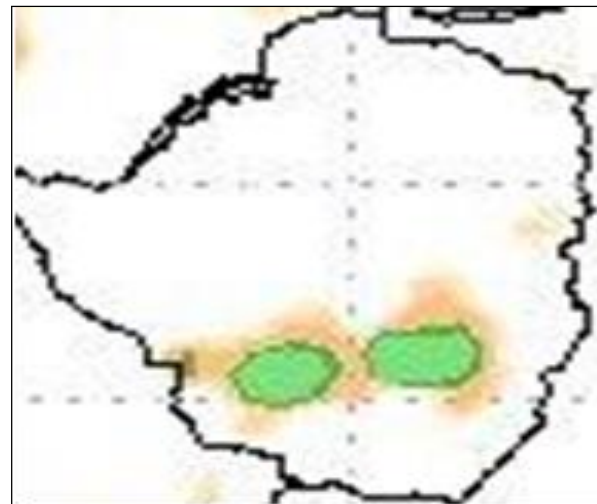


Figure 3. b) TRMM rainfall on 28 December 2013 from 10:30 UTC to 13:30 UTC.

In Figure 4 the validation of the RDT is shown. For the purpose of this more quantitative validation, the lightning intensity was divided into 2 categories – light lightning was defined as grid boxes with less than 20 strokes of lightning, while moderate to intense lightning was defined as more than 20 strokes of lightning per grid box in the 30 minutes following the RDT time. In Figure 4 the percentage of moderate to intense lightning is calculated which fell inside the RDT polygons. It is clear that RDT identified close to 70% of the moderate to intense lightning cells for the 10 cases.

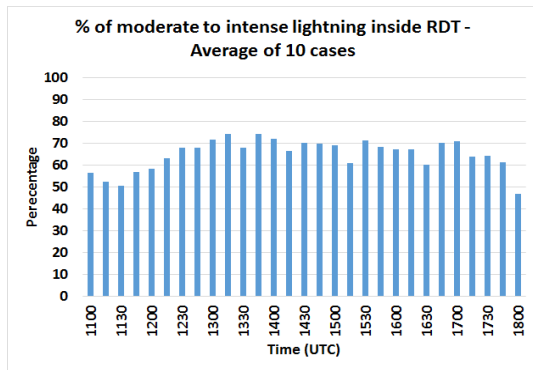


Figure 4. The average percentage of all grid boxes with more than 20 lightning strokes that occurred inside the RDT polygons over South Africa.

For the SADC region a contingency table approach was followed. It was not possible to use only moderate to severe lightning, since the amount of lightning captured by the WWLLN is already quite low. In Figure 5 the Hanssen-Kuiper scores (red line) show that the RDT product identified the lightning cells for the 10 cases reasonably well, especially if one considers that the WWLLN lightning network only detects about 10% of the lightning.

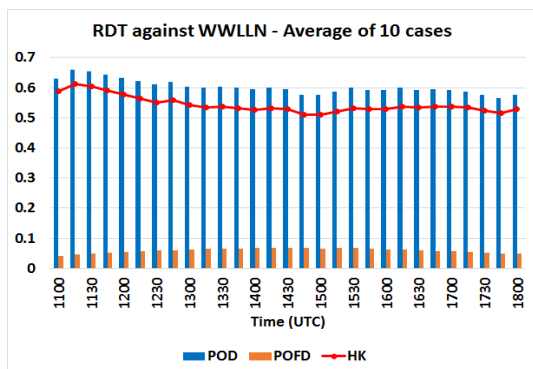


Figure 5. The average Probability of Detection (POD), Probability of False Detection (POFD) and Hanssen-Kuiper (HK) scores for RDT validated against WWLLN data over SADC for 10 cases.

#### 4. Summary and future work

Both the qualitative and quantitative evaluations show that the RDT product performs quite well over the SA and SADC domain. Over SA the qualitative evaluations of RDT against radar and lightning images show excellent agreement while quantitative evaluations showed that RDT identified close to 70% of the moderate to intense lightning cells detected by the SALDN for the 10 cases. Over the SADC domain the quantitative evaluations of RDT against WWLLN data indicates that HK scores ranged between 0.5 and 0.6 for the 10 cases, which is quite good considering that WWLLN only detects about 10% of all the lightning.

All of the evaluations were performed with the 2012 version of the NWC SAF software. More recently the 2013 version of the software was made operational at SAWS in real time. Future work can include the testing of the new 2013 software and also to include and test the option of the RDT software to add lightning data in order to enhance the product.

#### 5. Permission to Publish

This work forms part of a Water Research Commission project (WRC K5/2235/1) for the period 1 April 2013 to 31 March 2015.

#### 6. Acknowledgments

We are grateful to Andrew Collier who provided the WWLLN lightning data that was used in this project, as well as the University of Washington who hosts the WWLLN lightning detection network.

#### 7. References

- Collier A.B., Bremner S., Lichtenberger J., Downs J.R., Rodger C.J., Steinbach P., & McDowell G. 2010, 'Global lightning distribution and whistlers observed at Dunedin', *Annales Geophysicae*, **28**:499–513
- De Coning E., Koenig M., & Olivier J. 2011, 'The combined instability index: a new very-short range convection forecasting technique for southern Africa', *Meteorological Applications*, **18**:421-439
- EUMETSAT n.d., *Satellite Application Facilities*, viewed 28 July 2014 from: <http://www.eumetsat.int/website/home/Satellites/GroundSegment/Safs/index.html>
- Gijben M. 2012, 'The lightning climatology of South Africa', *South African Journal of Science*, **108(3/4)**: 44-53
- NWC SAF 2013, *Validation Report for "Rapid Development Thunderstorms" (RDTPGE11 v3.0)*, viewed 29 July 2014 from: <http://www.nwcsaf.org/HD/MainNS.jsp>
- NWC SAF n.d., *Rapid Development Thunderstorm (PGE11 v3.0) v2013*, viewed 29 July 2014 from: <http://www.nwcsaf.org/HD/MainNS.jsp>
- Siewert C.W., Koenig M., & Mecikalski J.R. 2010, 'Application of Meteosat second generation data towards improving the nowcasting of convective initiation', *Meteorological Applications*, **17**:442-451
- VAISALA n.d., *Optimized Dual Polarization Performance: VAISALA Weather Radars*, viewed 29 July 2014 from: <http://www.vaisala.com/Vaisala%20Documents/Brochures%20and%20Datasheets/MET-WR-Radar-folder-B210696EN-E-LowRes.pdf>
- Virts K.S., Wallace J.M., Hutchins M.L., & Holzworth R.H. 2013, 'Highlights of a new ground-based, hourly global lightning climatology', *Bull. Amer. Meteor. Soc.*, **94**:1381–1391

# A study on Bio-meteorological indices for forecasting heat waves over SA

Patience T. Shibambu<sup>1</sup> and Willem A. Landman<sup>2</sup>

<sup>1</sup>South African Weather Service, 442 Rigel Avenue South, Erasmusrand, Pretoria 0002, [www.weathersa.co.za](http://www.weathersa.co.za)

<sup>2</sup>Council for Scientific and Industrial Research Pretoria, South Africa 0002, [www.csir.co.za](http://www.csir.co.za)

Climate change projections show an expected increase in the frequency and intensity of extreme weather phenomena, including heat waves. South Africa is geographically located in a region where extreme heating is common during summer months. In this paper different bio-meteorological indices for forecasting heat waves over South Africa are evaluated using subsets from the National Centers for Environmental Prediction (NCEP) Ensemble Prediction System (EPS) and observational data for South African Weather stations. The indices are evaluated over a 14-day lead time over a 4-year period (summer months). The indices include the discomfort index from the South African Weather Service, humidity, apparent temperature, wet-bulb global temperature and the Thom discomfort index. The index with the forecast highest skill will be used to develop a heat wave forecast system for mitigation and prevention of heat related illnesses and mortalities. SAWS DI shows more accuracy at 2 day lead time compared to the TDI. More analysis will be done and the results will be presented.

**Keywords:** Heat index, heat wave, heat watch-warning, discomfort index, evaluation, NCEP EPS.

## 1. Introduction

There is no internationally accepted definition of heat waves, but in most nations it is considered as a persistence of high temperatures for three or more consecutive days. Due to climate change and geographical location, most parts of South Africa (SA) are exposed to extreme heating during summer months. Heat waves are considered significant weather hazards and have a wide range of negative impacts on human health, economy and the environment. They may also result in loss of agricultural production and livestock, resulting in food shortage and bankruptcy of farmers, forest fires, and inadequate supply of clean drinking water, power failures and power cuts due to water shortage. Anthropogenic climate change is projected to bring with it an increase in frequency of heat waves, which can intensify droughts, increase the risk of fires and mortality rates.

South Africans most prone to the negative impacts of heat waves include the young, elderly, sickly, overweight, outdoor workers, the poor and low income groups and residents in cities. There is, therefore a need to accurately forecast heat waves in advance in order to prevent or mitigate the negative impacts of heat

waves.

## 2. Aims and objectives

The aim of this study is to identify the most appropriate heat index from a weather forecasting perspective. The index will be used to develop a real-time heat wave forecast system for the benefit of the health sector, SA citizens and other stakeholders. The objectives are:

- Identify the heat indices to investigate and the meteorological variables required for each index.
- Calculate the indices for each station, for the entire study period.
- Obtain forecast verification statistics for each index.

## 3. Data and methodology

The selected heat indices only require temperature and relative humidity. Hence, these variables were collected from the National Centers for Environmental Prediction (NCEP) Ensemble Prediction System (EPS) (1x1<sup>0</sup> resolution). The model was evaluated against observations from 167 South African Weather

Stations (SAWS) stations. Both datasets were retrieved from the archive system of SAWS.

The heat indices that were selected for the study were the discomfort index from the South African Weather Service (DI), humidity (H), apparent temperature (AT), wet-bulb global temperature (WBGT) and the Thom discomfort index (TDI). Equations for these indices are summarized in Table 1. Verification techniques used to evaluate these indices include bias, critical success index (CSI), false alarm ratio (FAR), probability of detection (POD), Heidke skill scores (HSS), Clayton skill scores (CSS), equitable threat scores (ETS), external dependence index (EDI) and the symmetric external dependence index (SEDI). Table 1 depicts the formulas for these techniques.

Table1: Summary of selected Bio-meteorological indices. T=surface temperature ( $^{\circ}\text{C}$ ), e=water vapour pressure,  $T_d$ =dew point temperature and RH=relative humidity.

Index	Equation
DI	$2T+RH(T+24)/100$
H	$T+(e-21)$ ; where $e=6.11 \times \frac{7.5T_d}{e^{273.7+T_d}}$
AT	$-2.653+0.994T+.368T_d^2$
TDI	$T-0.55[1-0.01(RH)](T-14.5)$
WBGT	$0.567T+0.393e+3.94$ ; where $e=6.11 \times \frac{7.5T_d}{e^{273.7+T_d}}$

Table2: Summary of the evaluation techniques used in the study, where a=hits, b=false alarms, c=misses and d=correct negatives.

Scheme	Formula
Bias	$(a+b)/(a+c)$
CSI	$a/(a+b+c)$
FAR	$b/(a+b)$
POD	$a/(a+c)$
HSS	$2(ad-bc)/((a+c)(c+d)+(a+b)(b+d))$
CSS	$(ad-bc)/((a+b)(c+d))$
ETS	$(a-a_{ref})/(a-a_{ref}+b+c)$ ; where $a_{ref}=(a+b)(a+c)/n$
EDI	$(\log FAR - \log POD)/(\log FAR + \log POD)$
SEDI	$(\log FAR - \log POD - \log(1-FAR) + \log(1-POD))/(\log FAR + \log POD + \log(1-FAR) + \log(1-POD))$

#### 4. Preliminary results

Heat waves are rare events and it is only certain parts of the country that are most prone to heat waves: the south and east coast, and the eastern interior. SAWS DI detected more cases of heat waves than the TDI. SAWS DI identified heat wave events over the eastern interior, and the south and east coast.

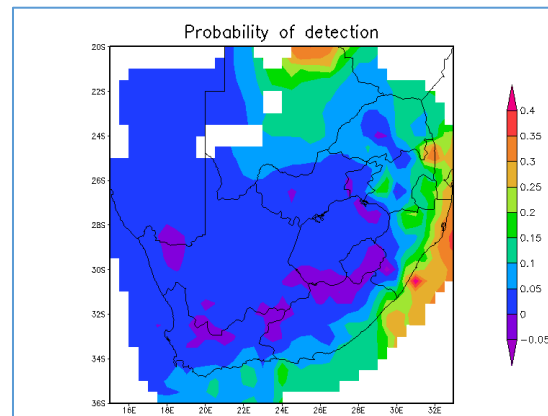


Figure 1. POD for SAWS DI at 2-day lead-time.

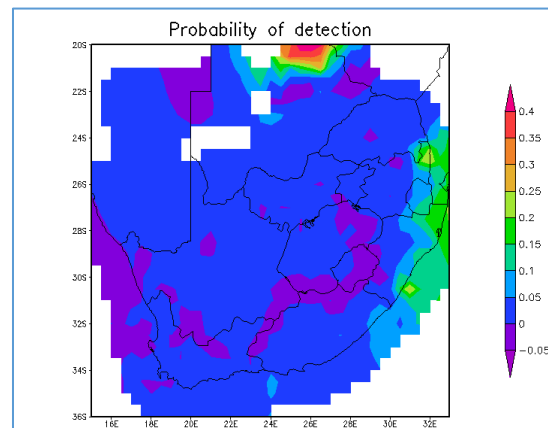


Figure 2. POD for TDI at 2-day lead-time.

#### 5. Discussions

SAWS heat index detects more heat wave events over the country, compared to TDI at 2-day lead time. Further study will be done and presented on the final paper.

#### 6. Acknowledgements

Thanks to SAWS staff for and Simon Mason assistance with modelling matters

## 7. References

- Jolliffe, I. T. & Stephenson, D. b. (eds.),  
2011. *Verification: A practitioner's  
guide in atmospheric science*. Wiley,  
New York.
- Kalkstein, L. S. & Sheridan, S. C. 2004.  
Progress in heat watch–warning  
system technology. *Bull. Amer.  
Meteor. Soc.* **85**: 1931-1941
- Lyon, B. 2009. Southern Africa summer  
drought and heat waves:  
observations and coupled model  
behavior. *Amer. Meteor. Soc.* **22**:  
6033-6046.
- Tennant, W., Toth, Z. & Rae, K. 2006.  
Application of the NCEP Ensemble  
Prediction System to medium-range  
forecasting in South Africa: new  
products, benefits and challenges.  
*Amer. Meteor. Soc.* **22**: 18-35.
- Wilks, D. S., *Statistical methods in the  
atmospheric sciences*. 2nd ed,  
Elsevier Academic Press, Oxford,  
UK.

# Projections of heat waves and health impacts in Africa in a changing climate

Rebecca M Garland\*<sup>1,2</sup>, Mary-Jane Bopape<sup>1,3</sup>, Mamopeli Matookane<sup>1</sup>, and Francois Engelbrecht<sup>1</sup>

<sup>1</sup> Climate Studies, Modelling and Environmental Health research Group, CSIR, Pretoria, South Africa, rgarland@csir.co.za, matooanemr@yahoo.com and fengelbrecht@csir.co.za

<sup>2</sup> Climatology Research Group, Unit for Environmental Sciences and Management, North West University, Potchefstroom, South Africa

<sup>3</sup> Meteorology Department, University of Reading, Reading, UK, m.m.bopape@reading.ac.uk

With a changing climate, the interior regions of southern Africa are expected to experience increases in temperature as great as 4-6°C by the end of the century under the A2 emission scenario. Such increases in ambient temperature have the potential to negatively impact human health as high ambient temperatures can lead to negative health impacts ranging from discomfort and fatigue, to cardiovascular and respiratory impacts, to heat stroke and death. High ambient temperatures and heat waves have been shown to lead to increases in morbidity and mortality, particularly in the elderly (>65 years), people with pre-existing diseases, those that live in cities, and those with compromised coping capacity. Thus, potential increases in temperature and heat waves may have large negative health impacts in Africa where there are large populations of vulnerable people as well as an over-burdened healthcare system coupled with large projected increases in temperature. This study investigates the projections of heat waves over Africa, with a focus on parameters (e.g. occurrence and duration) that are related to the health impacts.

Under a current climate (1961-1990), heat waves are an unusual event, with many areas experiencing only one or less than one heat wave per year. On average, the majority of heat waves in this time period last for less than five days. The projections for 2071-2100 show a drastic increase in heat wave occurrence and duration across Africa, with some regions projected to experience close to three months of their summer in a heat wave. Additionally, all seasons see increases in heat wave occurrence in this time period compared to 1961-1990. These changes in heat wave characteristics have the potential to have large public health impacts across Africa, and thus necessitate further research to develop early warning systems and heat-health action plans to mitigate health impacts.

**Keywords:** Regional climate modelling, Climate change impacts, human health, heat waves

## 1. Introduction

A changing climate can potentially have a large and negative impact on human health, especially in Africa where there are a large number of vulnerable people and an over-burdened healthcare sector (Confalonieri, 2007). In addition, the interior regions of southern Africa are projected to experience increases in temperature as great as 4-6°C under the A2 emission scenario, by the end of the century (Engelbrecht and Bopape, 2011). These increasing temperatures have the potential to negatively impact human health.

Exposure to high temperatures can lead to physical disorders ranging from discomfort and fatigue, to heat stroke and death. Oppressive temperatures have been shown to lead to increases in morbidity and mortality, particularly in the elderly

(>65 years), people with pre-existing diseases and those that live in cities (Semenza et al., 1996; Basu et al., 2005; Kovats et al., 2005; Stone et al., 2010). Thus, increasing temperatures from climate change pose a potentially serious public health threat.

Previous research over southern Africa has found that there is projected to be a large increase in the number of days when health may be impacted by heat, which may lead to increased events of consecutive days with high temperatures and heat waves (Garland et al., 2011). This is concerning as there are generally increased negative health impacts when high ambient temperatures persist for many days, e.g. a heat wave (e.g. Semenza et al., 1996; Basu and Samet., 2002; Fischer and Schaer, 2010). It is projected that the occurrence of heat waves will increase in the

future due to climate change, however less is known about how the characteristics of heat waves that impact human health (e.g. intensity, duration) may change, especially over Africa. In this study, the Conformal Cubic Atmospheric Model (CCAM) was used to project the frequency and duration of heat waves from present day climate until 2100 in order to begin to understand the potential health impacts from heat waves over Africa.

## 2. Methods

### 2.1 Heat Wave Definition

Heat waves were defined using the South African Weather Service definition of an episode of at least three consecutive days with maximum temperatures of more or equal to 5°C higher than the average maximum of the hottest month for the particular station/area of study. For this study, this threshold was determined per grid point over land and is thus region specific. The heat wave threshold was calculated for the current climate and kept constant for all projections.

### 2.2 CCAM

The variable resolution global atmospheric model applied in this study, CCAM, was developed by the Commonwealth Scientific and Industrial Research Organisation (CSIRO). It employs a semi-implicit semi-lagrangian method to solve the hydrostatic primitive equations (Engelbrecht et al.,2011). The CCAM was initially run with a quasi uniform resolution of about 200 km over the whole globe using sea surface forcing from the following models CSIRO, GFDL20, GFDL21, MIROC, MPI and UKMO CGCMs. The CCAM was then applied with a stretched grid resolution to obtain high resolution over Africa. A Schmidt stretching factor of 2.5 is used giving a resolution of about 60 km over southern and tropical Africa, decreasing to about 80 km over North Africa. and 400 km on the other side of the globe with 18 levels in the vertical (Engelbrecht et al.,2011). All outputs were interpolated to a 0.5 degree grid.

The simulations were made for the period 1961 to 2100 under the A2 emissions scenario. The period 1961 to 1990 is considered as present climate because the influence of anthropogenic forcing is expected to have been smaller then compared to future periods. Three future periods defined as 2011 to 2040, 2041 to 2070 and 2071 to 2100 are analysed, with the period 2071 to 2100 considered the period when the climate signal will be advanced, and the effects of climate change are expected to be highest then. The threshold used for the definition of a heat wave for all the periods is derived from the present day climate.

The model results presented here are ensemble averages of the CCAM realisations made with forcings from six global climate models used.

### 2.3 Heat Wave Characteristics Studied

Multiple characteristics of a heat wave can impact human health, such as the number of heat waves, their duration, intensity and timing (Fischer and Schaer, 2010). This presentation will focus on the number and duration of heat waves modelled for Africa across seasons from the current climate until the end of the century. The number of heat waves is important because more frequent heat waves can lead to increased negative health impacts. In addition, longer heat waves can have increased negative health impacts, and thus duration is important.

## 3. Results

Figure 1 below displays the modelled number of heat waves for Africa in the time period 1961-1990. The four seasons are separated, with December-February (DJF) in figure 1a (upper left), March-May (MAM) in figure 1b (upper right), June-August (JJA) in figure 1c (lower left) and September-November (SON) in figure 1d (lower right). The colour bar indicates the total number of heat waves that are modelled to occur in the 30 year period. As discussed above, a heat wave is defined as an event of at least three consecutive days; in totalling the number of heat waves, the duration was not accounted for, and thus a heat wave of three days or ten days, for examples, would still be counted as one heat wave.

It can be seen in figure 1 that heat waves are not a frequently occurring event in this time period. The eastern part of South Africa is modelled as experiencing the most frequent heat waves in the country, with fewer than 50 events (blue colour in figure 1) over the thirty year period, and most parts of the country have fewer than 20 events.

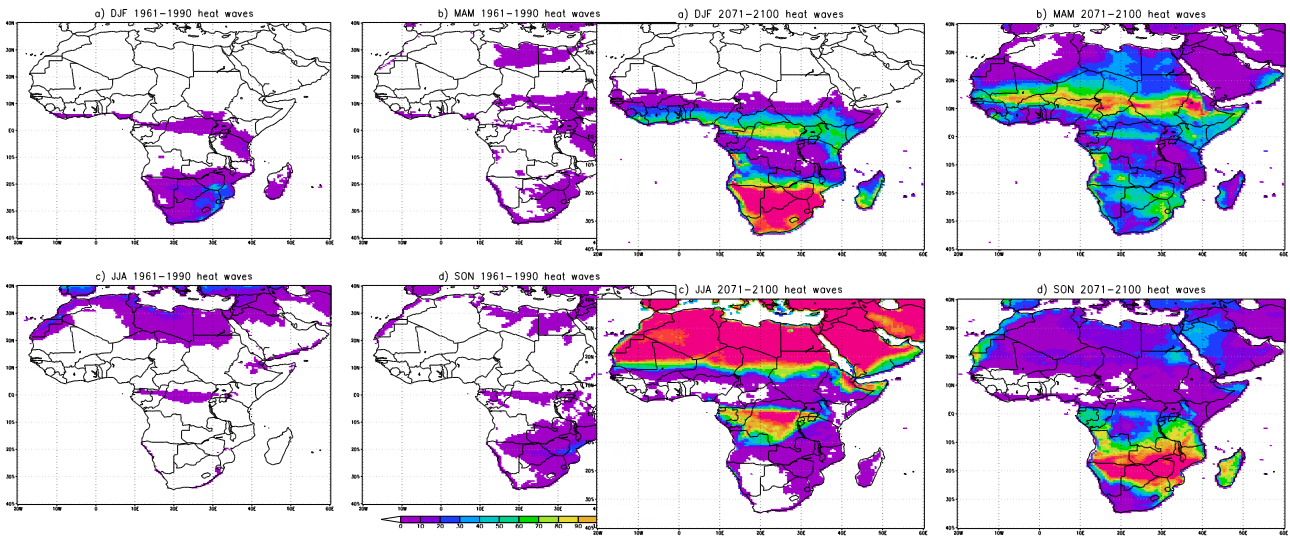


Figure 1: The modelled total number of heat waves over Africa for 1961-1990 for a) DJF, b) MAM, c) JJA and d) SON.

During the austral summer there is a region around the Democratic Republic of Congo (DRC) that is simulated to not experience heat waves. This is thought to be due to the Intertropical Convergence Zone, also known as cloud bands that produce rainfall and can shield the Earth's surface from the Sun.

The majority of heat waves in this time period last for fewer than five days (figure 2), though there are some regions in northern Africa that experience longer heat waves in boreal summer.

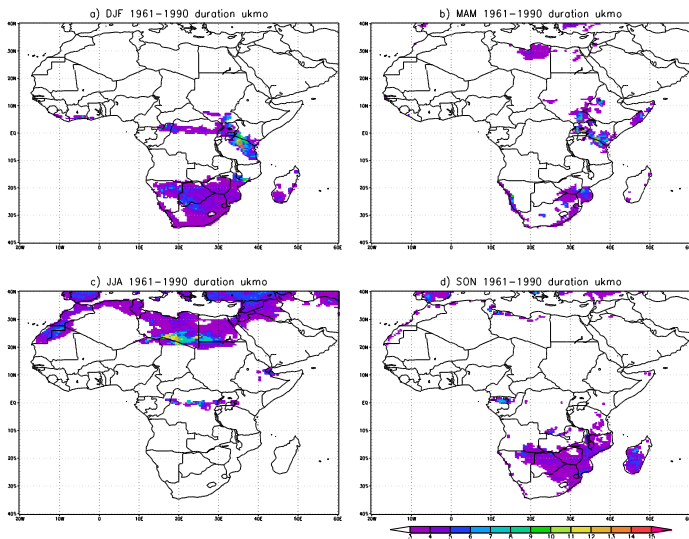


Figure 2: The modelled average duration of heat waves over Africa for 1961-1990 for a) DJF, b) MAM, c) JJA and d) SON. The colour bar range is 0-15 days.

Figure 3: The modelled total number of heat waves over Africa for 2071-2100 for a) DJF, b) MAM, c) JJA and d) SON.

Figure 3 displays the projected total number of heat waves over Africa for 2071-2100. The seasons are divided into four panels and the colour bar is the same as in figure 1.

From figure 3 it can be seen that the number of heat waves is projected to increase dramatically by the end of the century. Many areas experience up to 120 heat wave events (pink colour in figure 2) in a thirty year period during one of the seasons; which averages to four events per three month season per year. This increase is particularly evident in the sub-tropics because of strengthening high pressure systems over these regions. In addition, the area in southern Africa which was simulated as not experiencing heat waves in present climate is beginning to experience few events (purple colour over DRC) in DJF, with a dramatic increase in JJA. Across Africa these increases in heat waves are seen across seasons, with summer generally having the largest increases followed by spring, autumn and then winter.

The duration of the heat waves is projected to increase, with some regions experiencing an average duration of 15 days (pink in figure 4). These projections suggest that some areas (areas in pink in both figures 3 and 4) may experience up to 90 days (i.e. 3 months) of heat wave in their 3 month summer on average during the time period 2071-2100. These dramatic increases could have a large negative impact on human health.

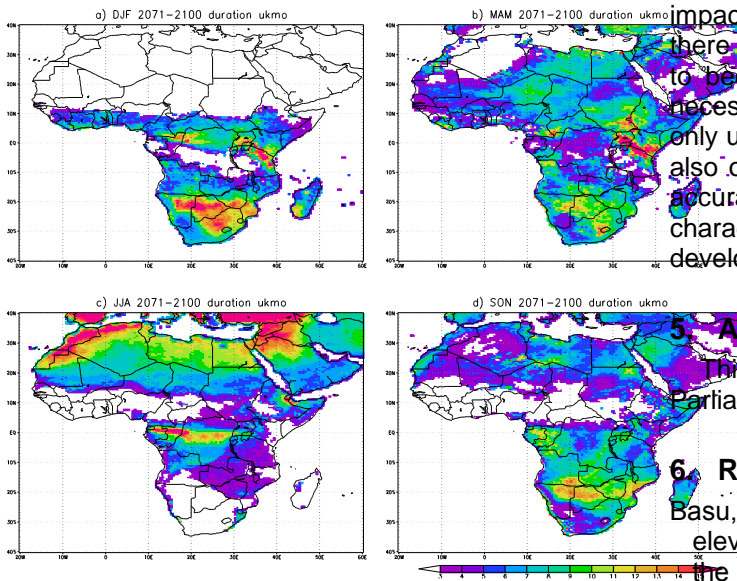


Figure 4: The modelled average duration of heat waves over Africa for 2071-2100 for a) DJF, b) MAM, c) JJA and d) SON. The colour bar range is 0-15 days

#### 4. Conclusions

This study has found that heat waves in Africa under a business as usual case, which is an optimistic case considering current greenhouse gas emission levels, are projected to increase from an unusual event to an event that occurs multiple times per summer across much of Africa. In addition, these increases do not occur only in the summer. In general, the increases are larger in the spring than in the autumn, though all seasons (including winter) see increases in heat wave events by the end of the century. The human health impacts from this have the potential to be large.

Very little research has been done to understand the magnitude of heat related health issues in Africa; most of the studies have been performed in temperate and industrialised countries. However, considering that the European heat wave of 1-15 August 2003 was estimated to have caused more than 14,800 deaths in France and in the range of 35,000 excess mortality in Belgium, the Czech Republic, Germany, Italy, Portugal, Spain, Switzerland, the Netherlands and the UK, it is probable that such dramatic increases in heat waves in Africa would have similarly large negative health impacts (Confalonieri, 2007).

The health impacts in countries in Africa may differ from countries elsewhere due to acclimatization of populations which may lessen the impact, as well as increased vulnerability, lack of coping capacity and over-burdened healthcare systems that may exacerbate the negative health

impact. However, from this study it is evident that there is the potential for heat related health issues to become a major concern in Africa. Thus, it is necessary for increased focus and research on not only understanding the health impacts in Africa, but also on developing early warning systems that can accurately predict heat wave occurrences and characteristics across lead times, as well as to develop heat-health action plans for communities.

#### 5. Acknowledgments

This work was supported through a CSIR Parliamentary Grant.

#### 6. References

- Basu, R and Samet, JM. 2002, 'Relation between elevated temperature and mortality: A review of the epidemiologic evidence,' *Epidemiol. Rev.* **24**:190-202.
- Basu R., Dominici F. and Samet JM 2005, 'Temperature and mortality among the elderly in the United States: a comparison of epidemiologic methods', *Epidemiology*, **16**:58-66.
- Confalonieri U., Menne B., Akhtar R., Ebi K.L., Hauengue M., Kovats R.S., Revich B. and Woodward A. 2007, 'Human health' *Climate Change 2007: Impacts, adaptation and vulnerability. Contribution of Work Group II to the Fourth Assessment Report of the Intergovernmental Panel on Climate Change*, M.L. Parry, O.F. Canziani, J.P. Palutikof, P.J. van der Lindern and C.E. Hanson Eds. Cambridge University Press: Cambridge, UK, 391-431.
- Engelbrecht FA, Landman, WA, Engelbrecht, CJ, Landman, S, Bopape, MM, Roux, B, McGregor, JL, and Thatcher, M, 2011, 'Multiscale Climate Modelling over Southern Africa using a variable-resolution global model,' *Water SA*, **37**:647-658.
- Engelbrecht F and Bopape MM. 2011, 'High resolution projected climate futures for southern Africa' *Paper presented at 2011 conference of South African Society for Atmospheric Sciences: the Interdependent Atmosphere, Land and Ocean, Hartbeespoort, South Africa.*
- Fischer, EM and Schaer, C. 2010, 'Consistent geographical patterns of changes in high-impact European heatwaves,' *Nature Geoscience*.
- Garland, RM, Matooane, M, Bopape, MM, Engelbrecht, F, Naidoo, M, Wright, CY, and Olwoch, J, 2011, 'Climate change impacts on human health in southern Africa,' *NACA conference, East London.*
- Kovats R.S., Campbell-Lendrum D. and Matthies F. 2005, 'Climate change and human health: estimating avoidable deaths and disease', *Risk Anal*, **25**:1409-1417.
- Semenza, JC, Rubin, CH, Falter, KH, Selanikio, JD, Flanders, D, Howe, HL, and Wilhelm, JL, 1996,

'Heat-related deaths during the July 1995 heat wave in Chicago, *The New England Journal of Medicine*, **335**:84-90.

Stone B., Hess J.J., and Frumkin H. 2010, 'Urban form and extreme heat: are sprawling cities more vulnerable to climate change than compact cities?' *Environ Health Persp.* **118**:1425-1428.

# FROST TRENDS ON A CITRUS FARM IN LIMPOPO, SOUTH AFRICA

Linda De Wet\*<sup>1</sup> and A. Stephan Steyn<sup>1</sup>

<sup>1</sup>Dept. Soil, Crop & Climate Sciences, University of the Free State, P.O. Box 339, Bloemfontein, 9300, South Africa, [dewetl@ufs.ac.za](mailto:dewetl@ufs.ac.za); [steynas@ufs.ac.za](mailto:steynas@ufs.ac.za)

The objective of this paper was to investigate the frost trends at Culmpine farm, to compare the results with other researcher analyses and to determine whether the trend would be ongoing or not. Correlation between Towoomba and Culmpine (2003-2011) was investigated, so that a better analysis could be done using both the long term Towoomba data and the Culmpine data. In the regression of Towoomba vs. Culmpine (2003-2011) for all the months and years  $R^2$  was only 0.32. This indicated that correlation showed poor agreement for minimum temperature ( $T_{mn}$ ) between the stations, which could be accredited to differences in local topography.  $T_{mn}$  at Culmpine revealed a weak negative linear trend from June to August, confirming gradual decrease in  $T_{mn}$  over the last nine years (2003 – 2011). Linear trends showed correlations with  $R^2 = 0.22$  and  $R^2 = 0.23$  for June and August, respectively. The nine years (2003 – 2011) in this study showed a decreasing trend in  $T_{mn}$ , but this could mean that these results are merely part of the bigger cycle in the climate. The trends shown for Culmpine were not observed for Towoomba. This means that the Culmpine trend is not significant, climate is variable and local topography could play an important role. In conclusion,  $T_{mn}$  variations throughout the data record indicate climate variability and therefore follow a definite cycle. Furthermore, the probability that future extreme temperatures could be experienced are not excluded. It is envisaged that farmers in the same area would be able to benefit from the results of the study.

**Keywords:** Climate variability, frost, minimum temperature

## 1. INTRODUCTION

Frost is an atmospheric phenomenon familiar to most people in temperate climates and is widely accepted as a natural recurrent risk in agriculture. In the plant cells direct damage by frost can occur through intracellular freezing while extracellular freezing causes indirect damage. Injury to the plant increases with decreasing temperature, which causes a specific level of damage at the so-called critical temperature (Snyder and de Melo-Abreu 2005).

Citrus production is an important part of the economy in South Africa. The citrus industry is the third largest horticultural industry after deciduous fruits and vegetables. During the 2010/11 production season the industry contributed R6.9 billion to total gross value of South African agricultural production (DAFF 2012).

According to DAFF (2014), citrus is not recommended in areas where regular, heavy frosts occur, but if frost does occur temperature decreases of up to  $-5^{\circ}\text{C}$  can be tolerated. Drier, inland areas are preferred to coastal areas to

avoid risk of pest and disease problems (DAFF 2014). High temperatures can be tolerated, but frost can cause damage to leaves, branches and fruit.

The study focused on Culmpine farm which is situated near Vaalwater, Modimolle Municipality, Waterberg district. The farm is planted with citrus orchards which are higher than the nearby river. The Vaalwater area has an average annual rainfall of 500 mm. The average maximum temperature is  $20.1^{\circ}\text{C}$  in July, while the average minimum temperature is  $2.4^{\circ}\text{C}$  (SA Explorer 2011), which indicates that frost events most likely occur every year. *Google Earth* coordinates place the orchards at an altitude of 1139 m and the farmhouse (and other orchards nearby) at a height of 1150 m. According to information given by farm owners, there was no severe frost in the recent past before 1996, but in 2007 there was a severe frost which caused much damage and so it is assumed that minimum temperatures ( $T_{mn}$ ) at Culmpine must have been below  $-6.6^{\circ}\text{C}$  (Wikipedia 2014) in 2007 when frost damage occurred.

The problem facing these farmers is the

possibility that severe frost occurrence will be an ongoing trend and that cold conditions would become progressively worse (personal communication, D. Woods 2012).

The objective of this paper was to investigate frost trends at Culmpine farm, to compare the results with other researcher analyses and to determine whether the trend would be ongoing or not. It is envisaged that farmers in the same area would be able to benefit from the results of the study.

## 2. MATERIALS AND METHODS

Daily quaternary catchment (QC) data was obtained for Vaalwater (1950-1999) from Lynch & Schulze (2006). Vaalwater falls within QC A42E. Quaternary catchment compilations are sets of data 50 years in length, but since there is only one dataset per QC, differences in height are not taken into account. In order to compensate for these possible height differences in the QC data, as well as for more recent years (after 1999) another dataset from a nearby weather station was obtained (SAWS 2012), i.e. daily  $T_{mn}$  for Towoomba from 1980 to 2011. Towoomba is the only weather station with a long term record of  $T_{mn}$  that falls within the same agroclimatic region as Culmpine.

Daily  $T_{mn}$  was also obtained from site Culmpine (2003-2011) from its own weather station at the farmhouse, about 1 km from some of the orchards. The assumption was made that the lemon trees at Culmpine were about 16 years old (planted in 1996) at the time of the study and therefore mature, placing them at a height equal to or higher than that of a standard automatic weather station (AWS). Because most of the data used in this study was measured by AWS, it was decided to assume frost occurrence at  $T_{mn} < 0.5^{\circ}\text{C}$ , i.e. the cut-off was taken as  $0.4^{\circ}\text{C}$ .

Correlation between Towoomba and Culmpine (2003-2011) was investigated, so that a better analysis could be done using both the long term Towoomba data and the Culmpine data.

Time series graphs for  $T_{mn}$  were also drawn for both Towoomba and Culmpine for each month (2003-2011) to compare  $R^2$  (coefficient of determination) differences for linear and polynomial trends. The latter trends were used to indicate cyclic variation particularly in the Culmpine data. A regression graph of

Towoomba vs. Culmpine for all the winter months and years (2003-2011) was drawn.

Cumulative distribution function (CDF) for Towoomba for all the winter months and years (1980-2011) was constructed. CDFs for Towoomba and Culmpine (2003-2011) for each month were also constructed and compared.

Since the temperature record at Culmpine was too short and incomplete, verification of the results was not possible, but the results were compared with the results from Tshiala *et al.* 2011.

## 3. RESULTS AND DISCUSSION

Linear correlation for May for Culmpine (Figure 1) was not significant ( $R^2 = 0.01$ ), which means that there was no significant linear trend in the nine years from 2003 to 2011. Lowest  $T_{mn}$  for May for Towoomba was  $-4.3^{\circ}\text{C}$  in 2007 (not shown) and for Culmpine  $-3.0^{\circ}\text{C}$  in 2007 (Figure 1).

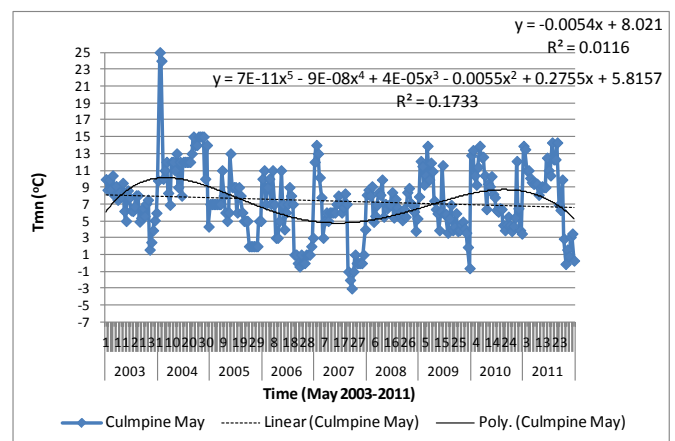


**Figure 1**  $T_{mn}$  for Culmpine for May from 2003 to 2011.

The  $T_{mn}$  at Culmpine revealed a weak negative linear trend from June to August, confirming gradual decrease in  $T_{mn}$  over the last nine years (2003 - 2011). Linear trends showed  $R^2 = 0.22$  and  $R^2 = 0.23$  for June and August, respectively. These findings partly disagree with the literature, which found that there was an increasing trend in average  $T_{mn}$  per decade ( $0.1^{\circ}\text{C}$ ) during the months June, July and August from 1950 - 1999. The nine years (2003 - 2011) in this study showed a decreasing trend in  $T_{mn}$  for Culmpine, but this could mean that these results are merely part of the bigger cycle in the climate.

Lowest minimums for Towoomba for all the

months May to September were lower than those at Culmpine. This means that Towoomba experienced lower  $T_{mn}$  temperatures than Culmpine in the months May to September in the years 2003, 2006, 2007 and 2010.

The linear regression for Towoomba vs. Culmpine (Figure 2) for all the winter months (May to September) and all the years (2003-2011) showed a  $R^2$  value of 0.32. This correlation shows poor agreement between the stations for daily  $T_{mn}$  and could be accredited to differences in local topography.

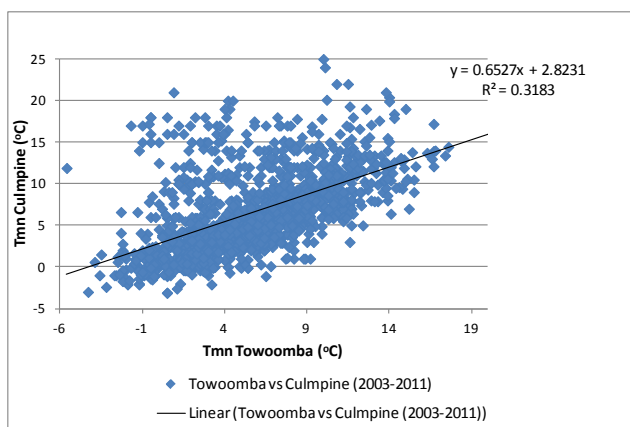


**Figure 2**  $T_{mn}$  for Towoomba vs. Culmpine for all the months (May to Sep) from 2003 to 2011 ( $R^2 = 0.32$ ).

CDFs can be used to determine probabilities of non-exceedance and are based on the long term historical data. The long term CDF for Towoomba (1980-2011) showed that there was a 10% probability that  $T_{mn}$  would not exceed 2.9°C in May; 0°C in June, -1.0°C in July; 1.5°C in August and 5.7°C in September (Table 1).

These values were very close to the values for the CDFs for Towoomba for 2003 to 2011 (2.8°C; 0.5°C; -1.1°C; 1.5°C and 6.6°C). The differences in  $T_{mn}$  were 0.1°C in May; 0.5°C in June; 0.1°C in July; equal in August and 0.9°C in September. The greatest difference was therefore 0.9°C in September. This makes it possible to use the Towoomba CDFs for 2003-2011 to compare with the Culmpine CDFs for the same years (Table 1).

According to Table 1 for 10% probability of non-exceedance  $T_{mn}$  for Culmpine was lower than  $T_{mn}$  for Towoomba (for same years) for May, June and September (e.g. 2.0°C vs. 2.8°C for May), but higher in July and August. Table 1

also shows that there is a 10% chance that July  $T_{mn}$  will not exceed 0°C at Culmpine. This means that there is a 10% probability that frost will occur at Culmpine in the month of July (0°C) and also possibly in June (0.4°C).

**Table 1** Monthly 10% probabilities of non-exceedance of  $T_{mn}$  for Towoomba (1980-2011), as well as for Towoomba and Culmpine (2003-2011)

Month	Probability of non-exceedance (%)	Towoomba	Towoomba	Culmpine
		$T_{mn}$ (°C)	$T_{mn}$ (°C)	$T_{mn}$ (°C)
		(1980-2011)	(2003-2011)	
May	10	2.9	2.8	2.0
Jun	10	0	0.5	0.4
Jul	10	-1.0	-1.1	0
Aug	10	1.5	1.5	1.6
Sep	10	5.7	6.6	6.4

**Table 2** Probabilities (%) for frost temperatures ( $T_{mn} \leq 0.4^\circ\text{C}$ ) for Towoomba from 1980-2011 and Towoomba and Culmpine (2003 to 2011) according to CDF results for non-exceedance of  $T_{mn}$  from May to August

Month	1980-2011	2003-2011	
	Towoomba	Towoomba	Culmpine
	Prob (%) $T_{mn} \leq 0.4^\circ\text{C}$	Prob (%) $T_{mn} \leq 0.4^\circ\text{C}$	
May	3	4	5
Jun	14	13	15
Jul	23	24	17
Aug	5	5	3

Table 2 showed overall that highest probabilities for frost occurred in June and July (13% - 24%). In May both datasets for Towoomba showed lowest  $T_{mn}$  as -4.3°C and in August they both showed lowest  $T_{mn}$  as -5.6°C (not shown). This is one proof of the presence of extreme  $T_{mn}$  throughout the data record. These results are in disagreement with those reported by Tshiala *et al.* 2011). According to Thisiala *et al.* 2011 there was an increase of 0.1°C for average annual winter temperature, as well as a diurnal increase of 0.03°C and this disagrees

with the findings of this study for Culmpine where there was a decreasing linear trend in  $T_{mn}$  during the months June, July and August from 2003 to 2011.

#### 4. CONCLUSIONS AND RECOMMENDATIONS

An attempt was made to answer the three objectives: to investigate frost trends on Culmpine farm; to compare the results with other researcher analyses and to determine whether the trend would be ongoing or not. Linear correlations for Towoomba and Culmpine for each month (2003 – 2011) showed poor  $R^2$  values, but polynomial trends were used to indicate cyclic variation particularly in the Culmpine data. In the regression of Towoomba vs. Culmpine (2003-2011) for all the months and years  $R^2$  was 0.32. This indicated that noteworthy differences exist between Towoomba and Culmpine and that results drawn from the longer Towoomba data should be used with caution.

According to the CDFs for Culmpine the months of June and July were more at risk (15%-17%) for experiencing frost with  $T_{mn}$  dropping to as low as  $-2.4^{\circ}\text{C}$  in June and  $-3.1^{\circ}\text{C}$  in July. In May there was a 5% probability that  $T_{mn}$  would drop to  $-3^{\circ}\text{C}$ . According to the trendlines and CDFs lowest  $T_{mn}$  temperatures at Culmpine were  $-3^{\circ}\text{C}$  in May 2007 and  $-3.1^{\circ}\text{C}$  in July in 2010. According to the literature  $-6.6^{\circ}\text{C}$  would be classified as severe frost, therefore  $-3^{\circ}\text{C}$  would fall in the medium frost category, but even at this temperature severe damage could have been caused to the citrus trees as was communicated by Culmpine farm if  $T_{mn}$  duration was longer or if the rate of  $T_{mn}$  decrease was rapid. Hourly, or even shorter time period temperature data would be required for such analyses.

The trends shown for Culmpine were not

observed for Towoomba. This means that the climate is variable and that local topography could play a significant role.

In conclusion,  $T_{mn}$  variations throughout the data record indicate climate variability and therefore follow a definite cycle. Furthermore, the probability that future extreme temperatures could be experienced are not excluded.

#### REFERENCES

- Dept of Agriculture, Forest and Fisheries (DAFF) 2012, 'A profile of the South African citrus market value chain', [Online] [www.daff.gov.za](http://www.daff.gov.za) (Accessed 24/03/2014).
- Dept of Agriculture, Forest and Fisheries (DAFF) 2014, 'Citrus land and Climate requirements', Queensland Government. [Online] <http://www.daff.qld.gov.au> (Accessed 24/03/2014).
- Lynch, S.D. & Schulze, R.E. 2006, Rainfall Database. In: Schulze, R.E. (Ed). South African Atlas of Climatology and Agrohydrology. WRC Report 1489/1/06. Water Research Commission, Pretoria. 18 pp.
- SA Explorer 2011, 'Information by location'. [Online] [http://www.saexplorer.co.za/southafrica/climate/vaalwater\\_/climate.asp](http://www.saexplorer.co.za/southafrica/climate/vaalwater_/climate.asp) (Accessed 02/06/2014).
- Snyder and de Melo-Abreu 2005, Frost protection: fundamentals, practice and economics. Environment and Natural Resources Series 1, Rome: FAO. [Online] [www.fao.org/3/a-y7223e.pdf](http://www.fao.org/3/a-y7223e.pdf) (Accessed 24/07/2014).
- South African Weather Services (SAWS) 2012, Climate data supplied by South African Weather Service. Climate databank. Pretoria: SAWS.
- Tshiala, M.F., Olwoch, J.M. and Engelbrecht, F.A. 2011, 'Analysis of Temperature Trends over Limpopo Province, South Africa', *J. Geography and Geology*, 3(1), 13-21.
- Wikipedia 2014, 'Frost'. [Online] [http://en.wikipedia.org/wiki/Frost\(temperature\)](http://en.wikipedia.org/wiki/Frost(temperature)) (Accessed 02/06/2014).

# The sinuous ways of SOMs

Liesl L Dyson

Department of Geography, Geoinformatics and Meteorology, University of Pretoria, Pretoria, South Africa,  
[liesl.dyson@up.ac.za](mailto:liesl.dyson@up.ac.za)

Self-organising maps are used increasingly in the South African meteorology research community. The application of the SOM technique is often used to create climatologies and in recent times it has found its way to verification and predicting scenarios. One of the allures of SOMs to meteorologists is the visualisation of synoptic circulation maps which are easily available and interpretable. This paper describes the results of a SOM experiment where the data used to train the SOM were adjusted for every training run. The different SOM training runs were all done over Southern Africa using NCEP reanalysis data. The first part of the experiment dealt with the geographical location for which the SOM was run. Three areas each containing a different number of grid points and altered geographical location were selected. In the second experiment the vector elements used as the input vectors in the SOM were calculated in two different ways. In the third and final part of the experiment, the SOM was trained with a varying number of meteorological variables. The maps of the different SOM runs were visually compared to one another to identify the similarities and the synoptic flow fields for 2 heavy rainfall days over Gauteng were compared as case studies. The tropical heavy rainfall day in February had a smaller root mean square error (RMSE) than the December, cut-off low day. Calculating the values of the vector elements by using the average and standard deviation over the entire domain results in smaller RMSE than when the average and standard deviation at each of the grid point were used. The RMSE error for Area 2 (north of 35° S) gave the smallest RMSE values. For derived variables, such as the moisture flux convergence, both methods of standardisation of vector elements gave unrealistic atmospheric fields as output.

**Keywords:** Self-organizing maps, synoptic climatology, heavy rainfall, Gauteng.

## 1. Introduction

Self-organizing maps (SOMs) have been widely used in meteorological applications since the start of the 21st century. There have been significant contributions to synoptic climatologies and synoptic patterns of atmospheric circulation (Hewitson and Crane 2002 and Tennant and Hewitson 2002). Climate variability and extreme events have been analysed with SOMs (Liu and Weisberg 2011) and trend analyses performed (Bermejo and Ancell 2009; Lennard and Hegerl 2014). Methods were developed to downscale both seasonal and short-range weather forecasts (Gutierrez et al. 2005). Tadross et al. (2005) used SOMs to explain the differences in synoptic circulation associated with early and late onset of the maize growing season over southern Africa and van Shalkwyk and Dyson (2013) associated different synoptic circulation features with the occurrence of fog at Cape Town International Airport.

Kohonen's SOM software (Kohonen, 2001) is freely available from (<http://www.cis.hut.fi/research/som-research>) and is mostly used as *black-box* software. There are a limited number of options a user can set when running the software. Lennard and Hegerl (2014) provide detail explanation of these options.

The question that this paper endeavours to answer is how do the options of the user influence the SOM results? For this research the SOM was run over different domains, the vector elements were constructed using 2 techniques and the number of meteorological variables used to train the SOM was adjusted. The nodal maps were visually compared to one another and the way that the different SOM runs dealt with two heavy rainfall days over Gauteng was investigated.

## 2. Data and methodology

The SOMs were trained with daily NCEP reanalysis data for austral summers (October to March) from 1979 to 2009. The geopotential heights, mixing ratios, and zonal and meridional winds at 850, 700, 500 and 300 hPa were used to construct different input vectors required by the SOM.

### 2.1 Experimental design

The SOM was trained for 42 different scenarios and a 25 node SOM was constructed for every run. The SOM was trained twice for each of these runs. The topology was set to rectangle, the

neighbourhood function type was set to bubble, the training length was set to 1 000 000 during the first and second training phases, the learning rate parameter was set to 0.1 during the first training phase and 0.01 during the second phase and the radius was set to 1 during the initial and second training phases.

### 2.1.1 Geographical location

Extra-tropical weather systems such as westerly troughs, cut-off lows, and ridging anticyclones occur frequently in early summer over South Africa. These weather systems are baroclinic and are characterised by large temperature gradients and vertical wind shear values (Dyson et al., 2014). They are also associated with large geopotential gradients as they migrate from west to east over the southern sub-continent. In late summer, as the atmospheric circulation over Southern Africa becomes tropical, the geopotential gradients become very weak and even heavy rainfall producing weather systems such as the continental tropical low (Dyson and van Heerden, 2002) have significant weaker geopotential gradients than heavy rainfall producing weather systems which occur in early summer. The Area 2 domain was chosen to capture tropical weather systems while Area 3 will exclude weather systems such as the Angola Low (Reason et al., 2006 ) but will capture the extra tropical weather systems which migrate over and south of South Africa. The location of Area 1 endeavours to represent the geographical location of all summer synoptic circulation systems over South Africa. The three areas are shown in Figure 1.

### 2.1.2 Calculation of vector elements

Input vectors which consist of elements where the absolute values of the elements are significantly different are not ideal as the SOM places more emphasis on large values. For instances if the 850 hPa (+- 1500 m) and 500 hPa (+- 5000 m) geopotential heights are used in an input vector, the 500 hPa heights will dominate the SOM calculations. Therefore the elements used to construct the input vectors of the SOM need to be standardised. A common method of standardisation is to use the average and standard deviation in order to calculate the values of the elements in a vector. In this paper the elements were standardised in 2 ways. First the average and standard deviation at each grid point were calculated and these grid point values were used to calculate the elements (Index 1) (Malherbe et al., 2013). The second way was to calculate the average and standard deviation over the entire domain and use these values to calculate the elements (Index 2) (Engelbrecht et al., 2014)

### 2.1.3 Variables used to construct the vector elements

For this part of the experiment the number of variables used in the input vectors was adjusted. The number of variables used in the input vectors varies from 1 (Var1 in Table 1) to 5, (Var5 and Var7). The variables used consist of basic variables such as geopotential heights and precipitable water and derived variables such as moisture flux convergence or relative vorticity advection. All the chosen variables are routinely used, in one way or another, by weather forecasters when predicting rainfall.

Table 1: The number and type of of variables used for the 7 different SOM runs. gph= geopotential heights, PW= precipitable water, mfc= moisture flux convergence, div= horizontal wind divergence, vrt= relative vorticity, vrt adv= relative vorticity advection.

Name of run	Number of variables	Meteorological Variables
Var1	1	850 gph
Var2	2	850 and 500 gph
Var3	3	850, 500 and 300 gph
Var4	4	850, 500,300 gph and PW
Var5	5	850, 500,300 gph, 700 mfc and PW
Var6	4	850, 500,300 gph and 700 mfc
Var7	5	850 div, 700 mfc, 500 vrt, 300 vrt adv and PW

## 3. Results

The results for 2 heavy rainfall days over Gauteng are discussed here. On the 26<sup>th</sup> of December 1994, a cut-off low was situated over the south-western Cape and heavy rainfall occurred over central and eastern South Africa. Over Gauteng the area average rainfall was 34 mm and more than 80% of the stations over Gauteng received some rainfall. On the 8<sup>th</sup> of February 2000, a continental tropical low was situated over Botswana and very heavy rainfall occurred southeast of this low. In Gauteng the average rainfall was 43 mm and 94% of the stations in the province had some rainfall. The SOM run for Area 1, Index 1, captures the position and strength of the Atlantic Ocean High (AOH) west of South Africa very well (Fig. 1). The depth of the Indian Ocean High (IOH) is underestimated but a ridge is present over the eastern interior. The depth of the low over Angola as well as the trough extending into South Africa is underestimated.

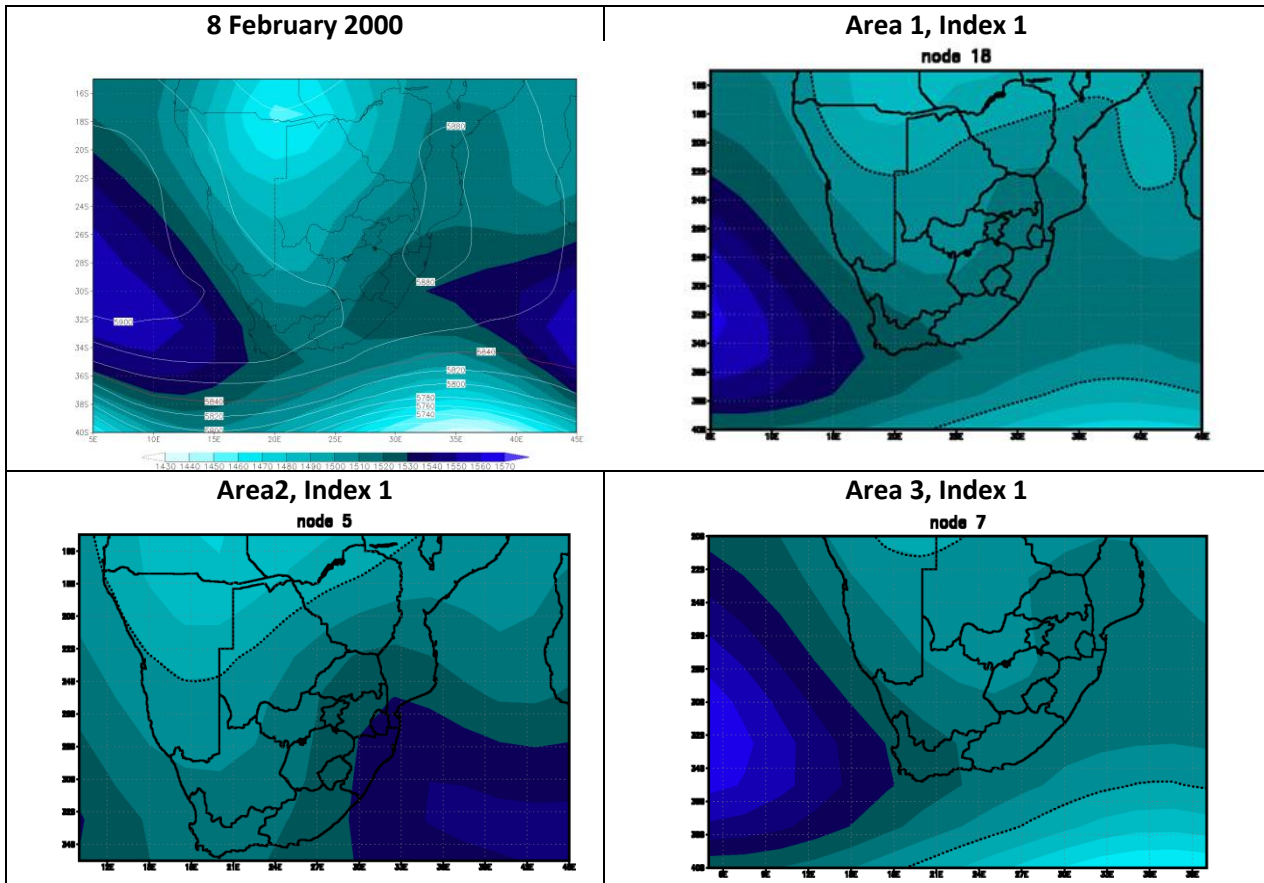


Figure 1: The 850 hPa geopotential heights for the 8<sup>th</sup> of February 2000 and the 850 hPa geopotential heights of the node to which this day was mapped using Index 1 for Area 1, 2 and 3

For Area 2 the IOH is stronger and located further west than reality. The Angola low is deeper than in Area 1 but still does not capture the depth and extend than the actual low. The circulation in Area 3 is similar to Area 1 but the depth of the Angola Low is underestimated the most in Area 3.

Table 2: The RMSE between the vector elements of the 2 heavy rainfall days and the different SOM runs. A=Area and I=Index

Date	SOM run	A1, I1	A1, I2	A2, I1	A2, I2	A3, I1	A3, I2
19941226	Var1	0.72	0.57	0.63	0.59	0.71	0.60
20000208		0.52	0.46	0.53	0.47	0.46	0.38
19941226	Var2	0.84	0.58	0.64	0.60	0.84	0.62
20000208		0.62	0.48	0.52	0.46	0.55	0.44
19941226	Var3	0.87	0.57	0.83	0.66	0.92	0.52
20000208		0.60	0.42	0.49	0.44	0.53	0.43
19941226	Var4	0.89	0.61	0.90	0.66	0.91	0.63
20000208		0.86	0.60	0.64	0.52	0.84	0.67
19941226	Var5	0.95	0.73	0.98	0.78	0.99	0.75
20000208		0.86	0.65	0.65	0.55	0.83	0.70
19941226	Var6	0.97	0.74	0.94	0.81	1.00	0.73
20000208		0.68	0.56	0.54	0.49	0.61	0.55
19941226	Var7	1.10	0.97	1.11	0.99	1.17	1.04
20000208		0.92	0.82	0.78	0.69	0.91	0.84
Ave		0.82	0.63	0.73	0.62	0.80	0.63

In order to objectively determine how representative the mapped-to node was for the different SOM runs, the RMSE (Willks, 2006) was calculated between the vector elements of the 2 heavy rainfall days and the node to which the different SOM runs mapped the days. The RMSE error is smaller for the February case than the December case for all the SOM runs (Table 2). The RMSE error using Index 2 is smaller than for Index 1. Area 2 which is located further north has smaller

errors for all the different SOM runs. The RMSE generally increase with an increasing number of variables.

The derived variables such as moisture flux convergence results in unrealistic atmospheric fields for both indexing techniques. Figure 2 shows how the node to which the 8<sup>th</sup> of February 2000 was mapped depicts large area of divergence over central South Africa while this was in fact an area of convergence.

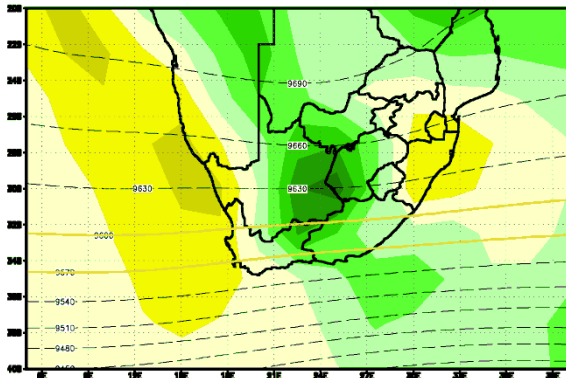


Figure 2: Moisture flux convergence at 700 hPa of the node that the 8<sup>th</sup> of February 2000 was mapped to for Area 3, Index 2 and Var6. Green is divergence and yellow convergence

#### 4. Discussion and conclusions

The preliminary results using only 2 case studies suggest that creating the vector elements in the SOM by using the areal average and standard deviation result in smaller errors than when the average and standard deviation at every grid point in the domain is calculated. The depth and position of significant large scale synoptic weather systems such as COLs and continental tropical lows are not directly captured by the SOM and the geographical area chosen influences how well these weather systems are resolved. The tighter geopotential gradient south of Africa results in larger errors when these areas are included in the domain.

When dealing with derived variables such as moisture flux convergence, different techniques need to be explored to create the vector elements.

It is recommended that the results be expanded to include all days in order to calculate significant statistical results. The spatial distribution of errors should also be considered.

#### 5. Acknowledgments

The author would like to express her sincere appreciation to Kohonen and co-workers who developed the SOM technique. It has opened the possibility of exploring many and winding metrological roads.

#### 6. References

- Bermejo M and Ancell R. 2009. Observed changes in extreme temperatures over Spain during 1957–2002 using Weather Types. *Revista de Climatologia* **9**: 45-61.
- Dyson LL and Van Heerden J. 2002. A model for the identification of tropical weather systems. *Water SA* **28**: 249–258. DOI: <http://dx.doi.org/10.4314/wsa.v28i3.4892>.
- Dyson LL, van Heerden J and Sumner PD. 2014. A baseline climatology of sounding-derived parameters associated with heavy rainfall over Gauteng, South Africa. *Int J Climatol*. DOI: 10.1002/joc.3967
- Engelbrecht CJ, Landman WA, Engelbrecht FA and Malherbe J. 2014. A synoptic decomposition of rainfall over the Cape south coast of South Africa. *Climate Dynamics*. DOI 10.1007/s00382-014-2230-5
- Gutierrez JM, Cano R, Cofino AS and Sordo C. 2005. Analysis and downscaling multimodel seasonal forecasts in Peru using self-organizing maps. *Tellus A* **57**:435-447.
- Hewitson BC and Crane RG. 2002. Self-organizing maps: applications to synoptic climatology. *Clim Res* **22**: 13–26. DOI: 10.3354/cr022013
- Kohonen T. 2001. *Self-organizing maps*. Third Edition, Springer
- Lennard C and Hegerl G. 2014. Relating changes in synoptic circulation to the surface rainfall response using self-organising maps. *Clim Dynamics*. DOI: 10.1007/s00382-014-2169-6
- Liu Y and Weisberg RH. 2011. A review of Self-Organizing Map applications in meteorology and oceanography. In *Self-Organizing Maps - Applications and Novel Algorithm Design*, Edited by: Mwasiagi JI 253–272. Rijeka, Croatia
- Malherbe J, Landman WA and Engelbrecht FA. 2013. The bi-decadal rainfall cycle, Southern Annular Mode and tropical cyclones over the Limpopo River Basin, southern Africa. *Clim Dynamics*. DOI 10.1007/s00382-013-2027-y
- Reason CJC, Landman W and Tennant W. 2006. Seasonal to decadal prediction of southern African climate and its links with variability of the Atlantic Ocean. *Bull Am Meteorol Soc* **87**, 941–955. DOI: <http://dx.doi.org/10.1175/BAMS-87-7-941>
- Tadross MA, Hewitson BC and Usman MT. 2005. The Interannual variability of the onset of the maize growing season over South Africa and Zimbabwe. *Journal of Climate*, **18**, 3356-3372.
- Tennant W and Hewitson BC. 2002. Intra-seasonal rainfall characteristics and their importance to the seasonal prediction problem. *Int J Climatol* **22**: 1033–1048. DOI: 10.1002/joc.778
- Van Schalkwyk L and Dyson LL. 2013. Climatological characteristics of fog at Cape Town International Airport. *Wea Forecasting*. **28**: 631-646. DOI 10.1175/WAF-D-12-00028.1.

Wilks D. 2006. *Statistical methods in the atmospheric sciences*. 2<sup>nd</sup> Edition, Elsevier Academic Press, California, United States of America, 661 pp.

# Radar Characteristics of Hailstorms in South Africa

Craig L. Powell\*

442 Rigel Avenue South, Erasmusrand, Pretoria, Gauteng, 0181, South Africa, [craig.powell@weathersa.co.za](mailto:craig.powell@weathersa.co.za)

The summer rainfall regions of South Africa frequently experience thunderstorms between September and April. The vast majority of storms do not contain hail. Despite this hailstorms still result in considerable damage throughout any given season, whether it be to crops, vehicles or buildings. Recently Gauteng has experienced two major hailstorms resulting in losses estimated at over ZAR1 billion each. Therefore the identification of such storms are crucial and the radar characteristics of severe hailstorms is ideal for this identification process. The research presented here provides an update to the research presented in Powell (2013). Additional cases were introduced to include more case days (including the notorious 28 November 2013 Gauteng hail event) as well as more radars, resulting in 23 cases, spanning 19 days and including 6 of the S-band Doppler radars operated by the South African Weather Service. This lead to 54799 storms being used for the study. TITAN's Hail Mass Aloft parameter was used to delineate storm types and then further into three categories of hailstorms. Results show that, of the storm track parameters available in TITAN, VIL and ETH are the best at discriminating between the 3 types of hailstorms in real-time. More than 75% of damaging hailstorms show a deviation of more than 10° to the left of the mean direction of non-hail-bearing storms, one of the properties of supercell thunderstorms.

*Keywords:* hail, hailstorms, large hail, TITAN, hail metrics, storm characteristics.

## 1. Introduction

The “*Introduction*” to this research was presented in Powell (2013) and therefore only selected excerpts from the afore-mentioned research will be repeated here.

Thunderstorms are a frequent occurrence over the summer rainfall regions of South Africa (SA) (Visser & van Heerden 2000). While the majority of thunderstorms are not severe, every thunderstorm has the potential to produce severe weather. Multicell- and supercell- thunderstorms (Foote 1985) have the greatest potential of producing severe weather. SAWS (2013) defines a thunderstorm as severe if it produces at least one of the following criteria:

1. Wind gusts  $\geq$  50kts, in association with a thunderstorm,
2. Localised urban flooding or flash flooding (non-urban),
3. Large amounts of small hail,
4. Hail  $>$  1.9cm in diameter, or
5. A tornado.

Severe thunderstorms are a primary concern to both forecasters and the general public due to their negative impact on human life as well as property (Lang *et al.* 2004). Major metropolitan areas are particularly vulnerable to hailstorms which produce large hail (criterion 4, above) due to building

exposure (Schuster & Blong 2004). Visser (2014) reported estimated market losses (from a reinsurance perspective) of ZAR1.02 billion and ZAR1.4 billion from the 20 October 2012 and 28 November 2013 GP hail events, respectively. Figure 1 depicts golf ball size hail (~4.5cm in diameter) observed in the East Rand of GP on 20 October 2012.



Figure 1: Golf ball size hail in the East Rand on 20 October 2012. Image from Beverley Vertue.

It is therefore essential that severe hailstorms are identified timeously and warnings issued accordingly. Determining the radar characteristics of hailstorms could aid in a faster decision making process at the South African Weather Service

(SAWS) when issuing warnings for severe hailstorms.

## 2. Data and Methods

Similar methodology was used to that in Powell (2013) with some updates to include more cases from more radars.

Radar reflectivity data from 6 of the horizontally polarized S band (10cm wavelength) Doppler radars operated by SAWS were acquired in Cartesian (flat projection) format. This data has a temporal resolution of ~6min and a spatial resolution of 1km. The maximum unambiguous range of all the radars was initially set to 300km, but later changed to 200km, the current operational range. For this reason, only storms (as defined by Dixon & Wiener 1993) with volume centroid locations within 200km of the radar were considered.

The TITAN (Thunderstorm Identification, Tracking, Analysis and Nowcasting; Dixon & Wiener 1993) software was utilized to track storms and retrieve storm track parameters. The dual-threshold tracking technique available in TITAN was used in an attempt to separate each of the storms into their individual tracks. More details on this methodology can be found in Powell (2013).

The calculation of Hail Mass Aloft (HMA) hail metric in TITAN differs somewhat from that provided by Foote *et al.* (2004) and is calculated using Equation 1, where  $M$  is the mass and  $Z$  is the reflectivity factor ( $10^{\frac{dBZ}{10}}$ ). This calculation is made for all reflectivities which exceed 55dBZ and are  $\geq 2$ km above the freezing level height simultaneously. The mass is then integrated throughout the volume of the storm to obtain a total HMA for the storm in ktons.

$$M = 3.6683 \times 10^{-6} Z^{1.416} \quad (1)$$

Due to the volume integral being used to calculate the HMA values of the storms, if two storms of different sizes (but identical in vertical reflectivity structure/intensity) are compared, the larger of the two would have a greater HMA value simply by virtue of the fact that it has a greater volume. For this reason HMA values needed to be normalised (units of  $g/m^3$ ) in order to compare storms (Powell 2013). Storms were stratified according to these normalized HMA values (see Table 1).

A total of 23 cases were selected for the study, resulting in 54799 storms being available for the study (See Table 2). Cases were updated to include various radars. Some cases have overlapping dates (e.g. 28 October 2013 for Bloemfontein, Irene and Ottosdal) due to, amongst other things, range effects affect the way in which a storm is observed by each of the radars. This was also done to include storms which were observed within one radar footprint and not necessarily in the others.

Table 1: Stratification of storms based on their normalized Hail Mass Aloft values.

Storm Type	Abbrev.	HMA
Non-Hailstorm	NH	= 0.0
Borderline Hailstorms	BHS	$0.0 < HMA < 0.5$
Normal Hailstorms	HS	$0.5 \leq HMA < 2.0$
Damaging Hailstorms	DHS	$\geq 2.0$

Table 2: Total number of storms available for each storm type.

Total Storms	NH	BHS	HS	DHS
54799	48340	3781	5296	1163

Numerous TITAN storm track parameters, including the four hail metrics, were considered for comparisons between the four storm types. A total of 196 storm histories were also selected manually in an attempt to identify possible precursor thresholds/tendencies for some of the storm track parameters.

## 3. Results

Of the parameters considered for comparisons, through the use of storm tracks, only the Vertically Integrated Liquid water content (VIL), 35dBZ Echo Top Height (ETH), Direction- and Speed-Anomaly showed discernable differences between BHS and DHS.

Figures 2 to 5 depict the storm types (NH in grey, BHS in blue, HS in yellow and DHS in red) plotted against storm parameters in the form of box plots. NH anomalies are not included in Figure 2 to prevent confusion. Figure 2 shows the Direction anomaly, with the anomaly calculated from the mean of NH. The height of the 35dBZ ETH is illustrated in Figure 3 with the approximate spring time (sometimes colloquially referred to as "hail season") freezing level height plotted as the solid black line. VIL is then shown in Figure 4 with the mean for NH plotted as a solid black line.

For the most part, BHS and HS showed similar interquartile ranges. This is particularly evident in the Direction- and Speed-anomaly (the latter not shown in this paper). Of the four parameters DHS shows marked differences when comparing storm type to VIL, ETH and Direction Anomaly. This is predominantly evident in the comparison of VIL where the 25<sup>th</sup> percentile of DHS being similar to the upper adjacent value of HS. VIL values also have a large spread for DHS owing to the fact that, generally storms which produce large hail have greater depths and higher reflectivities compared to other storms. This, combined with the vertical integral of liquid mass content, produce wide ranging values. That being said, the lower adjacent value for DHS is still of similar magnitude to that of the 25<sup>th</sup> percentile of HS. Direction Anomalies for DHS showed a mean of

approximately  $-30^\circ$ , while the means for the other two hailstorm type were approximately  $0^\circ$ . The 35dBZ ETH for DHS had a relatively narrow interquartile range and a narrower spread (compared to HS and BHS) with the lower adjacent value of DHS being approximately 13.5km. Speed Anomalies for each of the hailstorm types were similar to one another with all having a mean of  $< 0$ km/h.

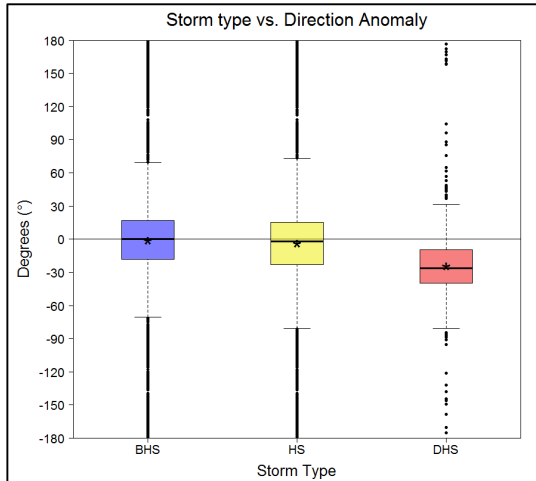


Figure 2: Box plot for Storm type vs. Direction Anomaly. The upper and lower levels of the box represent the 75<sup>th</sup> and 25<sup>th</sup> percentiles, respectively. The median is given as the thick black line within the box, while the asterisk (\*) represents the mean.

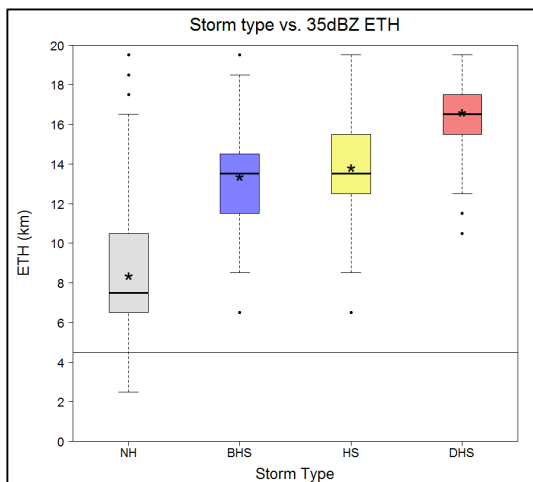


Figure 3: As Figure 2 for Storm type vs. 35 dBZ and including NH.

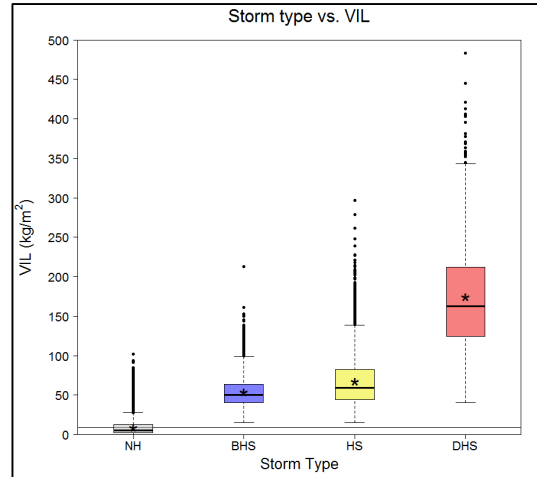


Figure 4: As Figure 3 for Storm type vs. VIL.

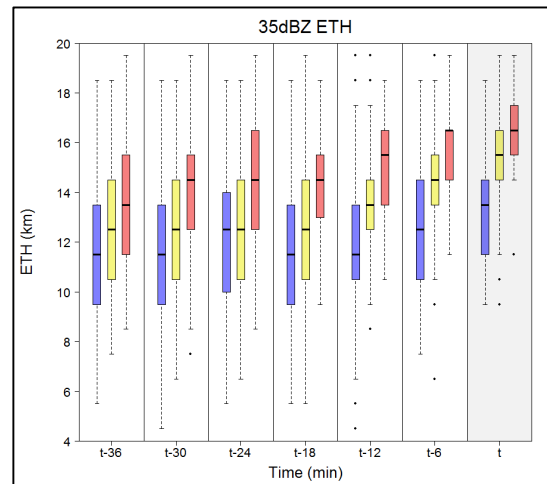


Figure 5: Box plot (as Figure 2) for 35dBZ ETH leading up to the time (t) where a storm reaches the BHS, HS or DHS category.

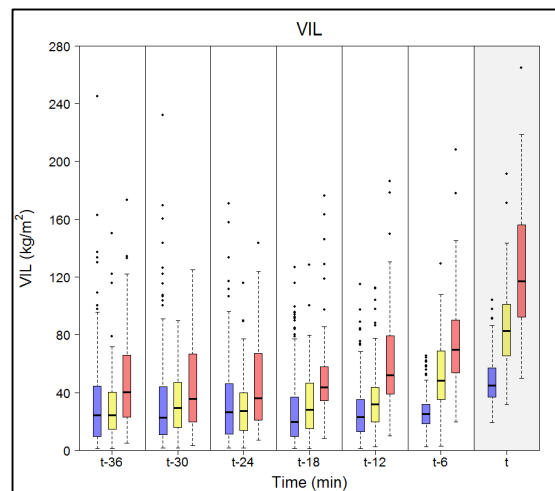


Figure 6: As Figure 5 for VIL.

When considering possible precursors to storms reaching any of the given hailstorm thresholds, only the 35 ETH and VIL appeared to show any sort of precursory indicators. Figure 5 shows that once the 35dBZ echo top height reaches 14.5km the storm could likely produce hail within the next 6min (HS boxes). If the ETH reaches 14.5km and it continues to increase 15.5km within 6min (looking at the DHS boxes) it could produce damaging hail a further 12min after that. This can also be observed in Figure 6 where once a storm obtains VIL values of 50kg/m<sup>2</sup>, similar timings can be deduced provided the storm maintains (or grows in) its vertical extent and reflectivity threshold of 55dBZ. There does however appear to be no clear indication of ETH threshold for BHS, except that the lower adjacent value is approximately 9.5km at the time of hail while at the same time the interquartile range of VIL for BHS is between about 40- and 60-kg/m<sup>2</sup>.

#### 4. Discussion and Conclusions

DHS appear to show the most distinct characteristics when comparing storm types to the typical TITAN storm track parameters. Most notably, VIL and the 35dBZ ETH appear to be the best at identifying such storms, which are the most important as these are the most likely to result in large hail for which warnings must be issued. While all hailstorm types show a fairly wide spread in Direction Anomalies, the fact that 75% of DHS show anomalies of less than approximately -10° (leftward deviation) together with an interquartile range centred around -30° leads to the conclusion that most DHS storms likely result from supercell thunderstorm activity.

The height of the 40dBZ echo was used by Held (1978) to determine a probability of hail from storms observed in the Johannesburg-Pretoria region. The heights of the 35dBZ ETH presented here are generally much greater than those found by Held (1978). While the height of the 35dBZ contour is expected to be greater than that of the 40dBZ contour, radar setup and TITAN interpolation techniques can also contribute to a greater deviation between the two sets of results.

The maximum VIL value for NH was approximately 100kg/m<sup>2</sup>, while the 3<sup>rd</sup> quartile for this storm type was below 25kg/m<sup>2</sup>. This, compared to 75% of DHS VIL values being > 125kg/m<sup>2</sup>, suggests that this value could possibly be used as a definite DHS indicator. However, it is also noted that the lower adjacent value for DHS is below 50kg/m<sup>2</sup>.

A combination of VIL and ETH, known as VIL density, was used with great success by Amburn & Wolf (1997). While this is not considered here, future work may be able to include this based on the prominent differences between the three hailstorm types.

The TITAN HMA values (provided as a storm track annotation in the TITAN display) cannot be used in real-time by forecasters at SAWS as values are greatly affected by the volumetric size of the storm. It is therefore suggested that if the TITAN annotations are to be used (in cases where hundreds of storms need to be considered in a 6min period), a combination of VIL and ETH should be utilized, but with some caution.

#### 5. References

- Amburn, S.A. and Wolf, P.L. 1997, 'VIL Density as a Hail Indicator', *Weather and Forecasting* **12**:473-478.
- Dixon, M. and Wiener, G. 1993, 'TITAN: Thunderstorm, Identification, Tracking, Analysis, and Nowcasting—A radar-based methodology', *Journal of Atmospheric and Oceanic Technology*, **10**:785-797.
- Foote, G.B. 1985, 'Aspects of cumulonimbus classification relevant to the hail problem', *Journal de Recherches Atmospheriques* **19**:61-74.
- Held, G. 1978, 'The Probability of Hail in Relation to Radar Echo Heights on the South African Highveld', *Journal of Applied Meteorology* **17**:755-762.
- Lang, T.J., Miller, L.J., Weisman, M., Rutledge, S.A., Barker III, L.J., Bringi, V.N., Chandrasekar, V., Detwiler, A., Doesken, N., Helsdon, J., Knight, C., Krehbiel, P., Lyons, W.A., MacGorman, D., Rasmussen, E., Rison, W., Rust, W.D. & Thomas, R.J. 2004, 'The severe thunderstorm electrification and precipitation study', *Bulletin of the American Meteorological Society* **85**:1107-1125.
- Powell C.L. 2013, 'Characteristics of hailstorms over the Highveld of South Africa', *Proceedings of the 29<sup>th</sup> Annual South African Society for Atmospheric Scientists Conference, Salt Rock, KwaZulu-Natal, September 2013*, South African Society for Atmospheric Scientists, pp. 121-124.
- Schuster, S. and Blong, R. 2004, 'Hailstorms and the estimation of their impact on residential buildings using radar', *6th International Symposium on Hydrological Applications of Weather Radar, Melbourne, Australia, February, 2004*, Australian Bureau of Meteorology, Melbourne, Australia.
- Visser, P.J.M. and van Heerden, J. 2000, 'Comparisons of hail kinetic energy derived from radar reflectivity with crop damage reports over the eastern Free State', *Water SA* **26**:91-96.
- Visser, P., 2014: 'The Insurance Institute of South Africa – Breakfast Session on "HAIL"', *IISA Insurance Forum Presentations, May 2014*, The Insurance Institute of South Africa, Hyde Park, Gauteng.

# Study of Surface Incident Shortwave Flux over Two Major Cities of South Africa

Jyotsna Singh<sup>1\*</sup> and V. Sivakumar<sup>1</sup>

<sup>1</sup>Discipline of Physics, School of Chemistry and Physics,

University and KwaZulu Natal, Westville Campus, Private Bag X54001, Durban 4001

\*jyotsna11217@gmail.com, svsk74@gmail.com

In the present study we have tried to analyse the variation of surface incident shortwave flux ( $SW_{Flux}$ ) of Modern-Era Retrospective Analysis for Research and Applications (MERRA 2D) reanalysis data over two major cities (Pretoria and Port Elizabeth) of South Africa. The  $SW_{Flux}$  has been studied for the period 1980-2009. The climatological mean of  $SW_{Flux}$  has shown minimum value in June ( $178.58 \pm 4.45 \text{ Wm}^{-2}$  and  $119.64 \pm 4.79 \text{ Wm}^{-2}$ ) and maximum value in November ( $301.99 \pm 22.95 \text{ Wm}^{-2}$ ) and December ( $337.39 \pm 14.28 \text{ Wm}^{-2}$ ) in Pretoria and Port Elizabeth, respectively. On seasonal scale the value of  $SW_{Flux}$  was always high in the urban region (Pretoria) located closer to the equator and at a higher altitude except during summer where value of  $SW_{Flux}$  for Pretoria was less than the coastal region (Port Elizabeth). This suggested that all year round Pretoria received good amount of  $SW_{Flux}$ . The decreasing trend in annual mean of monthly  $SW_{Flux}$  has been studied in three decades (1980, 1990 and 2000) with more decline over Pretoria ( $2.31 \text{ Wm}^{-2}\text{yr}^{-1}$ ) compared to Port Elizabeth ( $2.00 \text{ Wm}^{-2}\text{yr}^{-1}$ ) in 1980. The aerosols optical properties products (Aerosols Optical Depth ( $AOD_{550}$ ) and Angstrom Exponent ( $\alpha_{470-660}$ )) from Moderate Resolution Imaging Spectroradiometer (MODIS) onboard the TERRA Satellite from 2001-2013 have been analysed over Pretoria and Port Elizabeth. Higher values of monthly mean  $AOD_{550}$  have been observed over Pretoria compared to Port Elizabeth. Over Pretoria, Angstrom exponent ( $\alpha_{470-660}$ ) reaches a maximum in late spring (October) and summer (November, December, January), suggesting the presence of fine mode of aerosols. Based on the  $SW_{Flux}$  analysis, Pretoria has more solar energy potential for solar energy application than Port Elizabeth. However, this city is also under the pressure of increasing atmospheric aerosols because of urbanization which is responsible for scattering and absorption of incoming solar radiation.

**Keywords:** Surface incident shortwave flux, Aerosols Optical Depth, Angstrom Exponent, MODIS, MERRA 2D

## 1. Introduction

Solar energy is the alternative source of energy. Proper utilisation of this energy can reduce the pressure on other non-renewable natural resources. This natural resource is abundantly available in South Africa (Munzhedzi and Sebitosi, 2009). The analysis of solar radiation data is important to understand the atmospheric phenomenon as well as it also indicates about the solar energy potential of the place. Before installing any solar energy collecting device like photovoltaic we need the complete information of about the amount of solar radiation falling at the installation site. Solar radiation directly and indirectly plays many roles in the earth's climate. However, the role of solar variability on earth's climate is still poorly understood (Lockwood, 2012). In the present study we have analyzed 30 year's  $SW_{Flux}$  data over two

entirely different cities of South Africa (Pretoria and Port Elizabeth). The variation of  $SW_{Flux}$  over these cities has been studied on annual and seasonal scale. The long term trend in  $SW_{Flux}$  has been also studied in past three decades (1980, 1990 and 2000) over Pretoria and Port Elizabeth. Aerosol optical properties ( $AOD_{550}$  and  $\alpha_{470-660}$ ) have been studied over these regions using MODIS - TERRA Level 3 monthly products data to analyse the atmospheric condition over these two stations.

## 2. Study region and data set

The long term reanalysis data (1980-2009) of  $SW_{Flux}$  of MERRA 2D datasets have been used for two stations, Pretoria ( $25^{\circ}39-25^{\circ}49 \text{ S}$ ,  $28^{\circ}06-28^{\circ}17 \text{ E}$ ) and Port Elizabeth ( $33^{\circ}56 - 33^{\circ}64 \text{ S}$ ,  $25^{\circ}31- 25^{\circ}41 \text{ E}$ ) of South Africa. The spatial resolution of  $SW_{Flux}$  is  $2/3^{\circ}$  (Longitude)

$\times 1/2^\circ$  (Latitude). This data can be downloaded from the site (<http://gdata1.sci.gsfc.nasa.gov>). Pretoria and Port Elizabeth are located in Gauteng and Eastern Cape Province respectively. According to Köppen climate classification Pretoria falls under a *Cwb* climate zone (Warm temperate, Winter dry and Warm Summer) and Port Elizabeth has an oceanic climate *Cfb* (Warm temperate, fully humid, Warm Summer). Pretoria is urbanized with the source of pollution mainly anthropogenic whereas Port Elizabeth is a coastal area where aerosols from marine environment contribute the most. We have analysed MODIS TERRA monthly Level 3 products ( $AOD_{550}$  and  $\alpha_{470-660}$ ) for the period 2001 to 2013. The data can be downloaded from NASA website ([http://gdata1.sci.gsfc.nasa.gov/daac-bin/G3/gui.cgi?instance\\_id=MODIS\\_MONTHLY\\_L3](http://gdata1.sci.gsfc.nasa.gov/daac-bin/G3/gui.cgi?instance_id=MODIS_MONTHLY_L3)).

### 3. Methodology

In the present study  $SW_{Flux}$  data of Pretoria and Port Elizabeth has been analysed from 1980- 2009. Annual as well as seasonal variations of  $SW_{Flux}$  have been analysed and compared for both the stations. For better understanding of variation of  $SW_{Flux}$  over these two places the  $SW_{Flux}$  data has been divided into four different season: summer (December, January and February), autumn (March, April and May), winter (June, July and August) and spring (September, October and November). We have also studied the trend of  $SW_{Flux}$  in three decades 1980 (1980-1989), 1990 (1990-1999) and 2000 (2000-2009). The monthly mean (2001-2013) of MODIS TERRA Level 3 products -  $AOD_{550}$  and  $\alpha_{470-660}$  have also been calculated.

### 4. Results and discussions

#### 4.1 Annual Variation of $SW_{Flux}$

Figure 1 shows the variation of monthly average  $SW_{Flux}$  for each month of the year from 1980 to 2009 over Pretoria and Port Elizabeth. The climatological mean  $\pm$  Standard Deviation (SD) of  $SW_{Flux}$  has shown minimum value in June ( $178.58 \pm 4.45 \text{ Wm}^{-2}$  and  $119.64 \pm 4.79 \text{ Wm}^{-2}$ ) and maximum value in November ( $301.99 \pm 22.95 \text{ Wm}^{-2}$ ) and December ( $337.39 \pm$

$14.28 \text{ Wm}^{-2}$ ) in Pretoria and Port Elizabeth, respectively. On the other hand, the comparison of the  $SW_{Flux}$  values among the two cities shows maximum  $SW_{Flux}$  at Pretoria. However, in November and February the  $SW_{Flux}$  values in Pretoria and Port Elizabeth were nearly equal and in December and January the  $SW_{Flux}$  values were more for the coastal city. The lesser value of  $SW_{Flux}$  during December and January (Figure 1) is probably caused by higher cloud amounts at Pretoria during mid-summer.

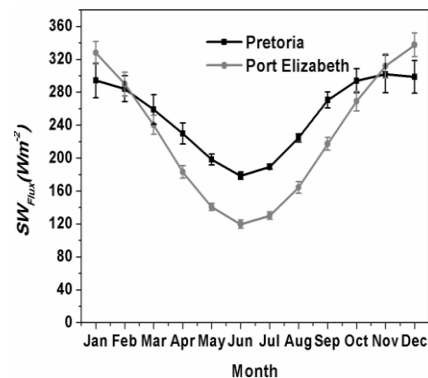


Figure 1. Climatological means of  $SW_{Flux}$  (1980-2009) over Pretoria and Port Elizabeth with standard deviation.

This suggested that the Pretoria have more solar energy potential all year round except summer. However, we can't ignore the good solar energy potential of Port Elizabeth. Analysis of  $SW_{Flux}$  on seasonal scale further explained the better solar energy potential of Pretoria.

#### 4.2 Seasonal Variation of $SW_{Flux}$

In Figure 2 the variation of  $SW_{Flux}$  has been shown for summer, autumn, winter and spring, respectively. The seasonal mean value  $SW_{Flux}$  was at a maximum in summer  $292.32 \text{ Wm}^{-2}$  ( $318.33 \text{ Wm}^{-2}$ ) followed by spring  $288.75 \text{ Wm}^{-2}$  ( $266.00 \text{ Wm}^{-2}$ ), autumn  $228.99 \text{ Wm}^{-2}$  ( $187.92 \text{ Wm}^{-2}$ ) and minimum in winter  $197.47 \text{ Wm}^{-2}$  ( $137.98 \text{ Wm}^{-2}$ ) for Pretoria (Port Elizabeth). The  $SW_{Flux}$  values were higher in Pretoria compared to Port Elizabeth in almost all the season except summer (Figure 2).

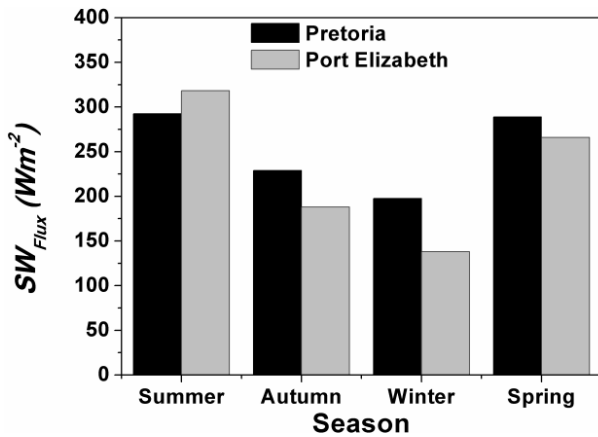


Figure 2. Trend of  $SW_{Flux}$  over Pretoria and Port Elizabeth (1980-2000).

### 4.3 Trend in $SW_{flux}$

The trend analysis of  $SW_{Flux}$  data over Pretoria and Port Elizabeth has been shown in Figure 3.  $SW_{Flux}$  has shown declining trend of  $-2.31(-2.00) Wm^{-2}yr^{-1}$ ,  $-1.25(-0.38) Wm^{-2}yr^{-1}$  and  $-1.09(0.15) Wm^{-2}yr^{-1}$  in Pretoria (Port Elizabeth) during 1980 and 1990. However, in the decade 2000,  $SW_{Flux}$  has shown increasing trend ( $0.15 Wm^{-2}yr^{-1}$ ) in Port Elizabeth whereas in Pretoria continual decline ( $-1.09 Wm^{-2}yr^{-1}$ ) has been observed.

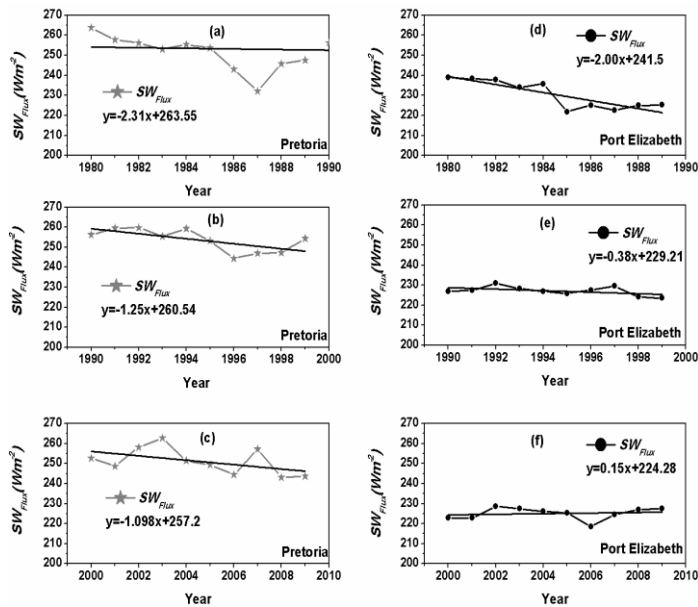


Figure 3. Trend of  $SW_{Flux}$  over Pretoria and Port Elizabeth (1980-2009).

This decline in  $SW_{Flux}$  in all the three decades (1980 (Figure (a), 1990 (Figure (b) and 2000 (Figure (c)) could be due to the more atmospheric load over Pretoria because of urbanization. Previous studies also indicated the high value of atmospheric turbidity over Pretoria (Power and Willmott, 2001). Over Pretoria the effect of cloud cover can also be discerned in the minima indicating the wetter periods in the time series as well. In the present study the aerosols optical properties have been analyzed over these two cities to understand the atmospheric load over these cities. In Port Elizabeth the decline in  $SW_{Flux}$  has not been observed in later decade (2000) (Figure (c) indicates the improvement of air quality in this city.

### 4.4 Variation of aerosol properties

In Figure 4, the climatological mean of  $AOD_{550}$  (Figure 4(a)) and  $\alpha_{470-660}$  (Figure 4(b)) has been shown for Pretoria and Port Elizabeth. The monthly mean values of  $AOD_{550}$  over Pretoria were always higher than Port Elizabeth and this may explains the larger decline of  $SW_{Flux}$  in Pretoria compared to Port Elizabeth. In both the stations  $AOD_{550}$  values was maximum during spring (October). This high value of  $AOD_{550}$  could be due to the biomass burning (Kumar *et al.*, 2014). In Pretoria during summer  $AOD_{550}$  was high.  $\alpha_{470-660}$  was highest during summer in Pretoria (Figure 4(b)). A large  $\alpha_{470-660}$  indicates fine mode aerosol (Yang and Wenig, 2009).

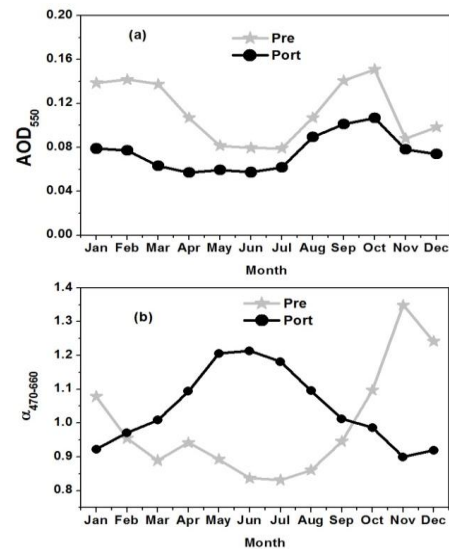


Figure 4. Climatological means of MODIS TERRA,  $AOD_{550}$  and  $\alpha_{470-660}$  (2001-2013) over Pretoria (Pre) and Port Elizabeth (Port).

## 5. Conclusions

In the present work we have studied the variation of  $SW_{\text{Flux}}$  (1980-2000) over two major cities of South Africa Pretoria (urban) and Port Elizabeth (coastal). Pretoria has shown good solar energy potential all year round. However, for the solar energy application mainly in summer season Port Elizabeth is better than Pretoria. A more declining trend in the  $SW_{\text{Flux}}$  has been observed in Pretoria in all the three decades  $-2.31 \text{ Wm}^{-2}\text{yr}^{-1}$  (1980),  $-1.25 \text{ Wm}^{-2}\text{yr}^{-1}$  (1990) and  $-1.09 \text{ Wm}^{-2}\text{yr}^{-1}$  (2000) compared to Port Elizabeth. The coastal city has shown declining trend in  $SW_{\text{Flux}}$  in 1980 ( $-2.00 \text{ Wm}^{-2}\text{yr}^{-1}$ ) and 1990 ( $-0.38 \text{ Wm}^{-2}\text{yr}^{-1}$ ) only. In 2000 an increasing trend ( $0.15 \text{ Wm}^{-2}\text{yr}^{-1}$ ) in  $SW_{\text{Flux}}$  has been observed. The monthly mean  $AOD_{550}$  values (2001-2013) were also high for Pretoria. The  $\alpha_{470-660}$  analysis results indicate the presence of fine mode of aerosols in summer over Pretoria. From the present study it could be concluded that Pretoria is a good place for solar energy application. However, we also can't ignore the high level of atmospheric aerosols in Pretoria compared to Port Elizabeth which is degrading the air quality of Pretoria. The poor air quality is affecting the incoming solar radiation.

## 6. Acknowledgments

We also want to acknowledge University of KwaZulu Natal for funding this work. Analyses used in this study were produced with the Giovanni online data system, developed and maintained by the NASA GES DISC. We want to give our special thanks to unknown reviewers of the present work for their valuable suggestions.

## 7. References

Kumar K. Raghavendra, et al. 2014,' Long-term (2003–2013) climatological trends and variations in aerosol optical parameters retrieved from MODIS over three stations in South Africa.' *Atmospheric Environment*, **95**, 400-408.

Lockwood M. 2012,' Solar influence on global and regional climates,' *Surveys in Geophysics*, **33**(3-4), 503-534.

Munzhedzi R. and Sebitosi, A. B. 2009. Redrawing the solar map of South Africa for photovoltaic applications. *Renewable energy*, **34**(1), 165-169.

MERRA Monthly History Data Collections (2D) Available from: <http://gdata1.sci.gsfc.nasa.gov> (Retrieved on 20 June 2014).

MODIS Terra and Aqua Monthly Level-3 Data Atmosphere Monthly Global 1X1 Degree Products Available from: ([http://gdata1.sci.gsfc.nasa.gov/daac-bin/G3/gui.cgi?instance\\_id=MODIS\\_MONTHLY\\_L3](http://gdata1.sci.gsfc.nasa.gov/daac-bin/G3/gui.cgi?instance_id=MODIS_MONTHLY_L3)) (Retrieved on 25 June 2014).

Power H. C. and Willmott, C. J, 2001,' Seasonal and interannual variability in atmospheric turbidity over South Africa,' *International journal of climatology*, **21**(5), 579-591.

Yang, X., and Wenig, M, 2009,' Study of columnar aerosol size distribution in Hong Kong. *Atmospheric Chemistry and Physics*, **9**(16), 6175-6189.

# Atmospheric Modelling for Seasonal Prediction at the CSIR

WA Landman<sup>\*1,2</sup>, FA Engelbrecht<sup>1,3</sup>, JL McGregor<sup>4</sup> and JH van der Merwe<sup>1</sup>

<sup>1</sup> Council for Scientific and Industrial Research, P.O. Box 395, Pretoria, 0001, [WALandman@csir.co.za](mailto:WALandman@csir.co.za)

<sup>2</sup> Department of Geography, Geoinformatics and Meteorology, University of Pretoria,

<sup>3</sup> School of Geography, Archaeology and Environmental Sciences, University of the Witwatersrand, Johannesburg

<sup>4</sup> Centre for Australian Weather and Climate Research, CSIRO, Aspendale, Australia

Three aspects of seasonal forecast modelling when using an atmospheric general circulation model (AGCM) are presented in this paper. The first aspect deals with the verification of simulations created by forcing the AGCM at its lower boundary by observed monthly sea-surface temperature (SST) and sea-ice fields. The AGCM is the conformal-cubic atmospheric model (CCAM) administered by the Council for Scientific and Industrial Research. Since the model is forced with observed rather than predicted values the skill of the CCAM in simulating seasonal-to-interannual climate variability through these so-called AMIP runs is thought to provide an upper boundary of the model's seasonal forecasting capabilities. The second aspect introduces hindcasts (or re-forecasts) made at lead-times which are the result of forcing the CCAM with predicted SST (while the sea-ice remains specified as climatological values) in order to determine how the model can be expected to perform under real-time operational conditions. Both the simulation and the hindcast runs are statistically downscaled from the horizontal resolution of the model (~200 km) to gridded seasonal rainfall and maximum temperatures at about a 50 km resolution. The focus area of the verification work is southern Africa south of 15°S for both deterministic as well as probabilistic simulations and hindcasts for the austral summer season. The third and final aspect describes the current operational forecast setting and provides the CCAM's rainfall and maximum temperature forecasts for the coming 2014/15 summer season over SADC.

*Keywords:* Seasonal forecasting, hindcasts, verification, downscaling, CCAM, SADC

## 1. Introduction

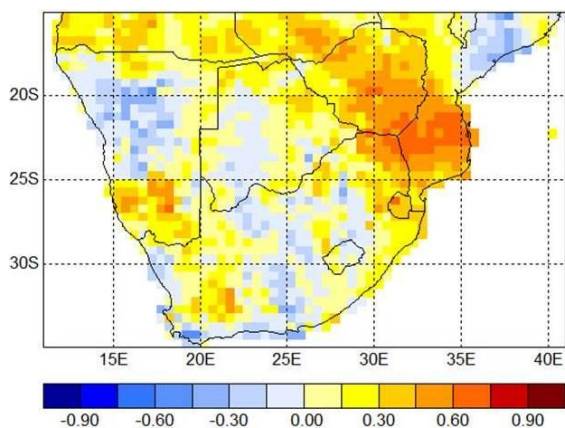
Seasonal rainfall and temperature variations over southern Africa are predictable, but this predictability is to a large extent associated with the time of the year as well as by the state of the Pacific Ocean (Landman and Beraki, 2012; Landman et al., 2012; Lazenby et al., 2014). Although dynamically based atmospheric models in South Africa as operational forecast models have been in use since the early 2000's, continued improvement of these models in South Africa at institutions such as the South African Weather Service and the University of Cape Town is still taking place. The conformal-cubic atmospheric model (CCAM; McGregor and Dix, 2008; Engelbrecht et al., 2011) has been the main focus of the atmospheric modelling initiative that started in 2009 at the Council for Scientific and Industrial Research (CSIR). The model has since been applied across a range of time scales and has in fact been extensively described in a recently completed research project funded by the Water Research Commission. Further support for this development was received by the Applied Centre for Climate and Earth System Science (ACCESS), by ESKOM and by an EU FP7 (DEWFORA) project. The CCAM forecasts,

currently produced once a month, are provided to the South African Weather Service for consideration in the official multi-model seasonal forecasts for South Africa.

## 2. Simulations

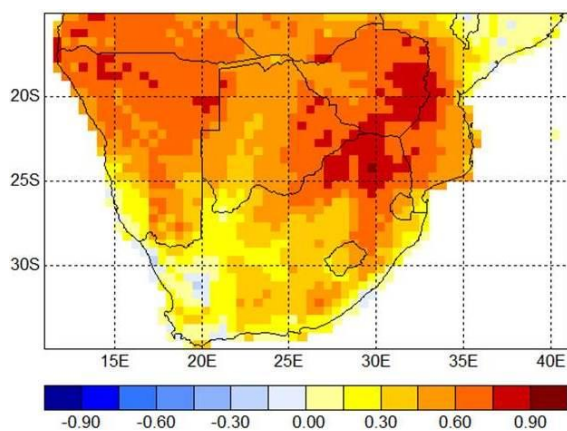
Details on the CCAM as a variable-resolution global atmospheric model can be found in Engelbrecht et al. (2011). Coarse-resolution (~200 km) simulations and hindcasts have been produced by running the CCAM at quasi-uniform resolution. The AMIP-style simulations to be verified span the period February 1979 to November 2005. An ensemble of 12 simulations is obtained by employing a lagged-average forecasting approach. Statistical downscaling (Landman and Beraki, 2012; Landman et al., 2012) is performed next by using the simulated CCAM large-scale atmospheric fields as predictors and then linearly projecting the CCAM output through model output statistics (MOS) on to the respective variables of seasonal total rainfall and maximum temperatures as described by the CRU TS3.1 data set (Mitchell and Jones, 2005). Here we have done verification over a 16-year period from 1989 to 2004 by using a retro-active forecasting procedure (Landman et al.,

2012). Skill is presented as maps of Spearman rank correlation for deterministic forecasts, and as relative operating characteristics (ROC) scores (for estimates of discrimination) and whether or not the probabilistic downscaled hindcasts are over- or under-confident as estimated through reliability diagrams (graphs not shown). ROC scores are calculated from the area underneath the curve that is produced by plotting the forecast hit rates against the false alarm rates. A score  $\leq 0.5$  means that the forecasts have no skill, and for a maximum ROC score of 1.0, perfect discrimination has been obtained. Although simulation skill has been calculated for the five run-on seasons of OND, NDJ, DJF, JFM and FMA, only the verification results for DJF rainfall totals and maximum temperatures are presented here (Figures 1 and 2) since real-time forecasts for DJF will be shown.



ROC A = 0.63; ROC B = 0.57; Rel A: under conf; Rel B: over conf

Figure 1. Spearman rank correlations, ROC scores and an indication of the reliability for the above- (>75th percentile) and below-normal (<25th percentile) thresholds, when downscaling CCAM 850 hPa geopotential height simulations to DJF rainfall totals.



ROC A = 0.78; ROC B = 0.75; Rel A: under conf; Rel B: conf

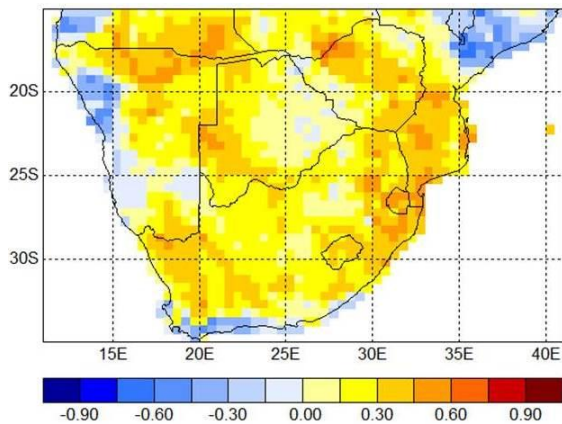
Figure 2. As for Figure 1, but for DJF maximum temperatures.

As a general conclusion, the CCAM has the ability to skillfully simulate seasonal rainfall and maximum temperatures. The following conclusions can be drawn from the verification statistics of the CCAM simulations for all the seasons considered:

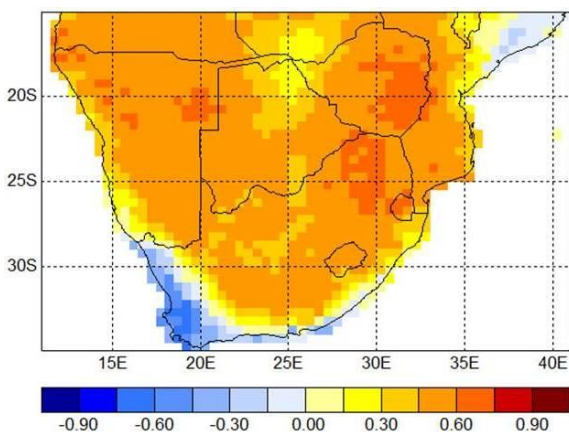
- Seasonal forecast skill is a function of both location and time of the year – the north-eastern parts of South Africa and adjacent regions are often associated with the highest levels of skill for both rainfall and maximum temperatures.
- Skill is generally the lowest during spring, improves towards mid-summer and then declines towards autumn.
- Maximum temperatures are associated with higher levels of skill than rainfall totals.
- Droughts are often simulated with over-confidence, while wet seasons are more likely to be simulated with high levels of reliability.

### 3. The operational CCAM forecast system

The CCAM is forced with predicted global sea-surface temperature (SST) anomalies and started from a set of atmospheric initial conditions in order to provide an ensemble of operational forecasts up to 6 months ahead. CCAM seasonal forecasts are produced each month from an ensemble of 12 members, generated by using a 24-hour lagged average forecast method. The model is initialized from the OZ analysis fields obtained from the Global Forecasting System (GFS) and is forced with SST anomalies predicted by the CSIR's multi-model system (Landman et al., 2011). The SSTs have been re-forecast over the period from 1983 to 2010. Global SST re-forecasts and operational forecasts are provided to the CCAM so that re-forecasts and real-time forecasts of the atmospheric model can respectively be produced. DJF is the most predictable season as has also been found with other modelling studies (e.g. Landman et al., 2012). This notion was subsequently further explored in order to test the CCAM's operational forecast skill in producing 26-years of re-forecasts (1983/84 to 2008/09) through mimicking a real-time operational forecast set-up for seasonal climate. The same downscaling procedure described above for the CCAM simulations are followed here, but this time by training the downscaling model on CCAM re-forecasts and testing it over the 16-year period from 1993/94 to 2008/09. Here the CCAM was initialised in November in order to produce a 1-month forecast for DJF. Figures 3 and 4 show the verification results.



ROC A = 0.54; ROC B = 0.55; Rel A: over conf; Rel B: over conf  
 Figure 3. As for Figure 1, but for predicted DJF rainfall totals.



ROC A = 0.74; ROC B = 0.61; Rel A: conf; Rel B: over conf  
 Figure 4. As for Figure 1, but for predicted DJF maximum temperatures

By comparing verification results of Figures 3 and 4 with Figures 1 and 2, similar levels of skill are obtained by the downscaled re-forecasts, albeit lower: lower ROC scores and enhanced over-confidence with the prediction of anomalously wet DJF seasons. For both simulation and re-forecast skill the CCAM is over-confident in the prediction of anomalously dry seasons, a result also found with other studies (e.g. Landman et al., 2012).

#### 4. CCAM Forecasts for summer 2014/15

CCAM global forecasts are currently produced once a month by about the 13<sup>th</sup>. These forecasts can be downscaled to rainfall, temperatures or any other variable that is sensitive to climate variations (e.g. Malherbe et al., 2014). Figures 5 and 6 show the real-time forecasts for DJF rainfall totals and maximum temperatures issued in August 2014. The forecast area has been downsized in order to show only the forecasts for SADC – presented as anomalies of the ensemble mean forecasts. Anomalously dry and hot

conditions are predicted for the larger part south of 10°S.

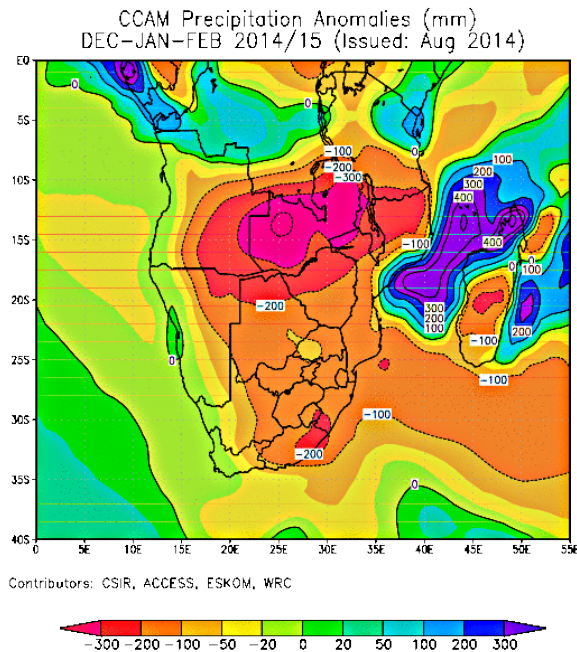


Figure 5. Rainfall anomaly forecast for DJF 2014/15 issued in August 2014.

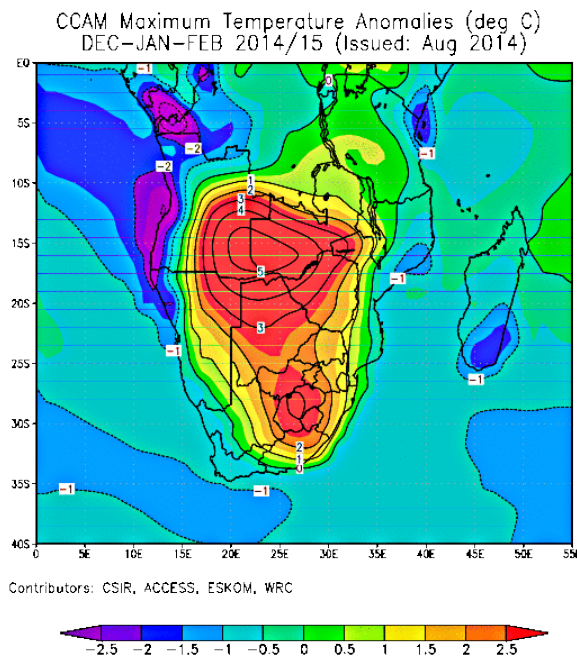


Figure 6. As for Figure 5, but for maximum temperatures.

These predicted conditions (dry and hot) are typical over the region when an El Niño event is occurring. Such an event is in fact predicted by the CSIR's multi-model SST forecast system (Landman et al., 2011) and so the CCAM seems to be responding to this predicted SST forcing. Figure 7 shows the SST anomaly forecast for DJF

issued in August 2014. Take note of the anomalously warm SST predicted over the eastern and central Pacific Ocean, as well as the high probabilities for an El Niño event to occur over the summer months as shown in Figure 8.

DECEMBER–JANUARY–FEBRUARY 2014/15

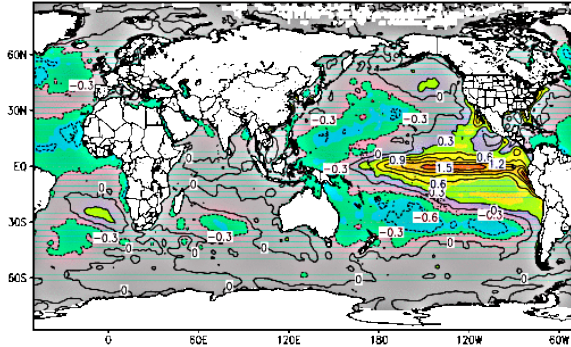


Figure 7. Sea-surface temperature anomaly forecast for DJF issued in August 2014 and produced by the CSIR’s multi-model. Take note of the anomalously warm surface temperatures predicted over the central and eastern equatorial Pacific Ocean.

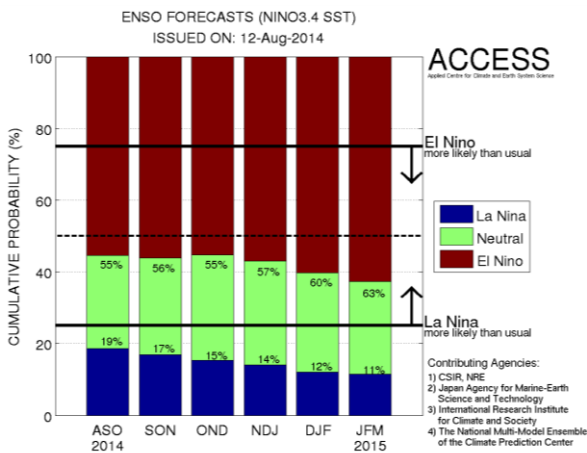


Figure 8. Probabilistic ENSO forecast produced by the CSIR’s multi-model. The increasing red bars are indicative of an increasing likelihood of an El Niño event to occur during the summer of 2014/15.

## 5. Conclusions

This CCAM forecast system is being run operationally each month at the CSIR. CCAM’s configuration presented here for operational forecast production is designed in such a way that it captures the uncertainties in the atmospheric initial conditions through lagged average forecasting, and is forced with skillful predictions of global SST. Such a forecast system is similar to what is in use at some international centres and therefore is a good representation of state-of-the-art seasonal forecast modelling when using

atmospheric general circulation models. Verification statistics show that the CCAM as seasonal forecast model has skill over southern Africa, but that the skill is restricted to certain areas and to certain times of the year. For the most part dry and hot conditions are predicted over these areas for the summer of 2014/15.

## 6. References

Engelbrecht, F.A., Landman, W.A., Engelbrecht, C.J., Landman, S., Bopape, M.M., Roux, B., McGregor, J.L. and Thatcher, M. (2011). Multi-scale climate modelling over southern Africa using a variable-resolution global model. *WaterSA*, 37, 647-658.

Landman, W.A., and Beraki, A. (2012). Multi-model forecast skill for midsummer rainfall over southern Africa. *International Journal of Climatology*, 32, 303-314, DOI: 10.1002/joc.2273.

Landman, W.A., DeWitt, D., and Lee, D.-E. (2011). The high-resolution global SST forecast set of the CSIR. *SASAS*, 22-23 September, 2011.

Landman, W.A., DeWitt, D., Lee, D.-E., Beraki, A. and Lötter, D. (2012). Seasonal rainfall prediction skill over South Africa: 1- vs. 2-tiered forecasting systems. *Weather and Forecasting*, 27, 489-501. DOI: 10.1175/WAF-D-11-00078.1.

Lazenby, M., Landman, W.A., Garland, R. and DeWitt, D. (2014). Seasonal temperature prediction skill over southern Africa and human health. *Meteorological Applications*, DOI: 10.1002/met.1449.

Malherbe, J., Landman, W.A., Olivier, C., Sakuma, H. and Luo, J.-J. (2014). Seasonal forecasts of the SINTEX-F coupled model applied to maize yield and streamflow estimates over north-eastern South Africa. *Meteorological Applications*, 21, 733-742, DOI: 10.1002/met.1402.

McGregor JL and Dix MR (2008) An updated description of the Conformal-Cubic Atmospheric Model. In *High Resolution Simulation of the Atmosphere and Ocean*, eds. K. Hamilton and W. Ohfuchi, Springer, 51-76.

Mitchell TD, Jones PD. 2005. An improved method of constructing a database of monthly climate observations and associated high resolution grids. *International Journal of Climatology* 25: 693–712, DOI:10.1002/joc.1181.

# Can intraseasonal to decadal forecasts benefit from consideration of lunar forcing?

Johan Malherbe\*<sup>1</sup>, Willem A. Landman<sup>2</sup> and Francois A. Engelbrecht<sup>2</sup>

<sup>1</sup> Agricultural Research Council – Institute for Soil, Climate and Water, 600 Belvedere Street, Arcadia, Pretoria,  
[Johan@arc.agric.za](mailto:Johan@arc.agric.za)

<sup>2</sup> Council for Scientific and Industrial Research, 627 Meiring Naude Road, Pretoria,  
[Walandman@csir.co.za](mailto:Walandman@csir.co.za) / [Fengelbrecht@csir.co.za](mailto:Fengelbrecht@csir.co.za)

## ABSTRACT

A possible forcing mechanism for intra-seasonal rainfall distribution to bi-decadal climate variability is explored. The atmospheric response to external forcing is demonstrated at a daily and annual time scale by noting variation in the Southern Annular Mode (SAM) as a function of changing lunar tidal potential. The predictability of the SAM, and the subsequent rainfall response over northeastern South Africa, is evaluated by using an index derived from lunar tidal forcing as a predictor. At intra-seasonal time scales, it is shown that an increase in rainfall between years with lower predicted SAM and years with a higher predicted SAM occurs on very specific parts of the lunar synodic month, providing indications that intra-seasonal outlooks for rainfall by forecast models may benefit from the consideration of lunar cycle characteristics.

**Keywords:** External forcing, decadal variability, intra-seasonal variability, Climate Prediction Tool

## 1. Introduction

Cycles with bi-decadal periods, identified in historical meteorological data, are frequently associated with the 18.6-year lunar nodal cycle (e.g. Currie 1981, Ray 2007). Tidal forcing is a function of lunar and solar distance, declination and alignment (Wood 1986). Possible lunar tidal forcing of the climate system is described by a number of authors (e.g. Ramos da Silva and Avisar 2005).

The influence of the moon (phase, declination and distance) on daily rainfall has been identified statistically in both Hemispheres (e.g. Brier 1965, Visagie 1966). Direct responses noted in certain aspects of the atmospheric general circulation (e.g. Krahenbul et al. 2011) and subsequent responses in rainfall and temperatures may be related to a direct tidal forcing on the atmosphere, or a response due to the oceanic tide or atmospheric anomalies associated with lunar declination such as a change in the concentration of cosmic rays.

The position of South Africa within the subtropical high pressure belt predisposes the country to large climate variability related to the position and strength during the rainy season of the high pressure systems over the Atlantic to the west and Indian Ocean to the east, and location and strength of upper air subtropical jet together with the position and amplitudes of standing waves in the westerlies (see Mason and Jury 1997 for an overview). These are in various degrees related to the Southern Annular Mode (SAM) which is sensitive to external forcings such as stratospheric ozone concentration and solar variability (Arblaster and Meehl 2006). At

bi-decadal scale, climate variability over parts of the summer rainfall region of southern Africa is related to hemispheric anomalies noticeable in the SAM (Malherbe et al. 2014a). Bi-decadal variation in regional climate in response to variation in the SAM may represent part of the ENSO-like variability (Reason and Rouault 2002) or a variation in atmospheric circulation patterns that fluctuates over and above SST variation in the Equatorial Pacific.

The current study aims to demonstrate that forecasts for intra-seasonal to decadal variability of hemispheric circulation anomalies (the SAM) and rainfall responses over subtropical southern Africa may benefit from the consideration of the lunar influence on the climate system. It provides an overview of the development of an index for the seasonal January-March (JFM) SAM (Malherbe et al. 2014b), whilst also reporting new research findings regarding intra-seasonal rainfall variability and lunar tidal potential.

## 2. Data and Methodology

The daily SAM is calculated by subtracting the normalized 850 hPa height at 65°S from that at 40°S using NCEP Reanalysis I data (Kalnay et al., 1996) for the years 1948 to 2013.

The multi-day SAM time series over the historical period during the SH summer are considered firstly according to position of the lunar Perigee and Apogee (distance) within the nodal (declination) period and secondly according to position of Perigee and Apogee within the synodic (phase) month. It is done separately for years during which

the maximum lunar declination (MLD) is restricted to 23° N/S and when it exceeds 25°N/S. Figure 1 describes the grouping of 41-day SAM time series (one SAM time-series group is represented by each horizontal broken line) according to the lunar nodal period (represented by vertical lines) and lunar distance (represented by diagonal lines – white for Apogee, black for Perigee).

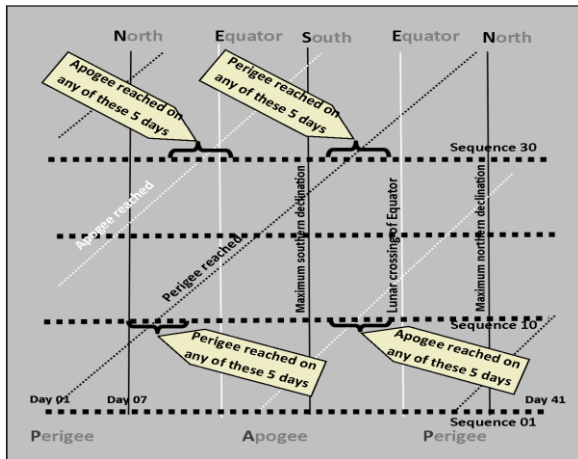


Figure 1 Stacking of daily sequences to identify possible significant deviations in the SAM with lunar distance and declination.

The method is repeated, with focus on the phase instead of declination. Significance of positive and negative deviations are calculated from 5000 reconstructions of the map based on randomized series generated through Monte Carlo simulations of the original time series data.

Through identification of areas of significant negative and positive deviations in the SAM, various rules are formulated regarding possible higher and lower latitudinal lunar tidal forcing and subsequent response in the SAM. These responses in the SAM are then related to lunar tidal potential instead of separate elements of the lunar cycle. An estimate of tidal potential per 5° latitude is calculated (Ahern 1993) for the period 1910-2013 using the algorithm of Longman (1959). The low latitude potential (at 0°-20°S) and high latitude potential (at 65°S) are considered separately. Tidal potential is taken as the normalized daily range in tidal potential for each latitude. An index is derived from the tidal potential values associated with the aspects of the lunar trajectory with which the SAM is shown to have a significant response at daily time scales (Malherbe et al. 2014b). The JFM period is considered (Malherbe et al. 2014a). The index (Tidal SAM Index) is a linear combination of 4 tidal potential values per year, associated with the characteristics of the lunar trajectory. The predictability of the JFM SAM by the index is evaluated through Climate Predictability Tool (CPT) of the International Research Institute for Climate and Society (IRI; <http://www.iri.columbia.edu>).

Towards investigating intra-seasonal rainfall variability, a daily rainfall index is derived for northeastern South Africa from rainfall data at 8 rainfall recording stations. The index is calculated by considering the number of stations out of the total of 8 (yielding a value between 0 and 1), where rainfall for a specific day in the year exceeds that of the long-term for the station for the day. The daily rainfall index time series per summer (Oct-Mar) since 1910 are synchronized according to the lunar synodic month. The 104 luni-synchronous time series are then rearranged according to increasing Tidal SAM Index. The trends with increasing Tidal SAM Index, per (synchronized) day of summer, are calculated and evaluated according to tidal potential.

### 3. Results and discussion

The major result deduced from the maps showing the SAM as function of lunar trajectory characteristics, is that the SAM is positively related to tidal potential at low latitudes. Figure 2 shows one of the 4 maps (Malherbe et al. 2014b) considered. It shows the major finding during periods when the MLD is small: a significant increase in the SAM during summer as the tidal potential increases towards new moon, followed by significantly lower values as the tidal potential decreases.

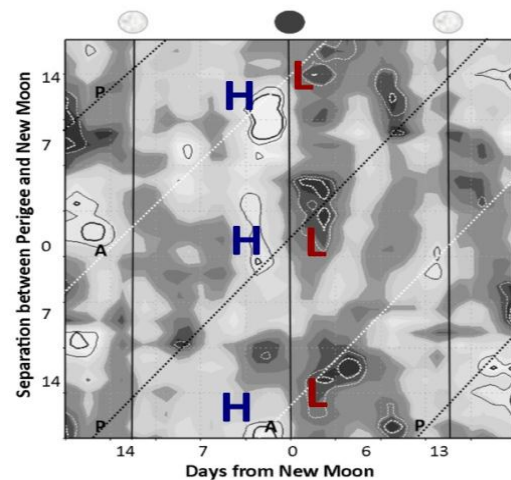


Figure2 Average daily SAM time series (left-right) stacked according to position of lunar Perigee (P) and Apogee (A) with respect to new moon within the lunar synodic month. Vertical (diagonal) lines indicate the position in the time series of new and full moon (Perigee and Apogee). The 90 and 95% positive (negative) significance levels are indicated in broken and solid black (white) lines respectively. The map is for Oct-Mar during years with small MLD (<23°). See Malherbe et al. (2014b) for detailed figure.

To find a method to apply the findings from the above-mentioned maps to a forecast for the

response in the SAM, lower and higher latitudinal tidal potential, related to the lunar declination, phase and distance, is used. Figure 3 shows the variation of the SAM with relation to low-latitude tidal potential, demonstrating the major finding when considering the SAM in relation to lunar declination and distance during periods with larger MLDs.

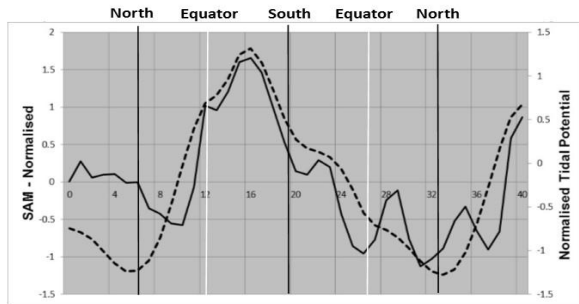


Figure 3 Normalized low-latitude tidal potential (broken line, secondary y-axis) and the SAM (solid line, primary y-axis) for cases with Perigee occurring with lunar equatorial passage towards southern MLD. Only summers (October-March) during which MLD is larger than  $25^\circ$  are considered.

Figure 3 shows the tidal potential, increasing as the moon moves from north to south, across the lower latitudes, and closer to the earth. There is a concomitant increase in the SAM, which decreases again as the tidal potential decreases a few days later. The situation is reversed during years when the closest point to the earth is reached between the equator and northern MLD.

The Tidal SAM Index (Malherbe et al. 2014b), which is a linear combination of the tidal potential values with which the daily variation in the SAM shows a significant response, can be used as a predictor in a linear statistical model. Figure 4 shows the retroactive hindcasts for the SAM for 1981-2013, the Tidal SAM Index and the JFM SAM for 1981-2013.

The hindcast for 1981-2013 is obtained by the process of retro-active forecasting using the IRI Climate Predictability Tool. The retro-active forecast is based on the relation obtained between the Tidal SAM Index and SAM during 1948-1980. With ROC (Relative Operating Characteristic) scores exceeding 0.75, the Index model is able to respectively discriminate positive and negative JFM SAM years from the remainder of the years.

Over and above the predictability of the SAM through the index, the index is also significantly positively correlated to rainfall over NE SA (Malherbe et al. 2014b). Figure 5 shows the grid points in the southern African region where the Spearman rank correlation of the JFM 850 hPa height with decreasing Tidal Sam Index is significantly negative or positive.

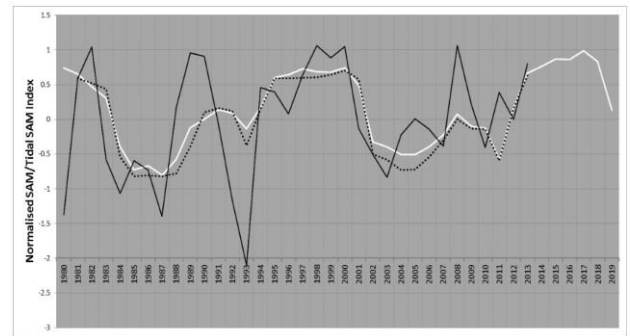


Figure 4 Observed detrended JFM SAM (solid black line) per year for 1980-2013 and Tidal SAM Index (solid white line) for 1980-2020. The retroactive hindcast for the SAM (broken black line) for 1981-2013 is also shown.

As indicated in Figure 5, the subtropical high pressure belt towards the south of southern Africa tends to strengthen (weaken) while the 850hPa heights decrease (increase) over southern Africa when the Tidal SAM Index increases (decreases), suggesting a positive correlation between the index and rainfall over the SA summer rainfall region. The Spearman rank correlation of 0.25 between the Tidal SAM Index and total summer rainfall (determined as the average of 8 stations over northeastern South Africa – Malherbe et al. 2014b) over the period 1910-2013 is significant at the 99% level of confidence. Rainfall trend with increasing Tidal SAM Index shows a 15% increase on average from the years represented by the 25% of lowest Tidal SAM Values to years falling within the highest 25%.

Figure 6 shows the lunar tidal effect on intraseasonal rainfall variability.

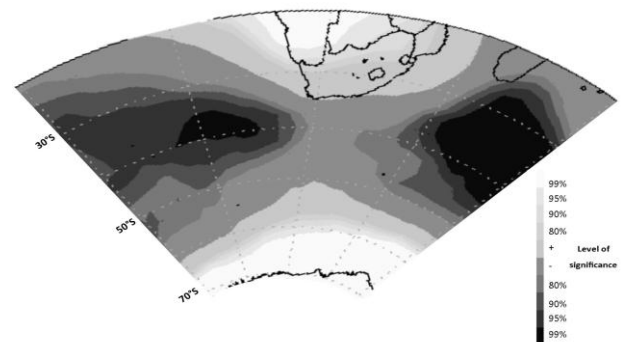


Figure 5 Grid points where significant positive (light shades) and negative (dark shades) trends in JFM 850 hPa heights occur with a decreasing Tidal Sam Index.

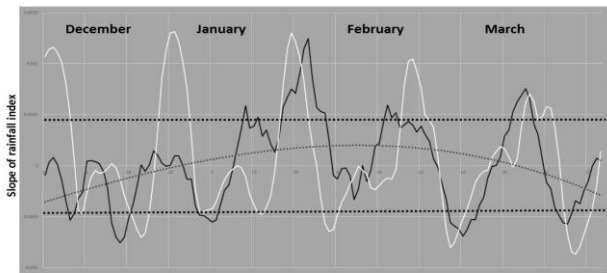


Figure 6 Trend in rainfall index (black line) and low latitude tidal potential (white line) during mid-to late summer as a function of increasing yearly Tidal SAM Index. The 95% upper and lower levels of significance for rainfall index trend are indicated (thick broken black lines). The thin broken black line is a trend line (4<sup>th</sup>-order polynomial) for the rainfall trend.

Figure 6 shows that while summer rainfall increases on average during summer over NE SA with an increase in the Tidal Sam Index, the largest increases occur during late summer (polynomial trend line). On daily time scale, significant increases between years with a low- towards years with high index values, are concentrated around the days with highest low-latitude tidal potential. During late summer, these days occur close to new moon. The Spearman rank correlation between the daily-rainfall-index-trend (with increasing Tidal Sam Index) and daily low-latitude tidal potential during November to March is 0.35, significant at the 99% confidence level. The association may be related at least in part to the variation in the SAM with changing low-latitude tidal potential.

#### 4. Conclusion

An Index, based on lunar tidal potential, has been demonstrated to provide a statistical forecast for the JFM SAM. It can therefore also provide statistical decadal outlooks for climate anomalies related to deviations in the JFM SAM. Significant trends in the 850 hPa heights during JFM with the Tidal Sam Index provide physical confirmation for a significant positive correlation between summer rainfall over northeastern South Africa and the Tidal SAM Index.

Using the Tidal SAM Index, it has been shown that decadal variability in rainfall is significantly related to the lunar tidal potential. Moreover, wetter intraseasonal periods are also related to variation in the lunar tidal potential. The bi-decadal rainfall cycle result from the accumulation of wetter periods on daily time scale that are related to short term daily responses in the climate system to variation in tidal potential. These findings suggest that the consideration of the lunar cycle in climate models may contribute to improved decadal-scale forecasts and improved intra-seasonal resolution and application of seasonal forecasts.

#### 5. References

- Ahern JL. 1993. A program for calculating the tidal acceleration due to the Moon and Sun. <http://gravmag.ou.edu/reduce/tide-acd.txt>
- Arblaster, JM and Meehl GA. 2006. Contributions of external forcings to southern annular mode trends. *Journal of Climatology* **19**:2896–2905.
- Brier GW. 1965. Diurnal and semidiurnal atmospheric tides in relation to precipitation variations 1. *Monthly Weather Review* **93**:93-100.
- Currie RG. 1981. Evidence for 18.6 year MN signal in temperature and drought conditions in North America since AD 1800. *Journal of Geophysical Research* **86**(C11):11055–11064.
- Kalnay E et al. 1996. The NCEP/NCAR 40-year reanalysis project. *Bulletin of the American Meteorological Society* **77**:437-457.
- Krahenbuhl DS, Pace MB, Cerveny RS and Balling RC Jr. 2011. Monthly lunar declination extremes' influence on tropospheric circulation patterns. *Journal of Geophysical Research* **116**:D23121.
- Longman IM. 1959. Formulas for computing the tidal accelerations due to the moon and the sun. *Journal of Geophysical Research* **64**(12):2351–2355.
- Malherbe J, Engelbrecht FA and Landman WA. 2014b. Response of the Southern Annular Mode to tidal forcing and the bidecadal rainfall cycle over subtropical southern Africa. *Journal of Geophysical Research (Atmospheres)* **119**:2032–2049.
- Malherbe J, Landman WA and Engelbrecht FA. 2014a. The decadal-scale rainfall cycle, Southern Annular Mode and tropical cyclones over the Limpopo River Basin, southern Africa. *Climate Dynamics* **42**:3121-3138.
- Ramos da Silva R and Avissar R. 2005. The impacts of the Luni-Solar oscillation on the Arctic oscillation. *Geophysical Research Letters* **32**:L22703.
- Ray RD. 2007. Decadal climate variability: is there a tidal connection? *Journal of Climate* **20**:3542-3560.
- Reason CJC and Rouault M. 2002. ENSO-like decadal variability and South African rainfall. *Geophysical Research Letters* **29**(13):L1638.
- Visagie PJ. 1966. Precipitation in South Africa and lunar phase. *Journal of Geophysical Research* **71**:3345-3350.
- Wood FJ. 1986. Tidal dynamics: Coastal flooding and cycles of gravitational force. D. Reidel: Norwell, MA. Pp.558.

#### Acknowledgements

ACCESS (Applied Centre for Climate and Earth System Science) is acknowledged for supporting this work.

# Impact of ENSO on South African Water Management Areas

Mathieu Rouault<sup>1, 2</sup>

<sup>1</sup> Department of Oceanography, MARE Institute, University of Cape Town.

<sup>2</sup> Nansen-Tutu Center for Marine Environmental Research, University of Cape Town.

**Abstract:** Time series of rain rate and patched observed stream flow gauges extracted from WR2005 are analysed and stratified according to the 19 Water Management Areas (WMA) of South Africa from 1922 to 2004. Correlation with ENSO is growing higher with time for all WMA. El Niño triggers drought and low streamflows and La Nina lead to high rainfall and high streamflows in summer rainfall regions most of the time while the opposite happen in winter rainfall regions. Flows are 2.8 to 1.7 higher during la Nina than during El Niño for summer rainfall WMA. This offer predictability at the WMA scale and also can help better manage water resources in summertime during ENSO year.

Keyword: ENSO, streamflow, rainfall, climate variability,

## 1 Data

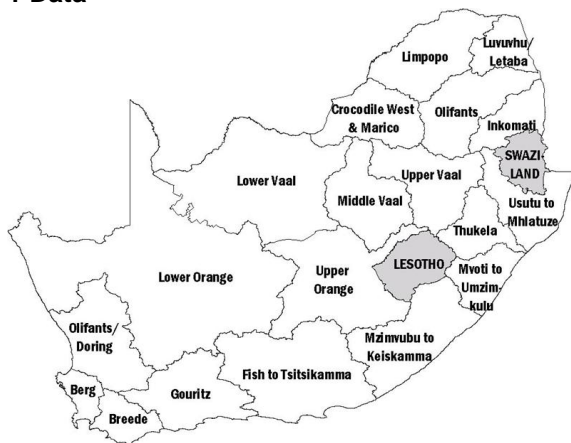


Figure 1: The 19 Water Management Areas of South Africa: 1 Limpopo, 2 Luvuvhu and Letaba, 3 Crocodile West and Marico, 4 Olifants, 5 Inkomati, 6 Usutu to Mhlatuze and Swaziland, 7 Thukela, 8 Upper Vaal, 9 Middle Vaal, 10 Lower Vaal, 11 Mvoti and Umzimkulu, 12 Mzimvubu and Umzimkulu, 13 Upper Orange, 14 Lower Orange, 15 Fish to Tsitsikamma, 16 Gouritz, 17 Olifants Doring, 18 Breede, 19 Berg.

### 1.1 Rainfall

According to WR2005 user guide (Middleton and Bailey, 2011) 609 rainfall stations were used in WR2005. They are stratified according to quaternary catchment, tertiary and water management area (WMA). Only stations within the quaternary catchment boundary and those in close proximity were considered (generally within 10 km) in WR2005. Furthermore, only those with more than 15 years of data were selected and evaluated. Quality control is well described in WR2005 and (Middleton and Bailey, 2011). Particularly, non-stationarity in the

individual monthly records was identified and gauges exhibiting excessive non-linearity were excluded from the evaluation, or only portions of such records were used. For modelling purposes, rainfall data from several gauges were averaged for a group of quaternaries making up a rainfall zone. Most stations start in 1920 and end up in 2004 while a few stations start in 1928. Here, an analysis of the 609 station corresponding to the 19 WMA is presented, namely, annual cycle of rainfall, annual total, peak seasonal total, peak seasonal anomalies with corresponding El Niño Southern Oscillation (ENSO) phase (El Niño years, La Nina years, normal years). A Morlet wavelet analysis of peak season anomalies is performed to outline periodicity and when there was periodicity during the study period, if any. A great advantage of wavelet analysis is to identify when there was periodicity in a time serie and what the period was. Various statistics are also inferred such as trends, correlations with ENSO, 10 driest and wettest peak season rainfall totals per WMA.

### 1.2 Streamflows

Streamflows and reservoirs data were patched and stored in ASCII format in the WR2005 DVD. I kept 255 stations with record longer than 30 years. Data are coded according to the quaternary catchment and tertiary or WMA they represent. Patched observed flow data files were added according to WMA. Other useful info available as spreadsheets in the WR2005 DVD include name of streamflows gauge; WMA number, gauge name, river name, latitude, longitude, catchment area, record period. For all streamflows gauges used, there is a spreadsheet for rejected records. Comments relevant to patching these observed flows are

included in WR2005 including dam spillages and other relevant information. I am presenting here time series of data averaged per WMA from 1960 to 2004 as well as 10 selected stations with long time series.

## 2 Results

### 2.1 Annual cycle

Results for all WMA can be found in Rouault et al., 2014. Mean rainfall was calculated by averaging all rain gauges of each WMA from 7 rain gauges for WMA Lower Vaal to 45 rain gauges for WMA Mzimvubu and Umzimkulu. Of concern was that the mean annual rainfall is the same for all WMA which could indicate that rainfall was scaled to one values of 1000 mm a year for all WMA. However, interannual variability is correct with dry and wet years well defined when compared with SAWS data. This result does not affect the patched observed dataset but does affect the naturalised dataset. Observed streamflows time series data from the common period 1969-2004 were summed per WMA when the most data was available across all WMA. For each WMA, I calculated the number of stations used to sum up each WMA, the mean annual total, the median annual total, the peak season total (November to March for WMA to 15, October to September for WMA 16. May to August for winter rainfall WMA 17 to 19), the percentage peak season total versus annual total, the maximum peak season total that occurred, the minimum peak season total, the average peak season total during El Niño years, the average peak season total during normal years, the average peak season total during La Nina years and the percentage of average peak season streamflows during La Nina versus El Niño. The number of stations used was from 10 to 20 stations per WMA. The annual cycle of patched streamflows gauges is following the annual cycle of rainfall with one to two months lag. WMA 16 has a bimodal flow all year long with a peak in November and a peak in March. Maximum peak season is 3 to 4 time the mean seasonal total while minimum peak season range from 25 % to 1 % of mean peak season total

### 2.2 Interannual variability

The interannual variability of rainfall is studied for the 19 WMAs using peak rainfall season normalised anomaly from climatology. The correlation between ENSO and the 19 WMA peak rainfall season is calculated and the 5 driest and wettest years for the 19 WMA as well as the 5 lowest and highest flow peak flow

season. Other climate index such as the Antarctic Annular Oscillation, the Indian Ocean Dipole, the subtropical Indian Ocean Dipole were found to be not well correlated with South African rainfall in a previous WRC report (Rouault et al, 2010) and in Pohl et al (2010). ENSO index used was the NINO3.4 Index

#### 2.2.1 Rainfall

18 Nina years and 18 Niño years out of 85 years are chosen by averaging the NIÑO3.4 Index, an index representing the El Niño Southern Oscillation quite well and usually well correlated with Southern African rainfall. About half of abnormal year (above or minus one standard deviation) occur during El Niño or La Nina. Years are picked up based on two criteria. First, the same number of Niño years and Nina years is used; second the index must be greater or smaller than one standard deviation. However, since the NIÑO3.4 Index seems to be skewed towards positive values, the limit for La Nina is set at -0.7 to have the same number of La Nina and El Niño events. It is by no mean a definitive ENSO classification but it is giving some indication of anomalous events in the Pacific. NIÑO3.4 Index is averaged from November to March for summer rainfall WMA 1 to 15, October to September for all year long WMA 16 and May to August for the winter region WMA 17 to 19.

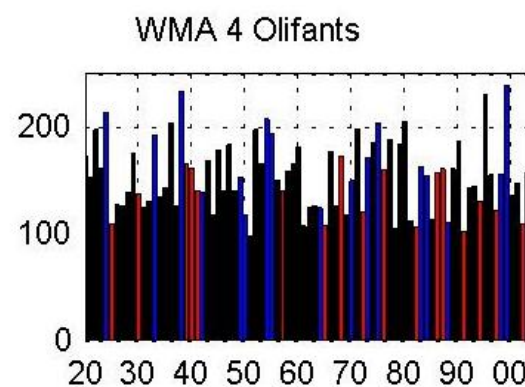


Figure 2: mean seasonal values (mm/month) for peak rainfall season for WMA 4. El Niño years are in red and La Nina years are in blue. Rainfall is averaged from November to March. Year correspond to start of hydrological year.

Mean seasonal values (mm/month) for peak rainfall season for WMA 4 is presented in Figure 2 while normalised anomalies is presented in Figure 3. The correlation with ENSO is higher and more significant during the second period of the study for most WMA. For the winter region correlation with ENSO only starts to be significant from the 1980's (Phillipon et al,

2012). On average it rains 20 to 25 % more during La Nina than during El Niño for the summer rainfall areas. However, during some El Niño years high peak season total can happen. Some El Niño years sometimes fail to create droughts.

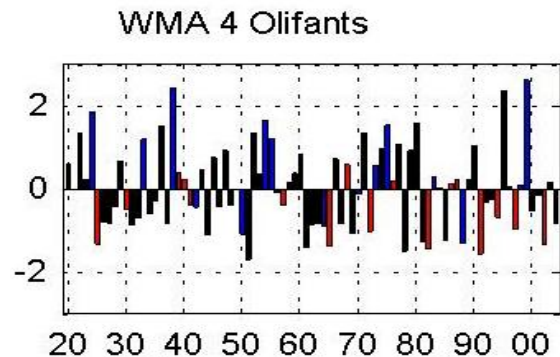


Figure 3: Peak season normalised rainfall anomalies (mean divided by standard deviation) for WMA 4. El Niño years are in red and La Nina years are in blue

Likewise, some La Nina years do not lead to higher than normal rainfall. The intensity of ENSO is not proportional to the climate disturbance for instance 1991/1992 was not a strong El Niño but led to widespread droughts similar to droughts created by the 1982/1983 strong El Niño event. Ranking of the 10 driest years and the 10 wettest years from 1920 to 2004 leads to the following results: from 1920 to 2004 more than half of the top ten the driest year occurred during El Niño years while more than half of the wettest years occurred during La Nina years confirming the study done by Rouault and Richard (2003) with SAWS rainfall data. Considering the recent period 1970 to 2004, the association between ENSO and dry and wet year is actually stronger

### 2.2.2 Observed patched streamflows

Observed streamflows time series data were summed per WMA for the period 1969 to 2004. I yearly total are calculated for peak season streamflows for each WMA which is presented in Figure 4 for WMA 4 Oliphants with corresponding El Niño years (red), La Nina years (blue) and normal years (black). The most striking result is that for WMA 1 to 15, summer rainfall areas, flows are between 1.6 to 2.8 times higher during La Nina years than during El Niño years. This confirms and extends Landman et al (2001). Because El Niño and La Nina start before austral summer, this gives predictability. The 5 highest flow and lowest flow years for all WMA were also calculated with corresponding

El Niño years, La Nina years and normal years (black). 4 or 5 out of the 5 lowest flow years for most WMA occur during El Niño while the opposite occurs for La Nina. During El Niño WMA 17 to 19 experiences about 30 % higher flow than during La Nina.

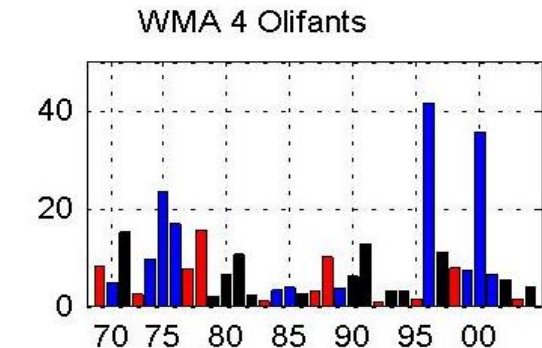


Figure 4: Mean total streamflow for WMA 4 during peak season. El Niño years are in red and La Nina years in blue. Rainfall is averaged from November to March. Year correspond to start of hydrological year.

**Acknowledgement:** WRC, Nansen Tutu Center, NRF and ACCESS

### References

Landman, W. A., Mason, S. J., Tyson, P. D., & Tennant, W. J. (2001). Statistical downscaling of GCM simulations to streamflow. *Journal of Hydrology*, 252(1), 221-236.

Middleton, BJ and Bailey AK (2011) Water resources of South Africa, 2005 study (WR2005) WRC report no. TT 512/11

Phillipon N, Rouault M Richard Y, Favre (2012) on the impact of ENSO on South Africa winter rainfall *International Journal of Climatology*,

Pohl, B., N. Fauchereau, C. J. C. Reason, M. Rouault, 2010: Relationships between the Antarctic Oscillation, the Madden-Julian Oscillation, and ENSO, and Consequences for Rainfall Analysis. *J. Climate*, 23, 238–254.

Rouault M; Fauchereau N; Pohl B ; Richard Y; Pegram GGS; Phillipon N; (2010) Multidisciplinary analysis of hydroclimatic variability at the catchment scale 2010/05/25; WRC Research Report No.1747-1-10

Rouault M. and Y. Richard, (2003) Spatial extension and intensity of droughts since 1922 in South Africa, *Water SA* 29, 489-500.

Rouault M, Pohl B, Dufois F, Phillipon N, Dieppois B, Roy S, Backeberg B. 2014 South African Climate Multidisciplinary, Analysis WRC project K5/2060.



## Austral summer relationship between ENSO and Southern African rainfall in CMIP5 coupled models

Bastien Dieppeois<sup>1,2</sup>, Mathieu Rouault<sup>2,3</sup>, Mark New<sup>1</sup>

<sup>1</sup> African Climate and Development Initiative, University of Cape Town, RSA.

<sup>2</sup> Department of Oceanography, MARE Institute, University of Cape Town, RSA.

<sup>3</sup> Nansen-Tutu Center for Marine Environmental Research, University of Cape Town, RSA.

**Abstract** – In studying the adequacy of 24 atmosphere-ocean global coupled models from CMIP5, overestimations of summer rainfall occur in Southern Africa. Abnormal extensions of ENSO patterns are a common feature of all CMIP5 models. This could explain problems in simulating the teleconnection between ENSO and Southern African rainfall in CMIP5 models. Large-scale anomalies of suppressed deep-convection over the tropical maritime continent and enhanced convection from the central to eastern Pacific are correctly simulated. Regional biases, however, occur above Africa and the adjacent Ocean, particularly in the position of the South Indian Convergence Zone during El Niño, which can lead to the wrong sign in rainfall anomalies in the northwest part of South Africa.

### 1. Introduction

The El Niño Southern Oscillation (ENSO) can be considered as the leading global climate mode of variability driving interannual rainfall variability in Southern Africa. El Niño events favour droughts in this region (Ropelewski & Halpert, 1987; Mason & Jury, 1997; Rouault & Richard, 2005). Cook (2001) proposed that ENSO generates atmospheric Rossby waves in the southern hemisphere which could be responsible for an eastward shift of the South Indian Convergence Zone (SICZ), where most of the synoptic scale bearing systems that affect Southern Africa preferably develop (Todd & Washington, 1999; Hart *et al.*, 2012).

Although a number of previous studies have attempted to evaluate the performance of coupled models to simulate the teleconnections between ENSO and tropical rainfall (Yang & Delsole, 2012; Langenbrunner & Neelin, 2013; Rowell, 2013), little has been done over Southern Africa. In this study, we examine the ability of atmosphere-ocean coupled climate models (AOGCMs) to reproduce observed teleconnections between ENSO and Southern African rainfall using historical runs of the Coupled Model Intercomparison Project 5 (CMIP5).

### 2. Data

This study uses the monthly, land only, rainfall data from the Climatic Research Unit (CRU) 3.21 precipitation dataset to provide observations at 0.5 degree horizontal resolution. The monthly ERSST v3b data is used for global Sea Surface Temperature (SST). We use NCEP/NCAR-1 (NCEP-1) reanalysis to infer monthly atmospheric dynamics.

Model outputs from 24 CMIP5 models from multiple ensembles, producing a total of 83 separate simulations, are used to assess the

AOGCMs. This study uses “historical” simulations, initialized from pre-industrial control runs and forced with natural and anthropogenic atmospheric composition and solar insolation changes for the 20<sup>th</sup> century.

### 3. South African rainfall

We first assess the ability of the simulations to produce a realistic climate.

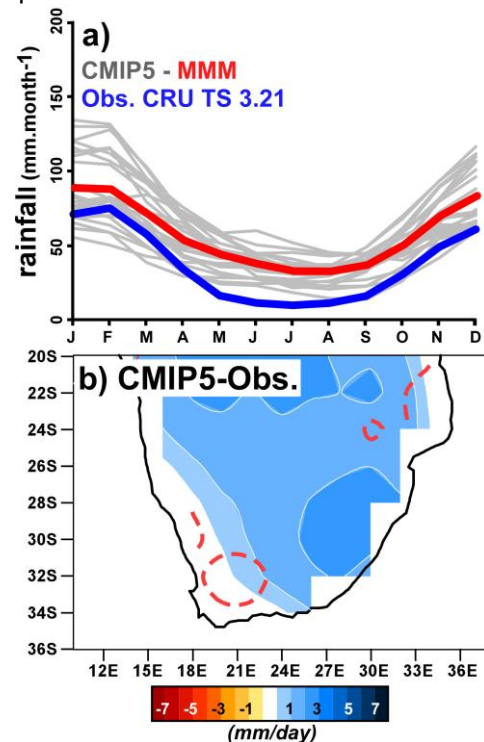


Figure 1. (a) Annual cycle of Southern African rainfall (36°-20°S, 10°-36°E) from CRU TS 3.21 observations (blue), CMIP5 models (grey) and a multimodel mean (MMM; red). (b) Summer (DJF) differences between simulated and observed rainfall fields (mm/day) between 1950 and 2005, as represented by a multimodel mean. The statistical significance of differences (red dashed contours) has been estimated using a Student t-test at  $p=0.05$ .

The annual cycle of Southern African rainfall, along with the individual CMIP5 models (averaged over all ensembles) and a multimodel mean is shown in Figure 1a. The models capture correctly the timing of the annual cycle but overestimate the annual cycle by 10 to 20 mm per month.

As illustrated through the DJF differences between simulations and observation (Fig. 1b), most of individual CMIP5 models, presented here through a multimodel mean, significantly overestimate DJF rainfall. These overestimations are distributed along a NW-SE direction. Maximal differences are identified over the southeastern coastal regions of Southern Africa, Botswana and Namibia.

#### 4. ENSO in CMIP5 models

By decomposing the tropical Pacific SST (35°-35°N/120°E-60°W) into unrotated empirical orthogonal functions, DJF ENSO SST patterns seem correctly reproduced in CMIP5 models (not shown). SST anomalies extending along the equator westward from the South American Coast are surrounded by the classic “horseshoe” patterns of opposite sign. ENSO CMIP5 patterns exhibit biases in three areas, also prevalent in CMIP3 experiment (AchataRao & Sperber, 2006; Lin, 2007; Bellenger *et al.*, 2013). Abnormal westward extension of ENSO patterns is a common and main feature of all CMIP5 models. Warm biases in the equatorial Pacific, resulting in the wrong “double ITCZ” (Lin, 2007; Windlansky *et al.*, 2012), are identified. Underestimation of SST anomalies east of California and Baja peninsula is also detected.

As proposed by Rowell (2013), such biases in the simulated ENSO variability can impact the teleconnection with Southern African rainfall in three distinct ways: i) erroneous forcing of the atmosphere overlying the oceanic source of the teleconnection, either due to an incorrect response of surface fluxes or boundary layer processes, ii) an erroneous representation of atmospheric bridge from the oceanic region to the African region and iii) an erroneous rainfall response over some African regions.

#### 5. ENSO vs. summer rainfall

Correlation patterns between PC-based ENSO indices and Southern African rainfall from observation and, through a multimodel mean, from CMIP5 models are first compared in Figure 2. As proposed by a number of authors (Ropelewski & Halpert, 1987; Mason & Jury, 1997; Rouault & Richard, 2005), significant anti-correlation between ENSO and South African rainfall is detected from the observation (Fig. 2a). In other words, El Niño events tend to be associated with dry conditions over Southern

Africa. The CMIP5 multimodel mean highlights a good skill in simulating the anti-correlation over the south-eastern regions, but some uncertainties are identified over the north-eastern regions (Fig. 2b). Indeed, by looking at the individual models, most of the CMIP5 models display a wrong correlation between ENSO and Southern African rainfall over the south-western and north-eastern regions (not shown). This is especially the case in ACCESS1-0, CanESM2, CCSM4, FGOALS-g2, IPSL-CM5BLR, MRI-ESM1 and all NorESM1 models. Better simulations of ENSO-South African rainfall teleconnections are observed where Pacific SST biases are lowest, such as in CNRM-CM5, MIROC5 and MPI-ESM-P.

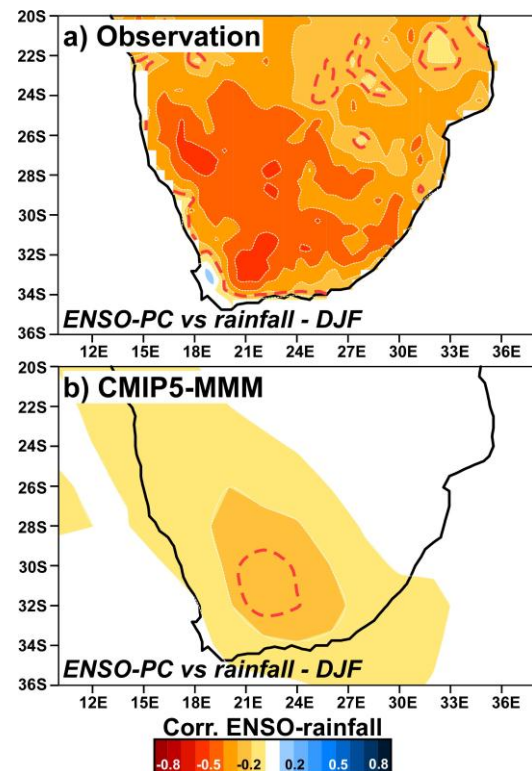


Figure 2. (a) Pointwise correlation between the ENSO component extracted by EOF and South African rainfall in observation between 1950 and 2005. (b) Idem in CMIP5, as represented by a multimodel mean. Red dashed contours indicate the 90% confidence level of Pearson's product moment correlation coefficient assuming independent normal distributions.

In summary, CMIP5 biases of South African rainfall seem closely related to differences in simulating ENSO teleconnections. Positive and negative correlation, respectively, between north-eastern and south-western regions could be associated with overestimations of north-eastern South African rainfall and underestimations of Western Cape rainfall.

## 6. El Niño large-scale convection anomalies

Tropical and extra-tropical deep convection is estimated using DJF NCEP-1 outgoing longwave radiation (OLR). Strong negative OLR anomalies (in green) are associated with higher than normal clouds while positive anomalies (in grey) refer to suppressed convection (Fig. 3). The Southern African summer rainy season is related to negative OLR anomalies (i.e., increased convection) in Southwest Southern Africa extending over the mid-latitudes (Fig. 3a), and can thus be considered as a precursor of tropical-temperate-troughs (TTTs). Indeed, a significant amount of summer rainfall over

Southern Africa is attributed to the occurrence of TTTs (Harrison, 1984; Hart 2012). During TTT events, convection over the continent is linked to the transients in the mid-latitudes, resulting in the presence of a convective cloud-band and rain concentrated along a NW-SE direction (Fig. 3a). These TTTs are related to the establishment of the so-called South-Indian Convergence Zone (SICZ in Fig. 3a). We therefore examined whether this convective pattern could be sensitive to biases of CMIP5 models in simulating the ENSO South African rainfall teleconnection.

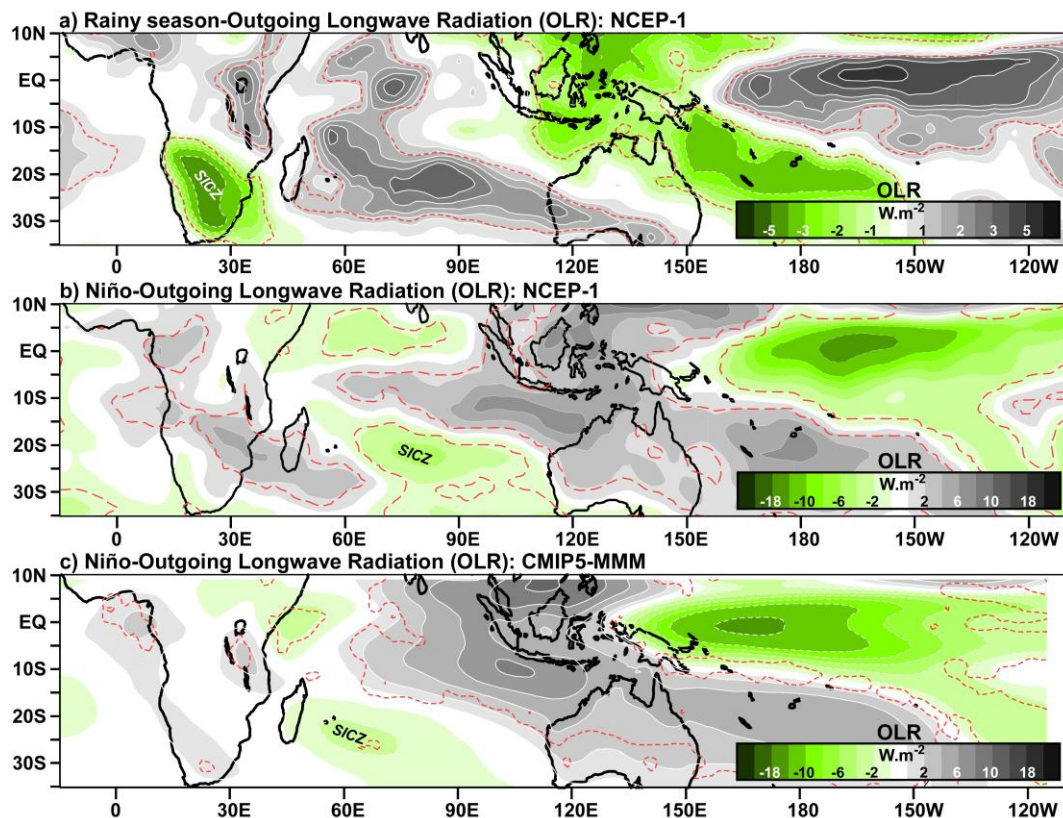


Figure 3. (a) Composite anomalies of OLR (in  $W.m^{-2}$ ) during austral summer rainfall in South Africa (i.e., DJF rainfall  $> 1.75$  mm/month). (b) El Niño composite anomalies (i.e., ENSO-PC $>0.01$ ) of OLR in the NCEP-1 reanalysis. (c) Idem in CMIP5, as represented by a multimodel mean (MMM). The statistical significance (red dashed contours) has been estimated using a  $t$ -test at  $p=0.05$ .

Figure 3b displays composite DJF anomalies of OLR values during El Niño years in the NCEP-1 reanalysis. At the southern hemisphere scale, El Niño years are associated with west-east contrast of suppressed deep-convection over the maritime continent and enhanced convection from the central to eastern Pacific (Fig. 3b). Suppressed deep-convection is also seen over the South Pacific Convergence Zone and the ITCZ, which has shifted toward the equator (Fig. 3b). For Southern Africa, El Niño anomalies are associated with a large band of suppressed convection being surrounded to the

east and to the west by enhanced deep-convection both extending in a NW-SE direction (Fig. 3b), which suggest an eastward shift of the SICZ and preferred location of the cloud band in accordance with Cook (2001).

Through a CMIP5 multimodel mean, global anomalous convective pattern seem correctly identified (Fig. 3c). However, following the abnormal westward shift of ENSO patterns, the CMIP5 models shift the enhanced deep-convection westward from the central to eastern Pacific (Fig. 3c). This appears to have substantial impact over Southern African and

the southern part of Madagascar in reducing the eastward shift of the SICZ (Fig. 3c). This is confirmed by looking at the individual models. Numerous models show a westward extension of suppressed deep-convection in the ITCZ and Africa, such as ACCESS1-0, BCC-CSM1.1, CanESM2, CCSM4, IPSL-CM5B-LR, and all NorESM1 models (not shown). Eastward shifts of the SICZ do not occur and deep-convection tends therefore to be favored over the northeastern regions of Southern Africa which explains the wrong correlation with ENSO discussed previously. Other models, such as CNRM-CM5, MIROC5 and MPI-ESM-P reproduce correctly and underestimate convective anomalies along the ITCZ between Africa and the Indian Ocean (not shown). In those models, eastward shifts of SICZ are well-simulated, and suppressed deep-convection is identified over Southern Africa.

## 7. Conclusion

This study provides an overview of the capability of CMIP5 coupled models to represent the impact of ENSO on Southern African summer rainfall. Although, the CMIP5 experiments show a realistic seasonal rainfall cycle, summer rainfall is always overestimated. Numerous weaknesses in the simulation of ENSO are still present in CMIP5. Notably, westward extensions of ENSO modes of variability are likely to disrupt the atmospheric bridge from the Indo-Pacific region to the South African region. Anomalous positive or negative correlation patterns are thus identified in CMIP5 models over the northeastern and the southwestern part of Southern Africa, respectively. This is partly due to CMIP5 model shortcomings above Africa and the Indian oceans in simulating eastward shift of the SICZ during El Niño events. According to Richard *et al.* (2000), an eastward shift of the SICZ is forced by warm anomalies in the tropical south Indian Ocean leading to a weakened subtropical high belt at the longitude of Madagascar. Difficulties in reproducing a warm Indian Ocean during El Niño events therefore are likely to drive such biases (Dieppois *et al.*, submitted). The latter study also show that Southern African rainfall biases are associated with biases in reproducing the shift and change in high pressure over the South Atlantic and South Indian Oceans during El Niño years.

## 8. References

- AchutaRao, K., and Sperber, K.R. (2006). ENSO simulation in coupled ocean-atmosphere models: are the current models better? *Clim Dyn.* **27**:1–15.
- Bellenger, H., Guilyardi, E., Leloup, J., Lengaigne, M., Vialard, J. (2013). ENSO representation in climate models: from CMIP3 to CMIP5. *Clim Dyn.* **42**:1999–2018.
- Cook, K.H. (2001). A Southern Hemisphere wave response to ENSO with implications for southern Africa precipitation. *J Atmos Sci.* **15**:2146–2146.
- Dieppois, B., Rouault, M., New, M. (submitted). The impact of El Niño on Southern African rainfall in CMIP5 Ocean Atmosphere coupled climate models. *Clim Dyn.*
- Harrison, M.S.J. (1984). A generalized classification of South African summer rain bearing synoptic systems. *J Climatol.* **4**:547–560.
- Hart, N.C.G., Reason, C.J.C., Fauchereau, N. (2012). Building a tropical extratropical cloud band metbot. *Mon Wea Rev.* **140**:4005–4016.
- Langenbrunner, B., Neelin, D.J. (2013). Analyzing ENSO teleconnections in CMIP5 models as a measure of model fidelity in simulating precipitation. *J Clim.* **26**:4431–4446.
- Lin, J-L. (2007) The double-ITCZ in IPCC AR4 coupled GCMs: Ocean-atmosphere feedback analysis. *J Clim.* **20**:4497–4525.
- Mason, S.J., and Jury, M. (1997) Climatic variability and change over the Southern Africa: a reflection on underlying processes. *Prog Phys Geo.* **21**:23–50.
- Richard, Y., Trzaska, S., Roucou, P., Rouault, M. (2000). Modification of the Southern African rainfall variability/El Niño southern oscillation relationship. *Clim Dyn.* **16**:883–895.
- Ropelewski, C.F., and Halpert, M.S. (1987). Global and regional scale precipitation patterns associated with the El Niño/Southern Oscillation. *Mon Wea Rev.* **115**:1606–1626.
- Rouault, M., and Richard, Y. (2005). Intensity and spatial extent of droughts in Southern Africa. *Geophys Res Lett.* **32**:L15702.
- Rowell, D.P. (2013). Simulating SST Teleconnections to Africa: What is the state of the Art? *J Clim.* **26**:5597–5418.
- Todd, M.C., and Washington, R. (1999). Circulation anomalies associated with tropical-temperate troughs in southern Africa and southwest Indian Ocean. *Clim Dyn.* **15**:937–951.
- Yang, X., and DelSole, T. (2012). Systematic comparison of ENSO teleconnection patterns between models and observations. *J Clim* **25**:425–446.
- Windlansky, M.J., Timmermann, A., Stein, K., McGregor, S., Schneider, N., England, M.H., Lengaigne, M., Cai, W. (2012). Changes in South Pacific rainfall bands in a warming climate. *Nature climate change.* **3**:417–423.

# Interannual rainfall variability over the Cape south coast of South Africa linked to cut-off low associated rainfall

Christien J. Engelbrecht\*<sup>1</sup> and Willem A. Landman<sup>2</sup>

<sup>1</sup> Agricultural Research Council, Institute for Soil, Climate and Water, Pretoria, South Africa, engelbrecht@arc.agric.za

<sup>2</sup> Climate Studies, Modelling and Environmental Health, CSIR, Pretoria, South Africa, walandman@csir.co.za

The influence of cut-off low (COL) associated rainfall on interannual rainfall variability over the Cape south coast region of South Africa for the period 1979-2011 is investigated. COLs are objectively identified and tracked on daily average 500 hPa geopotential height- and temperature fields. Daily station rainfall data over the Cape south coast are used to identify rainfall producing COLs. A positive statistical significant rank correlation is observed between COL associated annual rainfall totals and all rainfall annual totals, indicating that COLs are a source of interannual rainfall variability. The relationship is also valid for autumn, winter and spring.

**Keywords:** Interannual rainfall variability, Cape south coast, cut-off lows.

## 1. Introduction

The Cape south coast region of South Africa is considered to be a unique climate region in southern Africa as it receives rainfall throughout the year with small peaks during austral autumn and spring (Weldon and Reason 2014). Rainfall over the region results from cold fronts, west-wind troughs, COLs, ridging high pressure systems (e.g. Taljaard 1996, Favre et al. 2013, Weldon and Reason 2014) and tropical temperate-troughs (e.g. Taljaard 1996, Hart et al. 2013). Recently, the mean contribution of ridging high pressure systems, COLs and tropical temperate troughs to annual rainfall totals (January to December) was quantified to be 46 %, 16 % and 28 % respectively by application of a self-organizing map (Engelbrecht et al. 2014). It may be noted that COLs occurred in combination of ridging high pressure systems and tropical temperate-troughs. COLs are known to be mostly the cause for extreme rainfall events along the Cape south coast (e.g. Taljaard 1985, Singleton and Reason 2007). This region is also characterised by high rainfall variability (Weldon and Reason 2014). The aim of this study is to determine the influence of COL associated rainfall on interannual rainfall variability.

## 2. Data and methods

### 2.1 Rainfall data

Daily rainfall data for the period 1979-2011 over the Cape south coast were obtained from the South African Weather Service (SAWS). Twelve weather

stations (Figure 1) over the Cape south coast that complied to basic quality checks were chosen. In a particular month, more than 66 % of the days in that month need to be present and pass extreme and missing value checks. In the case that a station passed the completeness condition but failed the extreme or missing value check, those entries were replaced by estimated values derived from neighbouring stations.

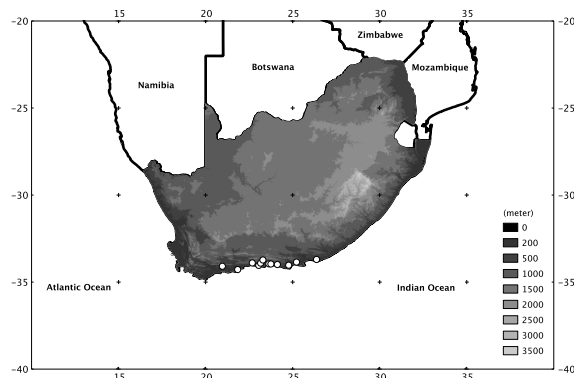


Figure 1. The geographic location of the weather stations is indicated by the white circles. The topography as represented by SRTM DEM data is shown in grey shades.

The rainfall station data are used to quantify the contribution of COLs to annual rainfall in order to investigate the role of COLs to interannual rainfall variability. Wet and dry years and seasons are identified by application of the tercile approach (33<sup>rd</sup> and 67<sup>th</sup> percentile thresholds) on area-averaged annual and seasonal rainfall totals respectively.

## 2.2 Identification of cut-off lows

NCEP reanalysis data (Kalnay et al. 1996) are utilized to identify and track COLs over the period 1979-2011. COLs have a typical length scale of 1,000 km (e.g. Singleton and Reason 2007) and are therefore well resolved on the 2.5° resolution of the NCEP data. A COL is defined as a cold cored closed-low on 500 hPa that is displaced from the westerly wind regime (Favre et al. 2012). The daily-average geopotential height- and temperature fields at 500 hPa are utilized for identifying and tracking COLs in the domain bounded by 40°S-20°S and 10°E-40°E. All COLs that occurred for at least 24-h over this domain are considered in this study. Firstly, closed-lows are identified by locating geopotential minima in a procedure where the geopotential at each grid point is compared to the geopotential values of the square of eight surrounding grid points on the latitude longitude grid. After closed-lows have been identified in the time-series of 500 hPa geopotential fields, tracks are constructed by identifying the geopotential minima at time step  $t+1$  nearest to the geopotential minima at time step  $t$ . The distance between the closed-lows at time step  $t$  and time step  $t+1$  needs to be <1,000 km in order to secure a sound mean daily speed of the potential COL. The mean daily speed of a COL in the South African region does not exceed 42 km/h (Favre et al., 2012). Any geopotential minima can only be used in a single track. From this closed-low track dataset, tests described in Favre et al. (2012) to ensure that tracks are of extra-tropical origin, detached from the westerlies and possess a cold-core are employed.

Rainfall associated with cold-cored systems occurs mainly some hundreds of kilometres to the northeast, east and southeast of the centres of these systems. From the constructed COL dataset for the period 1979-2011, all the COLs that occurred west of 32.5°E are considered to be potentially responsible for rainfall over the region. Such COLs associated with rainfall over the region, at least at a single station, are defined as rainfall producing COLs.

## 3. Results

The percentage of COLs associated with rainfall over the Cape south coast region during DJF, MAM, JJA and SON is 55 %, 61 %, 63 % and 68 % respectively. The seasonal mean rainfall attributed to COLs over the Cape south coast is 15 mm, 34 mm, 38 mm and 31 mm during DJF, MAM, JJA and SON respectively.

The contribution by COLs to annual rainfall is highly variable (Figure 2), with a minimum contribution of 2 % in 1984 and 2004 while 37 % of annual rainfall in 2006 is attributed to COLs.

COL related annual area-averaged rainfall over the Cape south coast is positively rank (Kendall's tau) correlated to all annual area-averaged rainfall with a statistical significance at the 99 % level of confidence (Figure 2). COLs are therefore found to be strongly linked to the interannual rainfall variability over the Cape south coast. High rainfall from COLs during 1979, 1997 and 2003 made it possible for those years to fall within the normal annual rainfall totals category with COLs contributing 23 %, 32 % and 25 % to annual rainfall totals respectively. During 1984, 1991, 1998 and 1999 rainfall attributed to COLs was a minimum (3 %, 3 %, 6 % and 6 % respectively), with annual rainfall totals observed to be below-normal.

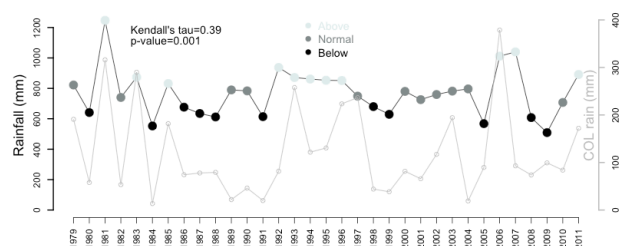


Figure 2. Time series of annual area-averaged rainfall (dark grey) as well as the COL-component (light grey) of the annual area-averaged rainfall. Light blue, grey and black circles respectively indicate years of above-normal, normal and below-normal rainfall totals.

The influence of rainfall associated with COLs on seasonal totals over the period 1979-2011 is shown in Figure 3. A weak but insignificant rank correlation exists for summer (DJF), the season with the lowest mean frequency of COLs and COL associated rainfall. Autumn (MAM) and winter (JJA) have the highest and most significant (99 % level of confidence) rank correlation between COL associated seasonal rainfall totals and all seasonal rainfall totals. A weak but significant rank correlation exists for spring (SON) which can probably be attributed to ridging high pressure systems that contributes largely to October rainfall, the month observed with the highest monthly rainfall totals along the Cape south coast (Engelbrecht et al. 2014).

The geographical location of COLs during wet and dry years exhibit different regions of preferred occurrence. The mean COL frequency anomaly for years of above-normal rainfall is characterized by COLs most frequently located over the western part of the Northern Cape and Southwestern Cape. Noteworthy, is a secondary maximum over the western interior of the Eastern Cape. During years

of below-normal rainfall, all of the aforementioned areas are characterized by a negative mean COL frequency anomaly.

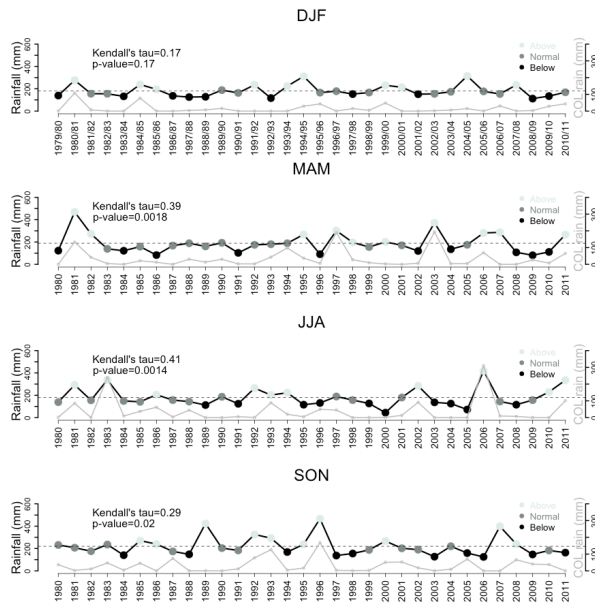


Figure 3. As for Figure 2, but for DJF, MAM, JJA and SON.

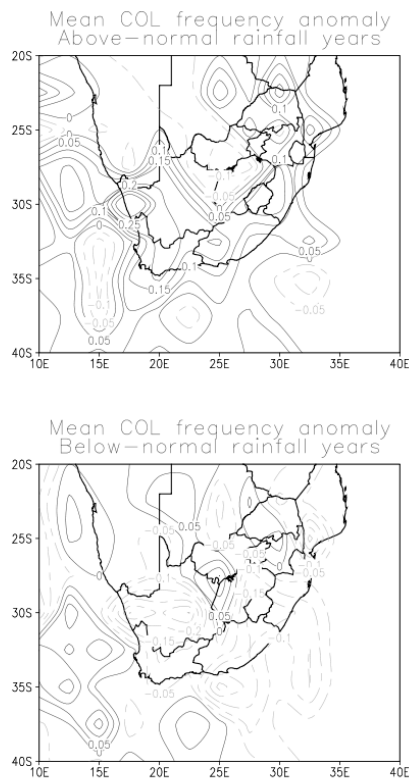


Figure 4. Mean COL frequency anomaly for years of above-normal rainfall (top) and below-normal rainfall (bottom).

#### 4. Conclusion

The contribution of COLs to annual rainfall over the Cape south coast is on average 16 %. Even though this contribution to annual rainfall seems moderate, COLs are strongly suggested to be a major contributor of interannual rainfall variability over this region. This relationship holds also for autumn, winter and spring with it being strongest for winter.

#### 5. Acknowledgments

This research was funded by the Water Research Commission (Project K5/2257/1) and the Applied Centre for Climate and Earth System Studies (ACCESS). Rainfall data were supplied by the South African Weather Service.

#### 6. References

Engelbrecht C.J., Landman W.A., Engelbrecht F.A. & Malherbe J. 2014, 'A synoptic decomposition of rainfall over the Cape south coast of South Africa' *Climate Dynamics*, DOI 10.1007/s00382-014-2230-5.

Favre A., Hewitson B., Tadross M., Lennard C. & Cerezo-Mota R. 2012, 'Relationships between cut-off lows and the semiannual and southern oscillations' *Climate Dynamics* **38**:1473-1487.

Favre A., Hewitson B., Lennard C., Cerezo-Mota R. & Tadross M. 2013, 'Cut-off lows in the South Africa region and their contribution to precipitation' *Climate Dynamics* **41**:2331-2351.

Hart N.C.G., Reason C.J.C. & Fauchereau N. 2013, 'Cloud bands over southern Africa: seasonality, contribution to rainfall variability and modulation by the MJO' *Climate Dynamics* **42**:1199-1212.

Kalnay E. & co-authors. 1996, 'The NCEP/NCAR 40-year reanalysis project' *Bulletin of the American Meteorological Society* **77**:437-471.

Singleton A.T. & Reason C.J.C. 2007, 'Variability in the characteristics of cut-off low pressure systems over subtropical southern Africa' *International Journal of Climatology* **27**:295-310.

Taljaard J.J. 1985, Cut-off lows in the South African region. South African Weather Bureau, Technical paper 14

Taljaard J.J. 1996, Atmospheric circulation systems, synoptic climatology and weather phenomena of South Africa. Part 6: Rainfall in South Africa, South African Weather Bureau, Technical paper 32

Weldon D. & Reason C.J.C. 2014, 'Variability of rainfall characteristics over the South Coast region of South Africa', *Theoretical and Applied Climatology* **115**:177-185.

# The annual cycle of Central Africa rainfall and its relationship with the surrounding tropical Oceans

Georges-Noel Tiersmondo Longandjo<sup>\*1,2</sup> and Mathieu Rouault<sup>1,2</sup>

<sup>1</sup> Oceanography Department, University of Cape Town, Rondebosch 7700, South Africa

<sup>2</sup> Nansen-Tutu Center for Environmental Marine Research, Rondebosch 7700, South Africa  
[longandjo@gmail.com](mailto:longandjo@gmail.com); [Mathieu.Rouault@uct.ac.za](mailto:Mathieu.Rouault@uct.ac.za)

The annual cycle of rainfall over Central Africa and its relationship with surrounding tropical Oceans sea surface temperature (SST) is evaluated using GPCP v2 Rainfall, NOAA OI v2 SST and wind of ERA-Interim reanalysis data. Central Africa rainfall variability depends on SST gradient (index SST) between eastern tropical Atlantic and western tropical Indian Ocean. During positive years of index SST, Central Africa is associated with above normal rainfall for MAM and JJA while the opposite lead to drought in SON and DJF. The positive (negative) SSTs anomalies over surrounding tropical ocean basins act by increasing the zonal component of low-level atmospheric circulation that suppress local rainfall by increasing (blocking) the additional supply of moisture over regions of large inter-annual rainfall variances.

*Keywords:* Central Africa; Atlantic Ocean; Inter-basin SST gradient index; Ocean – atmosphere interaction.

## 1. Introduction

Central Africa (7°-32°E; 15°S-10°N) is a vast bio-diverse region containing approximately 90% of Africa's remaining tropical forest and experiences the highest frequency of lightning strikes than anywhere else in the world (Nicholson and Grist, 2003; Balas et al, 2007). Recently some studies have shown that satellite data and coupled models used in CMIP3/5 fail to capture the spatial distribution and amount of annual precipitation (Washington et al, 2013). On inter-annual time scales, sea surface temperatures (SSTs) of tropical Oceans – particularly Atlantic and Indian – may impact climate in their surrounding continents such as Central Africa (Wang et al, 2009; Balas et al, 2007; Fisher et al, 2005). All these suggest that the physical process of formation of rainfall over Central Africa could be different to that of other tropical/equatorial regions (McCoullum et al., 1999; Balas et al., 2007). To the best of our knowledge, no studies have conducted to understand the discrepancy between model projections and the observations or documented the nature of the relationship between Central Africa rainfall and its surrounding tropical ocean basins. Here we study the annual cycle of rainfall over Central Africa and the response to SST gradient between tropical eastern Atlantic and western Indian Oceans (hereafter named Index SST).

## 2. Data and methodology

We use a combination of monthly observational and reanalysed climate data to investigate the mechanisms connecting Central Africa rainfall and surrounding tropical SSTs. 1) Rainfall dataset from version 2.2 of Global Precipitation Climatology Project (GPCP) (Huffman et al., 2009), 2) NOAA Optimum Interpolated (OI) SST (Reynolds et al., 2002), 3) ERA-Interim horizontal wind components (Dee et al., 2011). Because of the limited period covered by satellite SST, we study the 1982 to 2012 period where reanalysis are also more reliable. In order to investigate the impact of index SST on Central Africa rainfall, a compositing approach based on positive or negative years or seasons is used. We take only the five strongest positive and negative years (seasons). The index SST is the difference between normalized monthly anomalies of SSTs area-averaged over eastern tropical Atlantic Ocean region (0-12°E) and western tropical Indian Ocean region (40-50°E) over similar latitudes (5N-15°S) (cfr Figure 2).

## 3. Results and discussion

To analyze the regional characteristics of rainfall on annual cycle, the spatial distribution of rainfall and the standard deviations of rainfall over Central Africa and surroundings tropical oceans is shown in Figure 1. We notice that large range of variation of rainfall emerges over two regions in Central Africa,

over (i) the gulf of Guinea coast (7.5-10°E; 5°N-5°S) and (ii) the south of Central Africa (22-32°E; 12.5°-15°S). So to understand ocean-atmosphere interactions locally and regionally, we used these two regions together with CA and investigated the response of rainfall to surrounding tropical Atlantic and Indian SSTs.

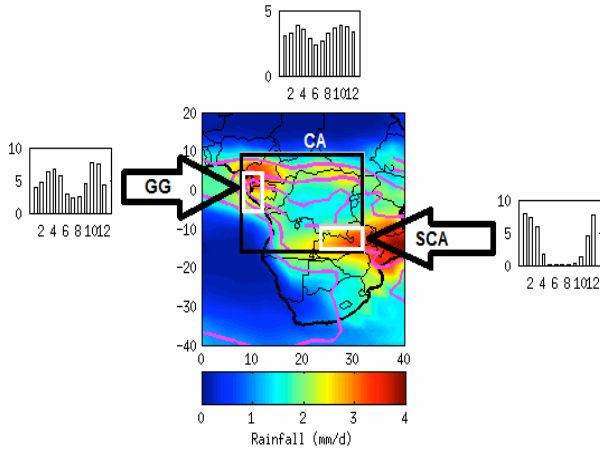


Figure 1 Standard deviations (shading) and mean (magenta contours  $\geq 3$ ) of rainfall from GPCP (1982 – 2012). Unit: mm/d, interval: 2mm/d. Black box represents Central Africa and white boxes represent gulf of Guinea coast and South Central Africa respectively.

The gulf of Guinea coast has the most distinctive bimodal annual rainfall cycle than the entire Central Africa with respectively the minimum and maximum peaks in June (or July) and April and October. But, over South Central Africa, the rainfall is characterised by a peak of rainfall in December or January (Figure 1). The inter-annual variability of rainfall over the three regions selected and index SST for four seasons – March to May, June to August, September to November and December to February suggest that these regions are not always wet (dry) during positive or negative years (not shown).

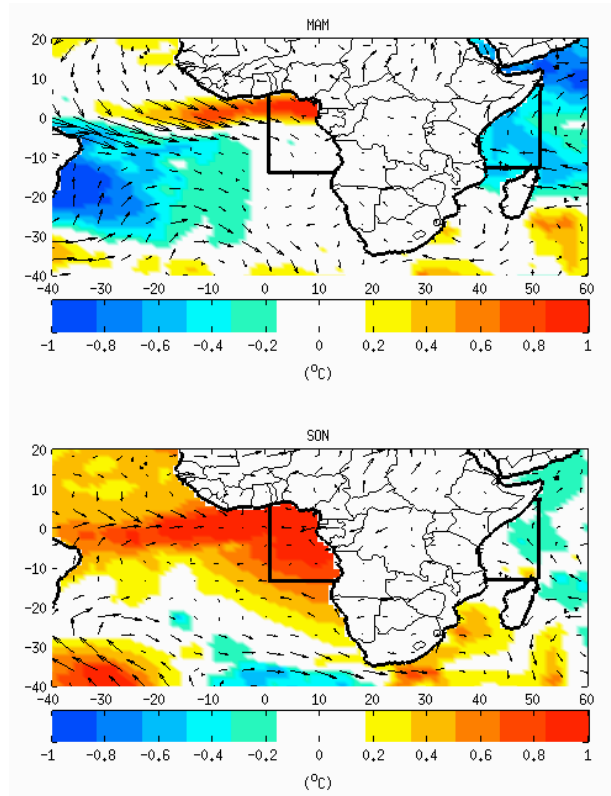


Figure 2 Difference in SST between positive and negative years of index SST for (a) MAM and (b) SON from Reynolds SST and ERA-Interim wind at 925 –hPa (1982-2012). The black boxes (in a and b) represent respectively eastern tropical Atlantic Ocean region and western tropical Indian Ocean region

The composite of SST and wind at 925-hPa of difference between positive and negative years of index SST is shown in Figure 2 for MAM and SON seasons. During positive years of index SST, when warmer SSTs anomalies are observed in one ocean, the SSTs anomalies in the other ocean are colder, except over South of Madagascar in Indian Ocean (20°-60°E; 20°-40°S) where SSTs anomalies are warm during all seasons. But over Central Africa, positive years are associated with positive rainfall anomalies in MAM (and JJA, not shown) and negative rainfall anomalies in SON (and DJF, not shown), except over regions of large rainfall variances where the rainfall anomalies are positive all year (Figure 4).

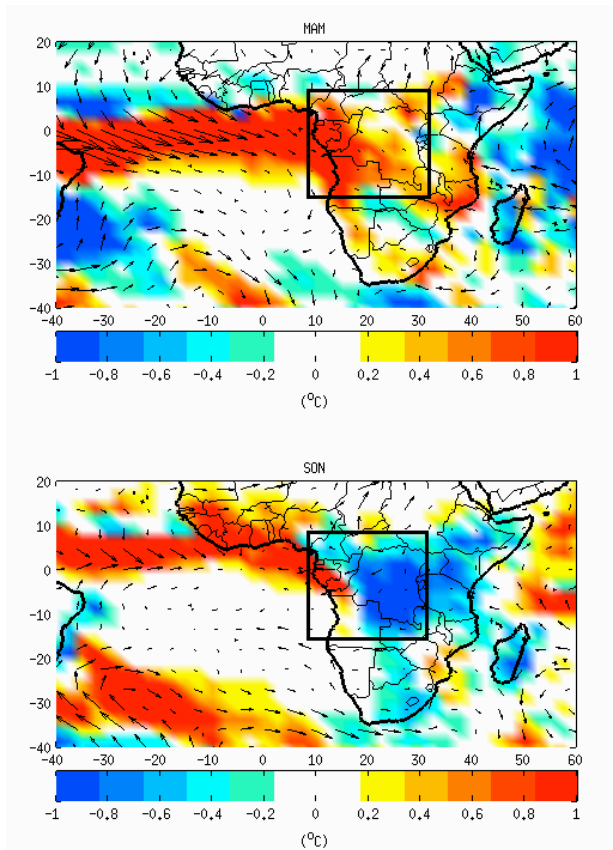


Figure 3 As figure 2, but for rainfall from GPCP (1982-2012). Black box (in a and b) represents Central Africa.

The stronger low-level atmospheric circulation flow in positive and negative years as well as their difference is shown in Figure 4. Low-level easterly winds over Central Africa (south of the equator), originating from the Indian Ocean, change to the southwesterly winds over around 0-10°N on JJA season when the ITCZ migrates northward (Figure 4a, b) reaching the minimum in September. But over 5°S-5°N, the easterly winds seem to increase throughout the annual cycle which is consistent with the decrease of rainfall in this region during January to June (Figure 4c). We presume that the low-level atmospheric flow is dominated by his zonal component that acts to suppress local rainfall by decreasing the supplying of moisture into golf of Guinea coast from tropical Atlantic Ocean.

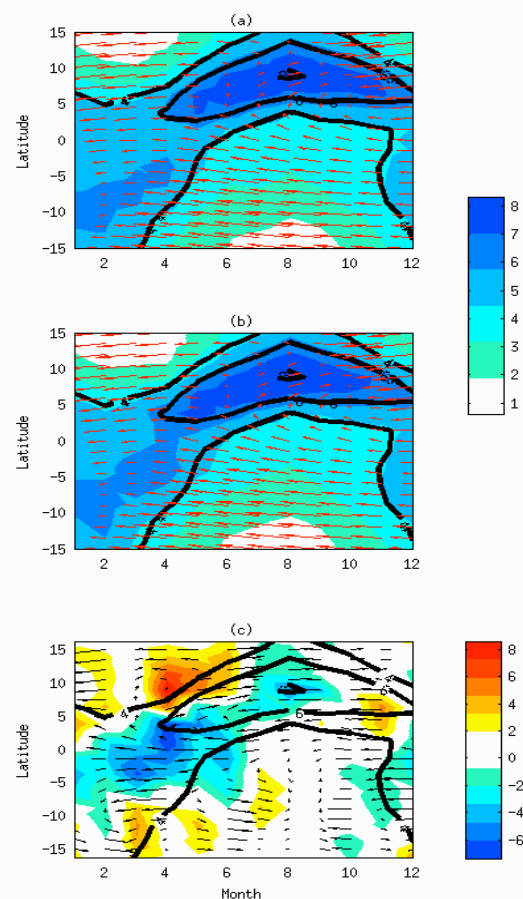


Figure 4 Annual cycle (averaged between 7° and 32°E) of rainfall from GPCP (shading, mm/d) and 925 -hPa wind vectors from ERA-Interim for warm (a), cold (b) years and their difference (c). Solid contours ( $\geq 4$ mm/d) indicate GPCP mean during normal years. Interval is 2mm/d.

This finding is consistent with Wang et al. (2009) who have found that zonal wind anomalies act as bridge linking the two ocean basins through the Walker circulation and oceanic processes.

#### 4. Conclusion

In this paper we find that the Central Africa rainfall is linked to index SST. In fact, during positive years of index SST, the Central Africa is associated to above normal conditions flood conditions for MAM and JJA seasons while the opposite leads to drought conditions in SON and DJF. Thus, the positive SSTs anomalies over surrounding tropical ocean basins would act indirectly by increasing the zonal component of low-level atmospheric circulation that suppress local rainfall by decreasing the additional supply of moisture over regions of pronounced inter-annual rainfall variances and thus, enhanced rainfall over ITCZ/SICZ.

## 5. Acknowledgments

ERA-Interim reanalysis data used in this paper were obtained from ECMWF at <http://ecmwf.int/>. NOAA OI v2 SSTs data are provided by the NOAA–CIRES Climate Diagnostics Center, Boulder, Colorado, from their web site (available online at <http://www.cdc.noaa.gov>). The research leading to these results received funding from EU FP7/2007–2013 under grant agreement no. 603521.

## 6. References

- Balas N, Nicholson SE, Klotter D. 2007. The relationship of rainfall variability in West Central Africa to sea-surface temperature fluctuations. *Int. J. Climatol.* **27**: 1335–1349.
- Dee D, Uppala S, Simmons A, Berrisford P, Poli P, Kobayashi S, Andrae U, Balmaseda M, Balsamo G, Bauer P (2011) The ERA-Interim reanalysis: configuration and performance of the data assimilation system. *Q.J.R. Meteorol. Soc* **137**(656): 553–597
- Huffman, G. J., R. F. Adler, D. T. Bolvin, and G. Gu, 2009: Improving the global precipitation record: GPCP version 2.2. *Geophys. Res. Lett.* **36** (17).
- McCoullum JR and Krajweski. 1999. Uncertainty of monthly rainfall estimates from rain gauge in the Global Precipitation Climatology Project. *Water Resource Res.* **35**:1695.
- Nicholson SE, Grist JP. 2003. The Seasonal Evolution of the Atmospheric circulation over West Africa and Equatorial Africa. *J.Clim.* **7**: 1013–1029.
- Reynolds, R. W., N. A. Rayner, T. M. Smith, D. C. Stokes, and W. Wang (2002), An improved in situ and satellite SST analysis for climate, *J.Clim.* **15**, 1609– 1625
- Wang C, F Kucharski, R. Barimalala and A Bracco. 2009. Teleconnections of tropical Atlantic to tropical Indian and Pacific Oceans: A review of recent findings. *Meteorologische Zeitschrift* (special issue). **18**, 445–454.

# Influence of the Subtropical Indian Ocean Dipole on the Agulhas Current

Mthetho Sovara<sup>1,3</sup>, Juliet Hermes<sup>2</sup>, and Chris Reason<sup>1</sup>

<sup>1</sup>Department of Oceanography, University of Cape Town, South Africa

<sup>2</sup>South African Earth Observation Network, Egagasini Node for Marine Offshore Systems, Foretrust Building, Cape Town

<sup>3</sup>Climate Studies, Modelling and Environmental Health Research Group, CSIR, Pretoria

## 1. INTRODUCTION

Numerous observational and model studies have successfully defined SIOD events Behera & Yamagata (2001) and linked them to weather patterns and climate (Reason, 2001, 2002). SIOD events are understood to be coupled atmospheric/ocean phenomena associated with austral summer rainfall patterns over coastal eastern South Africa, Mozambique, Zimbabwe and Botswana. Furthermore, SIOD events have been shown to have a significant influence over floods and droughts occurring in central and southern Africa, which previously could not be explained by El Nino and tropical Indian Ocean Dipole (IOD) events (Washington & Preston, 2006).

Recently, SIOD events have also been shown significantly influencing different types of southwestern Indian Ocean Tropical Cyclone trajectories (Ash & Matyas, 2012). A Positive (negative) phase of the SIOD phenomenon is characterized by positive (negative) SST anomalies in the south-western (north-eastern) region south of Madagascar and negative (positive) SST anomalies in the north-eastern (south-western) region of the south Indian Ocean off Australia (Behera & Yamagata, 2001). Investigations into the generation mechanisms of these events established that links with Antarctic Oscillation (AAO) and interannual variations of the intensity and position of the Mascarene High play a key role in the generation of SST anomalies (Suzuki *et al.*, 2004). Ekman transport accompanied with surface mixing process also play a role in the formation of the SST dipole (Hermes & Reason, 2004).

A similar forcing and evolution of dipole SST anomalies in has been found in the South Atlantic Ocean (Fauchereau *et al.* 2003). Thus far no studies have investigated the SIOD's influence on the Greater Agulhas Current System. This study examines influences of SIOD events on Agulhas Current dynamics using a regional ocean model forced with GFDL-CORE v.2b reanalysis winds and heat fluxes for the 1958-2007 to study the influence of SIOD events on Agulhas Current SST, SSH and the geostrophic velocity at the core of the current.

Ridderinkhof *et al.* (2010) showed that IOD events in the tropical Indian Ocean influence the South Equatorial Current (SEC) variability through modulations of the wind field anomalies over the tropical Indian Ocean making it conceivable that SIOD phenomena may play a similar role on the Agulhas Current.

## 2. MODEL, DATA, AND METHODS

The Regional Ocean Model (ROMS) is a widely used model with numerous applications in the southern African region (Penven *et al.* 2006b). It is a split-explicit, free-surface, ocean-only model discretized in coastline and terrain-following curvilinear co-ordinates which can be used to follow coastlines for irregular lateral boundaries which is important for coastal processes. The vertical resolution of the model is defined by 32 layers and regional bathymetry is derived from the high resolution dataset Global Earth Bathymetric Chart of the Oceans (GEBCO01) (Shepikin & McWilliams, 2005).

ROMS is used here as the ARC model configuration which is an eddy permitting implementation of ROMS constructed using ROMSTOOLS and has a resolution of  $1/4^\circ$ , with an Arakawa-C Mercator grid extending from  $29^\circ\text{W}$  to  $115^\circ\text{E}$  and from  $7^\circ\text{N}$  to  $48.25^\circ\text{S}$  (Loveday *et al.*, 2014). The ARC configuration used here enhances the grid spacing to a twelfth-degree between the region  $0^\circ$  to  $40^\circ\text{E}$  and  $45^\circ\text{S}$  to  $30^\circ\text{S}$ . The embedded  $1/12^\circ$  (about 2km) “child” nest spans the southern Agulhas Current, Cape Basin, and Southern Benguela.

Firstly, the dominant modes of SST variability in the SIO were explored through Empirical Orthogonal Function (EOF) analysis. Secondly, observational data along the Topex/Jason altimeter’s Track #020 (offshore Port Elizabeth) was used to characterize the Agulhas Current and its variability in a stream-coordinate approach which allows for better capturing of the intrinsic variability of the Agulhas Current at the annual time-scale (Krug & Tournadre, 2012). Wavelet transforms were used to investigate the temporal variability of SIOD index which is computed from the SST anomaly difference between the south-western ( $55^\circ\text{E}$ - $65^\circ\text{E}$ ,  $37^\circ\text{S}$ - $27^\circ\text{S}$ ) and north-eastern ( $90^\circ\text{E}$ - $100^\circ\text{E}$ ,  $28^\circ\text{S}$ - $18^\circ\text{S}$ ) subtropical regions of the SIO. The model simulated SST index was compared to the observational SST anomalies from Behera & Yamagata (2001).

Thirdly, composite map analysis was then used to identify consistent spatial patterns in the model data. Austral summer (JFM) SST & SSH averages during SIOD event years were computed and used to highlight the main features of the events.

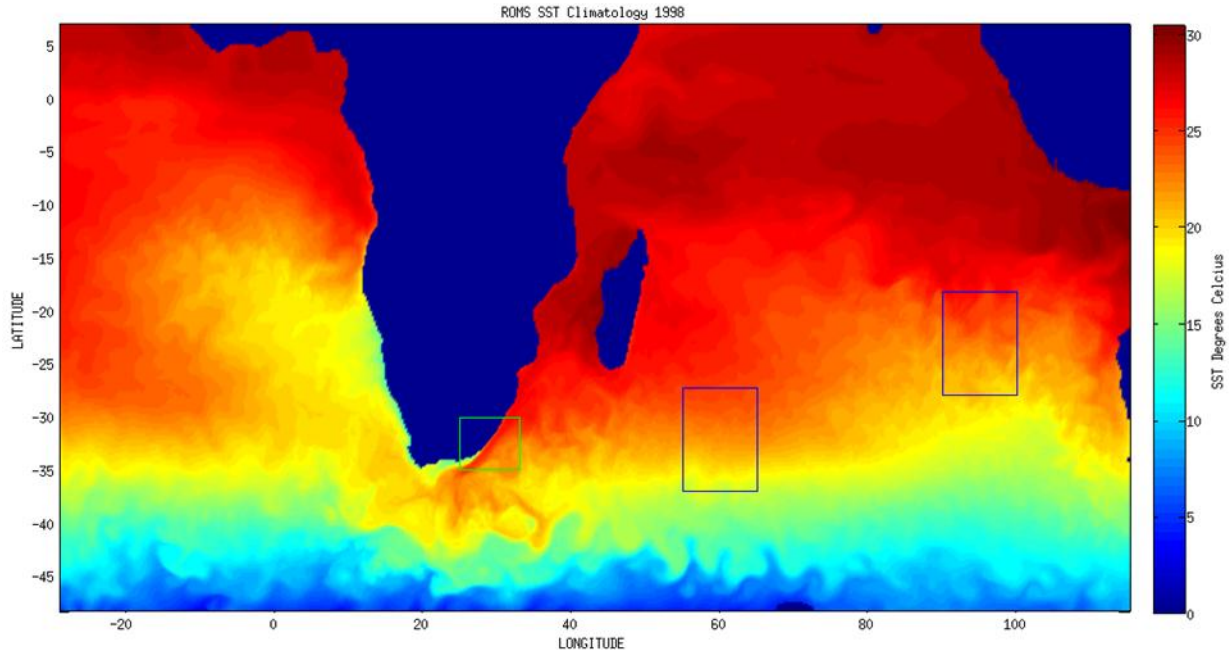


Figure 1: The ROMS domain is shown with the climatological SST map of the SIO with the SIOD boundaries where indices have computed. The blue boxes represent the western subtropical pole ( $55^{\circ}\text{E}$ - $65^{\circ}\text{E}$ ,  $37^{\circ}\text{S}$ - $27^{\circ}\text{S}$ ) and the eastern subtropical pole ( $90^{\circ}\text{E}$ - $100^{\circ}\text{E}$ ,  $28^{\circ}\text{S}$ - $18^{\circ}\text{S}$ ) respectively. The green box ( $25^{\circ}\text{E}$ - $35^{\circ}\text{E}$ ,  $30^{\circ}\text{S}$ - $35^{\circ}\text{S}$ ) represents boundaries of the Agulhas Current region where anomalous SSH and SST anomalies have been assessed for a correlation with the SIOD phenomenon.

### 3. RESULTS AND DISCUSSION

Wavelet analysis results suggest that the north-eastern Indian Ocean (NE IO) (off Australia), SST variability has periodicities in both the high and low frequency parts of the power spectrum density. In the high frequency, NE IO SST demonstrated periodicities in the order 15-24 months particularly during the years 1965-1975 and 1995-2000. Low frequency interannual variability was observed in the order of 78 months particularly during the years 1970-1985. These findings suggest a semi-annual and inter-annual variability in NE IO SST variability during the period 1958-2007.

For the SW IO region (south of Madagascar) SST exhibited variability mainly in the high spectral frequency in the order of 4-15 months especially during the years 1060-1965, 1993-1995 & 1995-2000. These findings also suggest a semi-annual to annual periodicity in the region. The model SIOD index exhibited both high frequency semi-annual to annual cycles in the order of 4-12 & 18 months and low frequency inter-annual variability was observed in the order of 78 months. Similar results were obtained in an identical assessment of the observed SIOD index. SST variability in the regions may well be driven by the AAO and Mascarene High (MH).

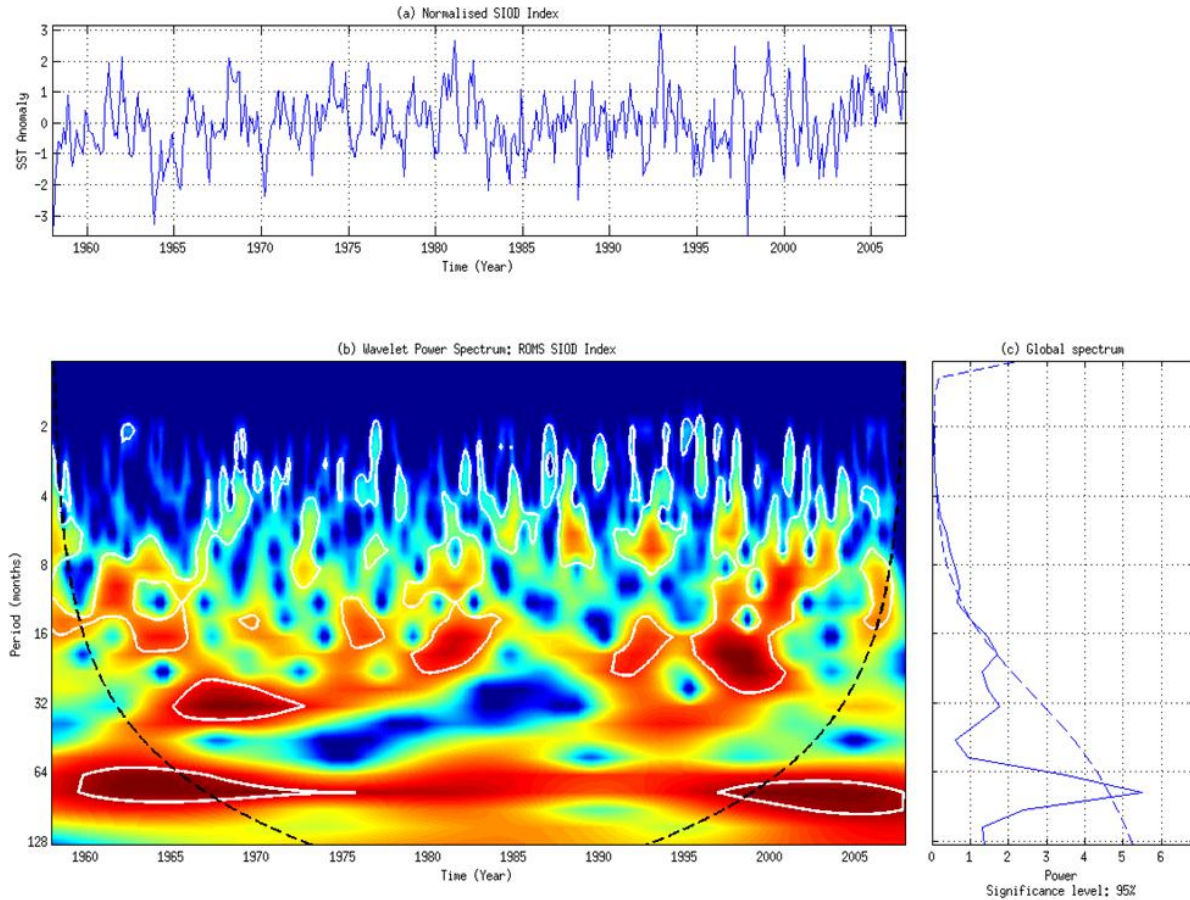


Figure 2: (a) The normalized time-series of ROMS SIOD computed from SST anomaly difference between western ( $55^{\circ}\text{E}$ - $65^{\circ}\text{E}$ ,  $37^{\circ}\text{S}$ - $37^{\circ}\text{S}$ ) and eastern ( $90^{\circ}\text{E}$ - $100^{\circ}\text{E}$ ,  $28^{\circ}\text{S}$ - $18^{\circ}\text{S}$ ) subtropical Indian Ocean.

EOF results of the whole period showed values of a single polarity dominating the analysis domain of the leading mode explaining 13.66% of the total variance for the period 1958-2007. The SIOD pattern emerged as the second EOF mode explaining 8.93% of the total variance, oriented in the northeast-southwest direction in the SIO in agreement with Behera & Yamagata (2001) and so was the second Principal Component (PC2). EOF analysis of only the austral summer months of January, February & March (JFM) for the same period yielded the SIOD phenomena as the leading mode of variability explaining 20.84% of the total variance. The second EOF mode explained 14.13% of the total variance and is a less intensified SIOD pattern with identical characteristics as the leading mode.

The influence of SIOD phenomena on Agulhas Current SST & SSH variability has been examined with the primary objective being to ascertain whether these phenomena have an impact on the Greater Agulhas Current System.

Austral summer composite map results suggest that positive SIOD event years are characterized by a slight anomalous warming of Agulhas Current SST in the regions of approximately 27°S to 40°S. The anomalous warming appears to be associated with the warm pole of the positive SIOD phenomena located south of Madagascar. The anomalous SST appears to be joining into the Agulhas Current through the East Madagascar Current and the recirculation of the SW IO anticyclone. Downstream the Agulhas Current a warming trend in SST was also observed. Conversely, a cooling trend in SST was also observed in certain parts of the Agulhas Retroflexion and Agulhas Return Current regions. These findings suggest both warming and cooling trends in different regions of the Agulhas Current however this anomalous behaviour is not pronounced

Comparatively, during negative SIOD years Agulhas Current SST were observed to be associated with the anomalously warm SST of the warm pole of the negative SIOD event located off Australia. This anomalous SST was observed to be linked to the Agulhas Current through the SEC and the Mozambique Channel eddies. Composite difference maps of Agulhas Current SST and SSH variability during the austral summer was also examined, composite negative event years were subtracted from composite positive event years and the output was then examined for anomalous SST and SSH behaviour in Agulhas Current. The composite difference maps produced similar results. It then becomes evident that the anomalous Agulhas Current SST variability during SIOD phenomena may not be pronounced or significant.

During positive SIOD event years positive SSH anomalies were observed to dominate the region around the east of Madagascar, the East Madagascar Current and the Mozambique Channel. These positive SSH anomalies in the SW IO are evidence of an intensified Indian Ocean anticyclonic gyre during positive SIOD years. Conversely, negative SIOD event years were observed to be characterized by negative SSH anomalies in the above mentioned regions of the subtropical Indian Ocean and this can be related to a relaxed Indian Ocean anticyclonic gyre during negative SIOD phenomena. Intensification and relaxation of the Indian Ocean anticyclonic gyre could drive SSH anomalies in the Agulhas Current. However, the composite difference map suggests that SSH anomalies in the Agulhas Current associated with SIOD events are not pronounced. This is shown by the mean SSH contours in the Agulhas Current region which did not exceed one standard deviation.

Lastly, the satellite derived geostrophic velocity at the core of the Agulhas Current was plotted against the model SIOD index for the period 1993-2007. Visual inspection of the overlaid indices shows how positive anomalies in Agulhas speed appear to be related to positive SIOD events and negative anomalies in the Agulhas speed appear to be related to negative SIOD events. However there were years observed when negative Agulhas speeds are related to positive SIOD events and vice-versa. This difference in the timescale suggests that the dynamics of the two systems could be driven by different forcing mechanisms. The 0-12 month lagged correlation confirms no relationship between the geostrophic velocity at the core of the Agulhas Current and the model SIOD index  $r\text{-coefficient} = 0.26$  ( $p = 0.05$ ).

This result lends credence to the fact that the Agulhas Current is primarily driven by positive wind stress curl over the subtropical Indian Ocean and the main controls on retroflection and leakage are the westerlies. SIOD events do not profoundly influence Agulhas Current speeds, SST & SSH variability. As a reference for future work an analysis of the dynamical ocean circulation would require a closer look into deeper hydrographic and circulation fields. Future research can focus also on the influence of the SIOD phenomena on the transport values through a defined vertical section of the Agulhas Current through observational (currently very limited) and model studies. Investigating the relationship between transport values from moored data across the Mozambique Channel and possibly East Madagascar to shifts in SIOD and IOD would also help to understand the influence of the SIOD on the variability in the Greater Agulhas Current system.

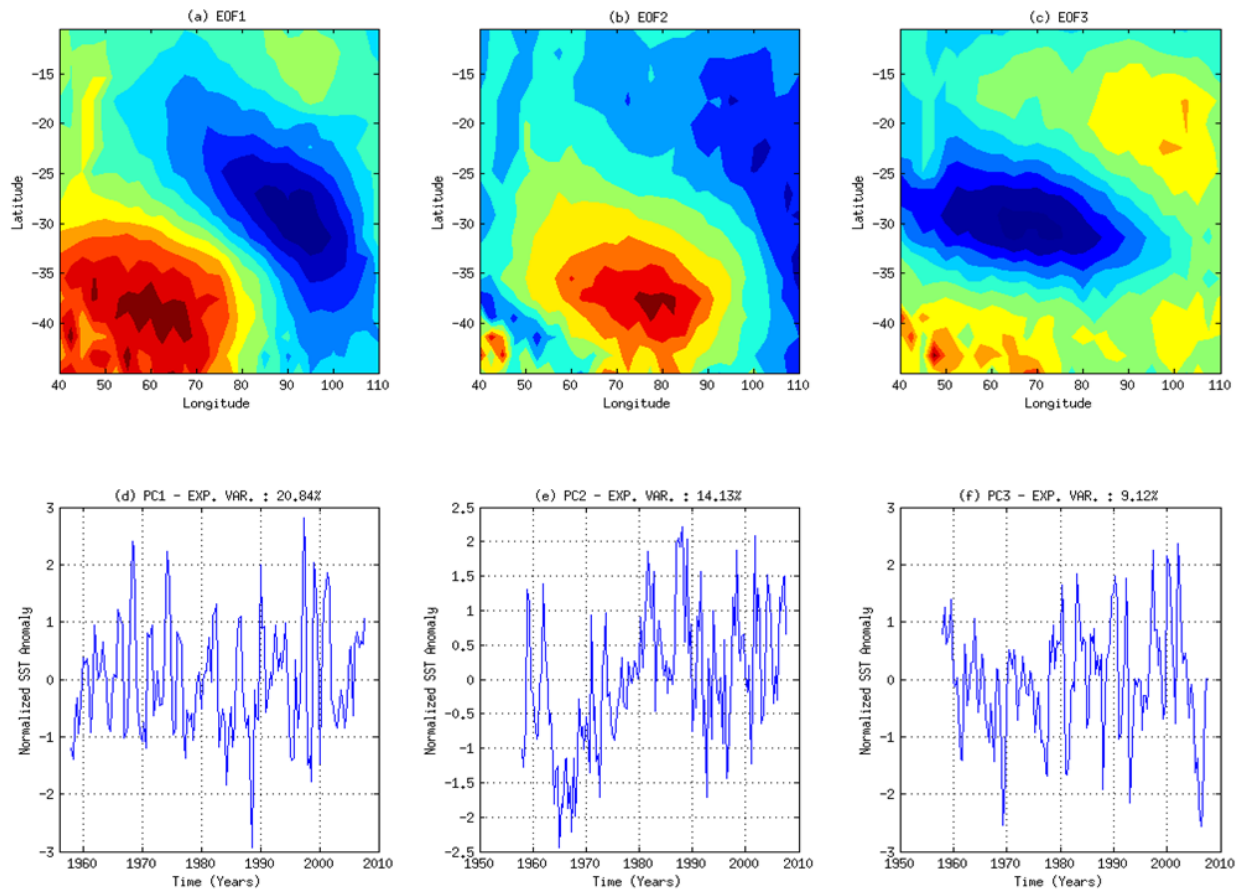


Figure 3: EOF analysis applied on ROMS monthly SST anomalies for only the austral summer (JFM) months. EOF spatial pattern (a, b and c) and time series (d, e and f) for the EOF modes of variability for the period 1958 to 2007 in the subtropical Indian Ocean ( $10^{\circ}\text{S}$ - $45^{\circ}\text{S}$ ,  $40^{\circ}\text{E}$ - $110^{\circ}\text{E}$ ).

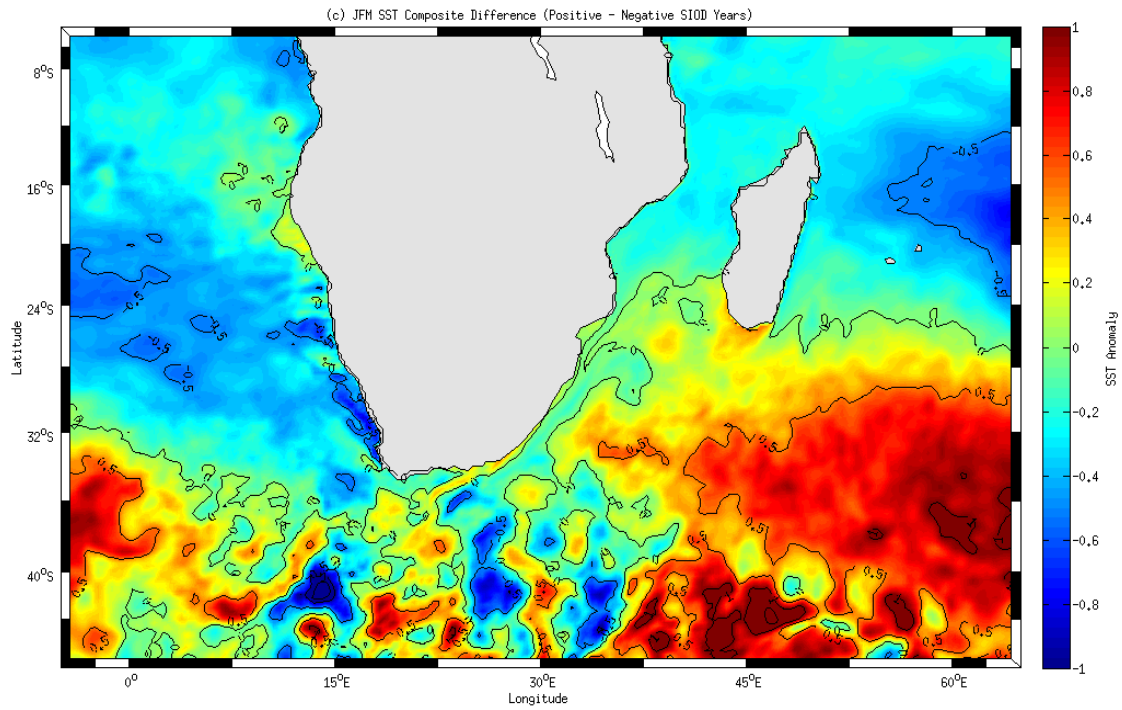


Figure 4: A zoom of the model JFM SIOD SST composite difference with mean SST contours ( $^{\circ}\text{C}$ ).

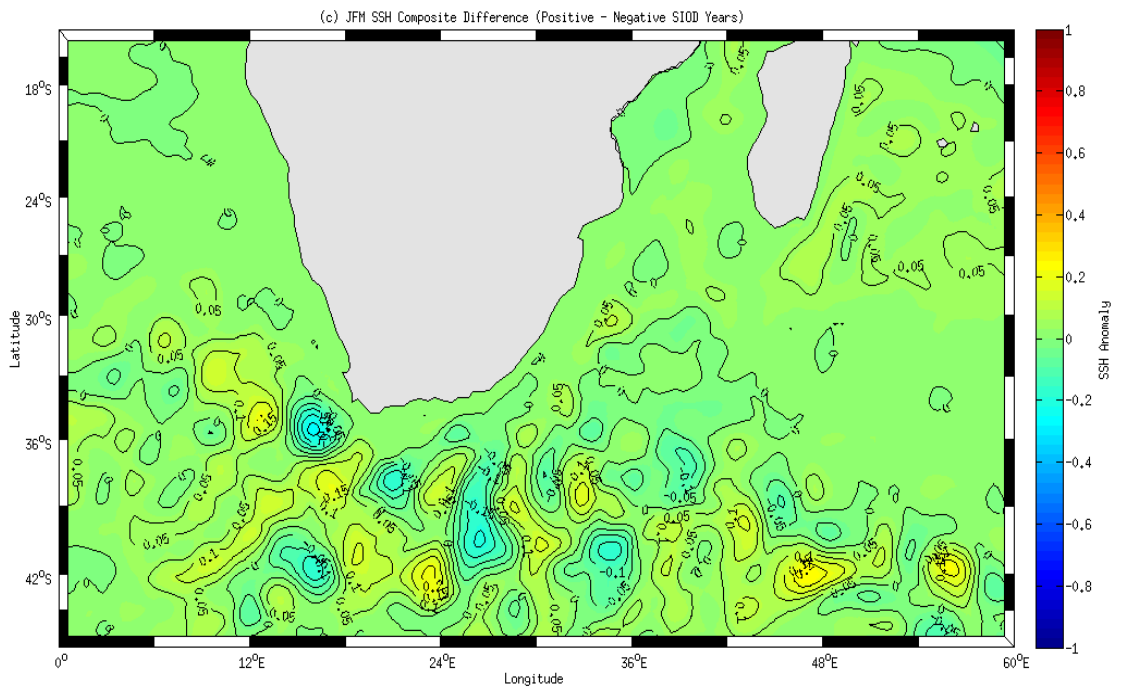


Figure 5: A zoom of the model JFM SIOD SSH composite difference with mean SSH contours (m).

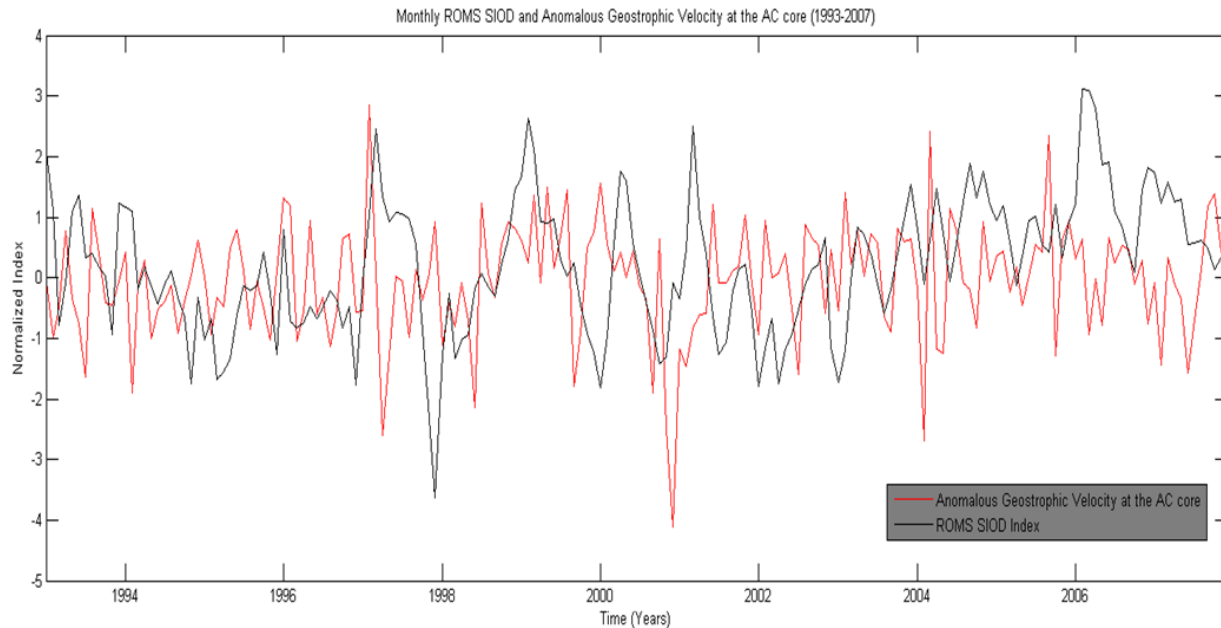


Figure 6: Anomalous ROMS SIOD index (black) and the anomalous geostrophic velocity at the core of the Agulhas Current (red) both from 1993-2007.

#### 4. References

Ash, K. D. & Matyas, C. J., 2012: The influences of ENSO and the subtropical India Ocean tropical cyclone trajectories in the southwestern Indian Ocean. *International Journal of Climatology*, [Online], 32, 41–56.

Behera, S. K. & Yamagata, T., 2001: Subtropical SST dipole events in the southern Indian Ocean. *Geophysical Research Letters*. 28, 327–330.

Fauchereau, N., Tzaska, S., Richard, Y., Roucou, P., & Camberlin, P., 2003: Sea-surface temperature co-variability in the southern Atlantic and Indian Oceans and its connections with the atmospheric circulation in the southern hemisphere. *International Journal of Climatology*, 23, 663–677.

Hermes, J.C. & Reason, C. J. C., 2005: Ocean model diagnosis of interannual coevolving SST variability in the southern Indian and south Atlantic Oceans. *Journal of Climate*, 18, 2864–2882.

Krug, M.J. & Tournadre, J., 2012: Satellite observations of an annual cycle in the Agulhas Current. *Geophysical Research Letters*, 39, L15607.

Morioka, Y., Tozuka, T., Masson, S., Terray P., Lou, J., & Yamagata, T., 2012: Subtropical Dipole Modes Simulated in a Coupled General Circulation Model. *Journal of Climate*, 25:1 140-155.

Penven, P., Lutjeharms, J. R. E., & Florenchie, P., 2006b: Madagascar: A pacemaker for the Agulhas Current system. *Geophysical Research Letters*, 33, L17 609.

Reason, C.J.C., 2001: Subtropical Indian Ocean SST dipole events and southern African rainfall. *Geophysical Research Letters*, 28, 11, 2225-2227.

Reason, C. J. C., and M. Rouault, ENSO-like decadal variability and South African rainfall, *Geophysical Research Letters*., 29(13), doi:10.1029/2002GL014663, 2002.

Ridderinkhof, H., van der Werf, P.M., Ullgren, J.E., van Aken, H.M., van Leeuwen, P.J., de Ruitjer, W.P.M., 2010: Seasonal and interannual variability in the Mozambique Channel from moored current observations. *Journal of Geophysical Research*, 115, C06010.

Shchepetkin, A. & McWilliams, J., 2005: The regional oceanic modeling system (ROMS): A split-explicit, free-surface, topography-following-coordinate oceanic model. *Ocean Modelling*, 9 (4), 347–404.

Suzuki, R., Behera, S. K., Iizuka, S., & Yamagata, T., 2004: Indian Ocean subtropical dipole simulated using a coupled general circulation model. *Journal of Geophysical Research*, 109, C09001.

Washington, R., & Preston, A., 2006: Extreme wet years over southern Africa: Role of Indian Ocean Sea Surface Temperatures. *Journal of Geophysical Research* 111: D15104, 1029/2005JD006724

# Separating local- and synoptic-scale variability in African rainfall

Piotr Wolski\*, Chris Jack, Mark Tadross, Lisa Coop, Bruce Hewitson  
Climate System Analysis Group, University of Cape Town, Private Bag X3, 7701 Rondebosch, South Africa  
wolski@csag.uct.ac.za

In this paper, we present a new method for separating rainfall variability due to synoptic-scale synoptic disturbances from other sources of variance. This is achieved by comparing Monte Carlo simulations of rainfall, stochastically conditioned on the observed seasonal progression of synoptic states, with similar simulations conditioned on the climatological progression of synoptic states, i.e. where the interannual variability of synoptic states is minimized. Preliminary results for the African continent indicate spatial and seasonal differences in the relative contribution of synoptic- and locally-forced variability to measures of the total, frequency and intensity of rainfall. The influence of ENSO on the annual progression of synoptic states is demonstrated for different regions and local-scale sources of variability are shown to contribute 20-90% of total variability in rainfall frequency and rainfall totals, and are responsible for >90% of variability in rainfall intensity.

*Keywords:* rainfall variability, limits to predictability, SOM

## 1. Introduction

Rainfall at a location is driven by both the synoptic-scale circulation responsible for the supply of precipitable water and generation of favourable meso-scale conditions, as well as local-scale processes such as recycling of moisture from the land/sea surface and orographic forcing. This scale separation is enforced within the global climate model paradigm, where synoptic-scale processes are explicitly simulated, while local-scale, sub-grid processes are not resolved but parameterized via empirical relationships. Local-scale sources of variability may be explicitly addressed within statistical downscaling procedures as a stochastic function (probability distribution function, or Markov chain transitional probability) conditioned on the atmospheric circulation pattern. Such an approach can successfully capture variability arising from local scales, separately for each circulation pattern/synoptic state. It is, therefore, only applicable at time scales comparable to the persistence time of the synoptic-scale atmospheric circulation features, i.e. at daily to multi-day periods. At longer time scales, however, the influence of small-scale processes on overall variability cannot be resolved easily.

Quantification of local-scale variability is extremely important, as it constitutes a potential limit to rainfall predictability, even under hypothetical conditions of perfect predictability of synoptic states, at both seasonal and annual time scales, as well as contributes to the irreducible uncertainty in longer-term rainfall projections.

In this paper, we separate rainfall variability arising at local- from that arising at synoptic scales using a method that defines the “climatological” progression of synoptic states, which expresses hypothetical conditions where there is no interannual variability in synoptic-scale circulations.

## 2. Data and methods

### 2.1. Observed rainfall data

Daily rainfall data for 1704 rain gauge stations on the African continent were obtained from a database created at Climate System Analysis Group, University of Cape Town. The database contains data from a number of sources, including NHMS's and GHCN. These data were screened for duplicates and unrealistic values. Selected stations are a subset of the database selected by the condition that station record should contain at least 10 years of data within the period of 1979-2012 and that there is at least 10 rainfall events per year, dictated by the need to have an adequate number of rain events to develop robust relationships between local rainfall and a range of synoptic states.

### 2.2. Relationship between local rainfall and synoptic scale atmospheric circulation pattern

The relationship between local rainfall and synoptic-scale circulation patterns was formalized using methods built into the statistical downscaling procedure developed by Hewitson & Crane (2006).

For each analysed location (raingauge) a number of relatively distinct meso-scale synoptic states are identified through clustering of mean daily fields of wind (at 10m and at 700mb), pressure (at sea level), relative humidity (at 850mb) and temperature (at 2 m), observed over that location in the NCEP II reanalysis product (see below). The clustering is done using the SOM method (Kohonen, 2001). A probability distribution function of the local daily rainfall is then determined for each cluster (or SOM node) from rainfall values observed during days when synoptic conditions corresponding to that node have occurred.

### 2.3. Assessing total inter-annual rainfall variability

In our analysis a 9 by 11 SOM was trained on the 1979-2012 NCEP 2.0 re-analysis product, and the same dataset was then re-mapped onto the SOM and used as a basis for generating output time series of daily rainfall. Sampling from the SOM node-specific rainfall PDFs was done using a Monte-Carlo approach, i.e. we generated 1000 daily time series of rainfall for 1979-2012 period for each analysed location. For each analysed station, and each member of the Monte-Carlo ensemble, three indices were derived representing rainfall frequency, rainfall intensity and total rainfall: number of rain days per year (with rain >0.2mm/day), median daily rainfall, and annual rainfall total. From their annual values, we calculated inter-annual variances. The mean ensemble value of that variance was taken as a measure of rainfall variability for each of the three rainfall indices.

### 2.4. Assessing interannual rainfall variability arising at local scales

In order to determine the influence of local-scale processes on interannual rainfall variability (i.e. removing synoptic-forced variability), we used a procedure analogous to the one described above, using a climatological progression of synoptic states instead of the observed (NCEP 2.0 reanalysis) one for each year. This progression was determined separately for each location over the African continent in the following way:

- We determined the observed frequency of synoptic states (SOM nodes) for a 31-day period centered on each day of year, for each year, and for the entire analysed period (32 years). We treated these frequencies as 'clouds' in 2-dimensional space defined by SOM nodes.
- For each 31-day 'cloud' we defined its Euclidean centroid. Although SOM nodes form a discrete space, we allowed the centroids to take continuous coordinates in the SOM space.

- The centroids allow for plotting the annual trajectory of synoptic states in individual years. The centroids obtained for the entire 32-year period plot roughly in the middle of the set of individual years' trajectories (Figure 1). We considered the mean 32-year trajectory to represent the climatological progression of SOM states, with deviations of individual years' centroids representing the effects of interannual variability in synoptics around that climatological progression. This assertion is confirmed by the fact that mean trajectories for ENSO-positive, -negative and -neutral periods are well separated, and the ENSO-neutral trajectory is similar to the climatological one (Figure 1).

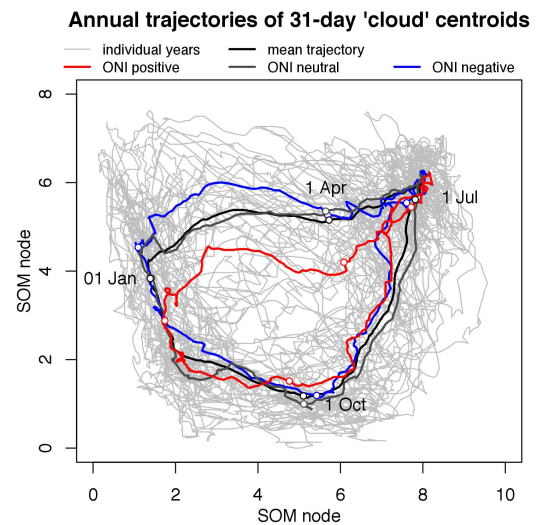


Figure 1 Trajectories of centroids of 31-day 'clouds' in SOM space for 21.5°S 17.0°E. Influence of ENSO on the position of trajectory is illustrated through separating years based on classification of Oceanic Nino Index (ONI > 0.5 - El Nino, < -0.5 La Nina).

- To determine the frequency of likely synoptic states associated with a given point on the climatological trajectory, we firstly clustered all 32 annual 'clouds' into 10 classes or patterns of SOM node frequencies. The clustering was done again using SOMs, using a 1 x 10 SOM. We selected the frequency pattern for which mean distance between source clouds' centroids and the climatological centroid was minimal. This procedure was done for each day of the year for each location.
- Subsequently, we generated a 32-year time series of synoptic states by random sampling from the selected frequency patterns. The result is a 32-year progression of synoptic states that maintains minimal level of interannual variability, and whose progression is representative of the climatological

progression of the original data. In this procedure, we do not explicitly account for the structure and pattern of day-to-day transitions between synoptic states, but instead represent the annual progression of the 'cloud' of synoptic states. Since our subsequent analyses consider only seasonal, annual and longer time scales, this is not expected to be problematic.

- Finally, the derived climatological progression of synoptic states was used in the Monte Carlo procedure to generate 1000 time series of daily rainfall.

### 2.5. Role of local-scale processes in overall rainfall variability

While the results of the first set of Monte Carlo simulations capture variability arising from both local-scale and synoptic-scale processes, the second, climatological set, reflects only the former. The fraction of total variance explained by the local-scale processes ( $V_{LS}$ ) can thus be expressed as a ratio of the mean variance in the ensemble based on climatological progression of synoptic states, to that in the ensemble based on observed data. The  $V_{LS}$  were determined separately for indices expressing rainfall frequency, intensity and totals, on a seasonal and annual basis.

Maps of spatial distribution of  $V_{LS}$  were calculated using ordinary kriging interpolation conducted only for areas with at least 5 stations within the distance of 3 geographical degrees. Kriging was based on a linear variogram with a single set of parameters derived from all stations within the analysed domain.

## 3. Results and discussion

Maps of  $V_{LS}$  calculated on an annual basis (Figure 2) can be interpreted in terms of both the role of local scale variability ( $V_{LS}$ ) or the role of synoptic scale variability ( $1-V_{LS}$ ), with  $V_{LS}$  equal 1 where there is no influence of synoptic scale variability on the particular rainfall index. The SOM space (node) trajectories for particular locations (noted in Figure 2) are presented in Figure 3.

In terms of rainfall frequency and total annual rainfall, the role of local scale variability in overall rainfall variability is relatively large – the local scale variance accounts for 20-90% of total variance, leaving 10-80% of variance to be explained by interannual variability in synoptic-scale systems. The spatial pattern of  $V_{LS}$  is broadly consistent with the understanding of the influence of ENSO on African rainfall. Namely, there is a low contribution of local-scale variability in the central southern and eastern equatorial part of the continent – the areas dominated by ENSO influence. Additionally the

southern and eastern African coasts indicate a relatively high contribution of local-scale forcing (thus low contribution of synoptic-scale) variability to the total rainfall variability at the annual timescale. This may be linked to the year-round availability of moisture from the warm Agulhas current and nearby Indian Ocean, which is capable of producing rainfall with little influence from synoptic-scale atmospheric dynamics. However, the role of synoptic-scale variability is stronger in the winter rainfall zone of South Africa, where rainfall is influenced by the strength and frequency of mid-latitude cyclones. Similarly the relative contribution of synoptic-scale atmospheric dynamics (although not necessarily ENSO-related) and meso-scale moisture transport dominates in the western and northern coasts of Africa.

Variability in rainfall intensity appears to be dominated by local-scale processes throughout the continent at the annual timescale. This is consistent with the understanding of total rainfall variability being driven primarily by differences in frequency of events rather than event intensity. It might, however, be indicative of relatively low sensitivity of the SOM clustering to variables affecting rainfall intensity.

Figure 3, which shows the trajectories in SOM node-space for selected locations, under ENSO positive, negative and neutral conditions, indicates clear differences between locations. Those in the north and south (A, D, F and I) have 'linear' and more constrained trajectories, which suggests that they are influenced by a wide variety of synoptic states all year round, as might be typical of areas influenced by mid-latitude systems. Whereas tropical and sub-tropical areas indicate 'circular' trajectories which are more likely to be found in particular SOM-node regions at a particular time of year. Furthermore point K illustrates a different 'figure of eight' structure, which is typical of a bimodal rainfall system (where similar synoptic states are encountered twice a year). Additionally the ENSO influence on synoptic states clearly varies with time of year and ENSO state.

## 4. Conclusions

The method presented here allows for separating rainfall variability arising through local-scale processes from that arising through regional and global circulation changes. The role of local-scale variability varies in space, and in time (not shown here) and between various aspects of rainfall (total, frequency and intensity). The differences in space appear to be broadly consistent with the understanding of the influence of synoptic scale climate system dynamics (such as ENSO) on rainfall, but also reveal other, non-ENSO related

effects. Overall, the local-scale sources contribute 20-90% of variability in rainfall frequency and rainfall totals, and are responsible for >90% of variability in rainfall intensity. These results are informative in the context of limits of rainfall predictability and uncertainty in determining the mean climate, and future climate change.

## 5. References

- Hewitson, B.C., Crane, R.G., 2006. Consensus between GCM climate change projections with empirical downscaling: precipitation downscaling over South Africa. *Int. J. Climatol.* **26**, 1315–1337.
- Kohonen, T., Schroeder, M.R., Huang, T.S., 2001. *Self-Organizing Maps*. Springer-Verlag New York.

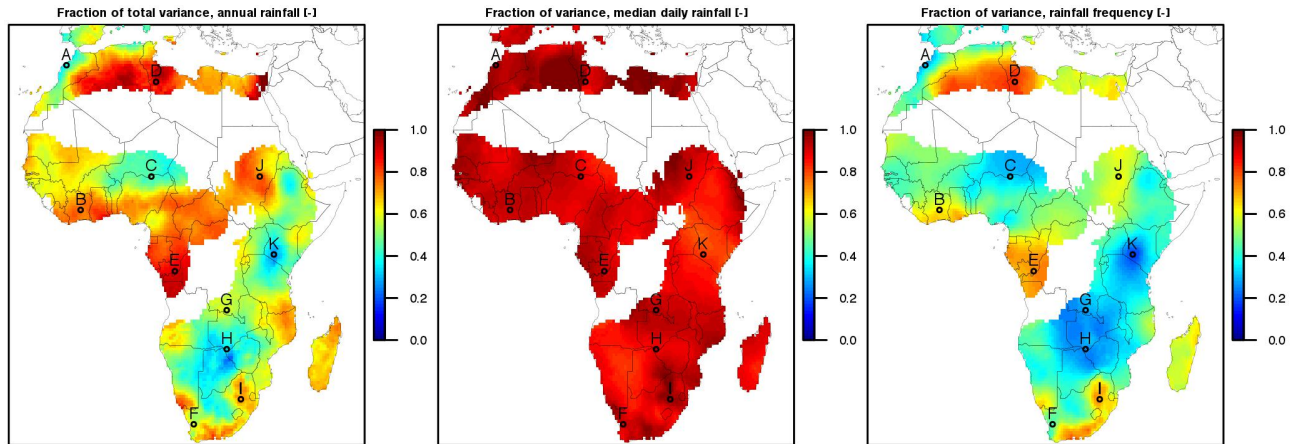


Figure 2. Fraction of variance ( $V_{LS}$ ) in annual rainfall indices explained by local scale variability

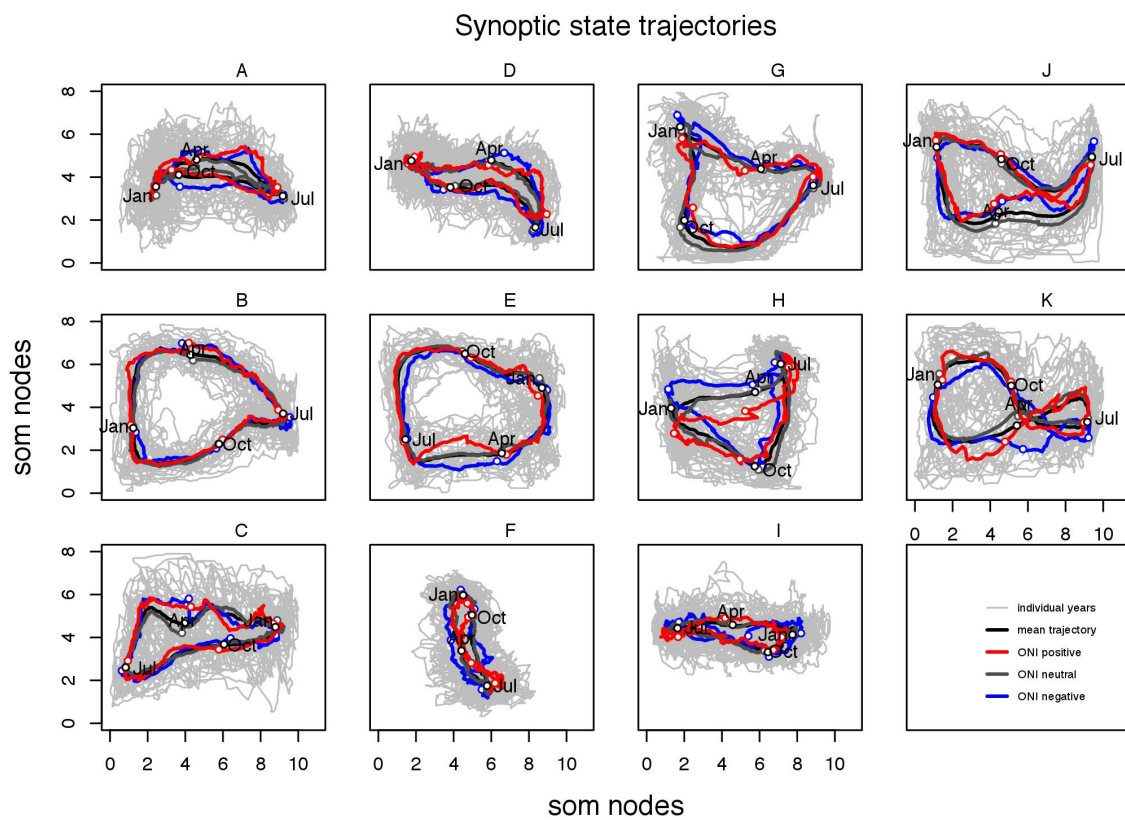


Figure 3. Trajectories through SOM space for selected locations (plotted in Figure 2)

# PREDICTABILITY OF DIFFERENT RAINFALL THRESHOLD VALUES FOR AUSTRAL SUMMER SEASONS OVER SOUTH AFRICA

Steven Phakula

South African Weather Service, Pretoria, South Africa, [steven.phakula@weathersa.co.za](mailto:steven.phakula@weathersa.co.za)

## Abstract

In this study the forecast skill of the 850hPa geopotential heights of ECHAM4.5 atmospheric general circulation model, both coupled to an ocean model and forced with prescribed sea-surface temperature anomalies (uncoupled), in predicting the low and high number of rainfall days exceeding different threshold values for the December-January-February seasons over South Africa is assessed. Using canonical correlation analysis as statistical downscaling tool the forecast skill of both the coupled and uncoupled models are tested through retro-actively generated area-averaged ROC scores. Both approaches have skill in predicting the low and high number of rainfall days exceeding different threshold values for the December-January-February seasons over South Africa. The skill of both models in predicting the low (high) number of rainfall days is decreasing (increasing) with higher rainfall threshold values.

**Keywords:** Rainfall threshold values, Retro-active validation, Forecast skill, ROC scores.

## Introduction

Southern Africa is a region of significant rainfall variability on a range of temporal and spacial scales and is prone to extreme droughts and floods events (Usman & Reason, 2004). For example, the devastating floods in northeast South Africa and southern Mozambique during February/March 2000 and severe droughts of 1991/92, 2002/03 and 2003/04 over northern South Africa and surrounding areas (Cook *et al.*, 2004). Most of African countries depend significantly on rain fed agriculture, which is highly vulnerable to the amount and distribution of rainfall (Kijazi & Reason, 2005). A small difference in the amounts and timing of rains at a

region may determine the success or failure of agricultural crops (Kijazi & Reason, 2011). The frequency and intensity distribution of rainfall have effects on dry and wet spells. The temporal distribution and nature of wet and dry spells are important to agriculture in South Africa. According to Usman and Reason (2004) the occurrence of extreme dry (wet) conditions over southern Africa during the austral summer have been associated with high dry spell frequency (wet spell frequency). The purpose of this research is to assess the skill of the ECHAM4.5 AGCM in predicting the low and high number of rainfall days exceeding different threshold values for the austral summer seasons over South Africa.

## Data and Methodology

The observed daily station rainfall data over South Africa obtained from the South African Weather Service (SAWS) are used to develop the indices of the number of rainfall days exceeding the threshold values of 5mm, 10mm, 15mm, 20mm, 25mm, 30mm, 35mm, 40mm, 45mm and 50mm for December-January-February (DJF) seasons over South Africa from 1982-2009. The rainfall stations considered in this study are shown in Figure 1. The large-scale 850hPa geopotential heights hindcast outputs for DJF seasons at 2.8 degree resolution for both coupled to an ocean model and forced with prescribed sea-surface temperature anomalies (uncoupled) ECHAM4.5 atmospheric General Circulation Model (GCM) are used. Both models are run at SAWS. The ECHAM4.5 was developed at the International Research Institute for Climate and Society (IRI). Using the Climate Predictability Tool (CPT) developed at the IRI the hindcast outputs of both the coupled and uncoupled GCMs are statistically recalibrated and downscaled to the number of days exceeding different rainfall threshold values over South Africa using the

Model Output Statistics (MOS) technique. The CPT apply cross-validation and retro-active processes to estimate the models forecast skill. The cross-validation is performed to determine the relation between the forecasts and the observed at each location over the domain of interest. However cross-validation process has a tendency of overestimating forecast skill (Landman *et al.*, 2001). On the other hand, retro-active forecast validation best indicate the model performance and give unbiased skill levels (Landman *et al.*, 2001). The forecast skill levels of both the coupled and uncoupled models are tested using area-averaged ROC scores from the canonical correlation analysis (CCA), retro-active option of the CPT. The ROC can be quantified by calculating the area beneath the ROC curve. The larger the area, the better the model skill. If the area is less than 0.5 (below the diagonal line of ROC diagram) of the whole (unit area), then the model is less skillful than a random or constant forecast. ROC is used because this score has the attribute of discrimination, so a high ROC score ( $>0.5$ ) indicates the models' ability to discriminate among the various thresholds.

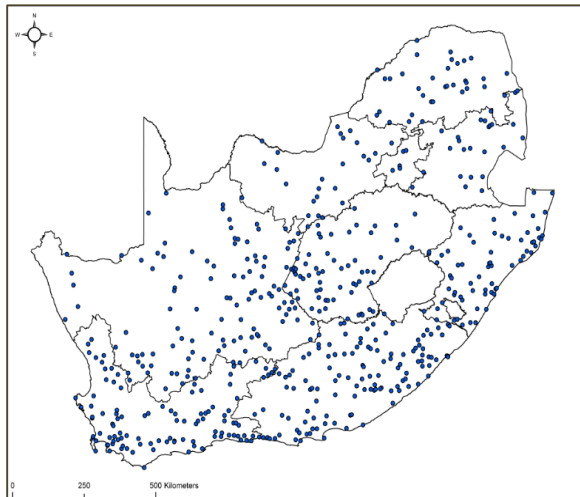


Figure 1. Rainfall stations network over South Africa.

## Results and Discussion

The uncoupled 850hPa geopotential heights of the ECHAM4.5 AGCM have skill in predicting the low and high number of rainfall days exceeding different threshold values for DJF seasons over

South Africa. The skill of predicting the low number of rainfall days exceeding the different threshold values is increasing with the threshold values. On the other hand, the skill of predicting the high number of rainfall days exceeding different threshold values is decreasing with higher threshold values. The skill of predicting the high number of rainfall days is limit to the thresholds of 1mm, 10mm, 15mm, 20mm, 25mm and 30mm, with skill scores greater than 0.5 (not shown). It is clearly visible from the ROC diagrams in Figure 2 that the skill of predicting the low (high) number of rainfall days exceeding 30mm is higher (lower) than that of days exceeding 10mm threshold.

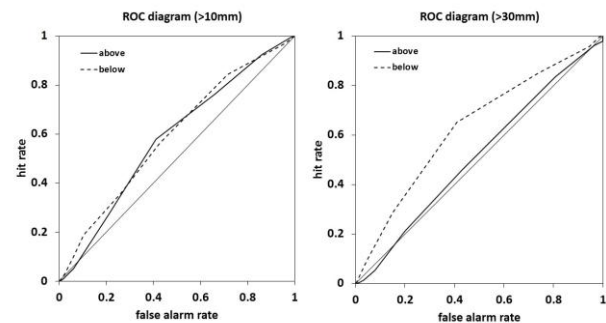


Figure 2. The ROC diagrams of the uncoupled 850hPa geopotential heights ECHAM4.5 AGCM in predicting the low (dash line) and high (thick line) number of rainfall days exceeding 10mm and 30mm threshold values for the DJF seasons over South Africa for 1982-2008.

The 850hPa geopotential heights of coupled ECHAM4.5 AGCM have skill in predicting the low and high number of rainfall days exceeding different threshold values for DJF seasons over South Africa. The skill of coupled model in predicting the low (high) number of rainfall exceeding different threshold values is increasing (decreasing) with higher rainfall threshold values for DJF seasons over South Africa. The ROC diagrams in Figure 3 shows that the skill of predicting the low (high) number of rainfall days exceeding 30mm is higher (lower) than that of days exceeding 10mm threshold. The skill of the coupled model in predicting the high number of rainfall days is also limit to the thresholds of 1mm, 10mm, 15mm, 20mm, 25mm and 30mm, with skill scores greater than 0.5 (not shown).

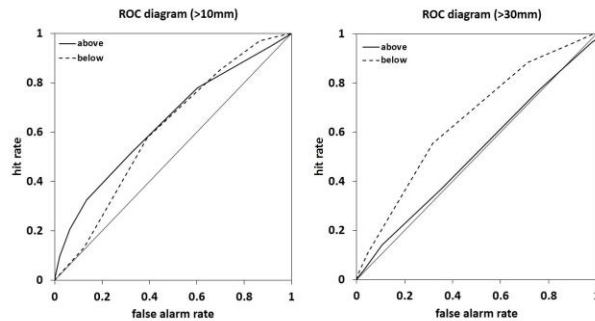


Figure 3. The ROC diagrams of the coupled 850hPa geopotential heights ECHAM4.5 AGCM in predicting the low (dash line) and high (thick line) number of rainfall days exceeding 10mm and 30mm threshold values for the DJF seasons over South Africa for 1982-2008.

### Conclusions

Both sets (uncoupled and coupled) 850hPa geopotential heights of the ECHAM4.5 AGCM have skill in predicting the number of rainfall days exceeding certain threshold values for the DJF seasons over South Africa. Both the models can successfully predict the high number of rainfall days exceeding the different threshold values, the skill is increasing with the threshold values. The skill of both the models in predicting the low number of rainfall days exceeding threshold values is decreasing with higher threshold values. The skill of both models is limited to 1mm, 10mm, 15mm, 20mm, 25mm and 30mm in predicting the high number of rainfall days. Generally the coupled model shows to be performing better than the uncoupled model in predicting both the low and high number of rainfall days exceeding different threshold values for DJF seasons over South Africa.

### Acknowledgements

The Applied Centre for Climate and Earth Systems Science (ACCESS) is acknowledged for funding this study. The South African Weather Service (SAWS) is acknowledged for providing the rainfall data and computing facilities and the International Research Institute for Climate and Society (IRI) for making available the CPT software package free.

### References

- Cook C., C.J.C. Reason and B.C. Hewitson. 2004, Wet and dry spells within particularly wet and dry summers in the South African summer rainfall region, *Climate Research*, **26**: 17-31.
- Kijazi A.L. and C.J.C. Reason. 2005, Relationships between intraseasonal rainfall variability of Coastal Tanzania and ENSO, *Theoretical and Applied Climatology*, **82**: 153-176.
- Kijazi A.L. and C.J.C. Reason. 2011, Intra-seasonal variability over the northeastern highlands of Tanzania, *International Journal of Climatology*, DOI: 10.1002/joc.2315.
- Landman W.A., S.J. Mason, P.D. Tyson and W.J. Tennant. 2001, Retro-active skill of multi-tiered forecasts of summer rainfall over southern Africa, *Int. J. Climatology*, **21**: 1-19.
- Usman M.T. and C.J.C. Reason. 2004, Dry spell frequencies and their variability over southern Africa, *Climate Research*, **26**: 199-211.

# A comprehensive study of air quality in urban, low-income areas of South Africa

<sup>1</sup>Scott P. Hersey, <sup>1</sup>Stuart J. Piketh, <sup>1</sup>Roelof P. Burger

<sup>1</sup>North-West University, Unit for Environmental Sciences and Management,

11 Hoffman Street, Potchefstroom, 2520, South Africa

[shersey@caltech.edu](mailto:shersey@caltech.edu), [Stuart.Piketh@nwu.ac.za](mailto:Stuart.Piketh@nwu.ac.za), [Roelof.Burger@nwu.ac.za](mailto:Roelof.Burger@nwu.ac.za),

**Abstract:** Multi-year ambient air quality data from 4 networks (19 sites) in Gauteng have been analyzed, in addition to data from intensive indoor and outdoor air quality monitoring in a small township in Mpumalanga province. PM<sub>10</sub> concentrations in township areas are 56% higher than in developed residential areas and 78% higher than in industrial areas as an annual average, with PM<sub>10</sub> in townships 63 and 136% higher than developed residential and industrial areas, respectively, in winter (June, July, August). Monthly PM<sub>10</sub> and PM<sub>2.5</sub> concentrations reach annual maxima during winter at all sites except in industrial areas. Diurnal profiles of PM<sub>10</sub> and PM<sub>2.5</sub> display maxima during morning (06:00-09:00 LT) and evening (17:00-22:00 LT) at nearly every site - especially during winter - and underscore the importance of domestic burning as a major source of primary particles. Multi-year averages indicate that evening maxima at some township sites average in excess of 400  $\mu\text{g m}^{-3}$ . These results from the urban/industrial Gauteng area quantitatively confirm previous studies suggesting that the lowest-income populations of South Africa experience the poorest air quality, and demonstrate that domestic burning results in frequent exposure to high concentrations of particulate pollution in the region comprising the cities of Johannesburg and Tshwane. Results from intensive township monitoring suggest that indoor air quality is closely related to indoor/outdoor temperature gradients and fuel usage, but that ambient air quality is a disconnected system controlled by local meteorology in addition to overall domestic emissions. **Keywords:** Aerosol, domestic burning, townships

## 1. Introduction

The impacts of aerosols on human health, visibility, and climate are well-documented. There are a number of natural sources of dust, sea salt, sulfate, and organic aerosol, but those most detrimental to human health are particles derived from anthropogenic fossil fuel burning. Combustion aerosol can be directly emitted as soot or formed in the atmosphere through photochemical reactions that produce low-volatility, secondary sulfate, nitrate, and organic species that either nucleate to form new aerosol or condense onto existing particles. Exposure to particulate pollution is typically worst in urban areas, where anthropogenic emissions are collocated with high population density. The lowest-income fraction of the population tends to experience the worst air quality because the least expensive property (or land available for informal settlements) is often close in proximity to major air pollutant sources like highways, power generation facilities, or industry. In developing countries, low-income households are significantly more likely to utilize non-electricity energy sources such as coal, wood, and paraffin (Fridge, 2004; Pauw et al., 2008). Suboptimal burning conditions in domestic settings often result in large emissions of particulates and particulate precursors, leading to high concentrations of PM (Fridge, 2004). In South Africa, the highest concentrations of PM<sub>10</sub> and PM<sub>2.5</sub> are measured in townships and informal settlements during winter, when domestic burning is most prevalent for heating and cooking, and when emissions are confined in a shallow boundary layer (Fridge, 2004). A number of reports and peer-reviewed articles have sought to characterize air quality in low-income areas of South Africa (e.g. Engelbrecht et al., 2000, 2001, 2002; Fridge, 2004; Pauw et al., 2008), but these studies have typically

been limited in geographic scope and have not characterized the major metropolitan centers where high densities of South Africans reside.

Particulates measured at the ground in South Africa are predominately dust, industrial secondary sulfate, and secondary organics (Piketh et al., 2002; Tiitta et al., 2014), but significant attention has been paid to the impact of biomass burning on particulates in the country. Regional biomass burning in Southern Africa occurs from June to October, and impacts AOD in South Africa during August and September (Formenti et al., 2003, Campbell et al., 2003; Queface et al., 2011; Tesfaye et al., 2011). The biomass burning emissions that most significantly impact South Africa originate in neighboring countries - particularly Zimbabwe and Mozambique (Magi et al., 2009). Because these emissions are transported in stratified layers aloft (Campbell et al., 2009), they may impact column aerosol properties such as AOD but not particulate concentrations at the ground. While transported biomass burning has been demonstrated to impact AOD seasonally, domestic burning - especially for heating and cooking during winter - is the source associated with the highest particulate concentrations in South Africa (Engelbrecht et al., 2000, 2001, 2002). Despite work to characterize emission factors and ambient air quality impacts of domestic burning, studies have been limited in scale to the household or township level and have never considered the dynamics and impact of domestic burning emissions across an entire major population center.

Here, we focus on air quality characteristic of low-income areas in South Africa. We analyze ground-based PM<sub>10</sub> and PM<sub>2.5</sub> from 4 separate air quality monitoring networks within Gauteng Province in order to understand seasonal, diurnal and regional trends in particulate concentrations at the

ground. We compare PM trends in townships with those in other environment types (industrial and urban/suburban residential), and explore the implications of township "maturity" processes (i.e. increasing commercialization and associated energy use changes) on particulate air quality. Finally, we investigate a rich and comprehensive dataset from Kwadela township in Mpumalanga Province to make links between indoor and outdoor air quality, fuel burning trends, and the impact of low-cost interventions.

## 2. Data Collection and Methods

Hourly ground-based air quality data were obtained from four different networks reporting to the South African Air Quality Information System (SAAQIS), all located within the Gauteng satellite grid box. Site classifications were made on the basis of site descriptions on the SAAQIS website (available at: <http://www.saaqis.org.za/NAAQM.aspx>), site visits, and personal correspondence with the NGO NOVA Institute, which works extensively in townships and informal settlements. Data were used as per approval from each monitoring network, and were subject to data quality controls. Negative values were discarded, as well as "repeat" values with the same value given for many hours at a time. Where > 30% of data points were missing over a given time-averaging period, data were discarded.

An intensive sampling campaign was conducted in Kwadela township in Mpumalanga Province, with 3 sampling periods analyzed (winter 2013, summer 2014, winter 2014), with an intervention introducing low-cost insulation and modified fire lighting techniques before the winter 2014 sampling period. Ambient gas and particle pollutant concentrations were measured at a central site in the township, while 15 randomly-dispersed houses received indoor air quality monitors. Sensors measured temperature gradients inside each of these 15 homes, and fuel consumption was measured by mass of coal burned per day. Finally, personal air quality monitors measured PM concentration exposure of select individuals in the township.

## 3. Results

Monthly averages of PM<sub>10</sub> and PM<sub>2.5</sub> (both in absolute magnitude and normalized by each site's maximum monthly average) are presented in Figure 1a. PM concentrations reach a maximum in winter (June, July, or August) for all sites except industrial areas. This maximum in PM concentrations corresponds to the coldest months, when the most significant domestic burning activity is expected and boundary layers are extremely shallow (often 50 m or less). The summer maximum in industrial areas may result from photochemistry of industrial precursors and generation of secondary particulates, or may be due to atmospheric dynamics. During winter, industrial stack emissions tend to be

released far above the very shallow boundary layer and into stable atmospheres. During summer, on the other hand, deeper boundary layers extend above stacks and industrial emissions therefore stay within a less stable boundary layer, resulting in mixing of emissions down to the ground. The average monthly ratio of PM<sub>10</sub> and PM<sub>2.5</sub> was calculated for sites with both parameters, and there is no statistically significant monthly trend, suggesting that fine particles comprise a relatively consistent fraction of total particulate concentration throughout the year, despite large changes in overall particulate concentration.

Diurnal averages of PM<sub>10</sub> and PM<sub>2.5</sub> for each season are presented in Figure 1b. PM<sub>10</sub> and PM<sub>2.5</sub> concentrations have been normalized by the maximum hourly average for each site for the entire year (typically 19:00-21:00 LT during winter), with the average concentration (in absolute magnitude) for each type of site displayed in the third row of diurnal plots. As was evident in monthly PM data, the highest concentrations occur in township areas where domestic burning is expected, followed by significantly lower PM concentrations in urban and suburban residential areas and the lowest concentrations on average in industrial areas. The clearest feature in the diurnal data is the significant enhancement in particulate concentrations in the morning (06:00-09:00 LT) and evening (17:00-22:00 LT) during all seasons. This trend is especially dramatic during winter, with typical evening PM<sub>10</sub> and PM<sub>2.5</sub> concentration maxima in township areas of 203 and 105  $\mu\text{g m}^{-3}$ , respectively, with evening PM<sub>10</sub> maxima averaging in excess of 400  $\mu\text{g m}^{-3}$  at some sites. That these diurnal patterns of enhanced PM concentration in morning and evening discernible in all seasons is evidence that domestic burning impacts air quality in South Africa throughout the year, but the significant enhancement in PM during winter underscores the fact that increased burning during cold months within shallow boundary layers consistently leads to dangerous concentrations of particulates - particularly in the lowest-income residential areas. It should be mentioned that the observed diurnal patterns may also reflect some contribution from on-road emissions - either primary combustion or vehicle-associated dust particles. However, the high density of domestic burning and relatively low density of vehicles in townships compared with other areas suggests that these on-road sources should be minor compared with primary burning emissions. The diurnal ratio of PM<sub>2.5</sub> to PM<sub>10</sub> is displayed in Fig.1b, and reaches a minimum at all township sites between 12:00 and 15:00 LT, indicating that morning and evening domestic burning activity tends to be a source of small particles.

On average, PM concentrations in townships are 51% higher than urban/suburban residential sites and 78% higher than industrial sites, underscoring the importance of domestic emissions as associated with the highest concentrations of particles in

the region. The difference between townships and other areas is more distinct in winter, when PM concentrations in townships are 63 and 135% higher than in urban/suburban residential and industrial sites, respectively. The average wintertime evening maximum in PM<sub>10</sub> of 203  $\mu\text{g m}^{-3}$ , approaching 400  $\mu\text{g m}^{-3}$  at many township sites, is 50-250% higher than 24-h PM<sub>10</sub> standards set by the United States Environmental Protection Agency, South African Department of Environmental of Affairs, and the World Health Organization (150, 180, and 50  $\mu\text{g m}^{-3}$ , respectively). There is significant variability in PM concentrations between sites just a few kilometers apart, indicating that the domestic burning that generates the highest concentrations of particulates is highly localized and most dramatically impacts air quality in a small area in the immediate vicinity of emissions. This result indicates that domestic burning PM source strength in low-income areas is highly variable, depending on factors such as the availability of electricity, the method of burning coal or wood, and thermal efficiency of homes.

Data from two township sites (Alexandra and Bodibeng) have diurnal trends that do not conform to the typical morning and evening PM enhancements typical of low-income areas, and represent intriguing case studies in the impact of township evolution and informal commercial activity within the township context. Alexandra was established in 1912 and in recent years has become fully electrified with paved roads and significant formal and informal commercial activity throughout the day. As the township has developed, residents have almost ubiquitously adopted electricity as the only energy source for both heating and cooking, meaning that coal and wood are not burned in stoves inside the home. However, Alexandra has a high density of informal food vendors that cook almost exclusively over open flames using inefficient three-stone fires which emit large concentrations of particulates. Vendors start cooking in the early morning and continue throughout the day and into the evening, resulting in a diurnal PM profile which does display moderate concentration enhancements in morning and (more pronounced) evening, but with elevated PM concentrations during midday as well. Bodibeng is a more extreme and localized example of the impact of informal commercial food service on PM concentrations. The Bodibeng monitoring site is located immediately adjacent to a major taxi rank, where hundreds of taxis congregate during the hours of roughly 10:00 am and 3:00 pm LT, between commute times and when the majority of taxi riders are at work. During these hours, informal food vendors cook meals for taxi drivers almost exclusively over open flames. The result is a tertiary PM peak in Bodibeng data between the hours of 10:00 am and 3:00 pm LT associated with informal commercial activity.

Results from intensive sampling in Kwadela are under analysis, but initial results suggest that while indoor air quality is correlated with fuel burning pat-

terns and indoor-outdoor temperature gradients, ambient air quality appears to be a decoupled system that may be more closely related to meteorological parameters than domestic burning. This result has implications for offsets programs proposed by industry, and suggests that any programs aimed at reducing human exposure to high particulate concentrations should focus on improving indoor, rather than ambient, air quality.

#### 4. Figures

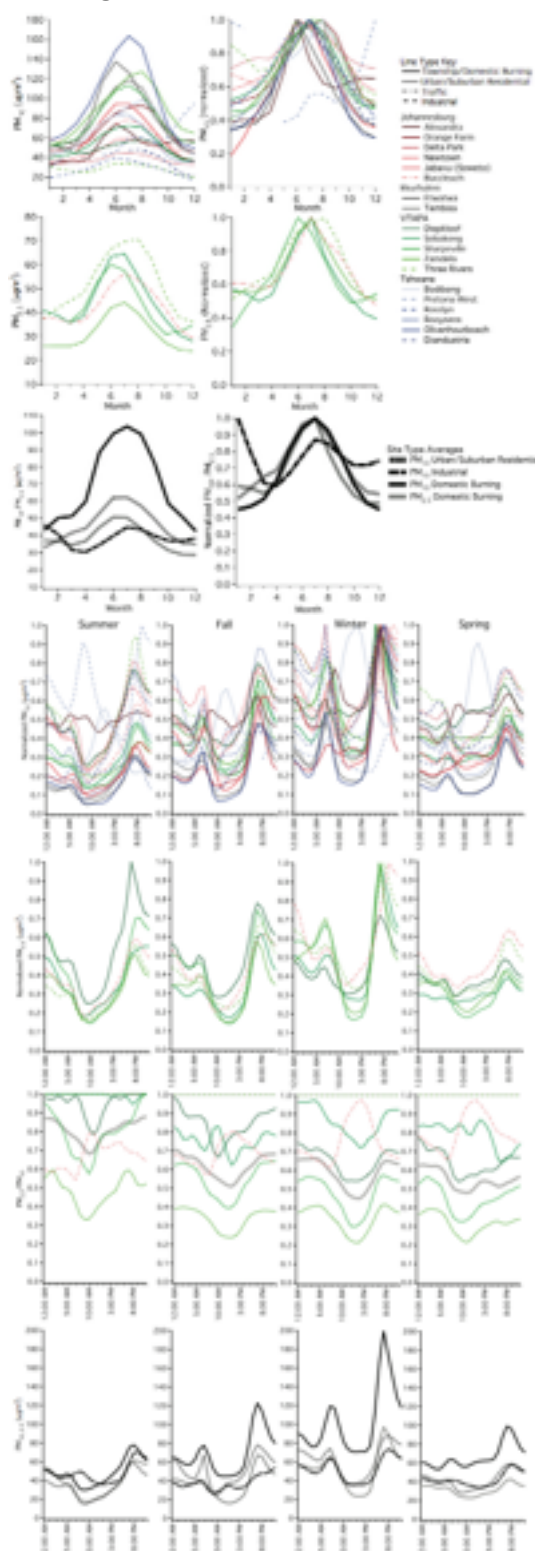


Figure 1: Multi-year ground PM<sub>10</sub> and PM<sub>2.5</sub> data, showing monthly (a) and diurnal (b) means.

## 5. Conclusions

We have presented a multi-year analysis of ground air quality data from 4 networks in Gauteng province. Data indicate that particulate concentrations reach a maximum during winter and are significantly higher in low-income areas than in urban/suburban or industrial areas. Particulate concentrations exhibit diurnal maxima during morning and evening in all seasons, corresponding to domestic burning. Indoor air quality is closely linked with domestic burning, but ambient air quality appears to be a disconnected system that is influenced strongly by local meteorology.

## 6. References

- Campbell, J. R., Welton, E. J., Spinhirne, J. D., Ji, Q., Tsay, S.-C., Piketh, S. J., Barenbrug, M., and Holben, B. N.: Micropulse lidar observations of tropospheric aerosols over northeastern South Africa during the ARREX and SAFARI 2000 dry season experiments, *Journal of Geophysical Research: Atmospheres*, 108, doi:10.1029/2002JD002563, 2003a.
- Eck, T. F., Holben, B. N., Ward, D. E., Mukelabai, M. M., Dubovik, O., Smirnov, A., Schafer, J. S., Hsu, N. C., Piketh, S. J., Queface, A., Roux, J. L., Swap, R. J., and Slutsker, I.: Variability of biomass burning aerosol optical characteristics in southern Africa during the SAFARI 2000 dry season campaign and a comparison of single scattering albedo estimates from radiometric measurements, *Journal of Geophysical Research*, 108, doi:10.1029/2002JD002321, 2003.
- Engelbrecht, J. P., Swanepoel, L., Zunckel, M., Chow, J. C., Watson, J. G., and Egami, R. T.: Modelling PM<sub>10</sub> aerosol data from the Qalabotjha low-smoke fuels macro-scale experiment in South Africa, *Ecological modelling*, 127, 235–244, 2000.
- Engelbrecht, J. P., Swanepoel, L., Chow, J. C., Watson, J. G., and Egami, R. T.: PM<sub>2.5</sub> and PM<sub>10</sub> concentrations from the Qalabotjha low-smoke fuels macro-scale experiment in South Africa, *Environmental monitoring and assessment*, 69, 1–15, 2001.
- Engelbrecht, J. P., Swanepoel, L., Chow, J. C., Watson, J. G., and Egami, R. T.: The comparison of source contributions from residential coal and low-smoke fuels, using CMB modeling, in South Africa, *Environmental Science & Policy*, 5, 157–167, 2002.
- Formenti, P., Elbert, W., Maenhaut, W., Haywood, J., Osborne, S., and Andreae, M. O.: Inorganic and carbonaceous aerosols during the Southern African Regional Science Initiative (SAFARI 2000) experiment: Chemical characteristics, physical properties, and emission data for smoke from African biomass burning, *Journal of Geophysical Research*, 108, doi:10.1029/2002JD002408, 2003.
- FRIDGE: Study to examine the potential socio-economic impact of measures to reduce air pollution from combustion. Part 1 report., Tech. rep., Airshed Planning Professionals/Bentley West Management Consultants report to the Trade and Industry Chamber/Fund for Research into Industrial Development, Growth and Equity (FRIDGE), Johannesburg, 2004.
- Magi, B. I., Ginoux, P., Ming, Y., and Ramaswamy, V.: Evaluation of tropical and extratropical Southern Hemisphere African aerosol properties simulated by a climate model, *Journal of Geophysical Research*, 114, doi:10.1029/2008JD011128, 2009.
- Pauw, C., Friedl, A., Holm, D. and John, J., Kornelius, G., Oosthuisen, R., and van Niekerk, A.: Report to the Royal Danish Embassy and the Department of Environmental Affairs and Tourism: Air pollution in dense, low-income settlements in South Africa, issue I., Tech. rep., NOVA Institute, 2008.
- Piketh, S. J., Annegarn, H. J., and Tyson, P. D.: Lower tropospheric aerosol loadings over South Africa: The relative contribution of aeolian dust, industrial emissions, and biomass burning, *Journal of Geophysical Research*, 104, 1597–1607, doi:10.1029/1998JD100014, 1999.
- Piketh, S. J., Swap, R. J., Maenhaut, W., Annegarn, H. J., and Formenti, P.: Chemical evidence of long-range atmospheric transport over southern Africa, *Journal of Geophysical Research*, 107, doi:10.1029/2002JD002056, 2002.
- Queface, A. J., Piketh, S. J., Eck, T. F., Tsay, S.-C., and Mavume, A. F.: Climatology of aerosol optical properties in Southern Africa, *Atmospheric Environment*, 45, 2910–2921, doi:10.1016/j.atmosenv.2011.01.056, 2011.
- Stroud, C., Nenes, A., Jimenez, J. L., DeCarlo, P., Huffman, J. A., Bruintjies, R., Nemitz, E., Delia, A. E., Toohey, D. W., Guenther, A. B., and Nandini, S.: Cloud activating properties of aerosol observed during CELTIC, *J. Atmos. Sci.*, 64, 441–459, 2007.
- Tesfaye, M., Sivakumar, V., Botai, J., and Tsidu, G. M.: Aerosol climatology over South Africa based on 10 years of Multiangle Imaging Spectroradiometer (MISR) data, *Journal of Geophysical Research*, 116, doi:10.1029/2011JD016023, 2011.
- Tiitta, P., Vakkari, V., Croteau, P., Beukes, J., van Zyl, P., Josipovic, M., Venter, A., Jaars, K., Pienaar, J., Ng, N., et al.: Chemical composition, main sources and temporal variability of PM<sub>1</sub> aerosols in southern African grassland, *Atmospheric Chemistry and Physics*, 14, 1909–1927, 2014.

# Clustering Forecast System for Southern Africa SWFDP

Stephanie Landman<sup>1\*</sup> and Susanna Hopsch<sup>2</sup>

<sup>1</sup>South African Weather Service, Private Bag X097, Pretoria, 0001, South Africa, stephanie.landman@weathersa.co.za

<sup>2</sup>Karlsruhe Institute of Technology, Kaiser Street 12, 76131, Karlsruhe, Germany, susanna.hopsch@kit.edu

A clustering forecast system was proposed in order to view a large ensemble forecast system for the southern Africa Severe Weather Forecast Demonstration Project (SWFDP) region. The clustering of the ensemble members was done through self-organising maps in order to provide four different future scenarios for daily rainfall, 2 m maximum temperature and 10 m wind speeds. The forecast system was evaluated for the months of December 2013 to February 2014. It was found that each of the four scenarios provide realistic and possible future states but with different spatial distribution and magnitude in bias for all three parameters used. The system is developed with the purpose of providing the user with a quick glance at possible scenario outcomes and possible regions where severe weather might occur. It also provides deterministic expected values for each parameter and not the typical probabilistic forecast of an expected threshold to be exceeded.

**Keywords:** TIGGE, Self-Organising Maps, SWFDP, forecast verification

## 1. Introduction

The Observing System Research and Predictability Experiment (THORPEX) Interactive Grand Global Ensemble (TIGGE) is a component of the THORPEX project which started in October 2006 (Bougeault, 2010). The TIGGE archive consists of nine global producing centres medium-range ensemble forecasts (Park *et al.*, 2008). This multi-model/multi-analysis forecast system addresses the issue of model uncertainty and observational error (Park *et al.*, 2008; Lavers and Villarini, 2013). Extensive studies on the TIGGE data have been done and improved on increased warning and guidance on high impact and severe weather (list of studies to be found in Su *et al.*, 2014)

The southern Africa Severe Weather Forecast Demonstration Project (SWFDP) is reliant on objective forecast data for days 1 to 5 for issuing guidance maps (Landman *et al.*, 2013). Forecasters at the National Forecasting Centre (NFC) at the South African Weather Service (SAWS) already have access to global centre forecasts through the SWFDP initiative where after they use the information to provide subjective guidance to the SWFDP region (Landman *et al.*, 2013). The TIGGE data represents the ideal forecast in which most of the forecasts from the global forecast centres are contained. In order to represent this large ensemble forecast data in a manner which does not overwhelm forecasters, a clustering method was proposed.

Clustering of data has a tendency to expose groups within a dataset and each group will result in

distinct classification of the clustering variable (Tambouratzis and Tambouratzis, 2008). Clustering therefore provides an ideal middle-ground between deterministic and probability forecasts where each cluster gives a probability of a specific future atmospheric scenario to occur. The technique used to cluster the forecasts was Self-Organising Maps (SOM; Kohonen, 2001). SOM is generally more applied in climate studies but was applied in this study on the medium-range time scale due to its ease of use and since it is already used extensively in atmospheric sciences in South Africa (Engelbrecht *et al.*, 2014), the system is well known by local users. The SOM was constructed for the region of 10°N to 45°S and 20°W and 70°E in order to cover the complete SWFDP region which includes the small south Indian Ocean islands of Mauritius and Reunion to the east. This domain will allow the SOM to be influenced by both the tropical and mid-latitude weather systems dominating the sub-continent.

## 2. Data and Methodology

### 2.1 TIGGE data

The 00 UTC analysis ensemble forecasts from four centres were used and consist of a total of 117 ensemble members. Each system consists of a control forecast and different number perturbed forecasts; ranging from 23 to 50. The ensemble systems used are: the European Centre for Medium-Range Weather Forecasts (ECMWF) with 51 members, the United Kingdom's MetOffice (UKMO) with 24 members, the National Centers for

Environmental Prediction (NCEP) with 21 members, and the Canadian Meteorological Centre (CMC) with 24 members. The four ensemble systems were chosen on the basis of their regular updates and completeness of archive as well as the different perturbation techniques and model uncertainty schemes used by each centre (Park *et al.*, 2008, Su *et al.*, 2014). The UKMO ensemble system is also shown to improve forecasts over the tropics (Park *et al.*, 2008) which is essential for the SWFDP domain since it is influenced by tropical weather. The TIGGE archive was accessed from ECMWF data servers (tigge.ecmwf.int) and all the members were interpolated to a common  $1^\circ \times 1^\circ$  grid before downloading. Since the availability of the TIGGE data has a lag-time of 48-hours after initialization (Bougeault, 2010), the forecasts were therefore from lead-times of 48- to 150-hours in order to correspond with the 5-day SWFDP guidance time. The surface variables investigated were 10 m wind speeds, maximum 2 m temperature and 24-hour rainfall totals (accumulated 06 to 06 UTC). These variables were chosen in order to adapt to the severe weather conditions guidance provided by SWFDP; excluding ocean conditions (Landman *et al.*, 2013). The time period of the investigation covers 1 December 2013 to 28 February 2014 (DJF 2013/14), adding to a total of  $90 \times 5 = 450$  days.

## 2.2 Forecast clustering

The SOM was set-up to create a  $2 \times 2$  matrix. Each of the nodes in the matrix consists of a regular two-dimensional structure, based on the variable being clustered. In this study 850 hPa geopotential heights (gpm) at 12 UTC for each of the forecast lead-times was used to develop the SOM. It was found that SOMs larger than a 4 node matrix in classifying 850 hPa heights more often than not result with at least one node being empty, possibly due to only one time step being used on the 117 members. The 850 hPa heights were chosen to develop the SOM as this low-level atmospheric circulation is influential in rainfall and 2 m temperatures over the higher altitudes of the sub-continent.

## 2.3 Verification

The TIGGE forecasts were compared to ECMWF ERA-Interim data due to its high quality 4D-Var analysis and the availability for the investigation period (Hagendorn *et al.*, 2012). It is however acknowledged that this dataset is not completely independent of the forecasts, but since the different scenarios or nodes were verified and not the whole forecast dataset, it was decided that the dependency might be negligent. However, for this reason, as an alternative the 06 to 06 UTC accumulated daily rainfall totals were also compared to the Famine Early Warning System (FEWS) data. The daily 2 m

maximum temperature and 10 m wind speeds were evaluated against ERA-Interim data only.

## 3. Results and Discussion

In Figure 1 the percentage number of members per node is given. It is seen that node 1 and node 4 generally have the most members and it was also found that the standard deviation for nodes 1 and node 4 tend to be smaller in comparison with the standard deviation of nodes 2 and 3 respectively due to the larger number of members.

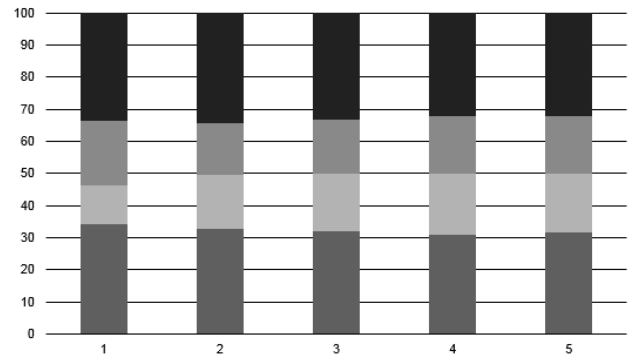


Figure 1: Percentage members in each node each forecast lead-time. Node 1 is the bottom section of each bar, with node 4 the top section.

This tendency is however not seen in the average spatial daily rainfall bias (Table 1) where no discernable pattern can be seen with regards to the size of the node. However, as expected the bias mostly increases with lead-time for all nodes.

Table 1: Average rainfall bias (mm/day) per node per lead-time

NODE / lead-time	NODE 1	NODE 2	NODE 3	NODE 4
1	0.16	0.26	0.08	-0.04
2	0.25	0.17	0.09	0.14
3	0.57	0.7	0.7	0.7
4	0.44	0.41	0.22	0.31
5	0.27	0.38	0.3	0.4

For ease of comparison and explanation, only rainfall verification will be discussed in detail in this abstract. It is further seen in Figure 2 that the spatial areas where each node has a dry or wet bias are similar for the DJF 2013/14 season. However, what is further evident is the difference in magnitude of the bias over different regions. An example is the lower bias over Angola and the Democratic Republic of Congo, as well as Mozambique when compared to the other nodes. Over Mozambique nodes 1 and 2 tend to have dry bias, whereas with nodes 3 and 4 the bias is much smaller and tend to be wet.

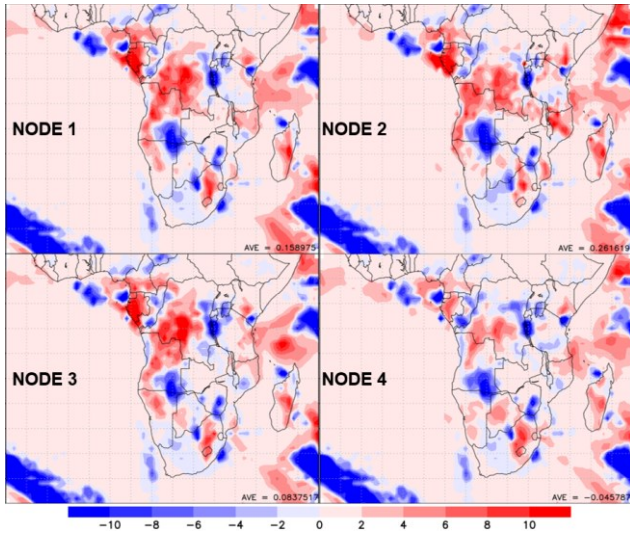


Figure 2: Average daily spatial rainfall bias (mm/day) per node for the DJF 2013/14 season for 48-hour lead time when compared to the FEWS rainfall dataset.

A case study example, 6 January 2014 of the output of the forecast clusters is presented in Figure 3. Figure 3a shows the average 850 hPa circulation forecast for each node with the subsequent resulting surface variables with rainfall totals in Figure 3b, expected 2 m maximum temperature in Figure 3c and lastly the 10 m wind streamlines and indicating areas where wind speed is expected to exceed 20 kts. Each node has a probability of occurring based on the number of members within each node. Even with a small difference in the average 850 hPa circulation fields are minimum between the nodes, spatial difference in the rainfall patterns are clear; especially when looking at the intensity of rainfall expected over certain areas. A region where this is evident in Figure 3b is the rainfall expected over the north-eastern parts of South Africa in node 1 which is not seen with the other nodes. Similarly the intensity of the rainfall west of Madagascar in both nodes 1 and 3 differs from nodes 2 and 4. The difference in the spatial extend of wind speed greater than 20 kts (black shaded areas) is also evident in Figure 3d. Similar patterns exist for temperature and wind speeds.

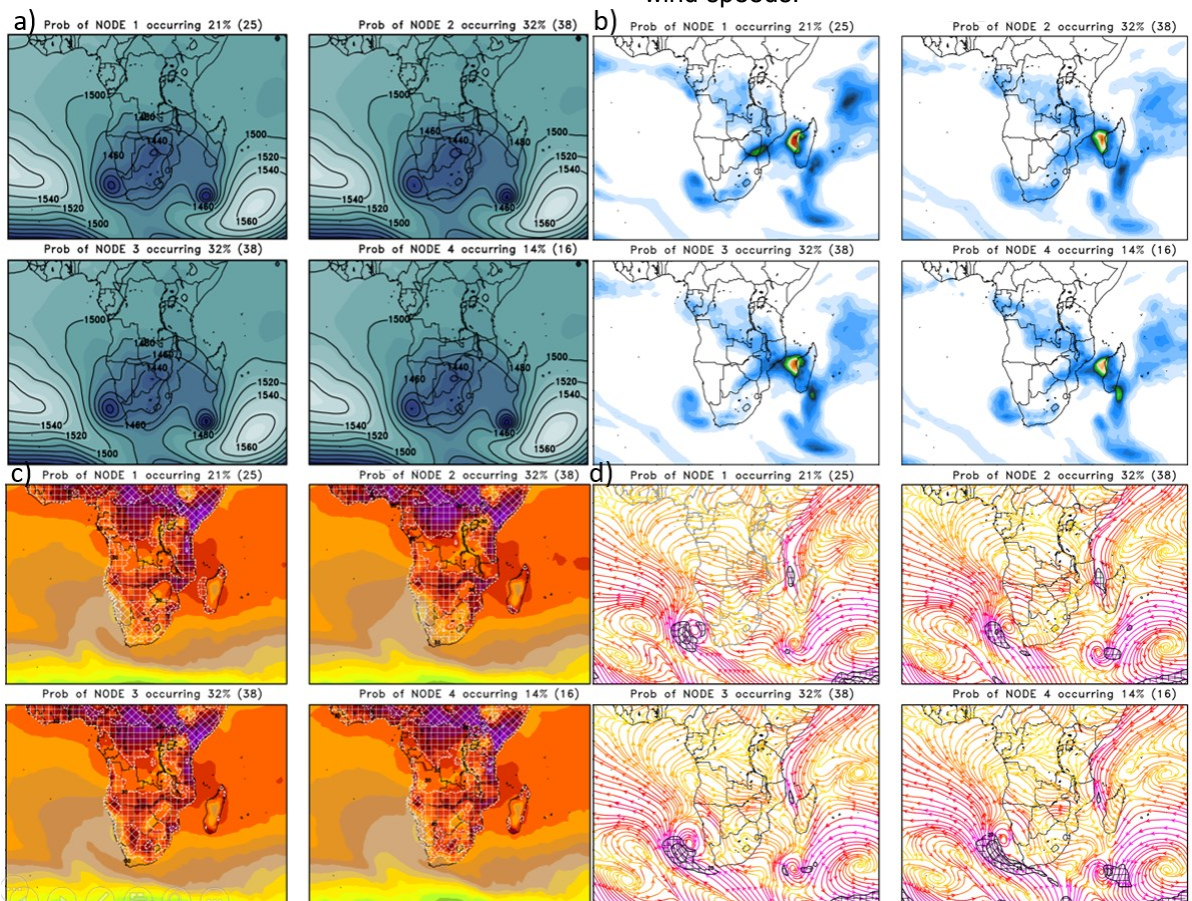


Figure 3: The  $2 \times 2$  cluster forecast for 12 UTC on 6 January 2014 with a 2 day lag time. Each of the nodes has a probability of occurring with regards to the number of members assigned to each node, with a) the 850 hPa circulation pattern, b) the four scenario daily total rainfall forecasts based on the average rainfall of the ensemble members identified in the SOM for each node, c) the maximum 2 m temperature and d) the 10 m wind streamlines.

#### 4. Conclusion and Recommendations

The TIGGE archive is a great source of ensemble forecasts. The cluster system developed is primarily a deterministic guidance product whereby the user can still gain explicit spatial daily forecast values for various parameters, but with an uncertainty assigned to each scenario forecast. Not shown here is also the ability of the system to focus on a specific country or region, depending on the user needs. Additionally, meteogrammes with 6-hourly intervals can also be created for areas of high vulnerability where additional information might be required. The system is therefore a very simplistic albeit effective manner to view a large data set since an optimized amount of information of expected severe weather conditions for the next couple of days are made available this way.

#### 5. Acknowledgements

The author would like to thank Dr Sarah Jones in providing a visiting scientist opportunity to visit KIT in Germany where invaluable knowledge was gained on the TIGGE data and clustering of ensemble forecasts. This opportunity was funded by the GEOWOW project (<http://www.geowow.eu/weather.html>).

#### 6. References

- Bougeault, P., Toth, Z., Bishop, C., Brown, B., Burridge, D., Chen, D. H., Ebert, B., Fuentes, M., Hamill, T. M., Mylne, K., Nicolau, J., Paccagnella, T., Park, Y.-Y., Parsons, D., Raoult, B., Schuster, D., Silva Dias, P., Swinbank, R., Takeuchi, Y., Tennant, W., Wilson, L., & Worley, S. 2010, 'The THORPEX Interactive Grand Global Ensemble', *Bull. Am. Meteorol. Soc.*, pp. 1059–1072
- Engelbrecht, C. J., Landman, W. A., Engelbrecht, F. A. & Malherbe, J. 2014, 'A synoptic decomposition of rainfall over the Cape south coast of South Africa', *Clim. Dyn.* doi: 10.1007/s00382-014-2230-5
- Hagedorn, R., Buizza, R., Hamill, T. M. & Palmer, T. N. 2012, 'Comparing TIGGE multimodel forecasts with reforecast-calibrated ECMWF ensemble forecasts', *Q. J. R. Meteorol. Soc.* **138**, 1814–1827
- Kohonen T. 2001, 'Self-organizing maps'. 3rd ed. Springer
- Landman, S., Marx, E., & Mchunu, N. 2013, 'Evaluation of Severe Weather Guidance Maps issued by the South African Weather Service.' 29<sup>th</sup> Annual Conference of the South African Society for Atmospheric Sciences, September 2013, Durban. ISBN 978-0-620-56626-1
- Lavers, D. & Villarini, G. 2013, 'Were global numerical weather prediction systems capable of forecasting the extreme Colorado rainfall of 9-16 September 2013?' *Geophys. Res. Lett.* **40**, 6405–6410
- Park, Y., Buizza, R. & Leutbecher, M. 2008, 'TIGGE : Preliminary results on comparing and combining'. *Q. J. R. Meteorol. Soc.* **134**, 2029–2050
- Su, X., Yuan, H., Zhu, Y., Luo, Y., & Wang, Y. 2014, 'Evaluation of TIGGE ensemble predictions of Northern Hemisphere summer precipitation during 2008-2012', *J. Geophys. Res. Atmos.*, **119**
- Tambouratzis, T. & Tambouratzis G., 2008, 'Meteorological Data Analysis Using Self-Organizing Maps', *International Journal of Intelligent Systems*, **23**, pp. 735-759

# Climate change and potato production in South Africa: impacts on yield and water use efficiency, and possibilities for adaptation

A.C. Franke<sup>1</sup>, J.M. Steyn<sup>2</sup>, A.J. Haverkort<sup>2,3</sup>

<sup>1</sup> Soil, Crop and Climate Sciences, University of the Free State, Bloemfontein 9300, South Africa

<sup>2</sup> Department of Plant Production and Soil Science, University of Pretoria, Hatfield 0028, South Africa

<sup>3</sup> Plant Research International, Wageningen University and Research Center, Wageningen, the Netherlands

This study aims to assess the risks and opportunities posed by climate change to potato growers in South Africa and to evaluate adaptation measures in the form of changes in planting time growers could adopt to optimise land and water use efficiencies (WUEs), using a climate model of past, present-day and future climate over southern Africa and the LINTUL crop growth model incorporating impacts of elevated CO<sub>2</sub> levels on radiation use efficiency and water use. We ran the model for three contrasting agro-ecosystems where potato is an important part of the cropping system: (i) the Sandveld (Leipoldtville), (ii) the Eastern Free State (Reitz-Bethlehem) and (iii) Limpopo (Dendron): a tropical dry climate with a dry winter and a warm and rainy summer. Potato crops in all three areas can reap benefits of increased CO<sub>2</sub> levels, increasing photosynthetic rate and reducing water use by the crop, if planting can be shifted to appropriate times of the year. Potato growers are likely to respond to climate change by advancing planting. In Limpopo, there may be a shift in preferred planting from late winter to autumn. WUEs of the crop in the Sandveld and Limpopo are likely to further improve as an advancement of planting coincides with the period when WUE is higher, irrespective of the effects of climate change. Changing lengths of the growing season could also affect yield and WUE if suitable varieties with appropriate growing periods can be found. Moreover, farmers would need to adjust pest and pathogen and nutrient management to take advantage of a higher potential yield.

Keywords: CO<sub>2</sub> concentrations, photosynthesis, agro-ecological zones, *Solanum tuberosum*

## 1. Introduction

Climate change in potato production areas of South Africa is expected to lead to higher temperatures. Given the detrimental impact of high temperatures (> 28 °C) on photosynthesis rate of potato, higher temperatures are expected to negatively impact yields. On the other hand, higher CO<sub>2</sub> levels are likely to enhance photosynthetic rate and reduce water use in potato.

The CO<sub>2</sub> concentration of the atmosphere increased from 315 to 380 ppm between 1960 and 2000. Model forecasts suggest that by 2050 this will have increased to about 550 ppm under the A2 scenario. Schapendonk et al. (2000) showed that potato yields increased on average by 38% when CO<sub>2</sub> concentration was doubled from 350 to 700 ppm CO<sub>2</sub>. The FACE experiments (Magliulo et al. 2003) showed potato yield increases between 29 and 54% with a CO<sub>2</sub> increase in the range from 370 to 550 ppm. Jaggard et al. (2010) found a 36% increase in potato yields due to an increased concentration of CO<sub>2</sub> and a 7.5% decrease in yield due to the increased ozone level, resulting in a net yield increase of 28.5%. According to Jaggard et al., potato will benefit most of rising CO<sub>2</sub> levels compared to other crops. C3 crops, such as wheat and rice, showed a benefit by about 6%, while C4 crops do not benefit from CO<sub>2</sub> enrichment at all

and will suffer from increased ozone levels, leading to between 5% (maize) and 7.5% (sugar cane) yield reduction. Greater intracellular CO<sub>2</sub> concentration due to increased atmospheric CO<sub>2</sub> concentration is expected to lead to a smaller stomatal aperture and reduced water losses through transpiration from individual leaves, which could lead to greater water use efficiency (WUE). In the trial by Magliulo et al. (2003) water use in potato was decreased by 11% with a CO<sub>2</sub> increase in the range from 370 to 550 ppm. Also Jaggard et al. (2010) observed an 11% decrease in water use with CO<sub>2</sub> concentrations increasing by 190 ppm.

This study aims to assess the risks and opportunities posed by climate change to potato growers in South Africa and to evaluate adaptation measures such as changes in planting time using a climate model of past, present-day and future climate over southern Africa and the LINTUL crop growth model incorporating impacts of elevated CO<sub>2</sub> levels on radiation use efficiency (RUE) and water use. A detailed description of the study can be found in Haverkort et al. (2013), Franke et al. (2013) and Van der Waals et al. (2013).

## 2. Methodology

Climate projections were obtained by downscaling the output of different coupled climate

models to high spatial resolution over southern Africa (Engelbrecht et al., 2013). The potato crop growth model is explained in detail by Haverkort et al. (2013) and Franke et al. (2011). RUE equalled  $1.25 \text{ g MJ}^{-1}$  intercepted radiation in 1990 at optimal temperatures, and decreased linearly to 0 when the maximum day temperature ( $T_{\text{max}}$ ) decreased from  $16^{\circ}\text{C}$  to  $8^{\circ}\text{C}$  or increased from  $30^{\circ}\text{C}$  to  $35^{\circ}\text{C}$  at all  $\text{CO}_2$  levels. We followed Jaggard et al.'s (2010) assumption that yields - hence RUE - increased by 28.5% with an increase in  $\text{CO}_2$  concentration from 370 to 550 ppm, while water use reduced by 11% over this  $\text{CO}_2$  range.

We ran the model for three contrasting agro-ecosystems where potato is an important part of the cropping system: (i) the Sandveld (Leipoldtville), representative of a Mediterranean climate with cool, wet winters, and hot and dry summers, (ii) the Eastern Free State (Reitz-Bethlehem): a continental mid-altitude climate with a cold and dry winter and a warm and rainy summer; the growing season is interrupted by frosts in winter, and (iii) Limpopo (Dendron): a tropical dry climate with a dry winter and a warm and rainy summer. Simulation involved planting of potato every 15<sup>th</sup> day of the month with a crop staying in the field for 120 days. To condense results, we present results for planting in three decades: 1961-1970, 2001-2010 and 2040-2049.

We also assessed changes in the length of the season suitable for potato cultivation, as determined by the frost-free and heat-free period. The heat-free period begins in autumn when average  $T_{\text{max}}$  is less than  $30^{\circ}\text{C}$  for two weeks and ends in spring when average  $T_{\text{max}}$  is more than  $30^{\circ}\text{C}$  over a period of two weeks. Yields are given as potential fresh tuber yields with a dry matter percentage of 20%. All crops were assumed to be irrigated when needed and drought stress was not considered. WUE was calculated as the potential fresh tuber yield divided by evapotranspiration. Irrigation losses, drainage and other factors were not considered here.

### 3. Results and Discussion

The length of the growing season in the Sandveld and Limpopo is determined by the heat-free period (Fig. 1A & 1C). The two lines indicating the approximate period in which potato can be grown without excessive heat stress converge, indicating a reduction in the suitable heat-free period for potato growth. The trends at Limpopo are similar to those of the Sandveld, but the cool period appropriate for potato growth is about 45 days shorter in Limpopo. Nevertheless, potato crops in Limpopo are occasionally damaged by frost in winter. Incidences of frost reduce over time, with no frost occurring anymore after 2025 (Fig. 1C). As frost from the middle of the growing

season usually results in severe crop damage or termination of growth, the reduction and disappearance of frost in Limpopo represent a major reduction in potato production risk. In the Eastern Free State, the growing season is primarily determined by the frost-free period (Fig. 1B). The first day with frost over the 90-year period tends to be later in the year and the last day with frost tends to be earlier, lengthening the growing season.

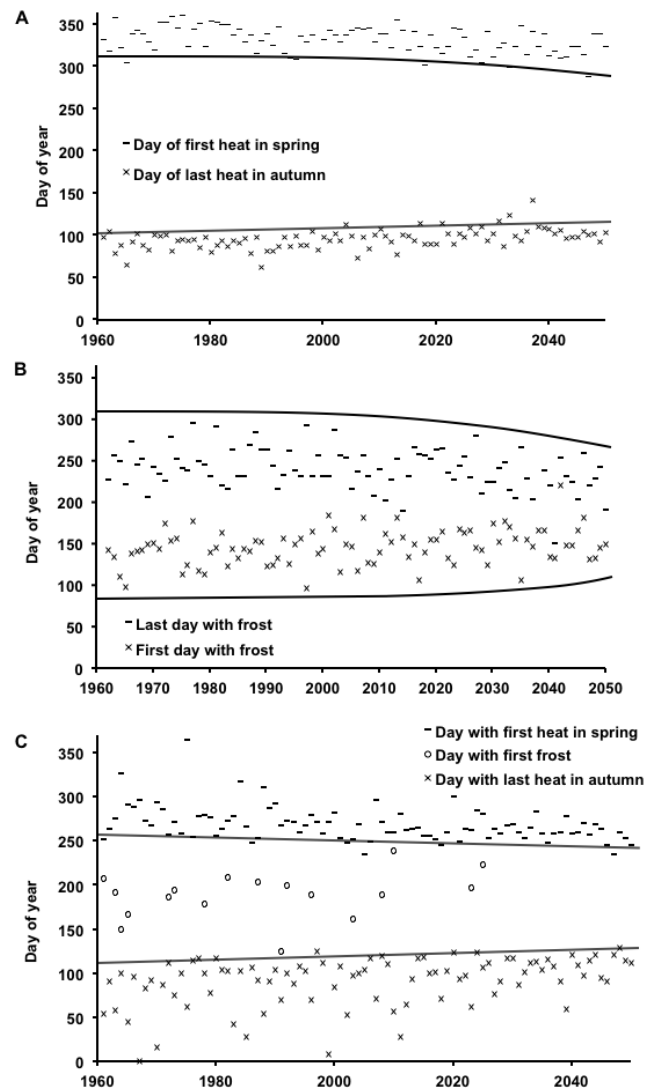


Fig. 1. Changes in the length of the growing season between 1961 and 2050: Day of the year with the last heat in autumn and the first heat in spring in A. the Sandveld and C. Limpopo, and the first and last frost of the year in B. the Eastern Free State. In Limpopo, frost events, occasionally interfering in the cropping season, are also indicated. In the Sandveld and Limpopo, the lines indicate approximate planting (lower) and harvest time (upper) of a crop avoiding most of the heat. In the Free State, the lines indicate approximate planting (upper) and harvest time (lower) of a crop grown in the period with a low risk of frost.

When planting in winter or early spring in the Sandveld, the crop model calculates a substantial yield increase over the 90-year period (Fig. 2A) with an increase from 46 to 67 Mg ha<sup>-1</sup> for the June planting (+46%). This increase is more than proportional to the CO<sub>2</sub> response of 28.5% because the rise in temperature leads to more efficient photosynthesis, as well as a more rapid development of foliage early in the season increasing the crop's ability to intercept radiation. Due to increasing temperatures in summer, photosynthesis rate is reduced leading to a yield reduction from 46 to 36 Mg ha<sup>-1</sup> when a crop is planted in December. Fig. 2A also shows that the months of planting with the highest yields shifts a month forward from August-September to July-August. WUE, expressed as g potato per litre of water evapotranspired, increases when planting in autumn and early winter. When planting later in winter or in early spring, the advantage of a lower water use caused by higher CO<sub>2</sub> levels are moderated by higher temperatures enhancing evapotranspiration. In a summer crop, WUE remains approximately the same. Growers in the Sandveld currently have a conflict of interest, as the planting period giving the highest yield does not coincide with the period giving the highest WUE (Franke et al., 2011). This conflict will become less in future as an advancement of planting to optimise yield will bring planting time closer to the time giving the highest WUE.

In the Eastern Free State, the highest absolute yield increases take place with planting between June and September (Fig. 2B). The plantings giving highest yields move forward from October-November to September-October. When planting occurs after October, the increase in hot days annuls the benefit of higher CO<sub>2</sub> levels. WUE is greatest in September. An advancement of planting will thus move the planting time closer to the time with the highest WUE.

In Limpopo there are currently two main planting periods: an early planting, which starts after the high summer temperatures have started subsiding in autumn (late February to March), and the main planting period, which starts in May and continues through the winter until the end of July,. Fig. 2C shows higher yields when planting outside this window, but growers try to avoid too hot conditions in summer due to its negative impacts on emergence and tuber quality, and the high water needs in summer. In addition, the niche winter crop yields the highest prices when other regions do not deliver to the market. The results show that with time, the period of highest production will coincide with the preferred operational and market requirements. The best months to plant in 2050 will be in April-May, with a strong yield increase over 90 years from 49 to 77 t ha<sup>-1</sup>. This increase is not only due to higher CO<sub>2</sub>

levels and more optimal temperatures, but also due to a reduction in the risk of frost damage. The increase in WUE over this period is from 20 to 30 g l<sup>-1</sup>. With water scarcities and boreholes that now go to depths well over 100 m, whereas 30 meter sufficed 20 years ago, planting when WUE is highest is expected to become priority.

The potential yields and WUEs simulated by the model are considered indicative of what can be achieved in each area. Whether actual yields and WUEs in farmers' fields will change proportionally depends on various other factors, especially farmers' ability to adjust crop genotypes to changing environmental conditions. Moreover, farmers would need to adjust pest and pathogen management (Van der Waals et al., 2013) and nutrient management to take advantage of a higher potential yield.

#### 4. References

- Engelbrecht CJ, Engelbrecht FA, Dyson LL (2013) High-resolution model-projected changes in mid-tropospheric closed-lows and extreme rainfall events over southern Africa. *Int. J. Climatol.* **33**:173-187
- Franke AC, Steyn JM, Haverkort AJ (2013) Climate change and potato production in contrasting South African agro-ecosystems 2. Assessing risks and opportunities of adaptation strategies. *Potato Res.* **56**:51-66.
- Franke AC, Steyn JM, Ranger KS, Haverkort AJ (2011) Developing environmental principles, criteria, indicators and norms for potato production through field surveys and modelling. *Agric. Syst.* **104**:297-306.
- Jaggard KW, Qi A, Ober AA (2010) Possible changes to crop yield by 2050. *Phil. Trans. Royal Soc. B.* **365**:2835-51.
- Haverkort AJ, Franke AC, Engelbrecht FA, Steyn JM (2013) Climate change and potato production in contrasting South African agro-ecosystems 1. Effects on land and water use efficiencies. *Potato Res.* **56**:31-50.
- Magliulo V, Bindi M, Rana G (2003) Water use of irrigated potato (*Solanum tuberosum* L.) grown under free air carbon dioxide enrichment in central Italy. *Agric. Ecosyst. Environ.* **97**:65–80.
- Schapendonk AHCM, van Oijen M, Dijkstra M, Pot SC, Jordi WJRM, Stoopen GM (2000) Effects of elevated CO<sub>2</sub> concentration on photosynthetic acclimation and productivity of two potato cultivars grown in open-top chambers. *Austr. J. Plant Physiol.* **7**:1119–30.
- Van der Waals JE, Krüger K, Franke AC, Haverkort AJ, Steyn JM (2013) Climate change and potato production in contrasting South African agro-ecosystems 3. Effects on relative development rates of selected pathogens and pests. *Potato Res.* **56**:67-84.

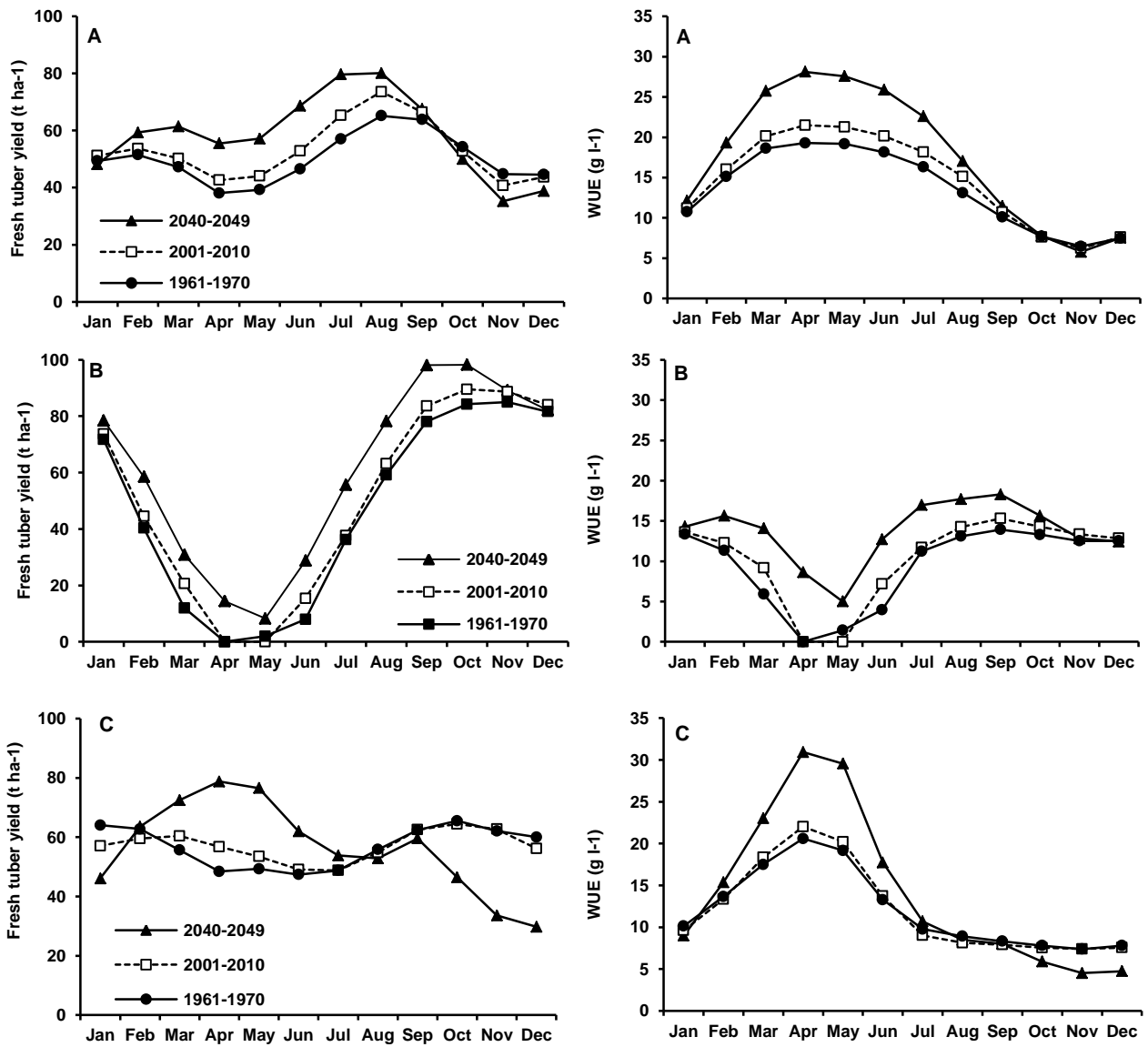


Fig. 2. Calculated potential fresh tuber yield (left) and water use efficiency (WUE) (right) of a 120 day crop planted on the 15<sup>th</sup> of each month grown for A. the Sandveld, B. the Eastern Free State, and C. Limpopo.

# Comparison study on high resolution rainfall forecast verification techniques

Anika Liebenberg<sup>\*1</sup> and Stephanie Landman<sup>1 2</sup>

<sup>1</sup>Department of Geography, Geoinformatics and Meteorology, University of Pretoria, Private bag X20 Hatfield, Pretoria, 0028, South Africa, anikaliebenberg@gmail.com

<sup>2</sup>South African Weather Service, Private Bag X097, Pretoria, 0001, South Africa, Stephanie.Landman@weathersa.co.za

The first, and arguably the most difficult part of data verification consist of matching the gridded forecast data to the observation data. The method chosen can have a significant influence on the results and can therefore artificially improve the verification results at a specific station. This is due to the fact that the observation stations are sparsely distributed as opposed to the equally spaced model grid points. In this research, the Advanced WRF dynamic core of the Weather Research and Forecasting model, at 4- and 12 km horizontal resolutions were used. Two verification techniques that are commonly used were evaluated and compared. The two techniques tested are, a closest grid point technique and an area average technique. The result was that both techniques provide very similar continuous statistics for the 4 case studies tested. The 4 km resolution statistics showed slightly smaller errors than the 12 km resolution. Therefore significance tests were computed and the area average technique yielded significantly improved results compared to the closest grid point technique. This was determined using a Monte Carlo procedure.

**Keywords:** verification, rainfall forecasts, horizontal resolution, Weather Research and Forecasting (WRF-ARW)

## 1. Introduction

Verification of weather forecasts is the important process of determining the accuracy and skill of the Numerical Weather Prediction (NWP) model (Warner, 2011). To start the process of data verification, the forecasts need to be spatially matched with the observations (Stanski *et al.*, 1989). This can be done in one of two ways; the forecast data needs to be spatially interpolated to the location of the stations, or the observations must be analysed on the model grid resolution. The verification process entails deciding what

comparison technique should be used. The verification process also allows for comparison between different models. From Figure 1, it is possible to see the differences in the detail and intensity between the 4 km (a) and 12 km (b) horizontal resolution forecast data. The 4 km horizontal resolution can capture more detail of the rainfall distribution compared to the 12 km horizontal resolution. Deciding how to match the model forecast to specific observation stations, which are not necessarily located on grid points, is therefore essential.

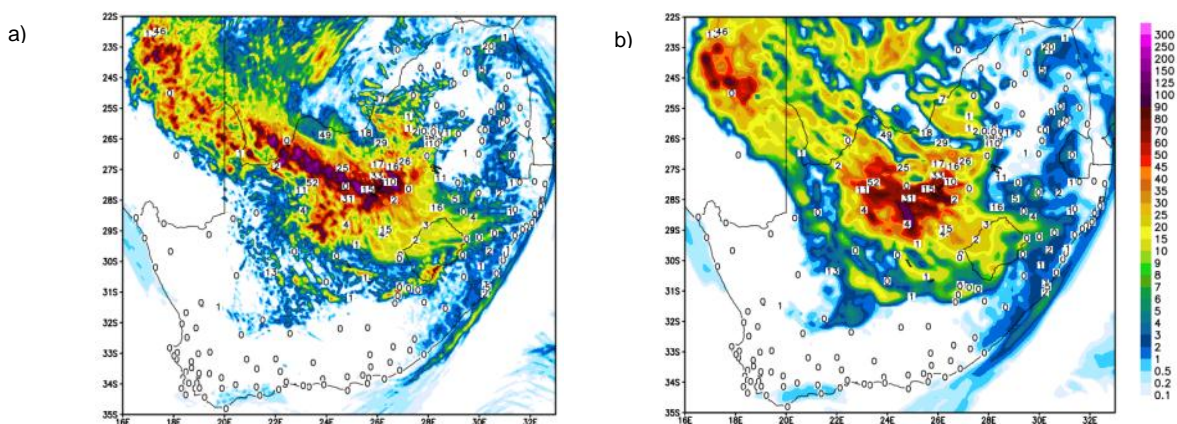


Figure 1. 24 hr WRF rainfall forecast (shaded) and the observed rainfall (mm) from 4 km (a) and 12 km (b) horizontal resolution for the 3<sup>rd</sup> of February 2014.

The spatial verification method inter-comparison project (ICP) is an initiative that was started in 2007 (Jolliffe & Stephenson, 2012). The project originated from a workshop on verification, held in Colorado. The ICP focusses on comparing different verification techniques and aims at providing guidelines and insight for other researchers when choosing a spatial verification method (Ahijevych *et al.*, 2009). This project has resulted in many new verification methods and these methods can be grouped into four main categories, namely: a) neighbourhood, b) scale separation, c) features based and d) field deformation (Gilleland *et al.*, 2009).

However, some of these techniques are similar to the traditional techniques with extra features incorporated to address some of the issues of matching grid points to randomly located stations. While some of these new verification methods might be implemented in the near future, the South African Weather Service (SAWS) has in the past made use of two simple rainfall verification techniques namely: a) point-to-point and b) area average (Ntleko *et al.*, 2012). The different techniques have different computational times and degrees of complexity. This study was a preliminary investigation into determining the value of the two techniques using the 4- and 12 km horizontal resolution precipitation forecast from a NWP model which is operational at SAWS.

## 2. Data and methodology

### 2.1 Forecast and observation data

NWP simulations were done for 4 case studies when wide spread rainfall occurred (15 November 2013, 7 January 2014, 30 January 2014 and 3 February 2014). Two comparison techniques were applied to the model rainfall forecasts and the *in situ* observations. The Weather Research and Forecast (WRF) model was configured using the Advanced Research WRF (ARW) dynamical core for the NWP simulations (Skamarock *et al.*, 2008), and the hindcasts were performed for the four case studies.

The Global Forecast System (GFS) output from the National Centres for Environmental Prediction (NCEP) archive were used for initial and lateral boundary conditions (nomads.ncdc.noaa.gov). All model runs were initialised at 00 UTC. The rainfall observation data consisted of rainfall stations managed by SAWS. The rainfall observation data are valid for 24 hrs from 06 to 06 UTC and the model data were accumulated to represent the same 24 hr period as the observations.

In addition to testing the two comparison techniques, the effect of horizontal resolution was also tested. For this part of the study, the WRF model was run for both 4- and 12 km horizontal

resolutions. Significance tests were computed to determine which technique yields better results.

### 2.2 Comparison techniques

The first technique is the 'grid-to-station' (closest grid point) technique which simply identifies the closest grid point to a specific rainfall station's geographical location. The value of rainfall forecast at that model grid point is then taken as the predicted rainfall value at that observation station, even though the location may be a significant distance from the station grid point.

The second technique is to construct an area of 25 km<sup>2</sup> around each rainfall station; and then to calculate the average of the NWP rainfall in the grid points located within the constructed area. This average predicted value is then taken as the forecast rainfall value at the station location. The observation remains in the centre of the 25 km<sup>2</sup> forecast grid area that was constructed.

The verification package within the R statistical software was used to calculate the statistics (R-project.org). For the continuous rainfall values, the bias, mean absolute error and the root mean square error were calculated in order to determine the accuracy of each model forecast per resolution. From these statistical properties it was possible to evaluate how the two techniques performed for the specific case studies and how they compare using different resolutions. The Matlab software package was used to determine if the difference between the results of the two techniques are significant, by computing Monte Carlo tests.

## 3. Results and discussion

The continuous statistical properties were calculated for both techniques using both horizontal resolutions. The mean error, root mean square error and the mean absolute error is tabulated for both horizontal resolutions (4 km in Table 1 and 12 km in Table 2). The positive values of the mean error indicate that on average the model over-forecasts rainfall for both resolutions. The mean error values of the two techniques are very similar, which also corresponds to what was found from the mean absolute error and the root mean square error as shown in Table 1 and 2. The mean absolute error of the 4 km resolution resulted in slightly smaller errors for both techniques, compared to the 12 km resolutions values.

On the day of the case study on the 3<sup>rd</sup> of February 2014, heavy precipitation occurred over the Northern Cape/North West (Fig. 1). When looking at Tables 1 and 2 we see that the root mean square error for this particular rainfall event when

using both techniques had large errors, compared to the other case studies.

Table1. Mean error (ME), root mean squared error (RMSE) and mean absolute error (MAE) for the two techniques using a 4 km horizontal resolution.

12km	Closest grid point			Area average		
	ME	RMSE	MAE	ME	RMSE	MAE
2013/11/15	5.10	423.16	11.94	5.19	442.11	12.31
2014/01/07	2.96	177.83	7.02	2.44	148.06	6.53
2014/01/30	2.43	164.50	7.17	2.97	214.74	7.71
2014/02/03	0.53	3514.28	9.11	0.48	3516.20	9.28
Average	2.76	1069.94	8.81	2.77	1080.28	8.96

Table2. Mean error (ME), root mean squared error (RMSE) and mean absolute error (MAE) for the two techniques using a 12 km horizontal resolution.

12km	Closest grid point			Area average		
	ME	RMSE	MAE	ME	RMSE	MAE
2013/11/15	3.83	489.06	12.86	3.91	505.41	12.94
2014/01/07	2.10	128.24	6.22	2.30	132.49	6.31
2014/01/30	2.56	162.14	7.34	2.76	181.62	7.63
2014/02/03	0.73	3530.19	9.52	0.83	3564.26	9.60
Average	2.30	1077.41	8.99	2.45	1095.94	9.12

The geographical distribution of the mean error is depicted in Figures 2 (4 km horizontal resolution) and 3 (12 km horizontal resolution). The Figures show how similar the results from the two techniques are when considering the station locations. The regions where the differences

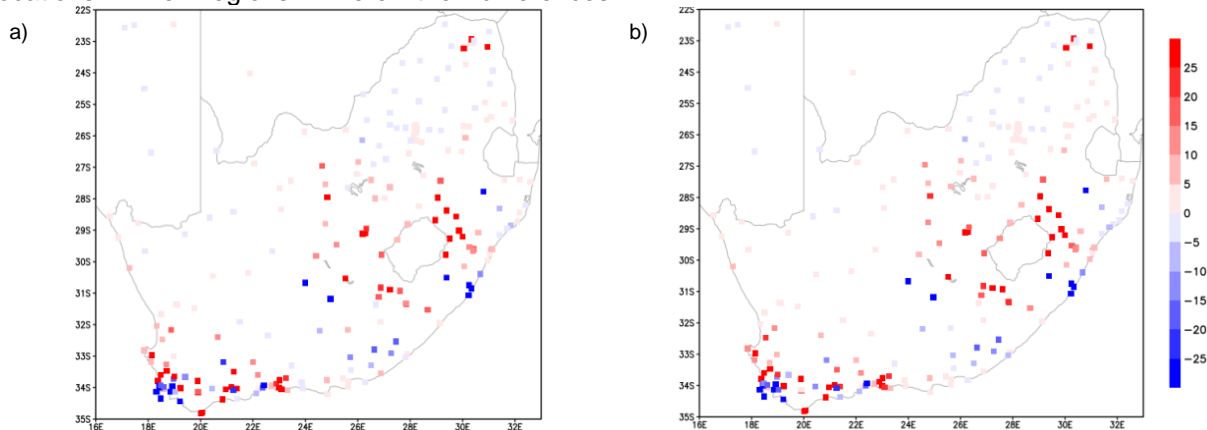


Figure 2. Area statistics of the mean error for the two comparison techniques a) point-to-point technique and b) area average technique using a 4 km horizontal resolution model for the 15<sup>th</sup> of November 2013

between the two techniques are the most are in the Western Cape, KwaZulu-Natal - near the Drakensberg escarpment and eastern Limpopo. The same difference distribution was found for the other case studies (not shown). Furthermore, the resolutions produced very similar results for these tested cases. As might be expected, the 4 km horizontal resolution had a much longer computational time when calculating the area average technique, with the same amount of stations as the grid-to-station technique.

The Spearman correlation coefficient between the observation and the forecasts were calculated for each technique, on both resolutions. From the correlation values the resulting p-values are indicated in Table 3. The miniscule p-values indicate that the forecasts generated, using the different techniques are significant at a 99% level, as  $p < 0.01$  for both techniques on both resolutions (Wilks, 2011).

Table3. P-values resulting from the Spearman correlation coefficient between the observation and forecasts.

p-values	Closest grid point	Area average
4 km	2.1402e-93	5.4215e-99
12 km	5.3951e-72	6.4382e-76

Monte Carlo tests were computed to determine if there is a significant difference between the two techniques. For the 12 km horizontal resolution, the area average technique performed better than the closest grid point technique with a significance level of 0.001. The 4 km horizontal resolution also showed a significant difference between the two techniques, with the area average technique showing improved results at a 0.05 significance level compared to the closest grid point technique.

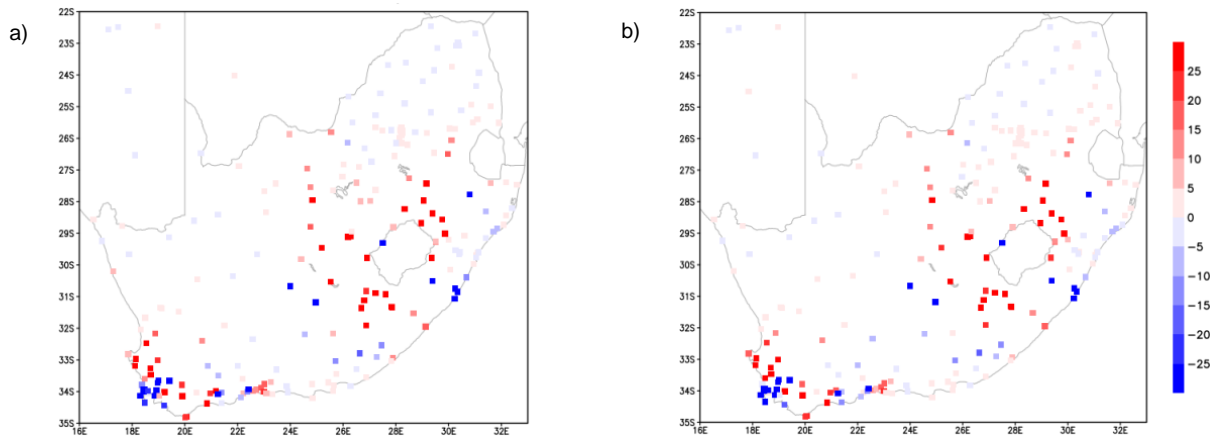


Figure 3. Area statistics of the mean error (ME) for the two comparison techniques a) point-to-point technique and b) area average technique using a 12 km horizontal resolution model for the 15<sup>th</sup> of November 2013

#### 4. Conclusion and Recommendations

The two techniques that were used to compare gridded model data to the randomly located stations were tested on both 4- and 12 km horizontal resolution. Both techniques yielded significant correlations between the forecast and the observation. The two techniques turned out to yield almost identical results for the mean absolute error, root mean square error and the mean error. The two techniques are also similar when the continuous statistics were analysed based on the location. Therefore, significance tests were computed using the Monte Carlo procedure to determine which technique is better. These tests showed that the area average technique provides significantly better results compared to the closest grid point technique. This was the case for both resolutions, using the 4 case studies. However, the area average technique requires more computational time, especially for the 4 km horizontal resolution. Further studies need to be conducted to determine if this is generally true. The impact of station density still needs to be determined. Other verification techniques may also be tested and compared in a similar manner.

#### 5. Acknowledgements

The data, as well as the modelling code and infrastructure needed for the project were provided by SAWS.

#### 6. References

- Ahijevych D., Gilleland E., Brown B.G. & Ebert E.E. 2009, Application of Spatial Verification Methods to Idealized and NWP-Gridded Precipitation Forecasts. *Wea. Forecasting*, **24**:1485–1497.
- Gilleland E., Ahijevych D., Brown B., Casati B. & Ebert E. 2009, Intercomparison of spatial forecast verification methods, *Weather and Forecasting*, **24**(5):1416-1430.
- Jolliffe I. & Stephenson D. 2012, *Forecast verification*, 1st ed., Hoboken: John Wiley & Sons, p. 288.
- nomads.ncdc.noaa.gov. 2014, TdsStaticCatalog <http://nomads.ncdc.noaa.gov/thredds/catalog.html>, [online] Available at: <http://nomads.ncdc.noaa.gov/thredds/catalog.html> [Accessed 23 July 2014].
- Ntleko T., Landman S., Marx E. 2012, The performance of ECMWF 6-day forecasts for the 2011/2012 half-year over the South African domain, South African Society of Atmospheric Science, Conference Paper, **28**.
- R-project.org. 2014, The R Project for Statistical Computing, [online] Available at: <http://www.r-project.org/> [Accessed 02 May 2014]. <http://iges.org/grads/gadoc/gadocinde.html>.
- Skamarock W.C., Klemp J.B., Dudhia J., Gill D.O., Barker D.M., Duda M.G., Huang X., Wang W. & Powers J.G. 2008, A Description of the Advanced Research WRF Version 3, Boulder, NCAR Technical Note (NCAR/TN-475+STR).
- Stanski H.R., Wilson L.J., & Burrows W.R. 1989, Survey of Common Verification Methods in Meteorology, World Weather Watch Tech. Rep. No. 8, TD No. 358, World Meteorological Organization, Geneva, p. 114.
- Warner T.T. 2011, *Numerical weather and climate prediction*, 1st ed., Cambridge, Cambridge University Press p. 526.
- Wilks, D.S. 2011, *Statistical Methods in the Atmospheric Sciences*, 3<sup>rd</sup> ed., Oxford, Academic Press p. 141.

# Study on variability and trend of Total Column Ozone (TCO) obtained from combined satellite (TOMS and OMI) measurements over the southern subtropic

Abdoulwahab M. Tohir\*<sup>1,2</sup>, Venkataraman Sivakumar<sup>2</sup>, Thierry Portafaix<sup>1</sup> and Hassan Bencherif<sup>1</sup>

<sup>1</sup>LACy, UMR 8105, 15 avenue René Cassin Université de la Réunion, St-Denis 97715, Réunion, France.

[mohamed.abdoulwahab@univ-reunion.fr](mailto:mohamed.abdoulwahab@univ-reunion.fr)

<sup>2</sup>School of chemistry and physics, Discipline of Physics, University of KwaZulu Natal, PB: X54001 Durban 4001, South Africa. [vankataramans@ukzn.ac.za](mailto:vankataramans@ukzn.ac.za)

In this paper, the total column ozone (TCO) from TOMS (Total Ozone Mapping Spectrometer) and OMI (Ozone Monitoring Instrument) measurements are merged to form a time series for 15 years of observation over four (4) southern subtropical sites (Melbourne, Buenos Aires, Springbok and Irene). The merged data are applied on Trend-Run model to study variability and trend of ozone observed over the four sites between 1998 and 2012. The Trend-Run is a multi-regression model based on the principle of breaking down the variations of ozone time-series into a sum of several forcings (seasonal cycles, QBO, ENSO, IOD, Solar cycles...) that explain most of its variability. The trend values are from the residual terms as a linear function. A preliminary study has been conducted to validate the merged satellite data by comparing with Dobson measurement. A good agreement that is expressed by regression coefficient ( $R^2$ ) > 0.92 is observed between the ground-based (Dobson) and satellite data for all stations. The results show positive trends over our study sites but more important over Africa (> 1.85% per decade) and Australia (> 1.38 per decade) than the Argentinian region (0.6% per decade). Ozone variability in the subtropical is dominated by an annual cycle, moreover, the weights of semiannual cycle, QBO and solar flux on ozone variability are clearly seen especially over the South African sites.

## 1. Introduction

Ozone plays a key role as it protects biosphere on harmful of ultraviolet solar radiation. Most of ozone is formed on the tropic but transported by the Brewer-Dobson circulation to high latitude and subtropical region where complex process such as the dynamical barrier and the polar vortex have been taken place (Bencherif et al., 2011). Ozone variation in this subtropical zone depends on several parameter such as stratospheric dynamical activity and chemical evolution of ozone depleting substances. Quantifying ozone variability and trends using historical observations is important to understand temporal variability and validating models used to predict future evolution. The Trend-Run model is a statistical tool adapted at Reunion University dedicated to study of ozone and temperature variability and trend estimates (Bègue et al, 2010). This model is adopted in this work to

study the case of South Africa, Australia and Argentina in the subtropical region. Contrarily of northern subtropic, the southern subtropic is poorly documented due to the limited number of observation sites. Satellite observation offer the best way for providing ozone measurements with good spatial coverage. The Total Ozone Mapping Spectrometer (TOMS) data is the primary continuous record of satellite based observation available to monitor total ozone for long-term and study the trend at global and regional scale. TOMS instrument have been successfully flown onboard several satellites from 1978 to 2006; the latest instrument was aboard the Earth Probe (EP) satellite operational from 1996 to 2006. In the frame of EOS (Earth observation System) program, TOMS is replaced by OMI (Ozone Monitoring Instrument) instrument launched onboard Aura satellite since July 2004 and operational up to now. OMI and

EP/TOMS data are combined to form the time - series used in this work. Uncertainties of satellite measurements are high than most of ground based, thus it is advisable to compare satellite data with ground based in order to validate satellite data before used for scientific purpose. In the present work, the combined satellite data is validated using Dobson spectrometer data recorded over collocated stations. The merged satellite is used after validation to study the variability and estimate the trend over the subtropical selected sites. This paper is organized as follow: next section gives brief description of instruments and method used for data combination and comparison. The obtained results on validation of satellite data, the variability and trend estimate are given in the section 3. A summary is presented in the last section.

## 2. Data source and analysis

### 2.1. Data Source

TOMS instrument have been onboard for the first time on Nimbus-7 (1978-1993), then Meteor-3 (1991-1994), ADEOS (1996-1997) and Earth Probe (1996-2006). The TOMS mission is to provide a global map of atmospheric ozone distribution with high resolution. TOMS measure Total Column Ozone (TCO) and others species such as sulfur dioxide. TCO used in this work are the version 8 overpass of EP/TOMS Satellite. As the previous TOMS instrument, EP/TOMS measured TCO by observing both incoming solar energy and backscattered ultraviolet radiation at six different wavelengths (379.95nm, 359.88nm, 339.66nm, 331.06nm, 317.35nm and 312.34nm). More detail on TOMS description and operator mode, readers may refer to McPeters, (1998).

OMI instrument is flown onboard Aura satellite since 15 July 2006 into a near polar sun-synchronous orbit at 705 km. OMI is a compact nadir viewing, wide swath, which measures atmospheric trace gas concentrations such as ozone and nitrogen, as well as cloud and aerosol properties in three broad spectral regions (UV-1, UV-2, and VIS). OMI has a spectral resolution of the order of ~0.5nm. OMI provide two (2) product of TCO: the OMI DAOS and OMI TOMS. However the OMI TOMS TCO overpass products Version 8 are used in this paper and are retrieved using two wavelengths (317.5 nm and 331.2 nm under most conditions while 331.2 nm and 360 nm are used for high ozone and high solar zenith angle). For more information on OMI instrument, the reader may refer to OMI Algorithm

Theoretical Basis Document Volume II (Bhartia, 2002).

Regarding the ground based data source, the Dobson data from collocated stations are chosen as reference to validate satellite observation. The Dobson spectrophotometer principal is based on the differential absorption method in the ultraviolet Huggins band where ozone exhibits strong absorption features. Total ozone observations are made with the Dobson spectrophotometer by measuring the relative intensities of selected pairs of ultraviolet wavelengths. The most used are the double pair (305.5/325.5 nm and 317.6/339.8 nm) and (311.45/332.4 nm and 316.6/339.8 nm) emanating from the sun, moon or zenith sky. One may refer to Khomyr et al., (1993) for further information on Dobson instrument and its operating mode.

### 2.2. Data analysis

First data analysis consist to compare the monthly mean of combined satellite data with ground measurements from Dobson using statistical descriptive method. Comparison index used are bias, RMS (Root Mean Square), correlation and relative difference (RD) between Dobson and satellite. RD for a given month 'm' is calculated as

$$\text{follow: } RD_m = 100 \times \frac{Sat_m - Dobson_m}{Dobson_m} \quad (\text{eq.1})$$

$Dobson_m$  and  $Sat_m$  represent the monthly mean values of Dobson and Satellite dataset respectively. During the simultaneous period of TOMS and OMI observation (October 2004-december 2006) a good agreement in term of correlation ( $R^2 > 0.98$ ) is observed between TOMS and OMI observations for all station. However, rarely TOMS measurement are slightly higher than OMI. The observed bias between OMI and TOMS for individual station is used to adjust the two observations. The merged satellite data of a given station is taken as the mean of adjusted measurement.

## 3. Results

### 3.1. Comparison between satellite and Dobson measurements

The monthly mean of TCO observed by Dobson Instrument from January 1998 to December 2012 over four subtropical sites are compared with the combined satellite data recorded over collocated stations. Good agreement is found between the two observations. Figure 1 present time-evolution of TCO observed over springbok by ground based and satellite instrument. It is clearly seen that Dobson

measurement fit well the combined satellite data. The observed agreement through figure 1 is quantified by regression coefficient  $R^2 = 0.95$  and bias evaluated at  $-0.30 \pm 1.69\%$  between measurements.

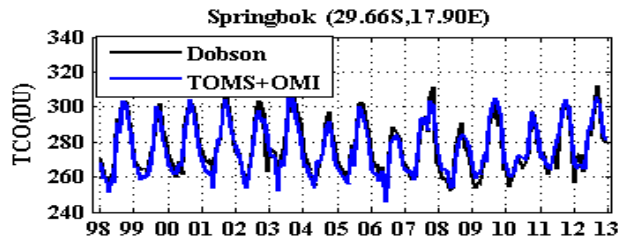


Figure 1: TCO from Dobson and combined satellite observed over Springbok from 1998 to 2012.

Result obtained on comparative study between Dobson and satellite data on the 4 subtropical sites are summarized on table 1. One can see through Table 1 the existence of good agreement between measurements for the four (4) selected sites.

Table 1. Comparison between satellite and Dobson instrument data for the period from January 1998 to December 2012 on Melbourne (Melb), Buenos Aires (Buen), Springbok (Spri) and Irene (Iren)

	Lat	Long	% bias	RMS (DU)	$R^2$
Melb	-37.80	144.97	$1.42 \pm 1.32$	4.86	0,99
Buen	-34.58	-58.48	$1.80 \pm 1.67$	5.70	0,97
Spri	-29.66	17.90	$-0.30 \pm 1.69$	4,72	0,95
Iren	-25.91	28.21	$0.41 \pm 2.04$	4.14	0,92

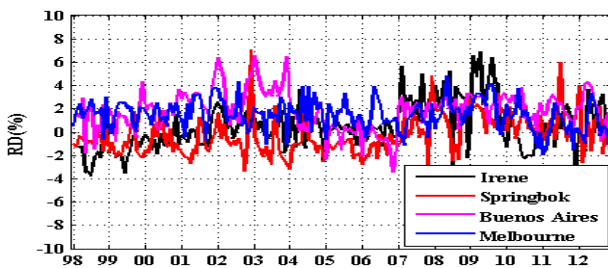


Figure 2. Relative difference between Dobson and combined satellite observed over 4 subtropical sites

Relative difference in percentage is presented on figure 2. The recorded difference is found to be low and within  $\pm 4\%$  for most of cases. Moreover some isolate cases are observed where difference is high than 4% but non-significant ( $< 8\%$ ). Because of this agreement, combined satellite data can be used in subtropical region to study long-term variability and predict future evolution of ozone.

### 3.2. Study on Variability and trend based on Trend-Run model.

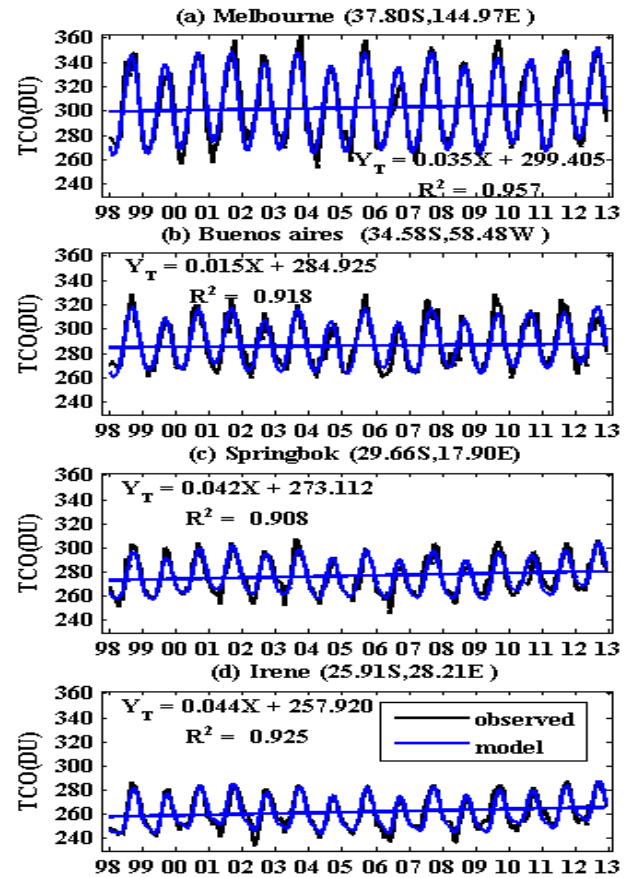


Figure 3. TCO observed by satellite (black) over selected subtropical sites and modeled by Trend-Run (blue).

Variability of TCO monthly mean observed between January 1998 and December 2012 is performed using the Trend-Run model. Inputs parameters are time-series of TCO monthly mean, Quasi-Biennial oscillation (QBO), El Niño Southern Oscillation (ENSO), Sunspot number of the 11 years solar cycle (SC), annual and semiannual cycle (AC and SAC). The annual and semiannual cycle are taken as being the mean of seasonal cycle. The Trend is parameterized as first degree linear function where the trend over the time scale is estimated based on slope function. Figure 3 exhibits the model time-evolution (blue curve) of TCO as defined by the Trend-Run for each selected sites. Black curve represent satellite observation.  $R^2$  is the correlation coefficient between model and observation; while  $Y_T(X)$  represent the trend equation estimated by the model through time (month). A Good Agreement between the model and observation is apparent in

figure 3. A coefficient  $C^2$  is used to quantify how well the fitting model describes the observed data. The coefficient is defined as the ratio of regression sum of squares to the total sum of squares.  $C^2$  measures the proportion of the total variation in total ozone in time, explained by the model. When the model explain all variability of signal,  $C^2$  is close to unity and zero on the other hand (Bencherif et al., 2006). The obtained coefficient  $C^2$  are 0.92, 0.84, 0.82 and 0.85 for Melbourne, Buenos Aires, Springbok and Irene respectively. These results explain that the Trend-Run model described the most of part of total ozone variability on the selected subtropical sites. Contribution from each forcing on total ozone variability is presented on table 2.

Table 2: Variability and trend of total ozone as estimated by Trend-Run on Melbourne (Melb), Buenos Aires (Buen), Springbok (Spri) and Irene (Iren).

	$C^2$	%CA	%CSA	%CS	%QBO	% ENS O	% Trend
Melb	0.92	84.07	0.86	0.70	1.93	0.10	1.38
Buen	0.84	72.45	0.94	0.41	3.48	0.77	0.62
Spri	0.82	64.27	2.77	3.49	3.17	0.10	1.85
Iren	0.85	62.01	7.06	3.55	3.88	0.27	2.04

Table 2 shows variability dominated by annual cycle (>62% for all stations) with positive gradient from tropical to mid-latitude region. The semiannual cycle exhibits also latitudinal dependence with negative gradient from tropical to middle-latitude region. Wherever the influence of semiannual cycle is not well pronounced (< 1%) on sites near middle latitude region. As well as solar flux influence on variability is not significant (<1%) on Melbourne and Buenos-Aires compared to Irene and springbok (station near tropical region). Furthermore QBO contribution on variability is clearly observed over the all stations. Contrarily the influence of ENSO do not carry enough contribution on ozone variability over the southern subtropical region.

Last column of Table 2 present the trend of total ozone in percentage per decade as estimated by Trend-Run from 1998 to 2012 on the selected subtropical site. Obtained result show an upward trend of total ozone over the subtropical during our time of observation. Moreover the observed trend is high in South Africa and Australia than Buenos Aires station. Note that this work is under development in order to understand the reason of observed variability and trend over our study region.

## 4. Summary and Conclusion

After having observed good agreement between Dobson and a combined satellite observation over the subtropical region, the satellite data is used to study variability and trend based on Trend-Run model. It is shown that the model fits the satellite observation well and describes most of ozone variability over the study region. Obtained variability exhibits latitudinal dependence and the influence of annual cycle and QBO on variability is clearly observed. Upward trend is observed but lower at Buenos Aires compared to other sites in South Africa and Australia.

## 5. Acknowledgments

The first author (AMT) acknowledges the Indian Ocean Bureau of AUF (Agence Universitaire de la Francophonie) and the University of KwaZulu Natal for travel and hosting under invited student exchange on the ARSAIO France- South African bilateral research project (UID 68668). The authors are thankful for the different individuals who have made the effort on data-sets used in this study via their website.

## 6. References

- Bencherif H. et al. 2011, 'Analysis of a rapid increase of stratospheric ozone during late austral summer 2008 over Kerguelen (49.4° S, 70.3° E)' *Atmos. Chem. Phys.*, 11, pp.363-373
- Bencherif H. et al. , 2006 ' Temperature climatology and trend estimates in the UT-LS region as observed over a southern subtropical site, Durban , South Africa' *Atmos. Chem. Phys.*, 6, pp.5121–5128,
- Bègue N. et al. 2011, 'Temperature variability and trend in the UT-LS over a subtropical site: Reunion (20.08S, 55.5E)' *Atmos. Chem. Phys.*, 10, pp.8563-8574
- Bhartia P. K. 2002, 'OMI Algorithm Theoretical Basis Document Volume II, OMI Ozone Products', ATBD-OMI-02, Version 2.0.
- Komhyr W. D. et al. 1993, 'Effective Bass-Paur 1985 Ozone Absorption Coefficients for Use with Dobson Ozone Spectrophotometers', *J. Geophys. Res.* Vol.98 D11 pp.20451-20465.
- McPeters R. D. 1998, 'Earth Probe Total Ozone Mapping Spectrometers (TOMS), Data product User's Guide' Naza Technical Publication, 1998-206895

# Maize yield simulations for small-scale farmers using APSIM for making on-farm decisions in Bethlehem and Bloemfontein, South Africa

Cassia N Mlangeni<sup>1</sup>, Linda De Wet<sup>1</sup> and Weldemichael A Tesfahuney<sup>1</sup>

<sup>1</sup>Dept. Soil, Crop and Climate Sciences, University of the Free State, P.O. Box 339, Bloemfontein

Maize is one of the four major cereals that serve as staple food in many parts of the world. Sowing season in South Africa commences in October until December under rain-fed production. Adjustment of management practices such as sowing dates, fertilization levels and plant densities affect maize yield. Use of crop growth simulation models such as APSIM can help determine favourable management options for improved yield. Results indicate that sowing early and in mid-season is suitable for Bethlehem, while Bloemfontein results indicated all planting dates to be suitable. Application of fertilizers and high plant population are favourable for both areas. Therefore, APSIM could play a significant role in understanding crop agronomic characteristics for various on-farm management adaptation strategies in reducing risks and improving yield.

**Keywords:** *Semi-arid, Maize, sowing date, plant population, fertilization, APSIM*

## 1. Introduction

In arid and semi-arid areas, the maize production levels are low and crop failures are frequent. For example, in the semi-arid areas of central and eastern part of Free State, South Africa, the cultivation of maize production by small-scale farmers is characterized by highly variable rainfall and low soil fertility (du Plessis 2003). In these semi-arid areas, improvement of the current maize is therefore a major challenge for researchers, extension officers and farmers. In South Africa, maize in the rain-fed regions is usually planted from October to December and harvested in March to May (du Pisani *et al.* 1998; Nape 2011; Baloyi 2012). Late sowing (December/January) can result in poor harvest as growing season is shorter. Thus, on-farm management decisions are strategies that minimize the potential negative impacts of climate change, while maximizing options of adjustment of sowing dates, cultivar, plant densities, fertilization and other adaptation strategies which are all crucial for better production.

During recent years, several crop growth simulation models were frequently used for climate change and variability studies to incorporate the effect of soil-crop and climate continuum. Crop growth and development as influenced by climate variability can be estimated by crop growth simulations models such as Support System for Agrotechnology Transfer, DSSAT (Jones *et al.* 2003) and APSIM (Keating *et al.* 2009). As a result, models are of importance and can be used to provide information about different management options. Thus, reliable

simulation results are vital for farmers in making on-farm decisions for better maize production in semi-arid areas. Furthermore, a combination of a seasonal forecast information and model simulation results to decide on management practices can also maximise profitability and yields by reducing climate risk vulnerability (Keating *et al.* 2003; CSRIO n.d.).

With the changing climate and rainfall variability, rain-fed agricultural production (as is the case for semi-arid areas of Bloemfontein and Bethlehem) can be negatively affected. Yield can be reduced if crop management practices are not changed to adapt to the changing climate. Maximum yields can thus be obtained with implementation of successful adaptation management strategies. This study hypothesised that adjustment of different management practices will affect maize yield improvements. The aim of the study was therefore, to assess the effect of different sowing dates under various fertilization levels and plant densities in two semi-arid areas of Free State, South Africa by using Agricultural Production system Simulator (APSIM).

## 2. Materials and methods

Two semi-arid areas of Free State, South Africa were selected for long-term maize yield simulation, using APSIM. These two study areas, Bloemfontein and Bethlehem are located in the central and north-eastern part of the Free State and are suitable for dryland maize production. However, both areas possess different soil properties, rainfall characteristics and temperatures that influence on-farm management decision making. Therefore, it is important to take

into account the variations in soil, climate and management options for better assessment of the model simulation results.

Daily climate data of 41 years (1959 to 1999) for Bethlehem and Bloemfontein were obtained from the quaternary catchment, QC C52H (Schulze *et al.* 2005). Weather variables included: daily rainfall, minimum and maximum temperatures, solar radiation, and reference evapotranspiration. The data were manipulated accordingly and formatted for entry into the crop simulation model. Cumulative Distribution Function (CDF) graphs were constructed to show rainfall variability between the two locations (Bloemfontein and Bethlehem). The soils at two study areas were chosen according to the land-type data base obtained from the Agricultural Research Council (ARC 2006), which includes key soil parameters required by the model.

In the study, the APSIM-Maize model was used to simulate potential changes in maize physiological responses (yields, biomass and extractable soil water in a daily time step) using different historical climate data. The model was parameterized, calibrated and evaluated to simulate the small-scale maize production systems practiced in the study areas.

In the model simulations, effects of sowing date on yield were shown by CDF results from the model output. Using a maize medium maturing cultivar (PAN6479), a total of 36 management strategy combinations that are frequently used by maize growers were applied. Three adaptation strategies were selected in this study, *viz.*, sowing date, plant population and fertilization levels. Sowing date comprised early, mid and late season sowing. Low plant population density refers to 8,000 plants ha<sup>-1</sup>, medium plant population density to 12,000 plants ha<sup>-1</sup> and high plant population density to 18,000 plants ha<sup>-1</sup>. Fertilizer levels used ranged between no fertilizer application (0 kg ha<sup>-1</sup>) and 120 kg ha<sup>-1</sup>. Therefore, in order to assess historical conditions, APSIM was set up to simulate all these management combinations with historical weather conditions for rain-fed maize growing under small-scale farming systems. The non-exceedance graphs were constructed on the basis of historical data to evaluate the probability that will not exceed the amount of expected yield for different scenarios.

### 3. Results and discussion

Figure 1 shows that the correlation between observed (DAFF 2013) and simulated maize yields. R<sup>2</sup> for Bethlehem (BH) is 0.69 high. Bloemfontein (BF) indicates a lower R<sup>2</sup> of 0.51. The model can be used with reasonable accuracy for both study areas, by considering the observed data used for verification are only district mean values, assuming the common cultural practices used by small scale farmers in the district.

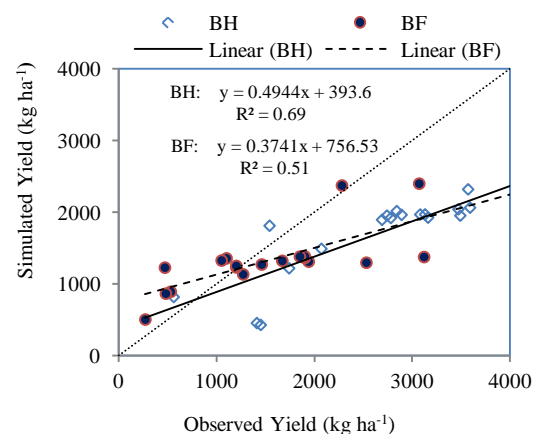


Figure 1 Correlation between the observed and simulated maize yields for Bethlehem and Bloemfontein (1959-1999).

The simulated mean yield values with standard deviations for both study areas are summarized in Table 1. In both study areas, the simulated mean yield showed higher in early and intermediate planting dates compared to late planting in January with addition of various N fertilizers for both low and high plant populations. However, with fertilization in Bethlehem, December planting yield simulations (1409 - 1689 kg ha<sup>-1</sup>) gave near to half of the October planting (2780 - 2950 kg ha<sup>-1</sup>) while planting in October, November and December in Bloemfontein showed closer yields in the range of 2000 - 2230 kg ha<sup>-1</sup>. It is apparent that late planting in January is only advantageous with low amount of fertilization and low plant populations.

#### Early sowing

Under low plant population density, slightly higher yields probabilities of non-exceedance are visible for Bloemfontein (Figure 2a) as compared to Bethlehem where fertilizers are not applied. For example, Bloemfontein yield is 841.1 kg ha<sup>-1</sup> and is higher than 836.6 kg ha<sup>-1</sup> for Bethlehem at 50% probability of non-exceedance. However, with application of fertilizers, Bethlehem indicates fairly higher yields than Bloemfontein (Figure 2a).

Table 1 Simulated mean yields for different sowing dates under 4 levels of fertilization using low and high plant populations

Sowing dates	Pl. Pop. (pl.ha <sup>-1</sup> )	Low (8000)				High (18000)			
		Fert. (kg ha <sup>-1</sup> )	0	30	60	120	0	30	60
Bethlehem	Oct.	173	1110	1129	1553	200	2780	2883	2950
		(95)*	(474)	(475)	(468)	(78)	(653)	(703)	(695)
		179	1078	1080	1478	166	2226	2547	2558
		(66)	(461)	(578)	(479)	(54)	(580)	(621)	(641)
		70	1034	1030	957	154	1689	1390	1409
Bloemfontein	Oct.	410	707.6	610	790	603	2143	2191	2227
		(180)	(355)	(328)	(371)	(254)	(926)	(986)	(996)
		330	1029	1029	1178	639	2030	2154	2075
		(156)	(463)	(511)	(459)	(239)	(875)	(838)	(884)
		220	1023	1024	1226	257	1999	2205	2199
Bethlehem	Nov.	188	639	639	707	27	522	496	522
		(53)	(296)	(292)	(274)	(14)	(270)	(251)	(330)
		179	1078	1080	1478	166	2226	2547	2558
		(66)	(461)	(578)	(479)	(54)	(580)	(621)	(641)
		70	1034	1030	957	154	1689	1390	1409
Bloemfontein	Nov.	410	707.6	610	790	603	2143	2191	2227
		(180)	(355)	(328)	(371)	(254)	(926)	(986)	(996)
		330	1029	1029	1178	639	2030	2154	2075
		(156)	(463)	(511)	(459)	(239)	(875)	(838)	(884)
		220	1023	1024	1226	257	1999	2205	2199
Bethlehem	Dec.	166	835	884	704	64	343	377	378
		(84)	(238)	(301)	(249)	(32)	(124)	(158)	(186)
		179	1078	1080	1478	166	2226	2547	2558
		(66)	(461)	(578)	(479)	(54)	(580)	(621)	(641)
		70	1034	1030	957	154	1689	1390	1409
Bloemfontein	Dec.	410	707.6	610	790	603	2143	2191	2227
		(180)	(355)	(328)	(371)	(254)	(926)	(986)	(996)
		330	1029	1029	1178	639	2030	2154	2075
		(156)	(463)	(511)	(459)	(239)	(875)	(838)	(884)
		220	1023	1024	1226	257	1999	2205	2199
Bethlehem	Jan.	188	639	639	707	27	522	496	522
		(53)	(296)	(292)	(274)	(14)	(270)	(251)	(330)
		179	1078	1080	1478	166	2226	2547	2558
		(66)	(461)	(578)	(479)	(54)	(580)	(621)	(641)
		70	1034	1030	957	154	1689	1390	1409
Bloemfontein	Jan.	410	707.6	610	790	603	2143	2191	2227
		(180)	(355)	(328)	(371)	(254)	(926)	(986)	(996)
		330	1029	1029	1178	639	2030	2154	2075
		(156)	(463)	(511)	(459)	(239)	(875)	(838)	(884)
		220	1023	1024	1226	257	1999	2205	2199

\*Brackets indicate the standard deviations of the mean simulated yields.

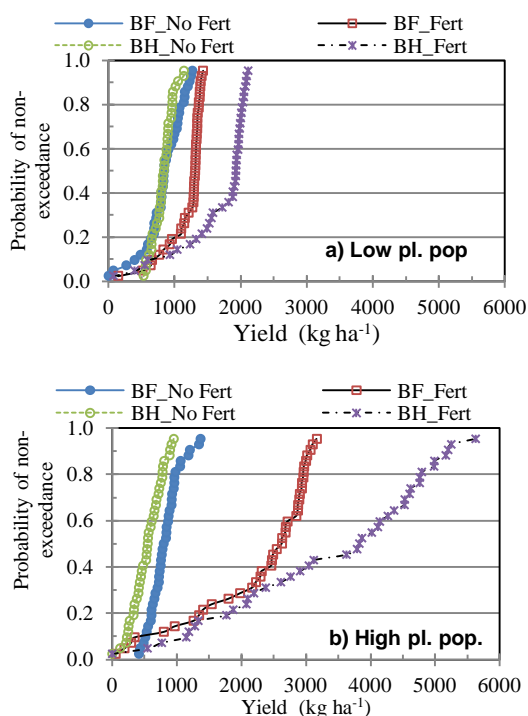


Figure 2 CDF graphs (a) low b) high plant population (pl. Pop) for Bethlehem and Bloemfontein (1959-1999).

Fertilizer application shows higher yields in Bethlehem (1926.1 kg ha<sup>-1</sup>) than in Bloemfontein (1309.2 kg ha<sup>-1</sup>) at 50% probability of non-exceedance (Figure 2a). Bloemfontein continues to show higher yield probability (796.2 kg ha<sup>-1</sup>) under high plant population density with no fertilizer application compared to Bethlehem (Figure 2b) with 549.6 kg ha<sup>-1</sup>. On the other hand, Bethlehem yield probability is still higher (3823.5 kg ha<sup>-1</sup>) than the yield of Bloemfontein (2627.0 kg ha<sup>-1</sup>) when fertilizer is applied. Early sowing with fertilizer application proves to be effective for Bethlehem maize producer because of the

response in yield. It is true that Bloemfontein yield is lower than Bethlehem yield but there is a clear improvement with fertilizer application in both cases.

#### Mid-season sowing

Bloemfontein yield probability (913.6 kg ha<sup>-1</sup>) is higher than 748.1 kg ha<sup>-1</sup> of Bethlehem (Figure 3a) under low plant population density and no fertilizer application. The low plant population density results indicate 50% probability that maize yield in Bloemfontein would not exceed 1318 kg ha<sup>-1</sup> with application of fertilizers (Figure 3a). Bethlehem yield probability under low plant population density is again lower (836.3 kg ha<sup>-1</sup>) than Bloemfontein yield. Bloemfontein continues to show yield probability of 694.6 kg ha<sup>-1</sup> under high plant population density and no fertilizer application, while Bethlehem has yield probability of 493.8 kg ha<sup>-1</sup>. Application of fertilizer at high plant population brings a remarkable change where yield probability in Bethlehem is 4239 kg ha<sup>-1</sup>, thus higher than the Bloemfontein yield of 2676 kg ha<sup>-1</sup> at 50% probability of non-exceedance (Figure 4b).

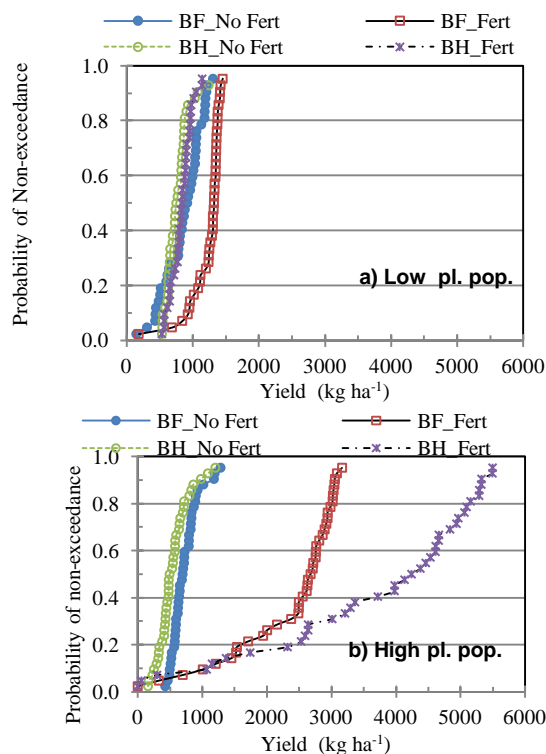


Figure 3 CDF graphs (a) low b) high plant population (pl. Pop) for Bethlehem and Bloemfontein (1959-1999)

#### Late sowing

Yield in Bloemfontein is slightly higher (683.8 kg ha<sup>-1</sup>) than yield in Bethlehem (652.2 kg ha<sup>-1</sup>) under low plant population density without

fertilizer application. The graphs for Bloemfontein and Bethlehem in this regard are very close and difficult to distinguish (Figure 4a). When fertilizer is applied under low plant population density (Figure 4a), however, Bethlehem yield probability is higher (1914.7 kg ha<sup>-1</sup>) when compared to Bloemfontein yield probability (1288.1 kg ha<sup>-1</sup>). Bloemfontein yield lies at 2506.6 kg ha<sup>-1</sup>, which is higher than Bethlehem (773.9 kg ha<sup>-1</sup>) when sowing is done under high plant population density and fertilizer application (Figure 4b).

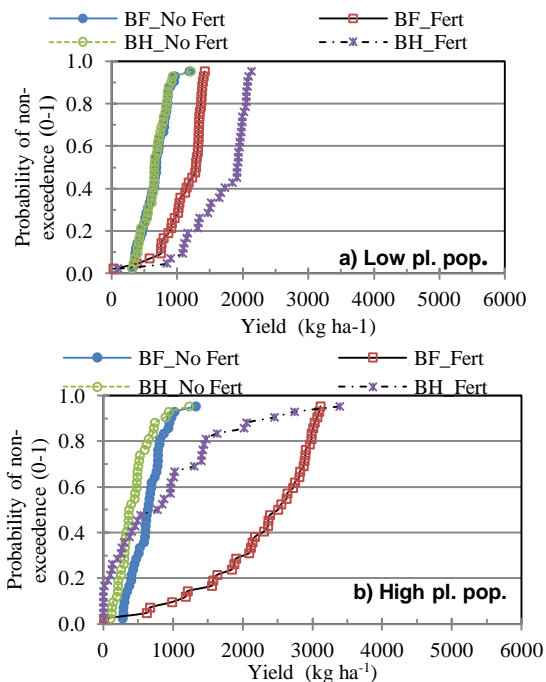


Figure 4 CDF graphs a) low b) high plant population density for Bethlehem and Bloemfontein (1959-1999).

#### 4. Conclusions

The use of crop models can help reduce the negative impacts of climate variability where the user is able to see the impacts of various management decisions on the yield. From APSIM-Maize simulations, it was indicated that early, mid-season and late sowing (October to December) are all suitable for Bloemfontein under high plant population density (18,000 plants ha<sup>-1</sup>) and high fertilizer level application (120 kg ha<sup>-1</sup>). In the case of Bethlehem, it is more suitable to choose early and mid-season sowing (October and mid-November) under high plant population density and high fertilizer level application. As a result, APSIM model can serve as an effective tool to help farmers with decision-making if used in combination with accurate seasonal weather forecast information. Therefore, crop models such

as APSIM could play a significant role in understanding crop agronomic characteristics for various on-farm management adaptation strategies in reducing risks and improvement of maize yield.

#### References

- Agricultural Research Council 2006, Land Type Survey Staff, 2006. Land types of South Africa: Digital map (1:250 000 scale) and soil inventory datasets. Agricultural Research Council - Institute for Soil, Climate and Water, Pretoria
- Baloyi C.D., 2012, Evaluation of selected industrially manufactured Biological Amendments for Maize Production. PhD Thesis. University of the Free State, Bloemfontein, South Africa.
- CSIRO n.d. Simulating agricultural production with APSIM. [Online]. Retrieved from <http://www.csiro.au/Organisation-Structure/Flagships/Sustainable-Agriculture-Flagship/APSIM.aspx> (Accessed 24/11/2013).
- DAFF 2013, Maize yield data obtained from Dept. of Agriculture, Forest and Fisheries (DAFF), Pretoria.
- Du Pisani L.G., Fouche H.J., & Venter J.C., 1998, Assessing rangeland drought in South Africa. *Agricultural Systems*, 57(3), 367-380.
- Du Plessis J. 2003. Maize Production. Department of Agriculture. [Online]. Retrieved from <http://www.arc.agric.za/arc-gci/Fact%20Sheets%20Library/Maize-infopak.pdf> (Accessed 24/11/2013).
- Jones J.W., Hoogenboom G.M., Porter C.H., Boote K.J., Batchelor W.D., Hunt L.A., Wilkens P.W., Singh U. Gijsman A.J. & Ritchie J.T. 2003, The DSSAT Cropping System Model. *European Journal of Agronomy*. 18: 235-265.
- Keating B.A., Carberry P.S., Hammer G.L., Probert M.E., Robertson M.J., Holzworth D. Huth N.I., Hargreaves J.N.G., Meinke H. Hochman Z. McLean G. Verburg K. Snow V. Dimes J.P., Silburn M. Wang E. Brown S. Bristow K.L., Asseng S. Chapman S. McCown R.L., Freebairn D.M., & Smith C.J., 2003, An overview of APSIM, a model designed for farming systems simulation. *European Journal of Agronomy*. 18: 267-288.
- Nape K.M., 2011, Using seasonal rainfall with APSIM to improve maize production in the Modder river catchment. Masters' thesis. University of the Free State, Bloemfontein, South Africa.

# Influence of horizontal resolution and ensemble size on model performance

Amaris Dalton\*<sup>1</sup>, Willem A. Landman <sup>1,2</sup>

<sup>1</sup>Department of Geography, Geo-informatics and Meteorology, University of Pretoria, Pretoria, South Africa  
dalton.amaris1@gmail.com

<sup>2</sup>Council for Scientific and Industrial Research, Natural Resources and the Environment Pretoria, South Africa  
walandman@csir.co.za

Computing costs increase with an increase in global model resolution and ensemble size. This paper strives to determine the extent to which resolution and ensemble size affect seasonal forecast skill when simulating mid-summer rainfall totals over southern Africa. Furthermore a comparison is made between forecast skill of the 850 hPa geopotential heights and raw model rainfall outputs. The determination of skill was done by way of empirical post-processing procedures in order to project ensemble mean model forecast fields onto observed gridded mid-summer rainfall over South Africa. Spearman rank correlations are initially used to compare the performance of models with varying horizontal resolution as well as ensemble size. Further verification is also done on a set of probabilistic hindcasts through ROC scores and reliability diagrams. Skill increases with an increase in ensemble size and an increase in model resolution when 850 hPa geopotential heights are used to downscale to gridded rainfall, but when raw model rainfall is used for the downscaling similar improvement in skill is not observed. Finally, even with the best configuration (increased resolution and ensemble size) forecasts tend to be over-confident for both wet and for dry conditions notwithstanding their ability to discriminate.

*Keywords:* Model performance, canonical correlation analysis, Spearman correlation, ECHAM5, geopotential height, Southern Africa

## 1. Introduction

High computing costs result from running global models at high resolutions and for large ensembles (Mullen & Buizza 2002). With modeling studies it was found that with large scale structures represented by the 850 hPa temperature and the 500 and 1000 hPa geopotential heights, an increase in horizontal resolution lead to advances in short range forecast skill (Buizza 2010). Medium range forecasts however, showed no sensitivity to resolution (Buizza 2010). In this study, results based on hindcasts produced by a state-of-the-art global circulation model will be tested to ascertain whether the same is true for long range forecast skill.

This paper strives to determine the extent to which horizontal resolution and ensemble size effect skill of seasonal rainfall forecasts by considering the low level atmospheric circulation of a coupled model as predictor for seasonal rainfall totals. This skill analysis was done by comparing two configurations of the ECHAM5 atmospheric general circulation model (AGCM): horizontal resolutions of T42 (2.8°×2.8°) and T85 (1.4°×1.4°), over the study area.

A range of ensemble sizes was considered as a function of forecast performance for each resolution. A comparison was made between skill offered by using 850 hPa geopotential heights or raw model rainfall hindcasts as predictors in a simple statistical downscaling model. To achieve this aim it was decided to develop empirical post-processing procedures in order to project model forecast fields onto observed gridded mid-summer rainfall over South Africa (Landman & Beraki 2012). Furthermore, it was necessary to perform forecast verification for a range of ensemble sizes and the two horizontal resolution configurations.

Within this study hindcasts made by various configurations of the ECHAM5 atmospheric general circulation model (AGCM) were cross-correlated with observed data. Standard verification procedures were employed to ascertain which of these hindcasts were most skillful.

## 2. Data

Hindcasts of the geopotential heights at the 850 hPa level and hindcasts of raw model rainfall fields, were obtained from the data library of the International Research Institute of Climate and Society (IRI). These hindcasts were produced by the Max Planck Institute for Meteorology AGCM, ECHAM5. Roeckner *et al.* (2003) gives a comprehensive model description of ECHAM5.

Hindcasts were obtained for the December to February (DJF) season for the period 1979/80 to 2003/2004 for each resolution and a range of ensemble sizes. The ensemble sizes were: 4, 8, 12 and 16 members. These data served as the predictor fields whereas observed rainfall obtained from the Climate Research Unit (CRU) data set served as predictant fields. The CRU database is compiled of station observations of six variables over the entire globe, excluding Antarctica, which is later interpolated onto a 0.5° grid. As quality control, these data were compared to station records by a computerized method and uses neighboring stations as a reference series. Though this method does not have the advantages of manual checking, it is indispensable when considering vast amounts of data (Mitchell & Jones 2005). 850 hPa geopotential heights are obtained from NCEP reanalysis for the same period. These data will serve as an indicator of whether the skill attained from the downscaling done to the ECHAM5 850 hPa geopotential heights projections is justified or coincidental.

## 3. Methodology

The 850hPa geopotential height fields of the ECHAM5 AGCM were statistically downscaled to the DJF rainfall season over southern Africa. DJF was found to be a very good season for predictability studies due to southern Africa being dominated by tropical influences during this period (Landman & Beraki 2012). The AGCM predictor fields were confined over a domain between 20°S and 37°S, and 14°E to 35°E. The observed rainfall covers the domain between 22°S and 35°S, and 16°E and 33°E. The predictand fields cover a smaller area than the predictor fields so that any large scale systems that might have an impact on the smaller (observed) domain might be contained within (Lazenby *et al.* 2014). The downscaling was performed for 2 modes of canonical correlation analysis (CCA) over the period from 1979/80 to 2003/04 by projecting the model output onto the observed rainfall.

Similarly the rainfall hindcasts of the various ECHAM5 configurations were projected on the same domain and subsequently cross-correlated to observed gridded rainfall for the same period. Empirical orthogonal function (EOF) analysis was performed on both the predictor and predictand fields in both cases, where fields were separated into orthogonal or independent modes which might be interpreted as atmospheric structures. This procedure was done by transforming the predictor and predictant fields into a new set of variables – the uncorrelated principal components (Jolliffe 2002). Subsequently, to diminish system deficiencies, model output statistic (MOS) equations were developed for the statistical downscaling part to relate the 850 hPa geopotential heights to the gridded rainfall by using CCA (Barnston & Smith 1996). CCA is a viable way of clarifying cross covariance matrices. When allowing for two vectors containing arbitrary variables, CCA will find linear combinations of components of the random vectors which have maximum correlation with each other (Härdle & Simar 2007). Subsequently verification was conducted using the Spearman rank correlation. Relative operating characteristic (ROC) scores and reliability diagrams were obtained for the best configuration. In Spearman correlation ranks are assigned to data, meaning that data consists of integers from 1 to  $n$ , depending on the sample size (Wilks 2011). Spearman correlation serves as an indication as to the strength of monotone relationships and is a robust and resistant substitute for the Pearson correlation.

The p-value, also referred to as the observed significance level, is the smallest value at which the null hypothesis can be rejected (Devore 2011). The null hypothesis would be that there does not exist a correlation between the predictor and predictand fields. A test level of 5% is chosen as this is common, though tests conducted at other levels such as 10% or 1% are not unheard of (Wilks, 2011). Thus small p-values would favor the alternative hypothesis – that there does exist a correlation between predictor and predictant fields. Though there will be no formal rejection or acceptance of the null hypothesis, these p-values would rather serve as an indicator as to the confidence in the null hypothesis or the strength of the correlation.

Relative operating characteristics (ROC) scores and reliability diagram were additionally calculated for the best model configuration. For an explanation as to the interpretation of ROC scores and reliability diagrams are discussed in Troccoli *et al.* (2008),

Barnston et al. (2010) and Wilks (2011) amongst others. Their interpretation is however relevant to the reliability, resolution, discrimination and sharpness of a probabilistic forecast (Troccoli et al. 2008).

Finally, CCA analysis was done between the hindcasts of both the T42 and T85 850 hPa geopotential heights produced by ECHAM 5 and NCEP reanalysis of the same variable. Subsequently, if the NCEP reanalysis is assumed to be reflective of reality, the association between the two fields would serve as an indicator of whether the skill garnered by the downscaling of the 850 hPa geopotential heights onto the observed rainfall, is coincidental or due to the predictor fields in fact being a good representation of reality.

#### 4. Results and Discussion

There is an increase in the number of p-values at the 5% significance level with an increase in ensemble size (Fig. 1). It is also evident from Figure 1 that there are a larger number of p-values at the 5% significance level with the finer resolution of T85 than with T42. Consequently it can be concluded from Figure 1 that the null hypothesis stating the non-existence of a correlation between predictor and predictant fields, is weakened with an increase in ensemble size and resolution, for downscaling of the 850 hPa geopotential heights. Furthermore, for the larger ensemble sets consisting of 12 and 16 members, it is evident that downscaling of the 850 hPa geopotential heights outperforms the raw projected model rainfall as a predictor field for rainfall. A possible reason for this discrepancy is that observed rainfall structures are spatially much smaller than what can be resolved by climate models (Landman & Beraki 2012).

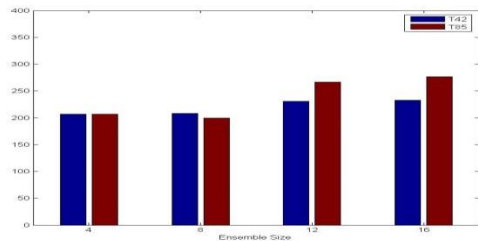


Figure 1. P-values obtained from Spearman correlation between projected 850 hPa geopotential heights and observed rainfall for the T42 (blue) and T85 (red) model runs.

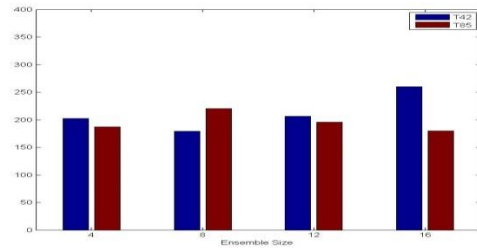


Figure 2. P-values form Spearman correlations between raw model output and observed gridded rainfall for the T42 (blue) and T85 (red) model runs.

Figure 2 illustrates that there is no reliable increase in skill, with an increase in resolution and ensemble size. Despite isolated cases where T85 outperforms the T42, the p-values do not increase with an increasing ensemble and resolution as seen in Figure 1.

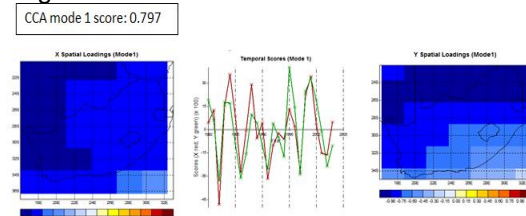


Figure 3

Figure 3. CCA pattern analysis between T42 850 hPa geopotential heights at 16 ensemble members and NCEP 850 hPa geopotential heights reanalysis

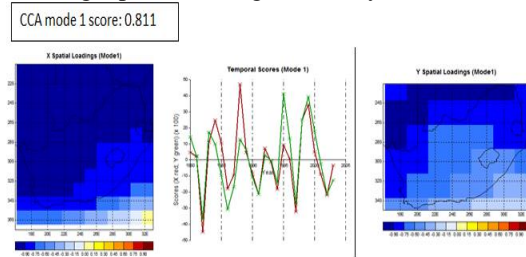


Figure 4

Figure 4. CCA pattern analysis between T85 850 hPa geopotential heights at 16 ensemble members and NCEP 850 hPa geopotential heights reanalysis

From both Figures 3 and 4 it is evident, based on the high CCA scores of 0.797 and 0.811 respectively, that there exists a strong association between the 850 hPa geopotential height hindcasts and the assumed reality of the NCEP reanalysis. Therefore the results portrayed by Figure 1 are physically justified and not coincidental.

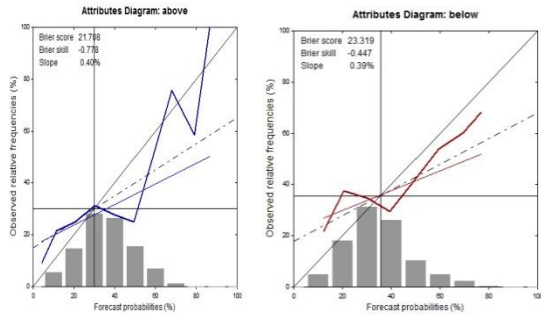


Figure 5. Reliability diagrams of above (left) and below (right) normal rainfall based on retroactive forecasting done using the 16 ensemble members of the T85 850 hPa geopotential heights as predictor and observed rainfall as predictant. The thin straight lines are weighted least squares regression lines of the respective reliability curves.

The ECHAM5 T85 850 hPa geopotential heights for 16 ensemble members (as best configuration) were employed as MOS-based predictors of mid-summer rainfall over the same period used for the p-value assessments. ROC scores of 0.555 (above-normal) and 0.543 (below-normal) were obtained and are indicative of the model's ability to discriminate (a ROC score has to be larger than 0.5 for discrimination to have been achieved). Fig. 5 shows the reliability diagrams obtained from the same run and displays a level of over-confidence for the probabilistic forecasts of both above- and below-normal rainfall totals.

## 5. Conclusion

For the two horizontal resolutions considered here, mid-summer forecast skill improved with increasing ensemble size and an increase in resolution only when using low-level large-scale atmospheric circulation to downscale to observed rainfall totals. Raw model rainfall did not show similar improvement, likely to be a consequence of the model's rainfall not being able to capture the sub-grid features associated with complex mid-summer rainfall patterns over southern Africa.

## 6. References:

Barnston, A.G. & Smith, T.M. 1996, 'Specification and prediction of global surface temperature and precipitation from

- global SST using CCA'. *Journal of Climatology*, **9**:2660–2697.
- Barnston, A. G., Li, S., Mason, S. J., DeWitt, D. G., Goddard, L., & Gong, X. 2010, 'Verification of the first 11 years of IRI's seasonal climate forecasts'. *Journal of Applied Meteorology and Climatology*, **49(3)**:493-520.
- Buizza, R., & Palmer, T.N. 1995, 'The singular-vector structure of the atmospheric global circulation.' *Journal of the Atmospheric Sciences*, **52(9)**:1434-1456.
- Devore, J., 2011, *Probability and Statistics for Engineering and the Sciences*. Cengage Learning.
- Härdle, W. & Simar, L. 2007: 'Canonical Correlation Analysis', *Applied Multivariate Statistical Analysis*. pp. 321–330.
- Jolliffe, I. T. 2002, 'Graphical Representation of Data Using Principal Components' *Principal Component Analysis*, pp. 78-110.
- Landman, W.A. & Beraki, A. 2012, 'Multi-model forecast skill for midsummer rainfall over southern Africa.' *Int. J. Climatol.*, DOI: 10.1002/joc.2273.
- Lazenby, M.J., Landman, W.A., Garland, R.M., & Dewitt, D.G. 2014, 'Seasonal temperature prediction skill over Southern Africa and human health' *Meteorological Applications*.
- Mitchell, T. D. & Jones, P.D. 2005: An improved method of constructing a database of monthly climate observations and associated high-resolution grids. *International Journal of Climatology*.
- Mullen, S. L., & Buizza, R. 2002, 'The impact of horizontal resolution and ensemble size on probabilistic forecasts of precipitation by the ECMWF Ensemble Prediction System.' *Weather and Forecasting*, **17(2)**: 173-191.
- Roeckner, E., Bauml, G., Bonaventura, L., & Brokopf, R. 2003, *The general circulation model ECHAM5. Part I: Model description*. Hamburg, Max-Planck-Institute for Meteorology.
- Troccoli A, Harrison M, Anderson DLT, Mason SJ. 2008, *Seasonal Climate: Forecasting and managing risk*. NATO ScienceSeries. Earth and Environmental Sciences Vol 82. Springer.
- Wilks, D.S. 2011, *Statistical methods in the atmospheric sciences* Vol. 100. Academic press 3d edition.



# Stability, accuracy and conservation properties of a flux-form advection scheme

Michael A. Barnes<sup>1</sup> and Francois A. Engelbrecht<sup>1,2,3</sup>

<sup>1</sup> Department of Geography, Geoinformatics and Meteorology, University of Pretoria, Pretoria, South Africa, u10313029@up.ac.za

<sup>2</sup> Council for Scientific and Industrial Research, Pretoria, South Africa, fengelbrecht@csir.co.za

<sup>3</sup> School of Geography, Archaeology and Environmental Sciences, University of the Witwatersrand, Johannesburg, South Africa

The horizontal advection equation is an important expression in atmospheric modelling due to its prominence in the dynamical equations of the atmosphere. It is therefore important to continually improve and test numerical schemes that solve the advection equation. This paper reports on the development of a new flux-corrected scheme under development at the Council for Scientific and Industrial Research in Pretoria. This scheme solves the advection equation in flux form. It is based on a high order discretization of the equation, but makes use of a lower order scheme to improve conservation properties. The stability, accuracy and conservation properties of the low order solution of the flux form equation are compared in this paper to a low order discretization of the equation in advective form. This is achieved by performing Crowley's cone test to evaluate the properties of the two schemes. It is found that the accuracy and conservation abilities of the low order scheme solving the flux form equation are superior to that of the low order scheme solving the equation in advective form. Decreasing the spatial-step and time-step simultaneously whilst preserving the Courant number, the accuracy and conservation properties of the scheme solving the advective form of the equation are improved substantially. Notable improvements occur for reductions of the Courant number up to a factor of 8, where after the solution apparently becomes grid-converged. This is not the case for the scheme solving the equation in flux-form, where a decrease in spatial-step and time-step has negligible effect on accuracy and conservation properties. This is the result of the high diffusive nature of the solution, which implies a grid-converged solution even at high Courant numbers.

*Key words: Numerical modelling, advection, flux form*

## 1. Introduction

The horizontal advection equation is one of the most important expressions in atmospheric modelling due to its prominence in the dynamical equations of the atmosphere. The horizontal momentum, continuity and thermodynamic equations all contain the advection terms on the RHS of the advection equation:

$$\frac{\partial c}{\partial t} = -u \frac{\partial c}{\partial x} - v \frac{\partial c}{\partial y} = -\bar{U} \cdot \nabla c \quad (1.1)$$

Here  $c$  is a scalar quantity and  $u$  and  $v$  are constant-in-time wind components in the  $x$ - and  $y$ -directions respectively. In reality though, advection occurs in three dimensions and the wind-components are time-dependent, which makes solving the advection equation very complex. In fact, the advection equation has no analytical solution (Warner, 2011).

Since the advection equation has no analytical solution, numerical methods are used in order to approximate its solution (Warner, 2011). These numerical methods are however associated with errors. It is therefore of extreme importance that the errors involved in using a particular numerical scheme are known in order to guide the choice of scheme as well as for the improvement of forecasts.

Many numerical schemes exist in order to calculate an approximation of the solution for the advection equation. One of the simplest is the forward differencing in time, centred differencing in space finite differencing scheme. In this scheme the advection equation (1.1) is discretised in the following way:

$$c_{(i,j)}^{n+1} = c_{(i,j)}^n - \frac{\Delta t}{2\Delta x} u_{(i,j)} [(c_{(i+1,j)}^n - c_{(i-1,j)}^n) + v_{(i,j)} (c_{(i,j+1)}^n - c_{(i,j-1)}^n)] \quad (1.2)$$

where, the postscripts express the time-step such that a time  $t$  is defined as  $t_n = t_o + n\Delta t$  and the subscripts express the spatial-step such that a position  $x$  is defined as  $x_i = x_o + i\Delta x$  and a position  $y$  is defined as  $y_j = y_o + j\Delta y$  (Mesinger & Arakawa, 1976).  $\Delta x$  and  $\Delta y$  are spatial increments and  $\Delta t$  is the time increment. The number of time-steps is represented by  $n$ .

Flux form equations have become a popular form of discretizing the advection equation. This form of numerical method has the advantage of conserving mass through the advection process (Rood, 1987) and avoiding numerical instabilities (Phillips, 1959). The advection equation in flux form can be written as follows:

$$\frac{\partial c}{\partial t} + \frac{\partial(cu)}{\partial x} + \frac{\partial(cv)}{\partial y} - c \left( \frac{\partial u}{\partial t} + \frac{\partial v}{\partial t} \right) = 0 \quad (1.3)$$

A flux corrected transport scheme has been developed at the Council for Scientific and Industrial Research (CSIR) in Pretoria, South Africa. The first step for setting up this scheme is to calculate a transported and diffused solution. This scheme can be constructed in the following way to approximate the advection equation (1.1) and (1.3):

$$c_{(i,j)}^{n+1} = c_{(i,j)}^n - \frac{\Delta t}{2\Delta x} \left[ u_{(i+1/2,j)}^n (c_{(i+1,j)}^n + c_{(i,j)}^n) - \left| u_{(i+1/2,j)}^n \right| (c_{(i+1,j)}^n - c_{(i,j)}^n) - u_{(i-1/2,j)}^n (c_{(i-1,j)}^n + c_{(i,j)}^n) + \left| u_{(i-1/2,j)}^n \right| (c_{(i,j)}^n - c_{(i-1,j)}^n) + v_{(i,j+1/2)}^n (c_{(i,j+1)}^n + c_{(i,j)}^n) - \left| v_{(i,j+1/2)}^n \right| (c_{(i,j+1)}^n - c_{(i,j)}^n) - v_{(i,j-1/2)}^n (c_{(i,j-1)}^n + c_{(i,j)}^n) + \left| v_{(i,j-1/2)}^n \right| (c_{(i,j)}^n - c_{(i,j-1)}^n) \right] \quad (1.4)$$

A key property of this type of solution is that the amplitude of the scalar property being advected cannot grow artificially large.

The aim of this paper is to test the numerical stability, accuracy and mass conservation properties of the new scheme in equation (1.4) and compare it to that of the relatively simple finite difference method in equation (1.2)

## 2. The numerical advection test

The study involves simulating the advection of a scalar parameter. In order to simulate the advection process, Crowley's (1968) cone test was performed. The test involves the advection of a scalar quantity in the form of a cone by a constant-in-time wind field. The test is appropriate since the analytical solution of the test is known and can therefore be compared easily to the numerically obtained solution.

The experimental design of the experiment was based on that of McDonald (1984) as written in McGregor (1993). A 33x33 grid was used with  $-16\Delta \leq x \leq 16\Delta$ ,  $-16\Delta \leq y \leq 16\Delta$ , where  $\Delta = \Delta x = \Delta y = 200km$ . The wind field can be described by:

$$u = -\Omega y \text{ and } v = \Omega x \quad (2.1)$$

where,  $\Omega = 0.3636 \times 10^{-4}$ . The cone with a height of 100 units can be described by the following equation:

$$c(x, y) = -25\sqrt{(x - 8\Delta)^2 + y^2} + 100 \quad (2.2)$$

Using this experimental set-up, the cone was advected using the two different numerical methods.

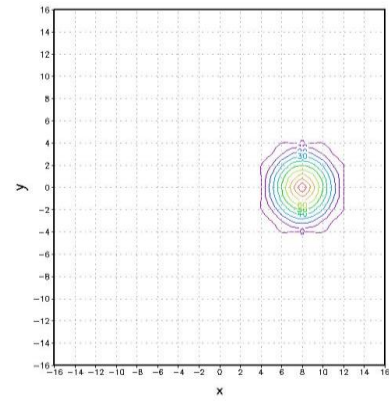


Figure 1.1. The cone in its initial state as described by equation (2.2)

Note that for the flux form scheme, the wind field was calculated at half-points by introducing a staggered C-grid. In order to test the numerical stability of each scheme, the maximum time-step (for a fixed spatial increment) that ensures stability of the cone after one revolution of the cone around the origin was found. Secondly, the accuracy of the cone after one revolution was tested by doing root-mean-square error (RMSE) calculations. The accuracy was tested for multiple time-step and spatial-step combinations (for all cases, the courant number was preserved). Finally, each schemes' ability to conserve mass was tested. This was done by applying a ratio of the sum of the absolute values of all the elevations of each of the points before and after advection. Since the position of the cone is irrelevant to its mass, for the case of advection, the test was performed after each time-step during one revolution of the cone. The conservation was also tested for multiple time-step and spatial step combinations.

## 3. Results

### 3.1. The stability of the schemes

It was found that the cone remained stable when advecting the cone through one revolution using the scheme solving the equation in advective form by using a time-step as large as 2.5 minutes. This means that it took the cone 1152 time-steps to complete one revolution.

Fig. 2.1 shows the cone throughout advection using the scheme solving the equation in advective form. Through advection, the cone was deformed significantly. In addition, as the cone was transported, unphysical negative values appeared in the cone's wake. The scheme also appears to underestimate the speed of the advection. This can be seen by the cone's final position in Fig. 2.1.4 in relation to the cone's analytical solution position in Fig 1.

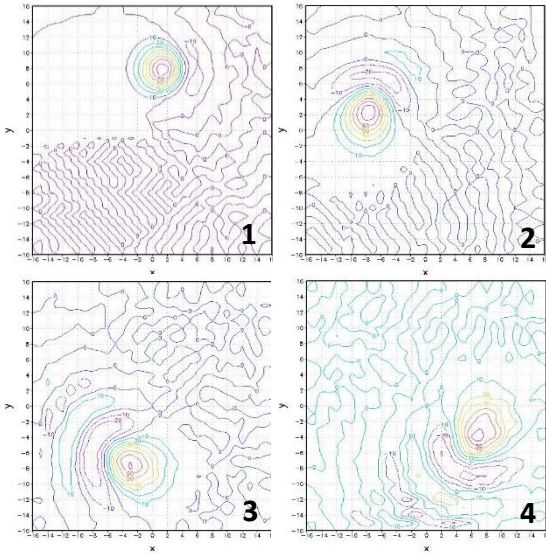


Figure 2.1. The cone after advection by means of the simple finite differencing scheme at 1) 0.25, 2) 0.5, 3) 0.75 and 4) a full revolution

Fig. 2.2 shows the cone throughout advection using the new flux form scheme. Through advection, the cone lost a lot of its height, with a maximum of just above 7 at its final position. However, as opposed to the simple scheme, no negative values appear through advection. These negative values are unrealistic. In addition, the speed of advection is correctly estimated, since the peak is found in the position that it started in (Fig. 2.1.4.).

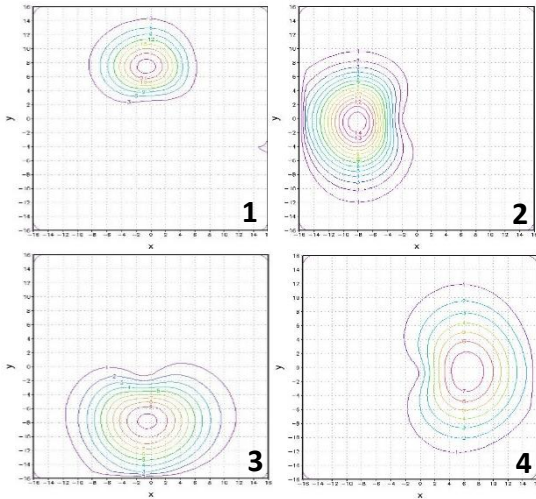


Figure 2.2. The cone after advection by means of the new flux form scheme at 1) 0.25, 2) 0.5, 3) 0.75 and 4) a full revolution

### 3.2. The accuracy of the schemes

Figure 3.1 shows the results of the RMSE tests performed after one revolution of the cone around the origin for the simple finite differencing scheme. The test was performed for multiple different time-steps and corresponding spatial-steps. For each test, the time-step and spatial-step were divided by  $2^\alpha$  for  $0 \leq \alpha \leq 5$  from the original time-step that ensured stability. The results show that the scheme is fairly inaccurate. The accuracy, however, does improve when the time-step (and spatial-step) are decreased.

This improvement tends to taper off when the time-step is decreased by a factor of 8 and above. This indicates that a decrease of time-step of a factor 8 only, is necessary to obtain a worthwhile increase in the accuracy.

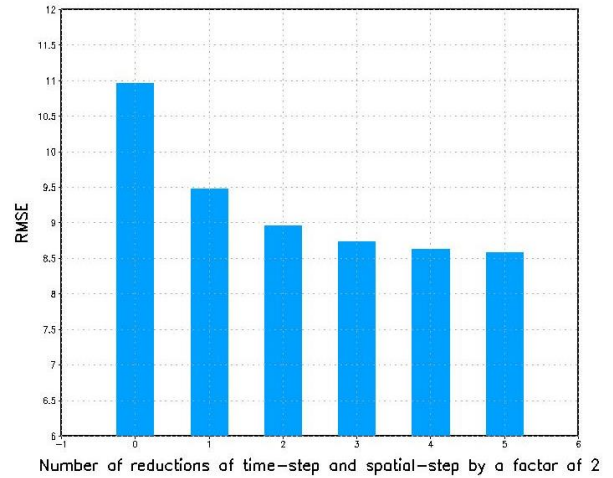


Figure 3.1. RMSE tests performed at various time- and spatial-steps for the simple scheme. The variable on the x-axis ( $\alpha$ ) denotes the number of times the original spatial step was divided by 2.

Figure 3.2 shows the results of the RMSE tests performed after one revolution of the cone around the origin for the new scheme. The test was again performed for multiple different time-steps and corresponding spatial-steps in exactly the same way as for the simple scheme. Although still fairly inaccurate, the scheme is more accurate than the simple scheme. Additionally, a decrease in time-step (and spatial-step) has a negligible effect on the schemes accuracy. The new scheme has about equal accuracy to the higher resolution runs of the simple scheme. Thus the scheme can be run at a lower resolution than the simple scheme whilst maintaining a similar accuracy.

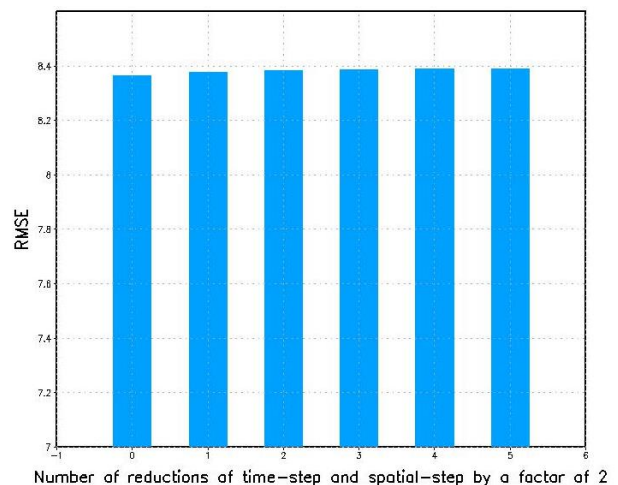


Figure 3.2: RMSE tests performed at various time- and spatial-steps for the new scheme. The variable on the x-axis ( $\alpha$ ) denotes the number of times the original spatial step was divided by 2.

### 3.3. The conservation of the schemes

Figure 4.1 shows the results of the conservation tests performed throughout one revolution of the cone around the origin for the scheme solving the equation in advective form. The test was again performed for multiple different time-steps and corresponding spatial-steps. For each test, the time-step and spatial-step was divided by  $2^\alpha$  for  $0 \leq \alpha \leq 5$  from the original time-step that ensured stability. The results show that the scheme results in the cone artificially quadrupling its mass. The conservation of the scheme does improve with a decreased time- and spatial-step. This improvement tapers off, again with a decrease of a factor of 8 and above.

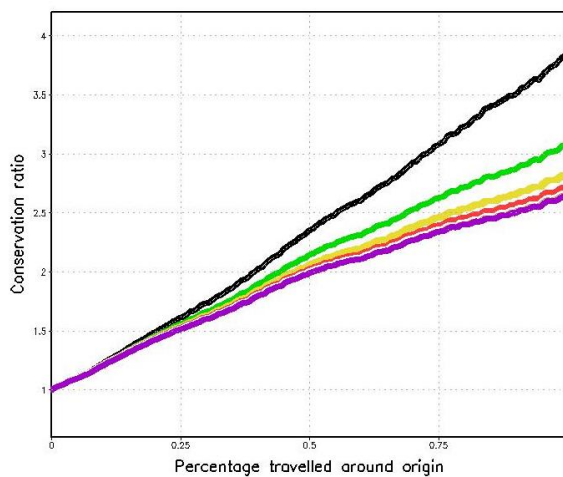


Figure 4.1. Conservation tests performed at various time- and spatial-steps for the simple scheme. The x-axis represents the variable  $\alpha$  whilst the y-axis represents the calculated conservation. The variable  $\alpha$  denotes the number of times the original spatial step was divided by 2. Black line:  $\alpha = 0$ , green line:  $\alpha = 1$ , yellow line:  $\alpha = 2$ , red line:  $\alpha = 3$  and the purple line:  $\alpha = 5$ .

Figure 4.2 shows the results of the conservation tests performed throughout one revolution of the cone around the origin for the new scheme. The test was again performed for multiple different time-steps and corresponding spatial-steps. For each test, the time-step and spatial-step was divided by  $2^\alpha$  from the original time-step that ensured stability. The results show that the cone loses mass as the cone is transported around the origin. A single line is seen in Fig. 4.2 since the conservation does not change with a decreased time- and spatial-step.

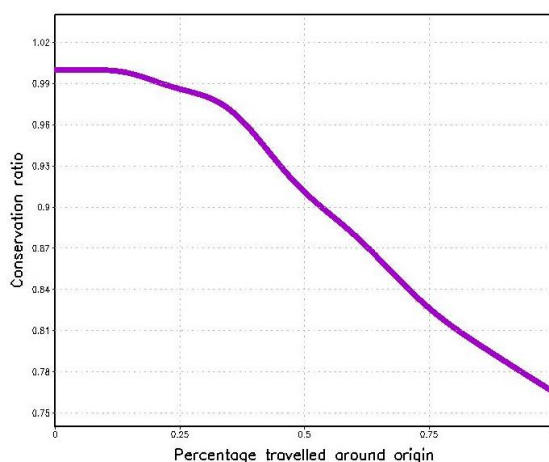


Figure 4.2. Conservation tests performed at various time- and spatial-steps for the new scheme. The x-axis represents the variable  $\alpha$  whilst the y-axis represents the calculated conservation. The variable  $\alpha$  denotes the number of times the original spatial step was divided by 2. Purple line is indicative of all values  $0 \leq \alpha \leq 5$ .

## 4. Conclusions and future work

The results show that the low order scheme solving the flux form equation is superior to the scheme solving the equation in advective form. Although mass is not fully conserved by the scheme solving the flux form of the equation, the artificial growth in mass resulting from solving the advective form of the equation with a low order scheme is avoided. The scheme solving the flux-form of the equation is also more accurate at lower resolutions. This is preferable so that computational expenses are kept to a minimum. In addition, the new scheme does not produce unrealistic, negative values and transports the cone at the correct rate. In future research, the low order scheme solving the flux form of the equation will be combined with a new higher order scheme in flux form, to improve on conservation properties and increase accuracy.

## 5. References

- Crowley, W. P., 1968. Numerical advection experiments. *Mo. Wea. Rev.*, **96**:1-11.
- McDonald, A., 1984. Accuracy of multiply-upstream semi-Lagrangian advection scheme. *Mon. Wea. Rev.*, **112**:1267-1275.
- McGregor, J. L., 1993. Economical determination of departure points for semi-Lagrangian models. *Mon. Wea. Rev.*, pp. 221-230.
- Mesinger, F. and Arakawa, A., 1976. *Numerical methods used in atmospheric models*. 1<sup>st</sup> ed. s.l.:Global Atmospheric Research Programme.
- Phillips, N. A., 1959. An example of non-linear computational instability. In: B. Bolin, ed. *The atmosphere and the sea in motion*. New York: Oxford University Press, pp. 501-504.
- Rood, R. B., 1987. Numerical advection algorithms and their role in atmospheric transport and chemistry models. *Review of Geophysics*, **25**:71-100.
- Warner, T. T., 2011. *Numerical weather and climate prediction*. New York: Cambridge University Press.

# SPATIAL AND TEMPORAL ASSESSMENT OF ATMOSPHERIC OC AND BC CONCENTRATIONS AT SOUTH AFRICAN DEBITS SITES

Petra Maritz\*<sup>1</sup>, Paul J. Beukes<sup>1</sup>, Pieter G. Van Zyl<sup>1</sup>, Engela H. Conradie<sup>1</sup>, Corinne Galy-Lacaux<sup>2</sup>, Cathy Liousse<sup>2</sup>

<sup>1</sup> Unit for Environmental Sciences and Management, North-West University, Potchefstroom Campus, Private Bag X6001, Potchefstroom, 2520, South Africa, \*[20229143@nwu.ac.ac](mailto:20229143@nwu.ac.ac)

<sup>2</sup> Laboratoire d'Aérologie, Université Paul Sabatier-CNRS, OMP, 14 Avenue Edouard Belin, 31400 Toulouse, France, [corinne.galy-lacaux@aero.obs-mip.fr](mailto:corinne.galy-lacaux@aero.obs-mip.fr)

## Abstract

The baseline of uncertainty in aerosol radiative forcing is large and depends on aerosol characteristics (e.g. size and composition), which can vary significantly on a regional scale. Sources (natural, anthropogenic and secondary) can be directly linked to the aerosol characteristics of a region, making monitoring campaigns to determine background aerosol composition in different regions very important. Up to 2005, Deposition of Biogeochemically Important Trace Species (DEBITS)-International Global Atmospheric Chemistry (IGAC) DEBITS in Africa (IDAF) project activities in southern Africa did not include aerosol measurements.

Campaigns to initiate aerosol monitoring were launched during the 2005 to 2007 period. Additionally OC/BC measurements for PM<sub>2.5</sub> and PM<sub>10</sub> fractions were started in 2009. OC and BC measured in SA were explored in terms of spatial and temporal patterns, mass fractions of the total aerosol mass, as well as possible sources. PM<sub>10</sub> and PM<sub>2.5</sub> samples were collected at five sites in SA operated within the DEBITS-IDAF network. OC were higher than BC concentrations at all sites in both size fractions. OC/BC ratios reflected the location of the different sites, as well as possible sources impacting these sites. The OC and BC mass fraction percentages of the total aerosol mass varied up to 24% and 12%, respectively. A relatively well define seasonal pattern was observed, with higher OC and BC measured from May to October, which coincide with the dry season in the interior of SA. An inverse seasonal pattern was observed for the fractional mass contributions of OC and BC to the total aerosol mass, which indicates substantially higher aerosol load during this time of the year. Biomass burning fires contribute significantly to regional OC and BC during the burning season, while large point sources did not contribute that significantly to regional OC and BC.

**Keywords:** organic carbon, black carbon, aerosol composition, spatial, temporal, DEBITS, IDAF

## SPATIAL AND TEMPORAL ASSESSMENT OF ATMOSPHERIC OC AND BC CONCENTRATIONS AT SOUTH AFRICAN DEBITS SITES

Petra Maritz\*<sup>1</sup>, Paul J. Beukes<sup>1</sup>, Pieter G. Van Zyl<sup>1</sup>, Engela H. Conradie<sup>1</sup>, Corinne Galy-Lacaux<sup>2</sup>, Cathy Liousse<sup>2</sup>

<sup>1</sup> Unit for Environmental Sciences and Management, North-West University, Potchefstroom Campus, Private Bag X6001, Potchefstroom, 2520, South Africa, \*[20229143@nwu.ac.ac](mailto:20229143@nwu.ac.ac)

<sup>2</sup> Laboratoire d'Aérologie, Université Paul Sabatier-CNRS, OMP, 14 Avenue Edouard Belin, 31400 Toulouse, France, [corinne.galy-lacaux@aero.obs-mip.fr](mailto:corinne.galy-lacaux@aero.obs-mip.fr)

## 1. Introduction

The baseline of uncertainty in aerosol radiative forcing is large and depends on aerosol characteristics (e.g. size and composition), which can vary significantly on a regional scale. Sources (natural and anthropogenic) can be directly linked to the aerosol characteristics of a region, making monitoring campaigns to determine aerosol composition in different regions very important. (Seinfeld and Pandis 2006)

Limited data currently exists for atmospheric aerosol black carbon (BC) and organic carbon (OC) in South Africa. In this study, BC and OC concentrations were explored in terms of spatial and temporal patterns, mass fractions of BC and OC of the overall aerosol mass, as well as possible sources.

Primary pollutants, of which BC is an example, are emitted directly from the source. Certain primary pollutants can react with other pollutants to form secondary pollutants. OC can either be a primary or secondary pollutant, e.g. formed by gas-to-particle conversion of volatile organic compounds (VOCs) in the atmosphere (nucleation and condensation of gaseous precursors) (Putaud et al. 2004; Pöschl 2005).

Greenhouse gases (GHG) and BC absorb terrestrial long wave radiation causing an increase of atmospheric temperature. In contrast, OC generally reflects incoming radiation, cooling the atmosphere. GHGs have a long residence time in the atmosphere (10 to 100 years), while the residence time of aerosols is usually only a week or more. The climatic effects of aerosols are therefore particularly important from a regional perspective. Aerosols are also important from an air quality perspective, especially since ultrafine particles (diameter smaller than 100nm) are small enough to go through the membranes of the respiratory tract and into the blood stream. They can then be transported to the brain (Oberdörster et al. 2004; Pöschl 2005).

Up to 2005, DEBITS (Deposition of Biogeochemical Import Trace Species) activities in South Africa did not include aerosol measurements. In order to initiate aerosol monitoring, campaigns were launched during the 2005 to 2007 period. Additionally, OC and BC measurements for the PM<sub>10</sub> and PM<sub>2.5</sub> (particulate matter smaller than or equal to 10 and 2.5 µm, respectively) fractions were started in 2009. PM<sub>10</sub> and PM<sub>2.5</sub> samples were

collected at five sampling sites in South Africa operated within the DEBITS network, i.e. Louis Trichardt, Skukuza, Vaal Triangle, Amersfoort and Botsalano, with MiniVol samplers. The selected sites are mostly located in rural areas, but with the surrounding atmosphere influenced by industries, transportation, biomass burning, etc. Winters are characterised by an increase in biomass burning (fires) and combustion for domestic use (cooking and space heating). Samples were analysed with a Thermal/Optical Carbon analyser (Desert Research Institute).

## 2. Experimental

### 2.1. Sampling sites

Aerosol samples were collected at five sampling sites in South Africa operated within the IDAF network, i.e. Louis Trichardt (LT), Skukuza (SK), Vaal Triangle (VT), Amersfoort (AF) and Botsalano (BS). The South African IDAF sites are located in the north eastern part of the interior of South Africa.

### 2.2. Sampling

24-hour PM<sub>2.5</sub> and PM<sub>10</sub> aerosol samples were collected on quartz filters (with a deposit area of 12.56 cm<sup>2</sup>) once a month from March 2009 to April 2011 at each site. A total of 258 samples were collected, i.e. 52 samples for each site, except for BS for which only 50 samples were collected. Since both size fractions were sampled each month at each site, one half of the samples were PM<sub>2.5</sub> and the other half PM<sub>10</sub>. The quartz filters were prebaked at 900°C for 4 hours and cooled down in a desiccator, prior to sample collection. MiniVol samplers developed by the United States Environmental Protection Agency (US-EPA) and the Lane Regional Air Pollution Authority were used during sampling (Baldauf et al. 2001). These samplers have a pump that is controlled by a programmable timer, which allows for the collection of samples at a constant flow rate over a pre-determined time period. In this study, samples were collected at a flow rate of 5 L/min, which was verified by using a handheld flow meter that was supplied with the MiniVol samplers. Filters were handled with tweezers while wearing surgical gloves, as a precautionary measure to prevent possible contamination of the filters. All thermally pre-treated filters were also visually inspected to ensure that there were no weak spots or flaws. After inspection, acceptable filters were weighed and packed in airtight Petri dish holders until they were used

for sampling. After sampling, the filters were again placed in Petri dish holders, sealed off, bagged and stored in a portable refrigerator for transport to the laboratory. At the laboratory the sealed filters were stored in a conventional refrigerator. 24 hours prior to analysis, samples were removed from the refrigerator and weighed just prior to analysis.

### 2.3. OC and BC analysis

Several methods can be used to analyse OC and BC collected on filters (Chow et al. 2001). It was decided to apply the IMPROVE thermal/optical (TOR) protocol (Chow et al. 1993; Chow et al. 2004; Environmental analysis facility 2008; Guillaume et al. 2008) by using a Desert Research Institute (DRI) analyser. In this method, filters are submitted to volatilization at temperatures of 120, 250, 450 and 550°C in a pure Helium (He) atmosphere and thereafter to combustion at temperatures of 550, 700 and 800°C in a mixture of He (98%) and oxygen (O<sub>2</sub>) (2%) atmosphere. The carbon compounds that are released are then converted to CO<sub>2</sub> in an oxidation furnace with a manganese dioxide (MnO<sub>2</sub>) catalyst at 932°C. Then, the flow passes into a digester where the CO<sub>2</sub> is reduced to methane (CH<sub>4</sub>) on a nickel-catalysed reaction surface. The amount of CH<sub>4</sub> formed is detected by a flame ionization detector (FID), which is converted to carbon mass using a calibration coefficient. The carbon mass peaks detected correspond to the different temperatures at which the seven separate carbon fractions, which include four OC and three BC fractions, were released. These fractions were depicted as different peaks on the thermogram, of which the surface areas were proportional to the amount of CH<sub>4</sub> detected.

The reflectance from the deposited sample is monitored throughout the afore-mentioned analysis. This reflectance usually decreases during the volatilization process due to the pyrolysis of OC. When oxygen is added, the reflectance is increased as the BC is burnt and removed. OC is defined as the fraction which evolves prior to re-attainment of the original reflectance (the non-absorbing light particles) and BC is defined as the fraction which evolved after the original reflectance has been attained (the light absorbing particles). The DRI instrument can detect OC and BC as low as 0.1 µg/cm<sup>2</sup>.

### 3. Results and conclusions

OC and BC results showed that the total carbonaceous content decreased during the summer due to less biomass burning (fires). BC was the highest at the industrially influenced sites, while OC was highest at regional background sites. OC was higher than BC concentrations at all sites in both size fractions. Most OC and BC occurred in the PM<sub>2.5</sub> fraction. OC/BC ratios reflected the setting of the different DEBITS sites, with sites in or close to anthropogenic source regions having the lowest OC/BC ratios, while background sites had the highest OC/BC ratios.

The OC mass fraction percentage of the total aerosol weight varied between 0 and 24% and the BC between 0 and 12%. The highest OC mass fraction was found at Skukuza, which was attributed to both natural (lies within the savannah biome) and anthropogenic (dominant path of air mass movement from the anthropogenic industrial hub of South Africa) reasons. The highest mass fraction of BC was found in the Vaal Triangle, since it is situated within a well-known anthropogenic source region. Household combustion for space heating and cooking also seemed to make a significant contribution to BC at this site in the cold winter months.

A relatively well-defined seasonal pattern was observed, with higher OC and BC concentrations measured from May to October, which coincides with the dry season in the interior of South Africa. Positive correlations between OC and BC concentrations with the distance back trajectories passed fires were observed, indicating that fires contribute significantly to both atmospheric OC and BC during the burning season.

### 4. References

- Baldauf, R.W., Lane, D.D., Marotz, G.A., & Wiener, R.W. (2001). Performance evaluation of the portable MiniVOL particulate matter sampler. *Atmospheric Environment*, 35, 6087-6091. PII: S1352-2310(01)00403-4.
- Chow, J.C., Watson, J.G., Pritchett, L.C., Pierson, W.R., Frazier, C.A., & Purcell, R.G. (1993). The dri thermal/optical reflectance carbon analysis system: description, evaluation and applications in U.S. Air quality studies. *Atmospheric Environment, Part A General Topics*, 27(8), 1185-1201.

Chow, J.C., Watson, J.G., Crow, D., Lowenthal, D.H., & Merrifield, T. (2001). Comparison of IMPROVE and NIOSH carbon measurements. *Aerosol Science and Technology*, 34, 23-24.

Chow, J.C., Watson, J.G., Kuhns, H., Etyemezian, V., Lowenthal, D.H., Crow, D., Kohl, S.D., Engelbrecht, J.P., & Green, M.C. (2004). Source profiles for industrial, mobile, and area sources in the Big Bend Regional Aerosol Visibility and Observational study. *Chemosphere*, 54, 185-208.

Environmental analysis facility. (2008). DRI Standard operating procedure. 86p. Laboratoire d'Aérodologie – UMR 5560. <http://www.aero.obs-mip.fr/spip.php?article489>. Accessed 18 July 2011.

Guillame, B., Liousse, C., Galy-Lacaux, C., Rosset, R., Gardrat, E., Cachier, H., Bessagnet, B., & Poisson, N. (2008). Modeling exceptional high concentrations of carbonaceous aerosols observed at Pic du Midi in spring-summer 2003: Comparison with Sonnblick and Puy de Dôme. *Atmospheric Environment*, 42, 5140-5149. doi: 10.1016/j.atmosenv.2008.02.024.

Oberdörster, G., Sharp, S., Atudorei, V., Elder, A., Gelein, R., Kreyling, W., & Cox, C. (2004). Translocation of inhaled ultrafine particles to the brain. *Inhalation toxicology*, 16, 437-445. doi: 10.1080/08958370490439597.

Pöschl, U. (2005). Atmospheric Aerosols: Composition, Transformation, Climate and Health Effects. *Atmospheric Chemistry: Reviews. Angew. Chem. Int. Ed*, 44, 7520-7540. doi: 10.1002/anie.200501122.

Putaud, J.-P., Raes, F., Van Dingenen, R., Brüggemann, E., Facchini, M.-C., Decesari, S., Fuzzi, S., Gehrig, R., Hüglin, C., Laj, P., Lorbeer, G., Maenhaut, W., Mihalopoulos, N., Müller, K., Querol, X., Rodriguez, S., Schneider, J., Spindler, G., Ten Brink, H., Tørseth, K., & Wiedensohler, A. (2004). A European aerosol phenomenology-2: chemical characteristics of particulate matter at kerbside, urban, rural and background sites in Europe. *Atmospheric Environment*, 38, 2579-2595. doi: 10.1016/j.atmosenv.2004.01.041.

Seinfeld, J. H., & Pandis, S. N. (2006). *Atmospheric Chemistry and Physics: From Air Pollution to Climate Change*. John Wiley & Sons Inc.

# AEROSOL OPTICAL DEPTH MEASUREMENTS OVER PRETORIA USING CSIR LIDAR AND SUN-PHOTOMETER: A CASE STUDY

Lerato Shikwambana<sup>1,2\*</sup> and Venkataraman Sivakumar<sup>1</sup>

<sup>1</sup>School of Chemistry and Physics, University of KwaZulu-Natal, Durban 4000, South Africa

<sup>2</sup>CSIR National Laser Centre, PO Box 395, Pretoria 0001, South Africa

The aerosol optical depth (AOD) was measured over Pretoria (25.75 S; 28.28 E) using the CSIR mobile Light Detection And Ranging (LIDAR) system and the sun photometer which is part of the Aerosol Robotic Network (AERONET). The measurements were well in agreement for 26 June 2014 with AOD values of 0.1206 and 0.1233 by LIDAR and the sun photometer, respectively. For 27 June 2014 the AOD values of 0.2656 and 0.2480 for LIDAR and the sun photometer were observed. However, for 23 and 24 June 2014 the AOD measurements were not in good agreement.

*Keywords:* AOD, LIDAR, Aerosols, Planetary boundary layer

## 1. Introduction

Tropospheric aerosols arise from natural sources, such as airborne dust, sea-spray and volcanoes, and also from anthropogenic sources as combustion of fossil fuels and biomass burning activities and from gas-to-particles conversion processes (Feiyue et al, 2008; Khor et al, 2014). Aerosols have significant potential to influence the radiation transfer through the atmosphere and atmosphere water cycle, thus influence the Earth's climate directly and indirectly (Hui et al, 2005).

The role of aerosol direct forcing on climate may be similar in magnitude to the effects greenhouse gases and can range from cooling to warming depending on the aerosol composition (Hand et al, 2004). In order to achieve a better understanding of aerosol role in meteorological and climatological processes, systematic observations with high vertical and temporal resolution with high accuracy are needed (Veerabuthiran et al, 2011).

The aerosol optical depth (AOD), which is the integral of the optical extinction coefficient of the atmospheric aerosols from the surface to the top of the atmosphere, is an important parameter for visibility degradation (due to atmospheric pollution), solar radiation extinction, climate effects, and tropospheric corrections in remote sensing (Qiu, 1997). Optical methods for measuring aerosol physical-optical parameters can be classified into two categories: passive and active (Qui, 1997). A sun-photometer is an example of a ground based passive instrument that can be used for the study of aerosols. The Aerosol Robotic Network (AERONET) is a federation of ground-based remote sensing aerosol network which provides a long-term, continuous and readily accessible public domain database of aerosol optical, microphysical and radiative properties for aerosol research and

characterization (Sivakumar et al, 2008). A Light Detection And Ranging (LIDAR) ground based system is an example of an active instrument which can be used for the study of aerosol properties. This system can also be used to study the planetary boundary layer (PBL). The PBL is directly influenced by the Earth's surface and responds to surface forcing by frictional drag, evaporation and transpiration, and sensible heat transfer with a timescale of an hour or less (Baars et al, 2008). The PBL is important because humans live in it and it is where and how most of the solar heating gets into the atmosphere.

In this study, we compare the AOD measured by LIDAR and a sun-photometer. Although the two systems have different methods, the sun photometer can be used to reinforce the aerosol profiling capabilities of a LIDAR (Khor et al, 2014).

## 2. Instrumentation and Method

### 2.1 Sun Photometer

The CIMEL spectral radiometer (sun photometer) is used and is part of the AERONET group. It makes direct sun measurements in eight spectral bands between 340nm and 1640 nm (Khor et al, 2014). The instrument is placed on top of a building at the Council for Scientific and Industrial Research (CSIR), (see Figure 1), and it is located at Pretoria with geo coordinates of latitude 25.75661° south and longitude 28.27972° east.

### 2.2 LIDAR

The CSIR mobile LIDAR system, (see Figure 2), was used to carry out aerosol measurements at the CSIR in Pretoria. The system uses an Nd:YAG laser operated at a wavelength of 532 nm with an average pulse energy of about 90 mJ. The laser



Figure 1: A picture of the AERONET sun photometer located at the CSIR.

beam has a pulse width of 7 ns and a pulse repetition rate 10 Hz. For the receiver the system uses a Newtonian telescope with a diameter of 404 mm, a Hamamatsu photo-multiplier tube (PMT) and a multicore optical fiber. Sharma et al (2011) describes the CSIR mobile LIDAR system in detail.



Figure 2: A picture of the CSIR mobile LIDAR system.

The received signal intensity is described in terms of the LIDAR equation as given by (Klett, 1981)

$$P(r) = P_o \frac{c\tau}{2} A \frac{\beta(r)}{r^2} e^{-2 \int_0^r \sigma(r') dr'} \quad (1)$$

where  $P_o$  is the transmitted laser power in terms of photon counts at 532 nm,  $c$  is the velocity of light,  $\tau$  is the pulse duration,  $A$  is the effective system receiver area,  $\beta(r)$  is the backscattering coefficient,  $\sigma(r)$  is the extinction coefficient and  $r$  is the range. The backscattering and extinction coefficients are

given by contribution of both aerosols and molecules and are expressed as:

$$\beta(r) = \beta_{aer}(r) + \beta_{mol}(r) \quad (2)$$

$$\sigma(r) = \sigma_{aer}(r) + \sigma_{mol}(r) \quad (3)$$

where subscript (*aer*) and (*mol*) indicate aerosols and molecules, respectively. Solving equations (1)-(3) yields equation (4)

$$\beta_{aer}(r) + \beta_{mol}(r) = \frac{X(r) \exp[-2(S_{aer} - S_{mol}) \int_{r_c}^r \beta_{mol}(r) dr]}{\beta_{aer}(r) + \beta_{mol}(r)} \quad (4)$$

$$2S_{aer} \int_{r_c}^r X(r) \exp[-2(S_{aer} - S_{mol}) \int_{r_c}^r \beta_{mol}(r') dr'] dr$$

where  $X(r)$  is the range normalized signal given by  $I(r)r^2$  and  $r_c$  is the reference height.

The extinction coefficient and optical depth (OD) is defined as follows (Chiang et al., 2007):

$$\alpha_{aer}(r) = S_{aer}(r) \beta_{aer}(r) \quad (5)$$

$$AOD = \int_{r_c}^r \alpha_{aer}(r) dr. \quad (6)$$

### 3. Results and discussion

Figure 3 shows four day (23, 24, 26, 27 June 2014) observations during the winter season of aerosols using the CSIR mobile LIDAR system. The planetary boundary layer (PBL) was observed at different heights in the mornings but in the afternoons the PBL was observed at heights of about 1000 m for 23, 24 and 26 June 2014. These observations suggest that the PBL starts becoming stable in the early afternoons. However, on 27 June 2014 a different profile was observed. In the morning around 09:58 until 10:15 a cloud at about 3000 m was observed. An increase of the PBL from 500 m to about 1200 m was observed from 09:58 to 15:28 local time. In the mid-afternoon (around 15:10) clouds at between 2000 to 3100 m were observed.

The AOD values integrated from ground to 1 km level are shown in Figure 4. The AOD trend for the different days was similar (see Figure 4), in the morning a high AOD value was observed and a steady decrease was observed. In the mid-afternoon the AOD value started to stabiles. However, different values of the AOD were

observed every day. This is caused by the different atmospheric conditions that occur daily.

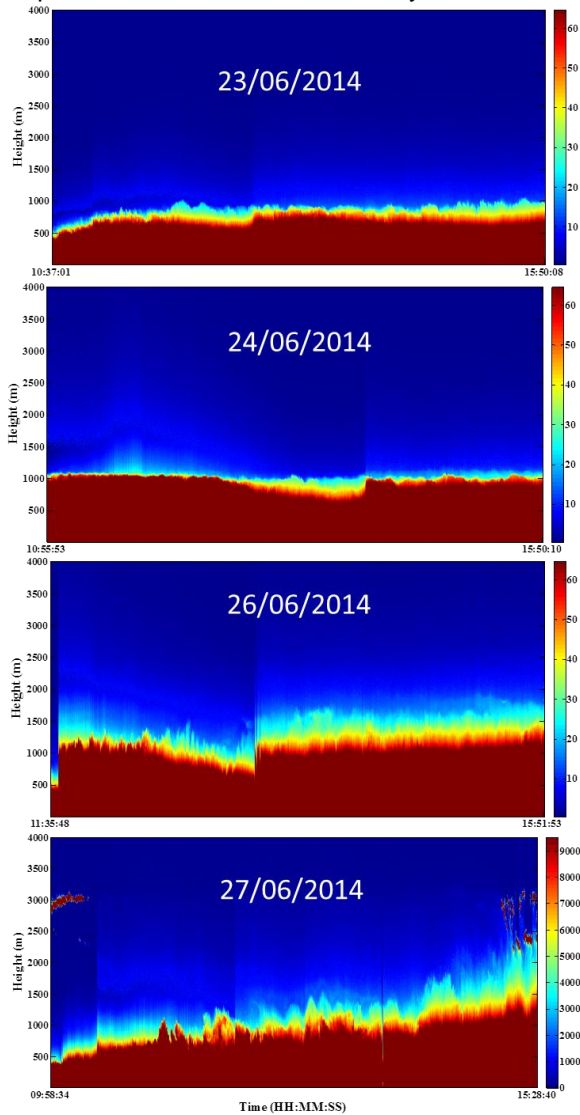


Figure 3: Height-time color map of CSIR-NLC mobile LIDAR backscatter signal returns at daytime in Pretoria on 23, 24, 26 and 27 July 2014.

The AOD was also calculated at the different heights of the atmosphere; 1-2 km, 2-3 km and 3-4 km for the different days. At heights of 1-2 km, higher values of AOD were observed compared to the AOD values at heights of 2-3 and 3-4 km. For the days of 23, 24 and 26 June 2014 this is clearly seen. However, on 27 June 2014 at around 15:15 local time there was a sudden increase in the AOD values at the heights of 1-2 and 2-3 km. This was caused by the clouds that were present at heights of 2-3 km.

The sun photometer AOD measurements for 23, 24 and 26 June 2014 showed low variations of the AOD values at around 0.1-0.12, 0.15-0.2 and 0.1-0.16 respectively (see Figure 5). However, the 27 June 2014 measurements showed big variations in the AOD value between 0.15-0.35. This might be

caused by the unstable PBL observed by LIDAR in Figure 3.

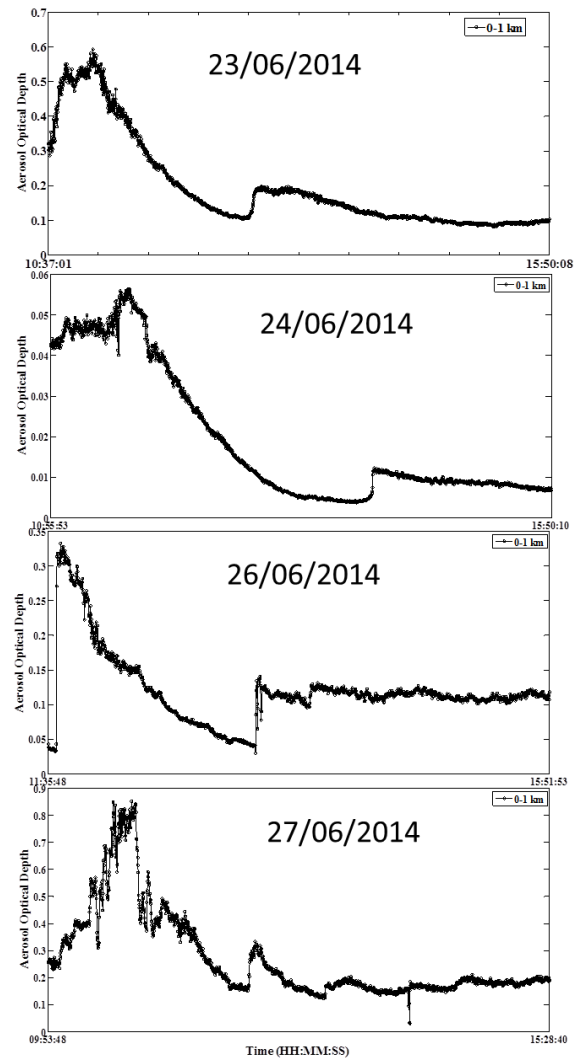


Figure 4: Aerosol optical depth obtained by LIDAR at the planetary boundary layer between 0-1000 m for the different days.

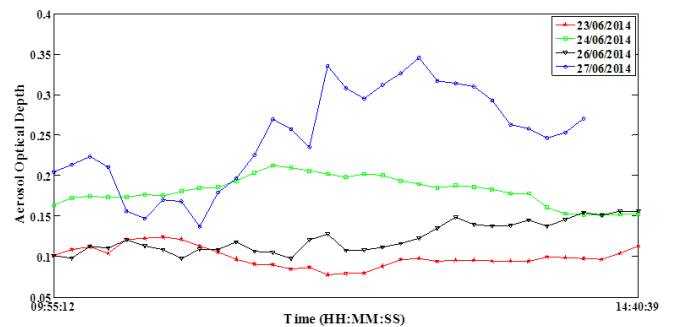


Figure 5: Aerosol optical depth obtained by the sun photometer at the 500 nm wavelength at different days.

The AOD measured using the 500 nm wavelength of the sun photometer was used because it is the closest one to the LIDAR operational wavelength of 532 nm. AOD is mostly

affected by smaller aerosol particles (with sizes of 100 to 300 nm, i.e. those belonging to the submicron fraction) (Kolev et al, 2006). The averaged LIDAR AOD from 0-4 km was calculated using equation 6 and compared to the sun photometer as shown in Table 1. For 26 and 27 June 2014 the LIDAR and sunphotometer measurements were in agreement with each other for the respective days. However, discrepancies might have been caused by the following: 1) The LIDAR measurements were carry out vertically while the sunphotometer carries out the measurements at an angle directly at the sun, 2) the LIDAR was operated at a particular period of the day for certain hours while the sunphotometer operates for about 12 hours in a day, 3) for LIDAR the AOD was calculated by integrating the extinction coefficient from ground to about 4 km, in our case, whereas in the sunphotometer the total column atmospheric aerosol optical depth from the sun to the ground was used. One of the advantages of using LIDAR is that it can give vertical extinction coefficients whereas the sunphotometer cannot. The AOD value of ~0.12 and 0.25 were observed on 26 and 27 June 2014 respectively. These values indicate a relatively clean atmosphere over the observation site.

Table 1: Comparison of LIDAR and sun photometer AOD measurements

Date	AOD LIDAR	AOD Sun photometer
26/06/2014	0.1206	0.1233±0.0188
27/06/2014	0.2652	0.2480±0.0605

#### 4. Conclusion

The AOD measurements were carried out for four days at Pretoria using the CSIR mobile LIDAR system. The measurements were compared to the sun photometer located at the CSIR. The measurements were in agreement for 26 and 27 June 2014 when the system was optimised. The mobile LIDAR system is reliable and can be used to carry out measurements in other parts of the country.

#### 5. Acknowledgments

We would also like to thank Henk van Wyk and Ameeth Sharma for their technical assistance on the LIDAR system. We thank Derek Griffith for his effort in establishing and maintaining the AERONET Pretoria CSIR-DPSS site.

#### 6. References

Baars H., Ansmann A., Engelmann R., Althausen D., (2008). Continuous monitoring of the boundary-layer

- top with lidar, *Atmospheric Chemistry and Physics*, vol 8, 7281–7296
- Chiang C.W., Chen W. M., Liang W. N, Das S.K., Nee J. B., (2007). Optical properties of tropospheric aerosols based on measurements of lidar, sun-photometer, and visibility at Chung-Li (25°N, 121°E), *Atmospheric Environment*, vol 41, 4128–4137.
- Feiyu M., Wei G., Zhongmin Z., Pingxiang L., (2008). The Ground-based Lidar Combined with Sunphotometer for Aerosol Optical Depth Retrieval, *Proceedings of SPIE*, Vol. 7145, 71452R-1-71452R-9
- Hand J. L., Kreidenweis S. M., Slusser J., Scott G., (2004). Comparisons of aerosol optical properties derived from Sun photometry to estimates inferred from surface measurements in Big Bend National Park, Texas, *Atmospheric Environment*, vol 38, 6813–6821.
- Hui Y., Wenqing L, Yihuai L, Jianguo L., Qingnong W., Dexi W., Cheng L, Takeuchi N, (2005). Tropospheric aerosol observations by Lidar at Naqu, Optical Technologies for atmospheric, ocean, and environmental studies, *Proceedings of SPIE*, Vol. 5832, 148-155.
- Khor W. Y., Hee S. W., Tan F., Lim H. S., Jafri M. M. Z. and Holben B, (2014). Comparison of Aerosol optical depth (AOD) derived from AERONET sunphotometer and Lidar system, *Earth and Environmental Science*, vol 20, 1-9.
- Klett J. D., (1981). Stable analytical inversion solution for processing lidar returns, *Appl. Opt.*, vol 20, 211–220
- Kolev N., Grigorov I., Kolev I., Devara P. C. S., Raj P. E., Dani K. K. (2007). Lidar and Sun photometer observations of atmospheric boundary-layer characteristics over an urban area in a mountain valley, *Boundary-Layer Meteorol*, vol 124, 99–115
- Qui J., (1997). A Method to Determine Atmospheric Aerosol Optical Depth Using Total Direct Solar Radiation, *Journal of atmospheric sciences*, vol 55, 744-757
- Sharma A., Sivakumar V., Bollig C, van der Westhuizen C. and Moema D (2009), System description of the mobile LIDAR of the CSIR, South Africa, *South African Journal of Science*, vol 105, 456-462
- Sivakumar V, Tesfaye M., Alemu W., Sharma A., Bollig C. and Mengistu G. (2008), Aerosol measurements over South Africa using satellite, sun-photometer and LIDAR, *Advances in Geosciences*, vol 16, 253-262
- Veerabuthiran S., Razdan A. K., Jindal M. K., Dubey D. K., Sharma R. C., (2011). *Mie lidar observations of lower tropospheric aerosols and clouds*, *Spectrochimica Acta Part A: Molecular and Biomolecular Spectroscopy*, vol 84, 32-36.